

THE UNIVERSITY OF HULL

DNA Bases in Crystal Engineering

Being a Thesis submitted for the Degree of Doctor of Philosophy

in the University of Hull

by

Kreshnik Hoxha

MChem (Hons)

November 2014

ACKNOWLEDGEMENTS

Though this thesis bears my name in the front page, I could have never reached the depths of this study without those who have helped me in innumerable ways and influenced my path in life. I consider myself lucky to have been surrounded by role models who taught me the value of diligence and education in one's life.

I am extremely grateful to my supervisor Dr Timothy J. Prior for providing me with a rare degree of intellectual support and invaluable advice throughout my PhD. Tim's erudition and attention for detail has been pivotal to my work and growth as a researcher. I cannot thank him enough for his continued support and I am especially indebted to him for his prompt feedback while writing the chapters of this thesis. The writing of this thesis would have not been possible without his guidance and help.

I am thankful to my chemistry teacher in Kosovo, Shyhrete Bilalli, who fostered my interest in chemistry with her impeccable teaching and enthusiasm. I owe my deepest gratitude to David Coulson at Seaford College who gave me the opportunity to experience the excitement of practical work in the laboratory – a concept that was alien to me until I moved to the United Kingdom for A-levels.

During my undergraduate and postgraduate years at Hull, Dr M. Grazia Francesconi and Prof. Tina Overton have provided me with indispensable support and I am thankful for this. I would also like to thank Dr Nigel Young, Dr Jay Wadhawan, Dr Jennifer Armstrong, Carol Kennedy, Ian Dobson and Bob Knight for all their help. I owe an important debt to Dr Charlotte Wiles for her insightful scientific comments and a rare ability of tackling problems with such analytical fervour. A special mention goes to the University of Hull for the provision of funding for this research.

Family and friends have been an indispensable source of support and motivation during the three years of my PhD. Mentioning names runs the risk of unfairly missing out many genuine people. However, I must stress that I am personally indebted to Besart Stavileci, Rrita Pula, Shkamb and Gurra Qavdarbasha, Gresa Islami, Lura Limani, Agon Maliqi, Dita Dobranja and Jeta Xharra for being pillars of support, inspiration and believing in me. I am thankful to my housemates over the three years Giorgos Vryonides, Maureen Wanjiku, Maria Anastasi and Kevin Wright for their ability to inject optimism when it got tough. My fellow colleagues have been a tremendous part of my PhD. I would like to especially thank Sophie Darragh, Luís Azevedo, Flore-Anne Poujade, Naomi Jones, Nadiyah Alahmadi, Lak Tapala, Matt Simmons and Simon Fellows for generating such riveting discussions about science and life in general. Special thanks go to Ahamd Al-Abdin and Eirini Arvanitaki for their support during the writing of this thesis.

My appreciation and respect goes to my aunt Prof. Natyra Karahoda and uncle Prof. Veton Hoxha for inspiring me to pursue a PhD and for always reminding me of the value of education.

To express any gratitude to my cousins Jehona and Era Gjurgjeala would be tantamount to understating their role in the completion of this PhD. I am truly indebted to both of them for most generously offering their guidance and priceless moral support throughout my education in the United Kingdom.

The writing of this thesis would have not been possible if it was not for the sincere moral support and continuous encouragement of my parents, Shukri and Valerija, and my sister Kaltrina. I am permanently indebted to them for their sacrifice, unwavering faith in me and for always being voices of reason. The least I could do in return is to wholeheartedly dedicate this thesis to the three of them.

ABSTRACT

The work described in this thesis focuses on understanding the solid state interactions of organic molecules such as DNA nucleobases using established principles from crystal engineering and the synthon theory. Studying the intermolecular interactions is an indispensable tool to the crystal engineer when it comes to identifying functional groups which generate synthons that govern molecular recognition and self-assembly.

Chapter 3 focuses on the growth and design of single crystal materials of DNA bases and their carboxylic acid derivatives with various other molecules. The aim of the chapter was to probe the hydrogen bonding displayed by these systems. The challenges associated with dissolving the nucleobases in organic and aqueous solvents prompted alternative synthetic route to mitigate solubility challenges. Altering the pH of the system was found useful in aiding dissolution. Such synthetic approach has led to the preparation of novel nucleobase salts of *bis*-guaninium sulphate in three different hydrate forms. The material obtained was a channel hydrate and it was possible to remove water partially and fully while retaining crystallinity. No structural collapse was observed upon full dehydration and the material obtained contained an empty channel hydrate. Co-crystallisation of cytosine with 1,10-phenanthroline is discussed in depth and the results are compared to crystal structure prediction results to rationalise co-crystal formation from an energetic perspective. Calculations on the energy landscape revealed that in the case of cytosine and 1,10-phenanthroline there is a favourable energetic driving force for co-crystallisation. This, however, does not apply to the co-crystallisation of the other DNA bases with 1,10-phenanthroline as these systems did not produce co-crystals and remained as mixtures of precursors. The chapter also describes structural features of thymine acetic acid, melaminium nitrilotriacetate trihydrate and co-crystals of caffeine with 2-nitroterephthalic acid. These structures are closely examined for their hydrogen bonding motifs.

Chapter 4 covers a wide range of coordination compounds which relate to hydrogen-bonded networks of DNA nucleobases and their carboxylic acid derivatives. These complex architectures contain both coordination bonds as well as intermolecular interactions in the form of hydrogen bonding and stacking interactions. Metal-dipicolinate complexes treated with adenine and cytosine afforded hydrogen-bonded networks where protonated DNA bases interacted with the ligand *via* hydrogen bonding. The chapter discusses the role of water molecules in acting as spacers and stabilising crystal structure, especially in cases where there is an imbalance of hydrogen bond donors and acceptors.

Orotic acid was heavily used owing to its chelating nature. This part of Chapter 4 focuses on novel crystal structures where orotic acid utilises its hydrogen bonding capability. An extensive discussion is provided on how the level of hydration impacts crystal packing and alters synthon formation. In addition, the chapter also focuses on the structural changes resulting from changing the position of the functional group in the ligands.

ABBREVIATIONS

CSD – Cambridge Structural Database

CIF – Crystallographic Information File

CSP – Crystal Structure Prediction

DNA – Deoxyribonucleic acid

ICP – Inductively Coupled Plasma

IUPAC – International Union of Pure and Applied Chemistry

RNA – Ribonucleic Acid

TGA – Thermogravimetric Analysis

Å - Angstrom

F_{hkl} – Structure Factors

PUBLICATIONS AND PRESENTATIONS

Publications and presentations containing work described in this thesis:

1. Hoxha, K.; Prior, T. J. *Solid State Sci.* **2013**, *23*, 102.
2. Hoxha, K.; Prior, T. J. *Acta Crystallogr., Sect. E* **2013**, *69*, o1674
3. Hoxha, K.; Case, D. H.; Day, G. M.; Prior, T. J. *Manuscript in preparation*
4. Hoxha, K. *DNA bases in crystal engineering*, Oral presentation, RSC Northern Division Dalton Conference, University of Huddersfield, 2014
5. Hoxha, K. *DNA bases in crystal engineering*, Oral presentation, Postgraduate Research Colloquia, University of Hull, 2014
6. Hoxha, K. *DNA bases in crystal engineering: the role of hydrogen bonding*, Poster presentation, Chemistry Conference for Young Scientists, Blankenberge, Belgium, 2014

LIST OF FIGURES AND TABLES

Figure 1.1: Crystal structure prediction. The two polymorphic forms of caffeine and glutaric acid taken from the Cambridge Structural Database ¹³ for illustration purposes. ¹⁴ ..4	
Figure 1.2: The structure of alloxan.....	10
Figure 1.3: Hydrogen bond motifs: a) dimer D; b) chain C; c) intramolecular hydrogen bond $S_1^1(6)$; d) dimer $R_2^2(8)$; e) $R_4^2(8)^{21}$	14
Figure 1.4:Crystal engineering from a molecule to the crystal ⁴¹	18
Figure 1.5: Aromatic crystal structures with the carboxylic acid dimer: a) benzoic acid; b) terephthalic acid; c) isophthalic acid.....	20
Figure 1.6: Hydrogen bonding interactions in carboxyl acid arising due to interference interaction: a) dimer; b) catemer	22
Figure 1.7: Expected dimer formation in cubanecarboxylic acid.....	22
Figure 1.8: Hydrogen bonding motifs in 4-chlorocubanecarboxylic acid.....	23
Figure 1.9: Representation of interaction between σ and π frameworks. ⁵⁰ (Extract from <i>Journal of the Chemical Society, Dalton Transactions</i> , 2000)	25
Figure 1.10: Base numbering and hydrogen-bond functionality ³³	27
Figure 1.11: : Watson-Crick base pairing	31
Figure 1.12: Hoogsteen mode of DNA base pairing ³⁶	32
Figure 1.13: Hydrogen bonding between adenine and thymine; a) Watson-Crick; b) Hoogsteen.....	33
Figure 1.14: Two tautomeric forms of adenine ^{59, 60}	35
Figure 1.15: Bidentate homosynthons formed between adenine molecules	36
Figure 2.1: Solvent Diffusion	41
Figure 2.2: Set up of vapour diffusion cells.....	42
Figure 2.3: Six unit cell parameters used to define a general unit cell.....	44

Figure 2.4: Illustration of the four lattice types showing the relationship between lattice points.....	46
Figure 2.5: 2_1 screw axis	49
Figure 2.6: Glide plane.....	49
Figure 2.7: Energy levels of the metal target and the denomination of emissions	52
Figure 2.8: Representation of the X-ray spectrum ⁷¹	53
Figure 2.9: The Bragg condition for X-ray diffraction from a crystal.....	55
Figure 2.10: Argand diagram representing wave behaviour by complex number	56
Figure 2.11: Schematic diagram of a single-crystal X-ray diffractometer	60
Figure 2.12: Scattering from a polycrystalline sample	65
Figure 3.1: Classification of solid forms by Friscic and Jones ⁸¹ (Extract from <i>Journal of Pharmacy and Pharmacology</i> , 2010).....	70
Figure 3.2: Three phases of proton transfer between a basic nitrogen and a hydroxyl fragment of a carboxylic acid. Denominations <i>a</i> , <i>b</i> and <i>c</i> refer to N-H, O-H and N-O distances, respectively ⁸⁹	75
Figure 3.3: Malonate salt of a cancer drug with hydrogen bonds containing shared protons as described by Li <i>et al.</i> ⁸⁹ (errors on distances were not cited in the original publication)	76
Figure 3.4: Hydrogen bond functionality of guanine.....	81
Figure 3.5: Hydrogen-bonding in $((\text{GH}_2)\text{SO}_4 \cdot \text{H}_2\text{O})$	81
Figure 3.6: Guaninium ribbons in methylguaninium nitrate	82
Figure 3.7: Asymmetric unit of (1a) with atoms drawn as 70 % probability ellipsoids. Dashed lines indicate hydrogen bonds between guaninium cations within the asymmetric unit	85
Figure 3.8: The hydrogen-bonded tape within (1a)	86
Figure 3.9: Depiction of hydrogen bonding between cations and anions in (1a).....	87
Figure 3.10: View of (1a) down [010] to show location of water molecules within channels.	88

Figure 3.11: Difference Fourier map for guaninium 1	90
Figure 3.12: Difference Fourier map for guaninium 2	90
Figure 3.13: Overlay of simulated and experimental patterns showing the presence of a single phase	91
Figure 3.14: Cation interactions in the singly protonated guaninium salt. ¹¹⁹	92
Figure 3.15: FTIR Spectrum of the 1a and guanine	93
Figure 3.16: Thermogravimetric data for 1a	94
Figure 3.17: Asymmetric unit of (1b) with atoms drawn as 70 % probability ellipsoids. Dashed lines indicate hydrogen bonds between guaninium cations within the asymmetric unit.	96
Figure 3.18: Comparison between structures; a) fully hydrated structure (1a); b) partially dehydrated structure (1b). The pink circles show the difference between the two structures. Cations in both (1a) and (1b) interact with each other by forming the same hydrogen-bond dimer	97
Figure 3.19: Representation of the asymmetric unit of (1c) with atoms drawn as 50 % probability ellipsoids. Dashed lines indicate hydrogen bonds.	98
Figure 3.20: Different hydrogen bonding in the fully dehydrated form (1c). Highlighted in pink is the unprotonated imidazole nitrogen.	99
Figure 3.21: View of 1c down [010]. Vacant channels extend parallel to <i>a</i> at positions (0,0) and ($\frac{1}{2}$, $\frac{1}{2}$) parallel to <i>yz</i> -axis	100
Figure 3.22: Comparison of synthons: a) synthon formation between two cytosine molecules; b) synthon formation between G:C. Dashed lines represent hydrogen bonds.	103
Figure 3.23: Structure of cytosine	104
Figure 3.24: Simulated X-ray powder diffraction patterns of cytosine and 1,10-phenanthroline hydrate, and experimental pattern obtained after milling their mixture.	107

Figure 3.25: X-ray patterns from co-crystallisation of adenine and 1,10-phenanthroline	108
Figure 3.26: X-ray patterns from co-crystallisation of thymine and 1,10-phenanthroline	109
Figure 3.27: X-ray patterns from co-crystallisation of guanine and 1,10-phenanthroline	110
Figure 3.28: Asymmetric unit of cyt:phen. Atoms are drawn as 70% probability ellipsoids. Dashed lines represent N—H···N hydrogen bonds	111
Figure 3.29: Chains formed by each crystallographically-independent cytosine. $R_2^2(8)$ homosynthons are generated with symmetry equivalent counterparts of each cytosine with the following symmetry operations: : i= $(-x, y-0.5, -z+1.5)$; ii= $(-x, y+0.5, -z+1.5)$; iii= $(-x+1, y-0.5, -z+0.5)$; iv= $(-x+1, y+0.5, z-0.5)$	112
Figure 3.30: View of cyt:phen just off [010] direction illustrating infinite chains of cytosine and stacking of phenanthroline molecules	113
Figure 3.31: The stacking of phenanthroline: a) packing of phenanthroline viewed from a -axis inclined at an angle 46.175° to b ; b) π - π stacking of 1,10-phenanthroline; c) stacking of each molecule with its symmetry generated counterpart	114
Figure 3.32: Observed (\times), calculated (line), and difference (lower line) X-ray powder diffraction profiles for cyt:phen at room temperature; tick marks indicate positions of allowed reflections from the $K\alpha_1$ diffraction.....	116
Figure 3.33: Patterns from mixing reagents, 30 min milling and starting materials	117
Figure 3.34: Representations of portions of crystal structures of cytosine and cytosinium compounds.....	120
Figure 3.35: Representations of portions of crystal structures of the co-crystals 5-fluorocytosine:terephthalic acid and cyt:phen.	121
Figure 3.36: Comparison of (cyt:phen) with cytosine:5-isopropyl-6-methylisocytosine.....	122

Figure 3.37: Comparison of (cyt:phen) with 5-fluorocytosine:6-methylisocytosine.....	123
Figure 3.38: Solid state UV-Vis Spectra comparing ferroin and cyt:phen.....	125
Figure 3.39: Comparison of (cyt:phen) patterns obtained from 1h hand grinding and 1h ball milling grinding.....	126
Figure 3.40: Unexpected homosynthon in cytosine systems.....	128
Figure 3.41: Hydrogen bonding and selected bond angles and distances in Lee and Wang's paper for cytosine and oxalic acid.....	130
Figure 3.42: Incorrect assignment of proton location.....	131
Figure 3.43: Illustration of hydrogen bonding in melamine salts. N—H···N hydrogen bonds between melaminium cations and carboxylate:melaminium heterosynthon form $R_2^2(8)$. Site of melamine protonation is highlighted in pink.....	132
Figure 3.44: Melamine using all of its hydrogen bonding sites with phthalimide.....	133
Figure 3.45: Structure and hydrogen bond functionality of NTA.....	133
Figure 3.46: Asymmetric unit of $(MH^+)_2nta^{2-} \cdot 3H_2O$ with atoms drawn as 70% probability ellipsoids. Dashed lines represent hydrogen bonds.....	135
Figure 3.47: Infinite melaminium tapes held together by N—H(amine)···N(endocyclic) hydrogen bonds.....	136
Figure 3.48: Stabilisation of the structure <i>via</i> $R_4^4(10)$ heterosynthon between adjacent anions and O3W.....	137
Figure 3.49: Anion-anion interaction <i>via</i> N—H···O hydrogen bonds.....	139
Figure 3.50: Carboxylate-melaminium interaction at the site of protonation.....	141
Figure 3.51: Comparison of C—N—C bond angles in the triazine ring.....	142
Figure 3.52: Fourier map showing the protonation of the first melamine moiety.....	142
Figure 3.53: Fourier maps showing the protonation of the second melamine moiety.....	143
Figure 3.54: IR Spectrum of $(MH^+)_2nta^{2-} \cdot 3H_2O$	144
Figure 3.55: Thermogram of melaminium nitrilotriacetate trihydrate.....	145
Figure 3.56: Comparison of cation interactions between two salts.....	146

Figure 3.57: Hydrogen bonding motifs in 4-chlorocubanecarboxylic acid. The catemer inhibits the formation of the carboxylic acid dimer.....	148
Figure 3.58: Hydrogen bonding in pure guanine acetic acid.....	149
Figure 3.59: Hydrogen bonding in thymine acetic acid.....	150
Figure 3.60: Asymmetric unit of tac•2H ₂ O drawn at 75% ellipsoids. Dashed lines represent hydrogen bonds	151
Figure 3.61: Pyrimidine-pyrimidine interaction in tac resembling the urea-urea embrace	152
Figure 3.62: Crystal packing in tac•2H ₂ O	153
Figure 3.63: O2W provides further stabilisation to the interaction.....	153
Figure 3.64: Comparison of the anhydrous and hydrated form	155
Figure 3.65: Thermal behaviour of tac•2H ₂ O	157
Figure 3.66: Heterosynthon formation in caffeine co-crystals.....	158
Figure 3.67: Second most common ($R_3^3(11)$) network based on ($R_2^2(7)$ and $R_2^2(6)$) synthons as observed in 1:1 caffeine:carboxylic acid co-crystals.....	159
Figure 3.68: The asymmetric unit of caf:2nitroTA drawn as 70% probability ellipsoids..	160
Figure 3.69: A single tape between caffeine and 2-nitroterephthalic acid.....	161
Figure 3.70: C—H···O hydrogen bond between caffeine and 2-nitroterephthalic acid	161
Figure 3.71: Crystal packing along <i>c</i> -axis	162
Figure 3.72: Classical and non-classical hydrogen bonds generating a ring between caffeine and 2-nitroterephthalic acid.....	162
Figure 3.73: Fourier maps showing that the carboxylic acid group is unionised: a) proton location in the first carboxylic acid; b) proton location in the second carboxylic acid	163
Figure 3.74: Determination of C—O distances in carboxylic acid and the C4—N9—C8 angle	164
Figure 3.75: IR spectrum for caf:2nitroTA.....	166
Figure 4.1: Metal binding sites in DNA nucleobases ¹⁷⁰	173

Figure 4.2: Hydrogen bonding of nucleobases through a metal centre ¹⁷¹	174
Figure 4.3: Hydrogen bonded network of adenine with manganese (II) quinoline-2-carboxylate.....	177
Figure 4.4: Adenine ribbon showing the presence of Watson-Crick and Hoogsteen interactions.....	178
Figure 4.5: Structure of 2,6-pyridinedicarboxylic acid.....	179
Figure 4.6: Asymmetric unit of compound (B) with atoms at drawn as 50% probability ellipsoids.....	182
Figure 4.7: View of the alternating organic and inorganic layers along the <i>b</i> -axis. Water molecules omitted for clarity	183
Figure 4.8: View of the crystal packing along the <i>c</i> -axis showing the role of water molecules in stabilising the structure.....	185
Figure 4.9: Difference Fourier maps showing the location of hydrogen atoms in the cations: a) protonation of [1H,9H AdH ⁺]; b) protonation of [3H,7H AdH ⁺].....	185
Figure 4.10: Difference Fourier maps showing the location of hydrogen atoms in the ligand: a) protonation of the first dipicolinato ligand; b) protonation of the second dipicolinato ligand	186
Figure 4.11: Asymmetric unit of compound (D) with atoms drawn as 50% probability ellipsoids.....	189
Figure 4.12: Hydrogen bonding motifs in two symmetry independent cytosinium cations. (Direct interactions with the anion have been omitted for clarity.)	191
Figure 4.13: Difference Fourier maps showing the location of hydrogen atoms: a) protonation of first cytosinium cation b) protonation of second cytosinium cation.....	193
Figure 4.14: Difference Fourier maps showing the location of hydrogen atoms in the ligands: a) proton locations in the first dipicolinato ligand; b) proton locations in the second dipicolinato ligand.....	194

Figure 4.15: Asymmetric unit of (D) with atoms drawn as shown 50% probability ellipsoids. Dashed lines represent hydrogen bonds	195
Figure 4.16: Crystal packing in (D) viewed along <i>b</i> -axis	196
Figure 4.17: Deviation of $R_2^2(8)$ heterosynthon from planarity by $36.21(11)^\circ$	196
Figure 4.18: Cation-cation stacking for the first cytosinium with a mean plane separation of $3.23(3)$ Å and centroid to centroid distance of $3.7195(4)$ Å	197
Figure 4.19: Carboxylic acid derivatives of thymine and uracil	200
Figure 4.20: Deprotonation of orotic acid: (a) orotic acid; (b) monoanionic orotate; (c) dianionic orotate ¹⁸⁶	202
Figure 4.21: Complexation of nickel (II) with fluoro-orotic acid ¹⁹²	204
Figure 4.22: Complexation of orotic acid and imidazoles with nickel ¹⁸⁴	204
Figure 4.23: Asymmetric unit of (F) with atoms drawn as 70% probability ellipsoids	207
Figure 4.24: Centrosymmetric $R_2^2(8)$ orotate-orotate homosynthon between two symmetry related orotate molecules generated by: $[-x, -y, -z+2]$	208
Figure 4.25: Crystal packing in (F). Hydrogen bonding and two distinct types of stacking interactions govern the crystal packing. Green lines represent hydrogen bonding.	209
Figure 4.26: Stacking interactions in (F). Dashed black lines represent: a) orotate-pyridine offset stacking; b) offset pyridine-pyridine stacking; c) the T-shaped/edge-to-face C—H \cdots π interaction between two pyridines;	210
Figure 4.27: Thermal behaviour of compound (F)	211
Figure 4.28: Asymmetric unit of (G) with atoms drawn as 55% probability ellipsoids	212
Figure 4.29: Crystal packing in Form (G). The orotate-orotate homosynthon extends parallel to <i>b</i> -axis	213
Figure 4.30: Coordination about each cobalt ion showing the bridging orotate	214
Figure 4.31: Asymmetric unit of (H) with atoms drawn as 55% probability ellipsoids	215
Figure 4.32: Crystal packing in Form (H)	216

Figure 4.33: Differences in pyridine orientation between the two polymorphs: a) Form (G) and b) Form (H)	217
Figure 4.34: Pattern from compound (I) compared to the simulated VEVZIG pattern.....	219
Figure 4.35: Asymmetric unit of compound (I) with atoms drawn as 70% probability ellipsoids	221
Figure 4.36: Depiction of pseudo-symmetry generated by a translation of $(\mathbf{0}, \frac{1}{2}, \mathbf{0})$	222
Figure 4.37: Structural implications of 05W	223
Figure 4.38: Formation of orotate-nicotinamide heterosynthon in VEVZIG	223
Figure 4.39: Orotate-orotate homosynthon between two fragments in compound (I).....	224
Figure 4.40: Stacking interaction in compound (J)	225
Figure 4.41: Crystal packing in (I) as viewed from <i>c</i> -axis. O1W and O2W interconnect the adjacent layers by acting as hydrogen bond donors	226
Figure 4.42: Overlay of simulated and experimental patterns showing the presence of a single phase	228
Figure 4.43: Structure of 3-nicotinamide and 4-nicotinamide.....	229
Figure 4.44: Asymmetric unit of compound (J) with atoms drawn as 70% probability ellipsoids. Dashed lines represent hydrogen bonds.....	230
Figure 4.45: Crystal packing in (I) showing π - π stacking between two orotate ligands, which replaces the orotate-orotate homosynthon.....	231
Figure 4.46: Possible coordination of orotic acid and adenine to transition metals.....	233
Figure 4.47: Predicted hydrogen bonding between adeninium and orotate ligand.....	234

Table 1.1: Analogies between molecular and supramolecular chemistry.....	19
Table 2.1: Seven crystal systems.....	45
Table 2.2: The 14 Bravais lattices.....	47
Table 2.3: Characteristic X-ray wavelengths for molybdenum.....	54
Table 3.1: Comparison of C2—N1—C6 bond angle in adeninium salts ⁹²	78
Table 3.2: Hydrogen bonds within bis(guaninium) sulfate 2.5 hydrate, 1a.....	89
Table 3.3: Hydrogen bonding in cyt:phen.....	115
Table 3.4: Energy landscapes for co-crystallisation of DNA bases with 1,10-phen.....	118
Table 3.5: Iron content for different preparations.....	127
Table 3.6: Selected hydrogen bond parameters.....	138
Table 3.7: Carboxylate bond lengths and the difference in C-O for nitrilotriacetic acid.....	140
Table 3.8: Characteristic IR absorption for (MH ⁺) ₂ nta ²⁻ ·3H ₂ O.....	144
Table 3.9: Hydrogen bond table for tac·2H ₂ O.....	156
Table 3.10: Hydrogen bond parameters for caf:2nitroTA.....	165
Table 3.11: Characteristic IR absorption peaks.....	166
Table 4.1: Bond angles of neutral and protonated nitrogen atoms.....	187
Table 4.2: Hydrogen-bond parameters of (B).....	188
Table 4.3: Differences in metal-ligand bond lengths for the nickel (II) complex (A) and cobalt (II) complex (B).....	188
Table 4.4: Hydrogen bond parameters for (D).....	192
Table 4.5: Hydrogen bond parameters for (D).....	198
Table 4.6: Hydrogen bond parameters in compound (F).....	208
Table 4.7: Crystal parameters for Compounds (G) and (H).....	218
Table 4.8: Selected hydrogen bond parameters for compound (I).....	227
Table 4.9: Selected hydrogen bonds for compound (J).....	232

TABLE OF CONTENTS

1.0	INTRODUCTION.....	2
1.1	Crystal Engineering.....	2
1.1.1	Inception.....	2
1.1.2	Development.....	2
1.2	Intermolecular Interactions.....	6
1.2.1	Isotropic and Anisotropic Interactions.....	6
1.2.2	Understanding Crystal Packing.....	7
1.3	Hydrogen Bonding.....	12
1.3.1	Definition.....	12
1.3.2	Critical Review of the new definition.....	13
1.3.3	Graph Set Notation.....	13
1.3.4	The Strong Hydrogen Bond.....	15
1.3.5	Conventional or Moderate Hydrogen Bonds.....	15
1.3.6	The Weak Hydrogen Bond.....	16
1.4	The Synthons Theory.....	16
1.4.1	The Supramolecular Synthons.....	17
1.4.2	Synthon Hierarchy in Crystal Engineering.....	21
1.5	Recent Advances in Understanding Synthons.....	23
1.6	π - π stacking interactions.....	24
1.7	DNA Bases in Crystal Engineering.....	26
1.7.1	Hydrogen Bonding in DNA nucleobases.....	26
1.7.2	The History of DNA Structure Determination.....	28

1.7.3	The Structure of DNA Suggested by Watson and Crick	29
1.7.4	Hoogsteen Pairing.....	32
1.7.5	Versatile Hydrogen Bonding in Adenine	34
1.7.6	Survey of the Cambridge Database	37
1.7.7	Solubility Challenges.....	37
1.7.8	Aims and Objectives	38
2.0	SYNTHETIC METHODOLOGY AND ANALYTICAL TECHNIQUES.....	40
2.1	Synthetic Methods	40
2.1.1	Solution Crystallisation.....	40
2.1.1.1	Controlled Cooling.....	40
2.1.1.2	Solvent Evaporation	41
2.1.1.3	Solvent Diffusion (Antisolvent Crystallisation)	41
2.1.1.4	Vapour Diffusion.....	42
2.1.2	Melt Crystallisation.....	42
2.1.3	Sublimation.....	43
2.1.4	Synthetic methods used during this research	43
2.1.4.1	Solution Crystallisation.....	43
2.1.4.2	Reflux.....	43
2.1.4.3	Recrystallisation from water	44
2.2	Structure Determination.....	44
2.2.1	Crystallography.....	44
2.2.1.1	Unit Cell and Crystal Systems	44
2.2.1.2	Lattice Types.....	45

2.2.1.3	Symmetry Analysis	47
2.2.1.4	Point Symmetry Operations.....	48
2.2.1.5	Space Symmetry Operations.....	48
2.2.1.6	Miller Indices.....	50
2.2.1.7	Space Groups.....	50
2.2.2	X-ray Diffraction	50
2.2.2.1	Generation of X-rays.....	51
2.2.2.2	Diffraction and Bragg's Law	54
2.2.2.3	Diffraction Intensities and the Structure Factor.....	56
2.2.3	Single-Crystal X-ray Diffraction.....	59
2.2.3.1	Data Collection.....	59
2.2.3.2	Data Collection at Low Temperatures	60
2.2.3.3	Fourier Syntheses.....	61
2.2.3.4	The Phase Problem and Structure Solution.....	62
2.2.3.5	Structure Refinement.....	64
2.2.4	X-ray Powder Diffraction	65
2.2.4.1	Phase Identification.....	65
2.3	Other Analytical Techniques	66
2.3.1	Infrared Spectroscopy	66
2.3.1.1	Infrared Absorption.....	66
2.3.1.2	Molecular Vibrations.....	67
2.3.2	Thermogravimetric Analysis.....	67
3.0	Multicomponent Crystals: SALTS, CO-CRYSTALS AND HYDRATES.....	70

3.1	Introduction	70
3.2	Definition of a co-crystal	71
3.3	Distinction between salts and co-crystals	72
3.3.1	The Effect of Proton Transfer	72
3.3.2	The Continuum Between Salts and Co-crystals	73
3.3.3	The Shared Proton – Co-crystal or Salt?	74
3.3.4	Examination of Carboxylic/Carboxylate Bond Lengths	77
3.3.5	Bond Angle at the Site of Protonation	77
3.4	Structural Cohesion in Guaninium Sulphate Hydrate	80
3.4.1	Introduction	80
3.4.2	Experimental	83
3.4.2.1	Single Crystal Preparation	83
3.4.2.2	Infra-red (IR) Spectroscopy and Thermogravimetric Analysis (TGA)	83
3.4.2.3	Single Crystal X-ray Diffraction Measurements	84
3.4.3	Results and Discussion	85
3.4.3.1	Crystal structure of $(\text{GH})_2\text{SO}_4 \cdot 2.5\text{H}_2\text{O}$, (1a)	85
3.4.3.2	Relationship of (1a) to previous compounds	92
3.4.3.3	IR spectrum and thermal behaviour of (1a)	93
3.4.3.4	Partially dehydrated form, (1b)	95
3.4.3.5	Fully dehydrated form (1c)	97
3.5	Co-crystallisation of DNA bases with 1,10-phenanthroline	101
3.5.1	Introduction	101
3.5.2	Experimental	105

3.5.2.1	Co-crystal screening.....	105
3.5.2.2	Single Crystal Preparation.....	105
3.5.2.3	Infra-red (IR) Spectroscopy.....	105
3.5.2.4	Single Crystal X-ray Diffraction Measurements.....	105
3.5.2.5	X-ray Powder Diffraction.....	105
3.5.3	Results and Discussion.....	106
3.5.3.1	Co-crystal screening and PXRD analysis.....	106
3.5.3.2	Evaluation of the results from co-crystal screening and solution crystallisation.....	110
3.5.3.3	Structure of (cyt:phen).....	111
3.5.3.4	Phase Purity and Rietveld Fitting.....	115
3.5.3.5	Rationalisation of Co-crystallisation and Crystal Structure Prediction...118	
3.5.3.6	Relationship of (cyt:phen) to other cytosine containing compounds.....	120
3.5.3.7	Investigations on the cause of colour change.....	124
3.5.3.8	Critical Evaluation of Lee and Wang's Paper.....	128
3.6	Structure of Melaminium Nitrilotriacetate Trihydrate.....	132
3.6.1	Introduction.....	132
3.6.2	Experimental.....	134
3.6.2.1	Single Crystal Preparation.....	134
3.6.2.2	Single Crystal X-ray Diffraction Measurements.....	134
3.6.2.3	TGA Study.....	134
3.6.2.4	IR Spectroscopy.....	134
3.6.3	Results and Discussion.....	135

3.6.3.1	Structure of Melaminium Nitrilotriacetate Trihydrate, $(MH^+)_2nta^{2-} \cdot 3H_2O$	135
3.6.3.1	Proton transfer and its structural implications	139
3.6.3.2	Confirmation of salt formation <i>via</i> IR Spectroscopy	143
3.6.3.3	Thermal behaviour	145
3.6.3.4	Relationship to other melamine salts with tricabroxylic acids	146
3.7	The missing carboxylic acid dimer due to competing hydrogen bonds in thymine acetic acid dihydrate	147
3.7.1	Introduction.....	147
3.7.2	Experimental.....	150
3.7.2.1	Synthesis of $tac \cdot 2H_2O$	150
3.7.2.2	Single Crystal X-ray Diffraction.....	150
3.7.2.3	Thermogravimetric analysis.....	150
3.7.3	Results and Discussion.....	151
3.7.3.1	Structure of $tac \cdot 2H_2O$	151
3.7.3.2	The role of water molecules.....	154
3.7.3.3	Carboxylic Acid Dimer vs <i>tac-tac</i> dimer	155
3.7.3.4	Thermal Behaviour	156
3.8	Co-crystallisation of Caffeine with 2-nitroterephthalic Acid:.....	158
3.8.1	Introduction.....	158
3.8.2	Experimental.....	159
3.8.2.1	Single Crystal Preparation	159
3.8.2.2	Single Crystal X-ray diffraction measurements	160

3.8.2.3	IR Spectroscopy.....	160
3.8.3	Results and Discussions.....	160
3.8.3.1	Structure of caf:2nitroTA.....	160
3.8.3.2	Determination of co-crystal formation.....	163
3.8.3.3	Confirmation of co-crystal formation by IR spectroscopy	165
3.8.3.4	Relationship to other compounds	167
3.9	Chapter Outlook and Conclusions.....	167
4.0	Hydrogen-bonded Networks Containing DNA bases or THEIR Derivatives	171
4.1	Introduction.....	171
4.2	Metal-Nucleobase Binding Motifs	172
4.2.1	Direct Metal-Nucleobase Interactions.....	173
4.2.2	Indirect Metal-Nucleobase Interactions	174
4.3	Recent Trends in Coordination Compounds with Nucleobases	176
4.4	Interaction of Nucleobases with Metal-Ligand Building Blocks.....	177
4.4.1	Introduction.....	177
4.4.2	Experimental.....	180
4.4.2.1	Single crystal preparation.....	180
4.4.2.2	[1H CytH ⁺] ₂ [Ni(dip) ₂ (H ₂ O) ₃] and [1H CytH ⁺] ₂ [Co(dip) ₂ (H ₂ O) ₃]	180
4.4.2.3	[3H-cytosinium] Co(dip) ₂] from methanol	181
4.4.2.4	Synthesis of thymine, uracil and guanine analogues	181
4.4.2.5	Single crystal X-ray diffraction.....	181
4.4.3	Results and Discussion.....	182
4.4.3.1	Structure of [1H, 9H AdH ⁺][3H, 7H AdH ⁺][Co(dip) ₂ (H ₂ O) ₃].....	182

4.4.3.2	Structure of $[1\text{H CytH}^+]_2[\text{Co}(\text{dip})_2(\text{H}_2\text{O})_3]$	189
4.4.3.3	Structure of $[1\text{H CytH}^+]_2[\text{Co}(\text{dip})_2]$ – anhydrous form	195
4.4.3.4	Unsuccessful Reactions with Guanine, Thymine and Uracil.....	199
4.5	Engineering of H-Bonded Networks with Carboxylic Acid Derivatives of Nucleobases: Thymine Acetic Acid and Orotic Acid.....	200
4.5.1	Introduction.....	200
4.5.1.1	CSD Survey	201
4.5.1.2	Thymine Acetic Acid Binding.....	201
4.5.1.3	Orotic Acid Binding.....	201
4.5.2	Structures with orotic acid	203
4.5.2.1	Orotic acid as the sole organic ligand.....	203
4.5.2.2	Orotic acid with N-donors.....	204
4.5.3	Experimental.....	205
4.5.3.1	Single crystal preparation.....	205
4.5.3.2	Single Crystal X-ray measurements.....	206
4.5.4	Results and Discussion.....	206
4.5.4.1	Metal-Orotate in the presence of pyridine.....	207
4.6	Metal-Orotate complexes with DNA bases	233
4.7	Chapter Outlook and Conclusions.....	235
5.0	APPENDICES	238
6.0	REFERENCES	252

Chapter 1: Introduction

1.0 INTRODUCTION

1.1 Crystal Engineering

“One of the continuing scandals in the physical sciences is that it remains in general impossible to predict the structure of even the simplest crystalline solids from a knowledge of their chemical composition.” (John Maddox, 1988)¹

1.1.1 Inception

Crystal engineering^{2, 3}, an area alien to most scientists back in the 1980s, gained momentum in the scientific world after John Maddox¹ presented his controversial and provocative argument on his opinion piece published in Nature in 1988. Maddox’s stance prompted many of the then emerging scientists to explore this area heavily. In retrospect, it is evident that the period 1988 – 1991 paved the way for the development of a nascent field of chemistry.

The first ever reference to crystal engineering was made by Pepinsky³ in 1955 during a meeting of the American Physical Society. Following on Pepinsky’s comments, Schmidt² used the term crystal engineering in the context of his synthetic work in 1971. He highlighted the importance of understanding the connection between intermolecular forces and the stability of the crystalline lattice. Schmidt further argued that a theory of solid state packing was necessary in order to “... *be able to ‘engineer’ crystal structures having intermolecular contact geometries appropriate for chemical reaction...*”²

1.1.2 Development

It was after Maddox’s 1988 statement that non-covalent interactions were given wider attention as noted by Wuest in 1991.⁴ This was the first time that non-covalent interactions were considered as a powerful tool for directing molecular assembly. As a result, crystal engineering morphed from being a mere concept to an invaluable discipline which continues to rapidly expand and develop to this day.

As the discipline grew over the years, the appreciation of the importance intermolecular interactions rose considerably. In the midst of these developments in the area, Desiraju⁵ provided a coherent definition for crystal engineering⁶, namely *“the understanding of intermolecular interactions in the context of crystal packing and in the utilisation of such understanding in the design of new solids with desired physical and chemical properties”*.⁵

Desiraju⁷ presented the pressing issues in contemporary crystal engineering and divided the area into three categories:

- 1) Understanding the intermolecular interactions in the context of crystal packing
- 2) Developing a strategic plan by which these interactions can lead to a certain desired packing
- 3) Fine-tuning of crystal properties to achieve a pre-determined goal⁸

It has been claimed that appreciation of the relationship between molecules and crystals is crucial to understanding and applying crystal engineering.⁹ This is especially true if one considers crystals as simply being extended ordered assemblies of molecules.⁹ This relationship was recognised as early as 1921 by Bragg¹⁰, who had compared the unit cell parameters of anthracene and naphthalene and had noted major similarities between the two. Bragg’s observations show that crystal structure is intimately related to the structure of the individual molecules involved in the crystal.

In his book published in 1979, Jack Dunitz⁹ argued that the relationship between molecules and crystals is akin to the relationship between structure and properties. Desiraju¹¹ takes Dunitz’s idea further by asking whether one can decipher the crystal structure of a compound given its molecular structure.¹¹ Even though the answer to this question is not as straightforward, such a school of thought guides the crystal engineer to consider molecules as being building blocks for generating more complex and ordered structures.

In a focus article published in 2003 in *Chemical Communications*, Dunitz¹² tackled the topic of crystal structure prediction. The answers he provided on the matter ranged from “no”, to “maybe” to a “conditional yes” in some cases. Dunitz formulated his theory by suggesting that a plausible way to begin predicting crystal structures is to analyse the structure of the molecules involved and generate hypothetical crystal structures. The reasoning is depicted in Figure 1.1, where two molecules (caffeine and glutaric acid) have been chosen by the author of this thesis to illustrate the idea.

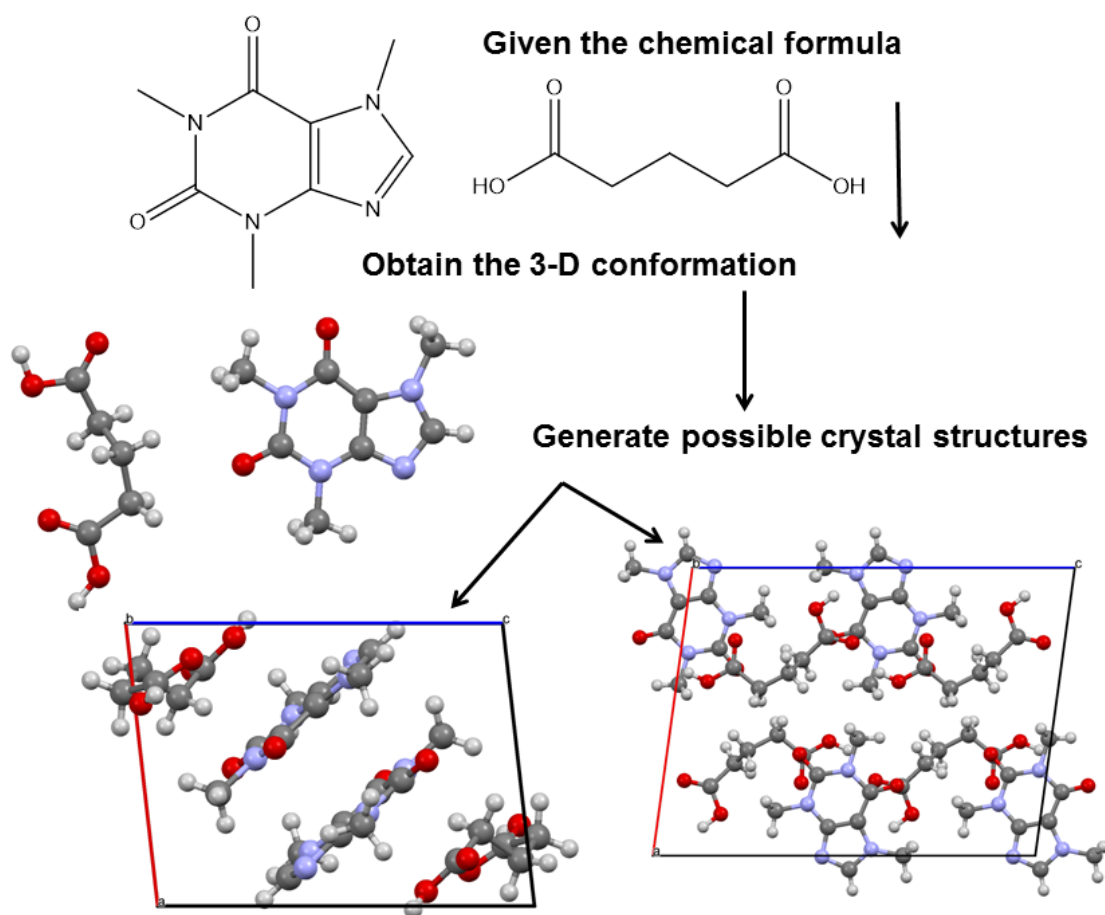


Figure 1.1: Crystal structure prediction. The two polymorphic forms of caffeine and glutaric acid taken from the Cambridge Structural Database¹³ for illustration purposes.¹⁴

As it can be seen from Figure 1.1, from the chemical formula of caffeine and glutaric acid the 3D conformation is obtained. This could then be used to generate all the possible arrangements for the crystal packing computationally.

According to Dunitz, upon calculating the energy of all these possible arrangements, it would be possible to find the one with the lowest energy. The important point here is that such computational methods for generating potential crystal structures would lead to many such structures. This would not be an issue if one of the candidate structures was considerably more stable than all others. In that case, the most stable one would be predicted to be the one which forms in reality. However, what complicates the problem is the fact that there might be many possible crystal structures with very similar energies. The challenge lies in selecting one crystal structure from many equi-energetic possibilities.

Dunitz rightly points out that such computational methods usually rely on molecules being at rest, which is a remarkable deviation from reality because molecules in a crystal vibrate. Moreover, Dunitz also evaluates the synthon theory put forward by Desiraju. Desiraju's theory concentrates solely on interactions between the functional groups of molecules with a particular focus on hydrogen bonding.¹⁵ Desiraju's theory will be discussed in more detail in the subsequent sections. However, according to Dunitz, Desiraju's approach on crystal structure prediction lacks physical basis and has a poor predictive capacity. Dunitz concludes that crystal structure prediction remains a challenge for today's crystal engineering, despite the modest progress achieved thus far. In retrospect, it transpires that John Maddox's statement about crystal structure prediction can be considered to be valid even nearly 30 years after he first wrote it.

1.2 Intermolecular Interactions

1.2.1 Isotropic and Anisotropic Interactions

Non-covalent interactions are crucial to determining the recognition between molecules and consequently they have a major impact on the properties displayed by the molecule. Desiraju¹⁶ regards intermolecular interactions as a supramolecular “glue” responsible for binding molecules in a crystal. He also emphasises that the emergence of a crystal structure comes as a result of compromises between several interactions of differing directionalities and strengths.¹⁷ Therefore, the understanding of the recognition and communication between molecules is crucial to identifying which structural patterns are more useful in engineering novel crystal structures.

One of the structural characteristics encountered in intermolecular interactions is the directionality of such interaction. Directionality of an intermolecular interaction can be manipulated in order to obtain specific and pre-desired intermolecular orientations within a crystal. Therefore, it is important to note that intermolecular interactions can be divided in two groups:

- a) Isotropic interactions
- b) Anisotropic interactions

Isotropic interactions are those that lack directionality and contribute to close packing within a crystal. This forms the basis of the crystal-packing principle established by Kitaigorodskii.¹⁸ On the other hand, anisotropic interactions are defined by the presence of directionality¹⁶ and hydrogen bonding is regarded as the most important directional intermolecular interaction.

1.2.2 Understanding Crystal Packing

Understanding what happens when two molecules approach one another is key to understanding crystal packing. Dunitz and Gavezotti note that when two molecules approach one another in a particular way, their potential energy decreases to a level that would be unachievable *via* an alternative approach between them. They attribute this kind of energetically-favoured approach to “*some specific interaction between molecules*”.¹⁹

The key question here is whether these specific interactions and therefore molecular self-assembly proceed *via* directional or non-directional interactions. Or in other words, do crystals emerge as a result of close-packing between molecules, where the directionality of an interaction is insignificant? Or do they emerge as a result of compromises between various intermolecular forces of varying strength and directionality? The question can be extended further by asking whether a combination of the two factors (close-packing and directionality) could be the driving force for crystal formation.

First thoughts on this area were provided by Kitaigorodskii who formulated his theory of close-packing which focuses on geometrical considerations. This model of crystal packing states that molecules in a crystal are arranged in a way that leads to an overall minimisation of the potential energy of the system.¹⁷ In this model, the most stable structure is the one originating from interactions which use the void space most economically compared to all other competing interactions. Molecules arrange in such a way that the bumps of one molecule fit into the hollows of the other molecule.²⁰ This essentially suggests that void space is undesirable in crystal formation and therefore any arrangement with void space would be unstable energetically. An alternative way of picturing such packing mode can be the dovetail principle, which generates the highest contact between molecules.

On the matter of hydrogen bonding, Kitaigorodskii argues that *“the formation of hydrogen bonds does not handicap the layout of molecules in conformity with the general rules of the packing of crystals”*.¹⁸

The above statement suggests that the directionality of hydrogen bonds is attenuated by the space-filling preference of molecules. Kitaigorodskii argues that every crystal structure emerges as a result of close-packing where molecules are arranged in a way that there is maximum contact between them. Therefore, according to his theory, once the close-packing interactions have been established, hydrogen bonding interactions can take place. The close-packing idea can be extended to hydrogen bonding somewhat vaguely. For the sake of the argument, a hydrogen bond $X-H\cdots A$ may be considered to form *via* the close packing of the $X-H$ with A from another molecule. Supporting the idea of minimal void space, it could be argued that the space between the donor X and the acceptor A is very small due to it being occupied by a hydrogen atom. Such point of view obeys the rule for the most economic use of void space.

The close-packing principle of Kitaigorodskii was a theory developed in the 1960s when the understanding of crystal packing was at its infancy. Some of the fundamental principles suggested by Kitaigorodskii have served as a building block for developing a theory on crystal packing from scientists researching this area in the subsequent decades. Research conducted since 1960s builds on Kitaigorodskii's theory and deepens the understanding of crystal packing.

A particularly important contribution in this aspect has emerged from the research group of Desiraju, who elegantly incorporated the close-packing principle of Kitaigorodskii (non-directional model) with directional interactions. Desiraju⁵ proposed that crystal packing in organic molecules would largely be governed by Kitaigorodskii's close packing principle. But, he also stated that there could be minor deviations from close-packing in the presence of strongly directing functional groups.

According to Desiraju, these functional groups can change the crystal structure remarkably.¹⁷ Desiraju acknowledges the close packing principle of Kitaigorodskii and the impact of van der Waals dispersion forces as pivotal to crystal packing. Furthermore, he proposes that the directionality of the hydrogen bond causes deviations from densely packed structures and leads to open arrangements.¹⁷ Indeed, much host-guest chemistry where the removal of the guest leaves a void space but does not cause major structural changes can be attributed to hydrogen bonding. According to Desiraju, owing to its strength in comparison to other intermolecular interactions, hydrogen bonding behaves in such a way that it can direct and control the structural aspects of molecules. This is why it has been regarded as the master-key of molecular recognition.⁷

In an attempt to rationalise the behaviour of the hydrogen bond, Etter *et al.*²¹ published a feature article in 1991 where they proposed three general rules on hydrogen bonding:

- 1) All good proton donors and acceptors are involved in hydrogen bonding
- 2) If the formation of a six-membered intramolecular hydrogen bond is feasible, then its formation will prevail over any other intermolecular interaction
- 3) Upon forming the intramolecular hydrogen bond, the next best proton donors and acceptors will be able to form intermolecular hydrogen bonds.

Etter *et al.*²² argue that, in most cases, proton donors in functional groups such as carboxylic acids, ureas, amides and imides are used in hydrogen bonding. Moreover, they argue that there is a competition between the formation of intermolecular and intramolecular forces. The latter is more stable than the former and therefore it forms first. Etter *et al.* note that these rules are not unchangeable and they would evolve with the passage of time as more crystal structures are studied.

Etter's rules suggest that if a functional group is capable of hydrogen bonding it will always participate in such interaction. Indeed, Gavezzotti²³ also believes that if a molecule has a hydrogen bonding functionality (donors and acceptors) it will form hydrogen bonds

as the most preferred interaction. He claims that in such cases the formation of hydrogen bonds occurs “...preferentially over and above or even at the expense of other intermolecular interactions”.²³

While such trend is true in most cases, there can be deviations from Etter’s hierarchic rules. A classic example is that of alloxan²⁴, which has hydrogen bond functionality in the form of two N—H donors and four C=O acceptors. Surprisingly, however, the crystal of alloxan does not contain even a single N—H···O interaction. Instead, it is the dipole-dipole interactions that govern the crystal packing.

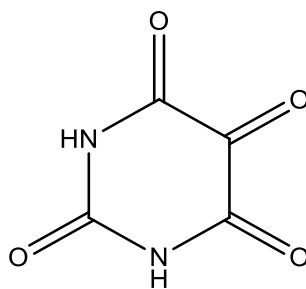


Figure 1.2: The structure of alloxan

Figure 1.2 shows the molecular structure of alloxan, where it is clear that there are permanent dipoles. Inspection of its molecular structure reveals that there is an imbalance between the number of hydrogen bond donors and acceptors, with a shortage of the latter. Commenting on the peculiar packing exhibited by the crystal structure of alloxan, Desiraju argued that “any way of minimising the free energy of the system is a respectable way”.²⁵

In the majority of cases, molecules that have hydrogen bond functionality will most certainly form hydrogen bonds. Once the strong and directional interactions are formed, others forms of close-packing interactions can follow suit. However, it is crucial to note that there may be cases when this trend is not followed, as is the case with alloxan. In fact,

alloxan is a great example which pinpoints to a potential trade-off between directional interactions and close-packing interactions. It is the energetic factors that dictate the extent of this trade-off. Rationalising the behaviour of alloxan, Dunitz and Schweizer state that the crystals of this molecule are “*held together by whatever factors contribute to the cohesive energies*”.²⁶ This essentially suggests that directional interactions and close-packing compete in order to achieve the lowest energy when it comes to crystal formation.

1.3 Hydrogen Bonding

One cannot proceed further into crystal engineering and intermolecular interactions without considering the significance of hydrogen bonding. Steiner notes that hydrogen bonds in crystalline materials can have energies ranging from 0.8–167 kJ mol⁻¹.²⁷ Such diverse strength of hydrogen bonds has extremely powerful structural implications on a supramolecular level. Arunan *et al.*²⁸ rightly state that the importance of this interaction cannot be overemphasised. A meeting organised under the auspices of IUPAC (International Union of Pure and Applied Chemistry) and co-chaired by Arunan and Scheiner in 2005 gathered a large number of scientists to discuss and propose a definition.⁸

1.3.1 Definition

Many scientists claim that all definitions proposed thus far bear some form of vagueness regarding this interaction. Despite early mentions of the phenomenon which today is attributed to hydrogen bonding, the credit for introducing and promoting this concept is given to Pauling. In his 1939 book, *Nature of the Chemical Bond*, Pauling described the hydrogen bond as follows: “*Under certain conditions an atom of hydrogen is attracted by rather strong forces to two atoms instead of only one, so that it may be considered to be acting as a bond between them.*”²⁹

However, it was the book of Pimental and McClean in 1960 which insisted that for an interaction to qualify as a hydrogen bond there should be some evidence of bond formation. Indeed, a recent recommendation submitted to IPUAC stated that “*the hydrogen bond is an attractive interaction between a hydrogen atom from a molecule or a molecular fragment X—H in which X is more electronegative than H, and an atom or a group of atoms in the same or different molecule, in which there is evidence of bond formation*”.³⁰

1.3.2 Critical Review of the new definition

There are some striking facets to the latest IUPAC definition which require attention. Perhaps the most remarkable facet is the fact that “*X is more electronegative than H*”, which implies that X is not limited to oxygen, nitrogen or fluorine only. The new definition suggests that the criterion for X is to be more electronegative relative to H. This requirement expands the number of interactions that can be classified as a hydrogen bond, for example, by incorporating the heavily discussed weak hydrogen bond. As far as the overall strength of a hydrogen bond is concerned, the H...Y strength will increase with an increase in the electronegativity of X. In addition, the strength is also linked to the X—H...Y angle, whereby angles close to 180° produce stronger hydrogen bonds and the angle should ideally be above 110°.30

The other remarkable facet of the hydrogen bond comes from the angular preferences, which make hydrogen bonds directional. The directionality of this interaction is a key concept in crystal engineering because it forms the basis of designing complex architectures. Owing to this characteristic, the hydrogen bond influences crystal packing by primarily deviating from the close-packing principle established by Kitaigorodskii.18

1.3.3 Graph Set Notation

In 1990, Etter *et al.*31 presented an elegant scheme for describing the topology of hydrogen bonding in a crystal. The nomenclature used graph set analysis and proposed clear definitions to aid the understanding of hydrogen bonds present in a crystal structure. A graph-set can be specified using the pattern designator (G), the degree (r), the number of donors (d) and the number of acceptors (a). The general graph-set notation is given below:

$$G_d^a(r)$$

The pattern designator G can be assigned as one of the four patterns: (S) referring to an intramolecular hydrogen bond, (C) relates to a hydrogen-bonded chain, (R) is the denomination for a ring and (D) corresponds to finite patterns. The parameter (r) referring to the degree can be defined as the number of atoms involved in a ring or the repeat length within a chain. It is also important to note that Bernstein *et al.*³² contributed further to Etter's graph set notation. Figure 1.3 illustrates these hydrogen bond motifs.

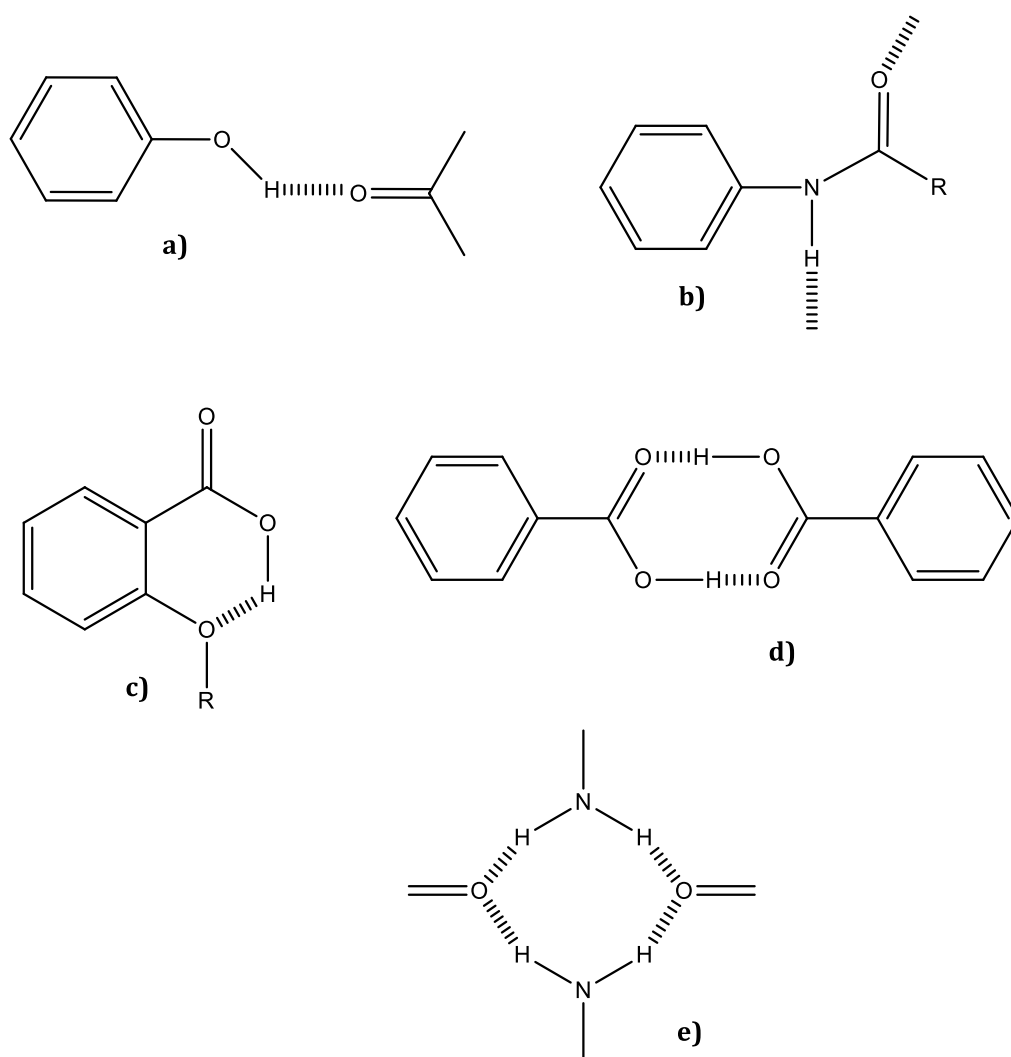


Figure 1.3: Hydrogen bond motifs: a) dimer D; b) chain C; c) intramolecular hydrogen bond $S_1^1(6)$; d) dimer $R_2^2(8)$; e) $R_4^2(8)$.²¹

1.3.4 The Strong Hydrogen Bond

A strong hydrogen bond can have the same order of strength as a weak covalent bond. According to Jeffrey³³, who classified hydrogen bonds as strong, moderate and weak, strong hydrogen bonds can be defined as interactions where the proton is shared by two strong bases. This group also includes hydrogen bonds where there is a considerable deficiency of electron density on the donor atom or an excess of electron density on the acceptor atom. Jeffrey states that these bonds are sometimes called ionic hydrogen bonds, positive- or negative-ion hydrogen bonds. Typical examples include $[F-H-F]^-$, $[O^- - H \cdots O]$ or $[N-H \cdots N^-]$. In addition, some strong hydrogen bonds arise as a result of the molecular configuration whereby the donor and acceptor atoms are in closer contact with each other.³³ This is known as the resonance assisted hydrogen bonding as described by Gilli *et al.*³⁴ in 1989.

One of the main characteristics of the strong hydrogen bond is the so-called hesitating proton. In these systems the $H \cdots O$ bond length can range from 1.2-1.6 Å and this is associated with elongation of the covalent $O-H$ bonds. This implies that the distance of the proton from the donor is similar to its distance to the acceptor.

1.3.5 Conventional or Moderate Hydrogen Bonds

This type of hydrogen bonding is formed between a neutral donor group and a neutral acceptor containing a lone pair of electrons. Typical bond angles for this type of interaction are 130-180°, whereas the donor-acceptor distance can range 2.5-3.2 Å.³³ Conventional hydrogen bonds occur widely in nature as most biological systems make use of the hydrogen bonding between neutral oxygen and nitrogen atoms. Both the Watson-Crick³⁵ and Hoogsteen³⁶ modes of DNA base pairing use conventional hydrogen bonds and present one of the main forms of interaction encountered in the present thesis.

1.3.6 The Weak Hydrogen Bond

The new definition of hydrogen bonding submitted to IUPAC allows for the consideration of the C—H interaction with an electronegative atom as a weak form of hydrogen bonding. The first argument on the weak hydrogen bond was presented by Taylor and Kennard³⁷ in 1982, who studied 113 previously determined and published crystal structures. They reported that majority of short C—H...O and C—H...N interaction are attractive in nature and should be classed as hydrogen bonds. Taylor and Kennard concluded that the weak hydrogen bond could be important in determining the minimum energy packing arrangement of small molecules that contain nitrogen.³⁷

Building on the conclusions of Taylor and Kennard, Desiraju argues that the C—H...O interaction has directional preferences³⁸ and it does not merely act as a bystander in a crystal.³⁹ According to Desiraju, this type of a weak hydrogen bond can dictate a particular crystallisation pathway. He adds that *“the energy of an individual C—H...O interaction may be small, but if their number crosses a critical threshold, the structure may focus into an unconventional packing”*.³⁹

1.4 The Synthons Theory

The chemistry of the covalent bond primarily focuses on understanding and applying the rules that dictate the structure, properties and the transformation of a molecule. Therefore, the concept of a bond is paramount to molecular chemistry and it is a focal point in explaining interactions between atoms. On the other hand, when it comes to explaining interactions between molecules, Jean-Marie Lehn defines supramolecular chemistry as *“the chemistry beyond the molecule”*.⁴⁰ He argues that supramolecules are to molecules and the intermolecular bond (*sic*), what molecules are to atoms and the covalent bond.⁴⁰

In a more concise definition to the one presented in 1989, Desiraju⁴¹ defines crystal engineering as target-oriented and property-directed synthesis of molecular crystals. This definition has been central to the analogies drawn by his research group between classical organic synthesis and supramolecular synthesis. The definition of crystal engineering prompted Desiraju to link this emerging field with the concepts of retrosynthetic analysis. The idea of retrosynthesis in organic chemistry is associated with a particular type of synthetic thinking whereby the reaction design starts by concentrating on the product rather than the reactant. Retrosynthesis involves the analysis of the product by scrutinising its bonds and disconnecting the product into smaller molecules, whose covalent interaction will yield the product. In retrosynthetic analysis, the term *synthon* is used to refer to the smaller units which are obtained by disconnecting the product.¹⁶

1.4.1 The Supramolecular Synthon

From a supramolecular chemistry point of view, strategic synthetic thinking can also be employed for engineering novel crystal structures. In this case, the retrosynthetic analysis would focus on disconnecting the interactions between two or more molecules in order to establish the sub-structures which generate the crystal. These considerations were taken into account by Desiraju¹⁵, who in 1995 proposed the idea of a *supramolecular synthon*, which he defined as “*structural units within supermolecules which can be formed and/or assembled by known or conceivable synthetic operations involving intermolecular interactions*”.

This essentially implies that patterns in a crystal which generate a supramolecular synthon would be present in other crystal structures; if they contain molecules that possess similar functional groups. As a result, it was argued that Corey’s definition of a synthon can be adapted to crystal engineering. Desiraju proposed that a supramolecular synthon can be dissected to give the sub-molecules, which upon crystallisation, would assemble to form the crystal with the same synthons.

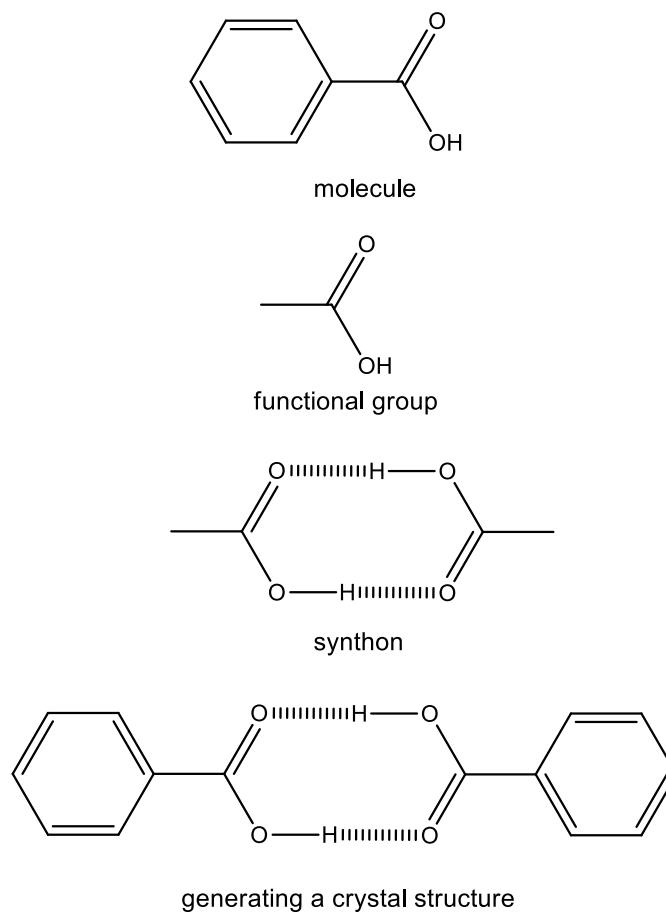


Figure 1.4:Crystal engineering from a molecule to the crystal⁴¹

Desiraju also pointed out that analogies can be made between what he calls molecular chemistry and supramolecular chemistry. According to Desiraju, molecules are formed by connecting atoms *via* covalent bonds and therefore a similar stance can be taken for crystals, which essentially represent molecules joined by intermolecular interactions. Figure 1.4 shows the steps involved in crystal engineering. The focus area in the molecule of benzoic acid is the carboxylic acid functional group. This group can easily recognise another molecule of benzoic acid to form a carboxyl dimer in this way giving rise to the synthon, which in turn generates the crystal structure.

Furthermore, any molecule which contains such functional group is expected to form a hydrogen bond in the absence of other competing intermolecular interactions. The

analogies used by Desiraju are presented in Table 1.1 and seek to emphasise the importance of perceiving crystal engineering as a continuation of the molecular chemistry.

Table 1.1: Analogies between molecular and supramolecular chemistry

Molecular Chemistry	Supramolecular Chemistry
Atom	Molecule
Covalent Bond	Intermolecular Bond
Molecule	Crystal
Synthesis	Crystal Engineering
Synthon	Supramolecular Synthon
Isomer	Polymorph
Transition State	Nucleus
Reaction	Crystallisation

Desiraju argues that the primary objective of crystal engineering should be the recognition and design of extremely robust synthon with a high degree of predictability. This implies that if any two different and unrelated molecules possess functional groups capable of synthon formation, then an intermolecular interaction, and therefore a crystal, should be achievable between the two molecules *via* the interaction between their respective functional groups. That said, one cannot overlook the impact of competing interactions.

Furthermore, synthons with strong and directional interactions form first. Once these robust synthons are formed, they would not dissolve. The subsequent synthons to be formed are those with weaker and less directional interactions. Allen *et al.*⁴² argue that synthon formation is a probabilistic event. This signifies that the more often a synthon is observed in existing crystal structures, the higher the likelihood of it appearing in new crystal structures, provided that they have the required functional groups.

In an attempt to explain the predictability of synthon formation, Desiraju uses the carboxylic acid dimer and concentrates on benzoic acid, terephthalic acid and isophthalic acid. All three compounds form the carboxylic acid dimer as shown in Figure 1.5. The

crystal of benzoic acid is obtained *via* the close packing of acid dimers, which would mean that terephthalic acid would also follow a linear arrangement similar to benzoic acid. The linear arrangement in terephthalic acid leads to the formation of a one dimensional tape, whereas the benzoic acid dimer is zero dimensional.

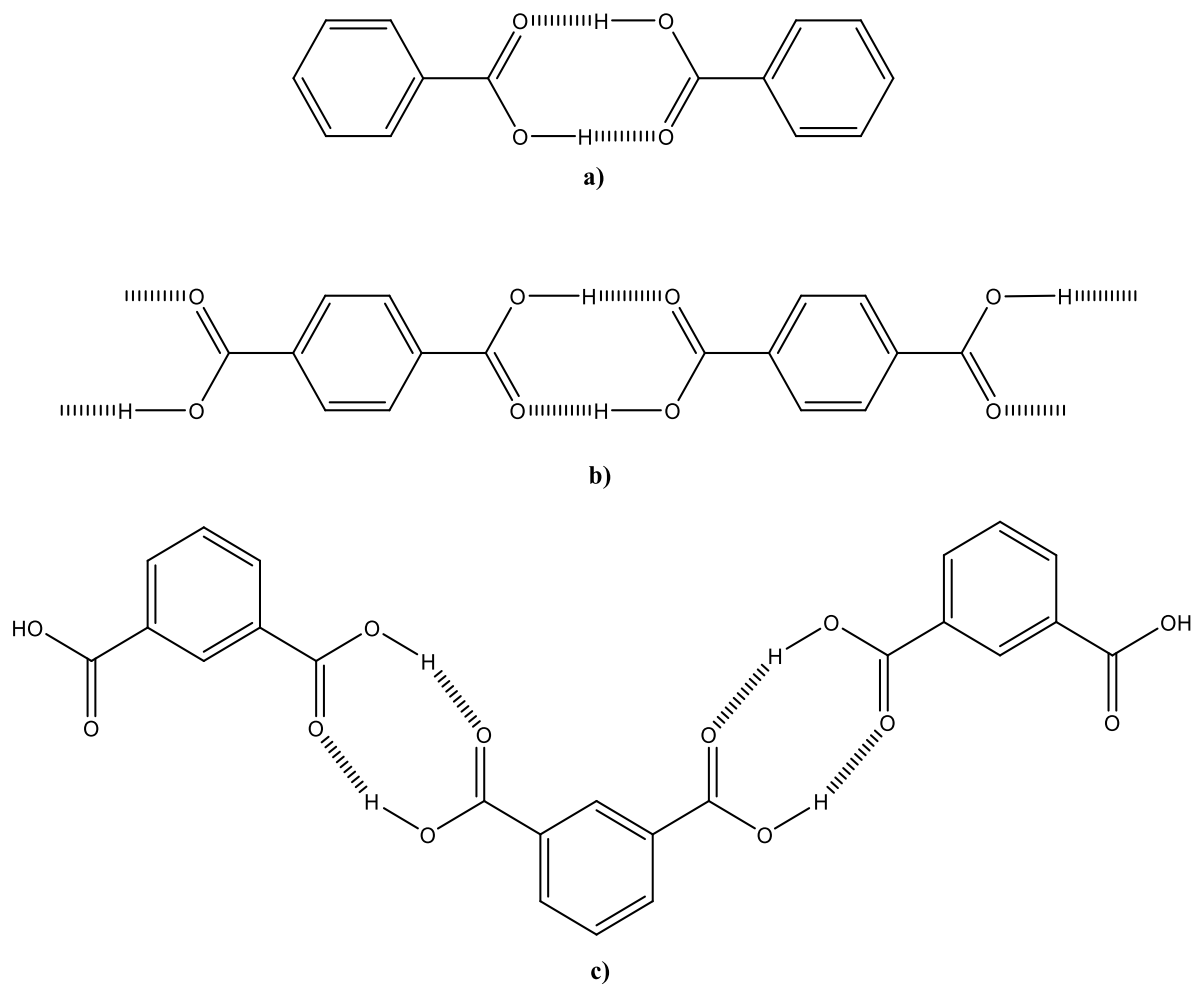


Figure 1.5: Aromatic crystal structures with the carboxylic acid dimer: a) benzoic acid; b) terephthalic acid; c) isophthalic acid

It is evident from Figure 1.5 that the location of carboxylic acid groups in isophthalic acid **c)** governs an alternative arrangement where the molecules form a ribbon with each other. This sort of behaviour in isophthalic acid can be extrapolated to other functional groups that form similar dimers with the carboxylate group given that the functional groups are located in the 1,5-position of the benzene ring. Such observation was backed previously by Jones *et al.*⁴³, who commented on structural mimicry by arguing that molecules with similar size, shape and functionalities have similar crystal structures.

1.4.2 Synthons Hierarchy in Crystal Engineering

The classification of various forms of intermolecular forces becomes crucial in understanding the frequency of particular synthons occurring in a crystal. Such classification is also important in understanding which synthon prevails over others and why. It would be correct to state that strong hydrogen bonds are the most directional interactions which govern crystal packing. However, such approach would fall short of being a coherent explanation because it completely neglects the implications which arise due to other competing interactions such as weak hydrogen bonds (e.g. C—H...O). It is precisely this weak hydrogen bond that is powerful enough to cause significant implications in the hydrogen bonding within structures where the formation of the carboxylic acid dimer is expected. Therefore, there can be cases when the interaction hierarchy is breached due to the competition between strong and weak hydrogen bonds.

In a highlight published in 2002, Desiraju⁴⁴ classifies this phenomenon as an interaction interference. The interference emanates from the C—H...O bond which hampers the formation of the carboxylic acid dimer, but instead governs the formation of O—H...O hydrogen bond known as catemer. The argument follows that in certain cases the weaker C—H...O bond acts as a discriminator and therefore alters the O—H...O dimer topology to generate the O—H...O catemer shown in part b) of Figure 1.6.

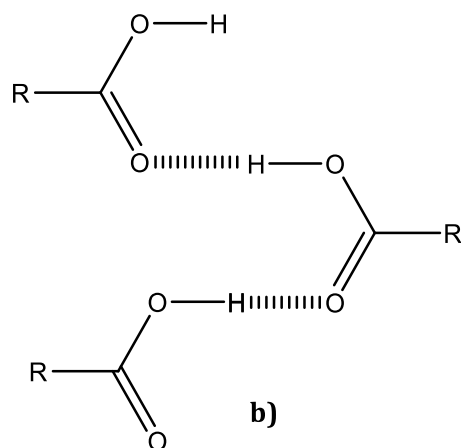
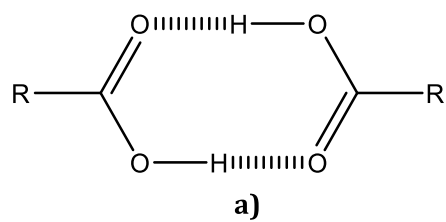


Figure 1.6: Hydrogen bonding interactions in carboxyl acid arising due to interference interaction: a) dimer; b) catemer

A typical example is highlighted by the family of cubanecarboxylic acids as observed by Kuduva *et al.*⁴⁵ in 1999.

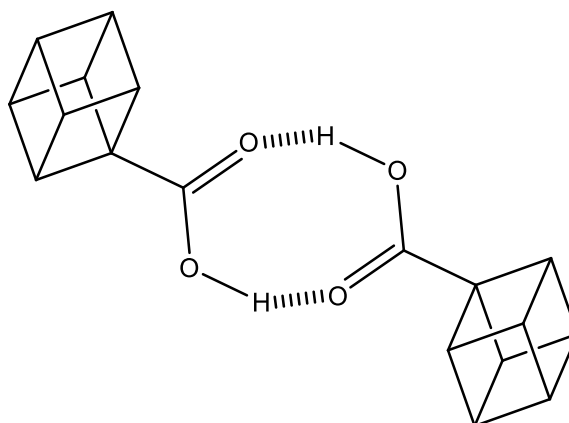


Figure 1.7: Expected dimer formation in cubanecarboxylic acid

As depicted in Figure 1.7, the presence of the carboxylic acid functional group would suggest the formation of the homosynthon dimer between the two molecules. Nevertheless, Kuduva *et al.* note that this is not the case in these cubanecarboxylic acids, because the crystal packing is governed by a combination of strong and weak hydrogen bonds. Figure 1.8 shows the hydrogen bonding present in 4-chlorocubanecarboxylic acid.

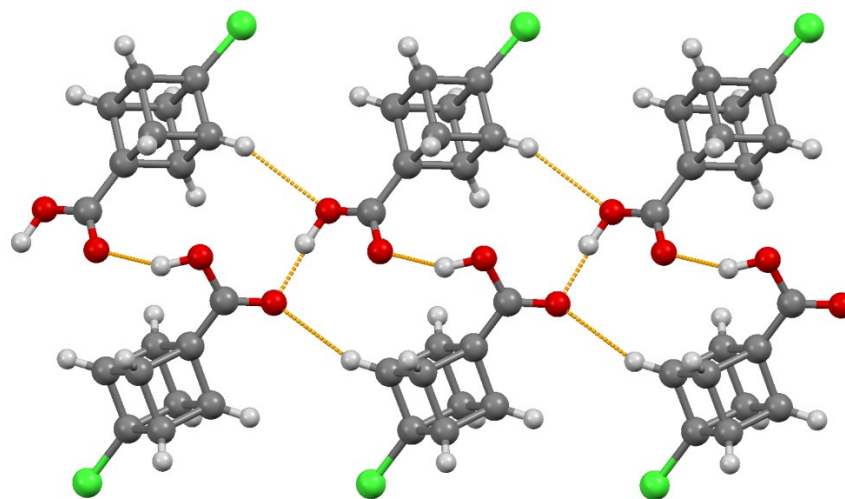


Figure 1.8: Hydrogen bonding motifs in 4-chlorocubanecarboxylic acid

1.5 Recent Advances in Understanding Synthons

Aside from the synthon theory developed by Desiraju, recently there has been work on predicting interactions between molecules by using new approaches. Hunter and co-workers⁴⁶ report the use of molecular electrostatic potential surfaces in order to understand the possible intermolecular interactions sites on the surface of the molecule. According to this research group, this co-crystal screening approach takes into consideration solvent effects in the formation of hydrogen bonding interactions between molecules.⁴⁷ The reader is also referred to consult the recently published paper of Losev and Boldyreva⁴⁸ which focuses on crystal screening methods by solvent-drop and neat grinding as a means of understanding whether co-crystallisation is achievable.

Molecular electrostatic potential surfaces have also been used by other research groups in understanding and predicting synthon formation. Aakeroy *et al.*⁴⁹ report the use of this method to predict self-assembly upon co-crystallisation of various biimidazole and aliphatic acids. Aakeroy and co-workers found that if a strong hydrogen bond donor has a choice between various acceptors, then the choice of the acceptor depends on the molecular electrostatic potential surface of the acceptor.

1.6 π - π stacking interactions

Apart from hydrogen bonding interactions, there is a wide variety of other non-hydrogen bonding intermolecular interactions which direct crystal packing and crystallisation. Aromatic interactions or π - π stacking interactions are especially important in directing self-assembly in many organic compounds which have aromaticity. This type of intermolecular interactions forms the basis of crystal packing in molecules such as benzene or naphthalene.

In a paper published in 2000, Christoph Janiak⁵⁰ distinguishes three different types of stacking interactions: parallel stacked, offset stacked and T-shaped C—H \cdots O interaction. The latter can also be viewed as a weak hydrogen bonding interaction. Janiak states that the usual π - π interaction is generally offset or parallel displaced. He also argues that face-to-face alignment of two aromatic rings is rather rare due to repulsion arising from π - π repulsion, but this problem is mitigated by having an offset alignment between the two rings.

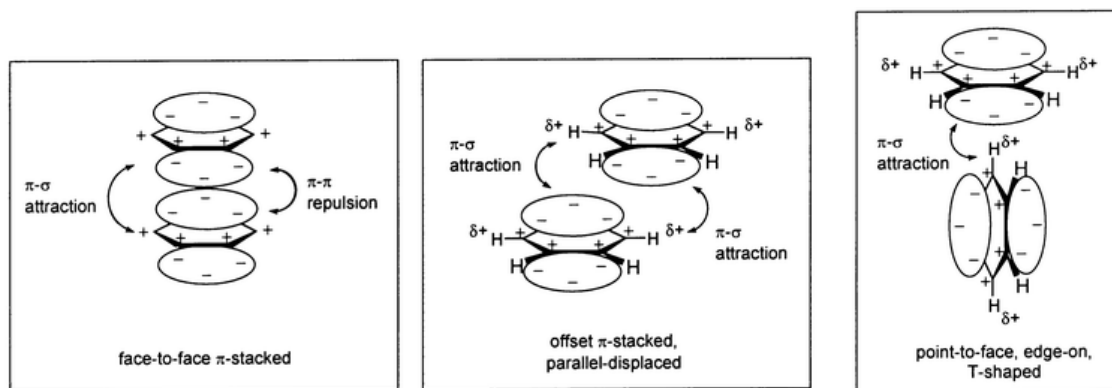


Figure 1.9: Representation of interaction between σ and π frameworks.⁵⁰ (Extract from *Journal of the Chemical Society, Dalton Transactions*, 2000)

Hunter and Sanders⁵¹ comment on π - π interactions by arguing that these interactions can be viewed as sandwiches of positively charged σ -bonds between two negatively charged π -electron clouds. Further discussion on π - π stacking interactions can be found on the review article of Hunter *et al.*⁵² published in 2012 and the references cited therein. For a discussion focusing on the terminology used to describe these interactions, the reader is referred to the perspective article of Martinez and Iverson.⁵³

1.7 DNA Bases in Crystal Engineering

1.7.1 Hydrogen Bonding in DNA nucleobases

The structural integrity of the DNA is ensured by the interactions between the DNA nucleobases. Combining the nucleobases and the sugar group *via* the glycosidic bond, gives rise to nucleosides. These are then joined to the phosphate group to generate nucleotides.⁵⁴ In structural terms, the phosphate and the sugar group comprise the backbone of the DNA, whereas the nucleobases hold the double helix together. The DNA nucleobases are divided in two groups: the purines and the pyrimidines. Adenine and guanine fall within the group of purines, whereas cytosine and thymine belong to pyrimidines.

The architecture and molecular mobility of the nucleic acid is closely linked with the rapid making and breaking of the hydrogen bonds. Hydrogen bonding is therefore responsible for stabilising the molecular conformations of the DNA.

As it can be gauged from Figure 1.10, purines and pyrimidines have different hydrogen-bond functionalities. The pyrimidines in general have an acceptor functionality that exceeds the donor functionality, bar cytosine, whereas in purines the two functionalities are equal.³³

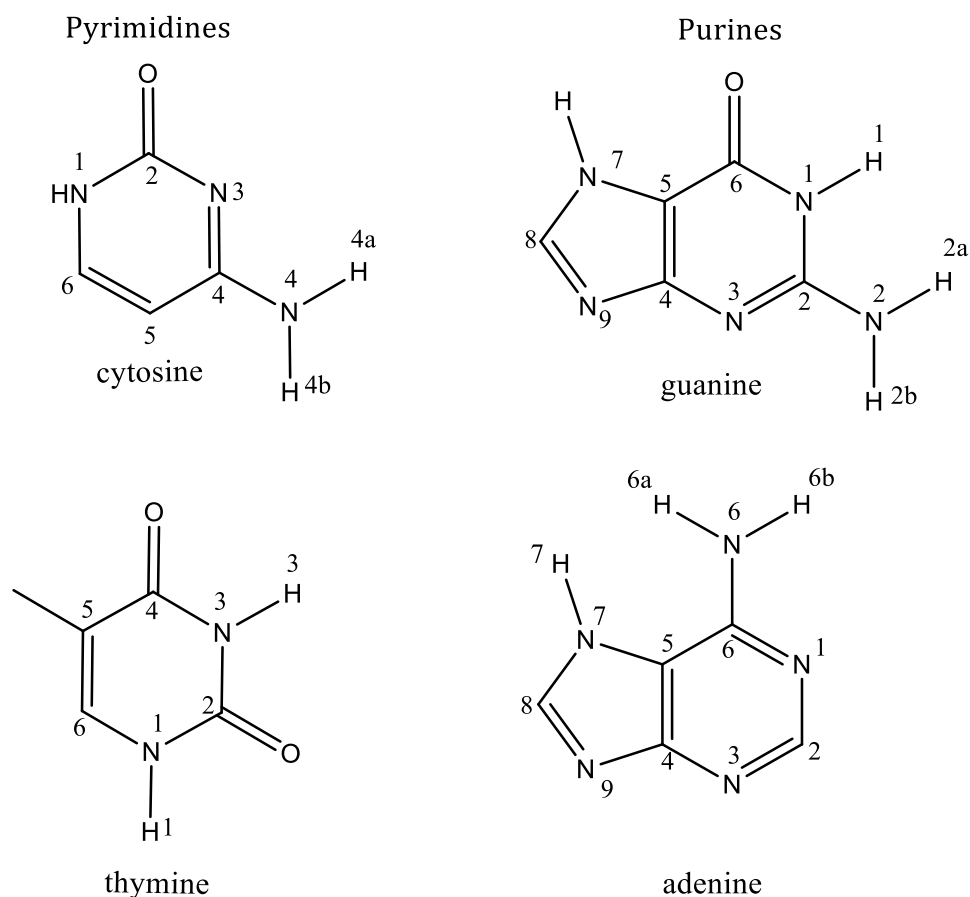


Figure 1.10: Base numbering and hydrogen-bond functionality³³

The hydrogen bond donor sites in cytosine are the N1—H1 bond, N4—H4A and N4—H4B, whereas the acceptor sites are: the oxygen on the carbonyl group and N3. The donor sites in thymine are N1—H1 and N3—H3, whereas the acceptor sites are two carbonyl oxygen atoms. Guanine has an equal number of donor and acceptor sites. The donor sites are as follows: N1—H1, N2—H2A, N2—H2B and N7—H7. The acceptor sites are the carbonyl oxygen, N3 and N9. Finally, adenine has also an equal number of donor and acceptor sites. The three donor sites are N6—H6A, N6—H6B and N7—H7, whereas the three acceptor sites are N1, N3 and N9.

1.7.2 The History of DNA Structure Determination

Determining the structure of the DNA with high degree of confidence was one of the main focus areas during 1950s and the plethora of publications in this niche field confirm this. A structure very different from the one accepted now was proposed by Pauling and Corey in 1953, who suggested that the nucleic acids must have three helices. Their claims were based on X-ray analysis and molecular structure, which, according to them, were in full compliance with some of the chemical properties of the substances comprising the DNA.⁵⁵

Pauling *et al.* suggested that the DNA structure involves three intertwined helices of polynucleotide chains with phosphate groups positioned on the inside and the nucleobases positioned on the outside of the helix. They proposed that each of the three chains contain the phosphate diester group, which is packed about the axis of the molecule and is surrounded by sugar groups, which, in turn, join to the nucleobases, purines and pyrimidines. These are positioned perpendicular to the molecular axis. The positioning of the nucleobases was also rationalised by the fact that such arrangement would enable hydrogen-bonding interactions with other molecules in the vicinity. In addition, Pauling *et al.* claimed that this form of arrangement allows the presence of all four nucleobases without any steric hindrance because they occupy the outside of the helix.⁵⁶

Though this structure is far from the model accepted today, it should be noted that the claim of Pauling and Corey, that the nucleobases must be positioned on the outside of the helix in order to circumvent steric problems, was a plausible suggestion. This is because in steric terms, the positioning of the nucleobases on the inside of the helix would cause steric hindrance, with purines contributing more due to their size. If the three helix model is taken into account, the nucleobases positioned in the inside of the three helices would hinder each other as well as the adjacent fragments. This arrangement would make the nucleic acid unstable.

But, Pauling and Corey failed to explain what precisely holds the triple helix together. Based on this model, the phosphate groups would be responsible for holding the triple helix together since they are on the inside of the helices. However, the phosphate groups are not known for having strong intermolecular interactions which would keep the molecule intact. Not only do the phosphate groups fail to interact with each other in a stabilising manner, but their overall negative charges would lead to repulsive forces, which in turn would make the molecule extremely unstable. Taking into account these remarks, it is evident that the proposed structure is not a clear and coherent representation of the true DNA structure.

1.7.3 The Structure of DNA Suggested by Watson and Crick

The major breakthrough in DNA research came by Watson and Crick in 1953.³⁵ They put forward a new model structure which was diametrically opposed to the suggestions made by Pauling and Corey.

The three helix model of Pauling and Corey was regarded as unsatisfactory by Watson and Crick on two grounds:

- 1) According to Watson and Crick, the isolated structure reported by Pauling and Corey was the salt of the nucleic acid, not the free acid itself. As result, they concluded that it would be impossible to understand what forces hold the entire structure together, if the hydrogen atoms are not present.
- 2) The van der Waals distances reported by Pauling and Corey were regarded as too short by Watson and Crick.

Taking into account the points outlined above, Watson and Crick suggested a model wherein the DNA molecule contains only two helices coiled round the same axis. Contrary to previous proposals, they claimed that the negatively charged phosphate group is positioned on the outside of the helix and the nucleobases on the inside.

Their claim was rationalised by pointing out that:

- 1) the negatively charged phosphate group can be accessed and stabilised by cations only if it is positioned on the outside, and
- 2) the only way to hold together the double helix must be the hydrogen bonding interactions of the nucleobases on the inside of the helix.

It was suggested that the bases are perpendicular to the molecular axis and a single base from one helix hydrogen-bonds to the base on the other helix. Their work claimed that the nucleobase interactions occur between purines and pyrimidines. Watson *et al.* found that only specific base pairs can hydrogen-bond together and therefore adenine hydrogen-bonds to thymine and guanine hydrogen-bonds to cytosine. These findings were also based on the fact that there is an equimolar amount of purines and pyrimidines in the DNA molecule as suggested by Chargaff *et al.*⁵⁷

Figure 1.11 below represents the interaction of the nucleobases which is known as the Watson-Crick base-pairing.

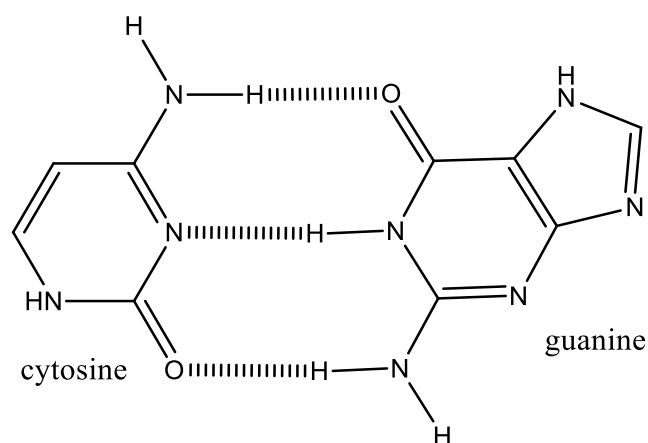
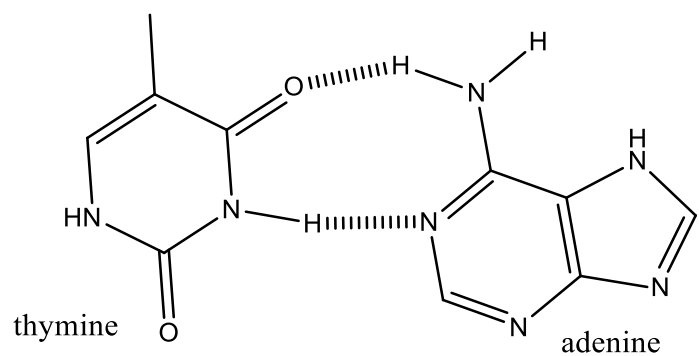


Figure 1.11: : Watson-Crick base pairing

The hydrogen bonds have been represented by dashed lines and it is evident from Figure 1.11 that the adenine:thymine pair consists of two hydrogen bonds, whereas the guanine:cytosine pair consists of three hydrogen bonds.

Watson *et al.* regarded this particular type of pairing as a possible mechanism of copying for the genetic material via self-duplication. It was stressed that one nucleobase pair must be a purine in one helix and the other must be pyrimidine in the other helix. The generation of a pair by two purines or two pyrimidines was deemed impossible.⁵⁸ This claim would be especially true in the case of purines considering they are bigger molecules. This would give rise to steric complications and therefore there would be no room for such pairing between the two helices.

1.7.4 Hoogsteen Pairing

Arguments regarding a different type of hydrogen bonding between nucleobases were put forward by Hoogsteen³⁶, who investigated co-crystals of derivatives of adenine and thymine. (Figure 1.12) Realising that in the structure of DNA positions N9 and N1 for adenine and thymine, respectively, are attached to the deoxyribose groups and considering that co-crystals between pure adenine and thymine would have these positions free for hydrogen bonding, Hoogsteen selected 9-methyladenine and 1-methylthymine as derivatives of adenine and thymine.

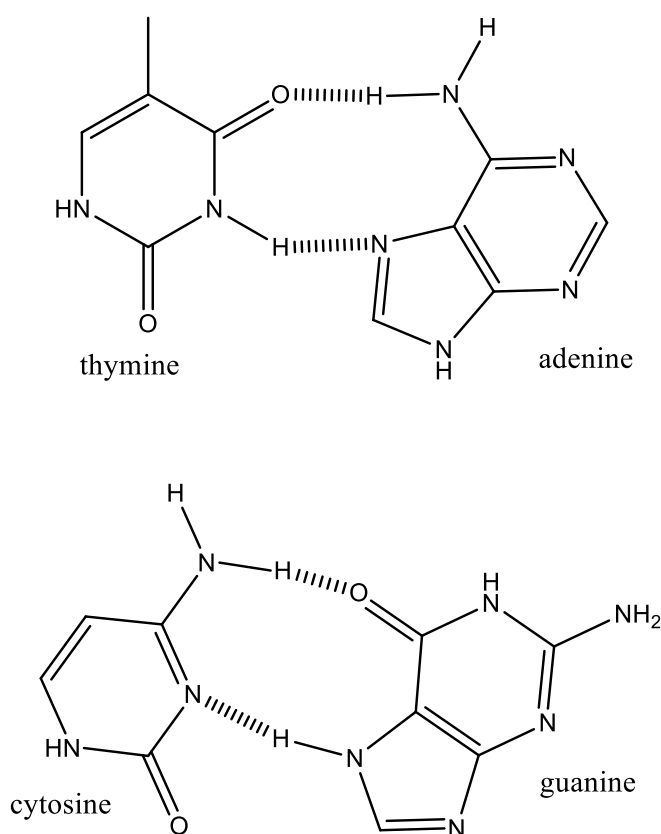


Figure 1.12: Hoogsteen mode of DNA base pairing³⁶

This choice would ensure that position N9 and N1 are blocked for hydrogen bonding - in this way mimicking the bonding between nucleobases and sugar groups in the DNA molecule. Figure 1.13 a) and b) represent the different modes of hydrogen bonding between nucleobases.

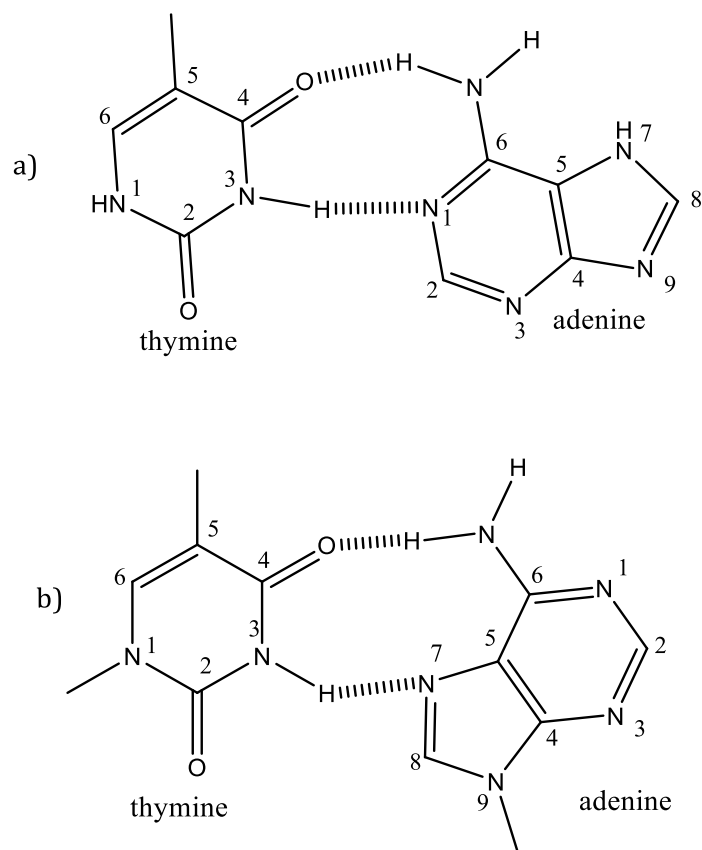


Figure 1.13: Hydrogen bonding between adenine and thymine; a) Watson-Crick; b) Hoogsteen

The most striking feature of the co-crystals grown by Hoogsteen is the way in which the two nucleobases are hydrogen-bonded to each other. A classical Watson-Crick base-pair would involve hydrogen bonding interactions between O4 of thymine and N6 of adenine as well as N3 of thymine and N1 of adenine.

However, Hoogsteen noticed that the hydrogen bonding in the adenine:thymine structure follows a different motif. The hydrogen bonding between O4 of thymine and N6 of adenine is still present; however, the amine hydrogen atom involved in the interaction is not the same. In addition, Hoogsteen also observed that N3 of thymine hydrogen-bonds to N7 atoms in the imidazole ring of adenine, unlike in the Watson-Crick model where N3 of thymine hydrogen-bonds to N1. The deviation from the Watson-Crick model could be explained by the fact that Hoogsteen blocked position N1 of thymine and position N9 of adenine by methylating them.

1.7.5 Versatile Hydrogen Bonding in Adenine

Synthon theory in crystal engineering is pivotal in predicting potential hydrogen bonding interactions that could arise in the crystal structure of a given molecule or molecules. Such approach is especially useful in predicting the formation of highly prevalent synthons such as the carboxylic acid dimer. This claim agrees with the reasoning of Allen *et al.*⁴², who argued that synthon formation is a probabilistic event. In other words, synthons occurring more frequently known in crystal structures generally tend to have a higher probability of appearing in novel crystals. However, in molecules such as the DNA bases, the presence of both hydrogen bond donors and acceptors can complicate the prediction of synthon formation. Numerous examples in literature demonstrate that DNA bases exhibit versatile hydrogen bonding motifs owing to their donor and acceptor functionality.

A striking example is adenine, which was studied by Thompson and co-workers⁵⁹ in order to understand its interactions with succinic, fumaric and maleic acid. In two independently conducted pieces of research, Thompson *et al.*⁵⁹ and Mahapatra *et al.*⁶⁰ argued that adenine-adenine (or adeninium-adeninium) interactions are formed via N—H \cdots N hydrogen bonds, which give rise to five different motifs:

- 1) Interactions along the base of the two molecules forming a $R_2^2(8)$ homosynthon;
- 2) Interactions between Watson-Crick³⁵ and Hoogsteen³⁶ edges of a neighbouring adenine generating a $R_2^2(9)$ homosynthon
- 3) Interactions between Hoogsteen pairing generating a $R_2^2(10)$ homosynthon and
- 4) Interactions between Watson-Crick⁵⁸ pairing generating a $R_2^2(8)$ homosynthon
- 5) Interactions along the base of two adeninium molecules of the less stable tautomeric form generating $R_2^2(8)$ homosynthon with different hydrogen bonding to motif 1 above

It is worth noting that adenine contains two tautomeric forms: [7H]-adenine and [9H]-adenine as shown in Figure 1.14. As a result, interaction **5** illustrated in Figure 1.15 relates

to the less stable tautomeric form [7H]-adenine.⁶¹ The existence of this form over the more stable form was rationalised by the stabilisation due to hydrogen bonding, since the unprotonated N1 site in adenine was available for hydrogen bonding and formed a non-classical C—H...O hydrogen bond with the acid.⁵⁹

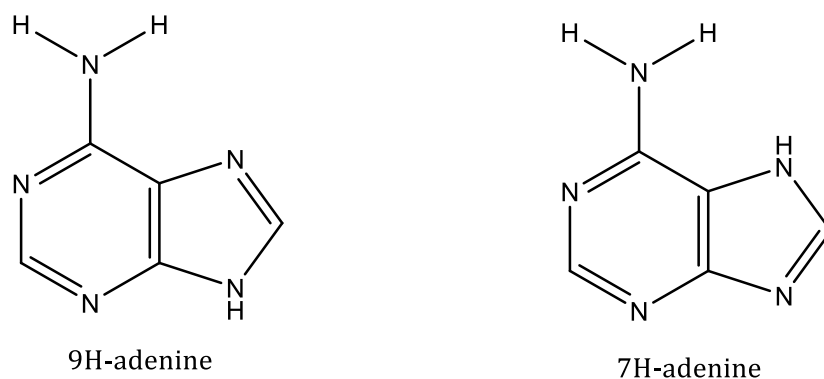


Figure 1.14: Two tautomeric forms of adenine^{59, 60}

The emergence of the less stable tautomeric form was associated with a significant change in the hydrogen bonding between adeninium dimers generating motif **5** as outlined in Figure 1.15. It was argued that the hydrogen bonding was different in salt and co-crystal structures because salt formation was associated with the emergence of the less stable tautomeric form [7H]-adenine.

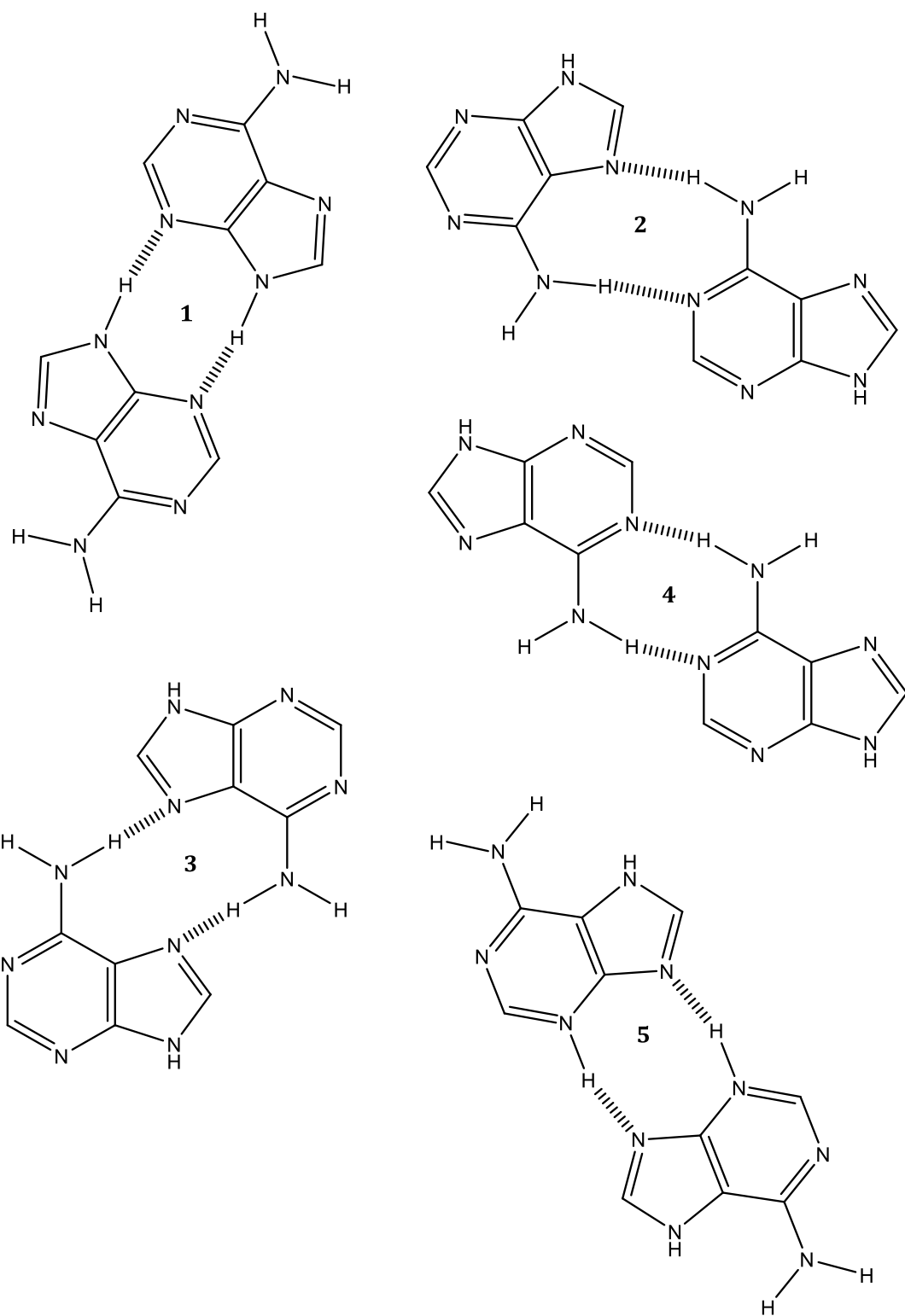


Figure 1.15: Bidentate homosynthons formed between adenine molecules

1.7.6 Survey of the Cambridge Database

The Cambridge Structural Database¹³ (CSD version 5.35, November 2013) was searched for crystals containing adenine and thymine or their derivatives. The search was carried out using the software ConQuest⁶² and the following filters were applied: “only organics” and “3D coordinates determined”. The search revealed only 11 entries with these two nucleobases. However, it is remarkable that none of these 11 entries correspond to a co-crystal between adenine and thymine. All of the structures are derivatives of these nucleobases, substituted nucleobase forms and two hydrates with adenine and thymine.

A similar survey was also carried for crystals containing guanine and cytosine and their derivatives. The search which was carried out using ConQuest⁶² and the same filters as above were applied. The search revealed only 29 entries for these two nucleobases. Surprisingly, none of the entries corresponded to a co-crystal of guanine and cytosine. The entries contained substituted forms of the bases and their derivatives. Contrary to adenine and thymine, the 29 entries for guanine and cytosine have no hydrate form between the two.

A survey for crystals containing adenine and cytosine and their derivatives yielded only one entry with nucleosides derivatives of adenine and cytosine. The CSD search for guanine and thymine revealed no entries.

1.7.7 Solubility Challenges

Research involving DNA nucleobases can be rather challenging given their poor solubility in many common solvents, which is perhaps reflected in the limited number of entries on the CSD for crystals containing solely the nucleobases. These difficulties were also faced by Chargaff *et al.*⁵⁷ when trying to discover suitable solvent systems and methods for quantitative separation of purines.⁶³

1.7.8 Aims and Objectives

The research presented in this thesis aimed to exploit and investigate the hydrogen bonding functionality of DNA nucleobases or their derivatives in order to engineer novel crystal structures. Crystal engineering principles were used in order to achieve the primary objectives of this thesis. The objectives were to:

- Grow previously undiscovered supramolecular architectures
- Characterise these using single crystal X-ray diffraction
- Understand the intermolecular interactions governing crystal packing in these systems and interpret synthon formation
- Explore co-crystal screening techniques based on neat grinding
- Engineer multicomponent complexes (co-crystals, salts, hydrates and solvates) and investigate their thermal stability
- Use metal-ligand complexes as a building block to generate hydrogen-bonded networks of DNA nucleobases and its derivatives

Given that hydrogen bonding is the key interaction exploited for the design of new crystals, it is essential to review the research conducted in determining the structure of the DNA. Furthermore, a coherent review and a solid understanding of the hydrogen bonding in DNA bases is imperative to generating new crystal structures with these bases.

Chapter 2:

Synthetic Methodology and Analytical Techniques

2.0 SYNTHETIC METHODOLOGY AND ANALYTICAL TECHNIQUES

2.1 Synthetic Methods

2.1.1 Solution Crystallisation

Solution crystallisation is the most flexible and commonly used method for obtaining crystals. A molecule or a mixture of molecules is dissolved in a solvent or a mixture of solvents (also referred to as co-solvents). The choice of the solvent usually depends on the type of the compound under study and it is generally accepted that “like dissolves like”. Therefore, factors such as polarity, alkyl chain length or functional groups should be taken into consideration when choosing a solvent. Dissolution can also be achieved in a mixture of solvents. It should be noted that the use of co-solvents allows the manipulation of solubility and it can improve dissolution compared to the use of one solvent alone. The composition of co-solvents can be altered by varying the proportions of solvents A and B present in the mixture. It is important that the vessels are free of any contaminants as these could act as seeds for nucleation. In addition, the reaction vessels should be left unperturbed as mechanical interference can compromise the quality of the crystals. After dissolution, the next step is to induce crystallisation which can be achieved in various ways and the choice of the crystallisation technique depends on the compounds under study.⁶⁴

2.1.1.1 Controlled Cooling

In cases where crystal formation requires controlled vessel cooling of the solution, the reaction vessel may be placed in an oil bath and heated until dissolution is achieved. Subsequently, the vessel is wrapped in aluminium foil to insulate the vessel and ensure slower cooling to room temperature.

2.1.1.2 Solvent Evaporation

Crystallisation can be induced by allowing the solvent to slowly evaporate in order to achieve supersaturation. The rate of evaporation can be controlled by capping the solution vessel and adjusting the size of the aperture through which the solvent can escape. It is imperative to control the rate of evaporation because fast evaporation of the solvent often leads to poor quality crystals or precipitation of powder.

2.1.1.3 Solvent Diffusion (Antisolvent Crystallisation)

This method exploits the solubility of a compound in different solvents that are miscible with each other. If a compound is highly soluble in one solvent, the overall solubility can be altered by introducing another solvent which known as the antisolvent. The compound is dissolved in the solvent and is placed in a narrow vessel. Subsequently, the antisolvent is introduced slowly so that it rests partially on top of the solvent.

The addition of the antisolvent should be done in a way that it does not disturb the solvent layer. This can be achieved by either adding it round the walls of the vessel or injecting it with a syringe. Figure 2.1 depicts a schematic diagram of the method. As the two solvents begin to mix slowly, the solubility of the compound in the bottom layer will be decreased and crystal growth occurs.

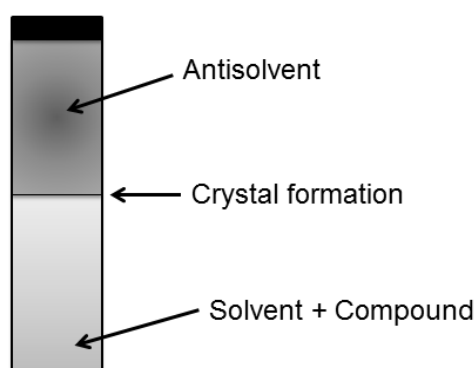


Figure 2.1: Solvent Diffusion

2.1.1.4 Vapour Diffusion

This method is similar to the one mentioned in Section 2.1.1.3 apart from the fact that it entails the diffusion of vapour into a solution. Reagents such as pyridine were utilised in the present work. The main advantage of this method is the control of the rate of diffusion by using one or two vessels contained in a bigger closed vessel. The two types of vapour diffusion cells are shown in Figure 2.2.

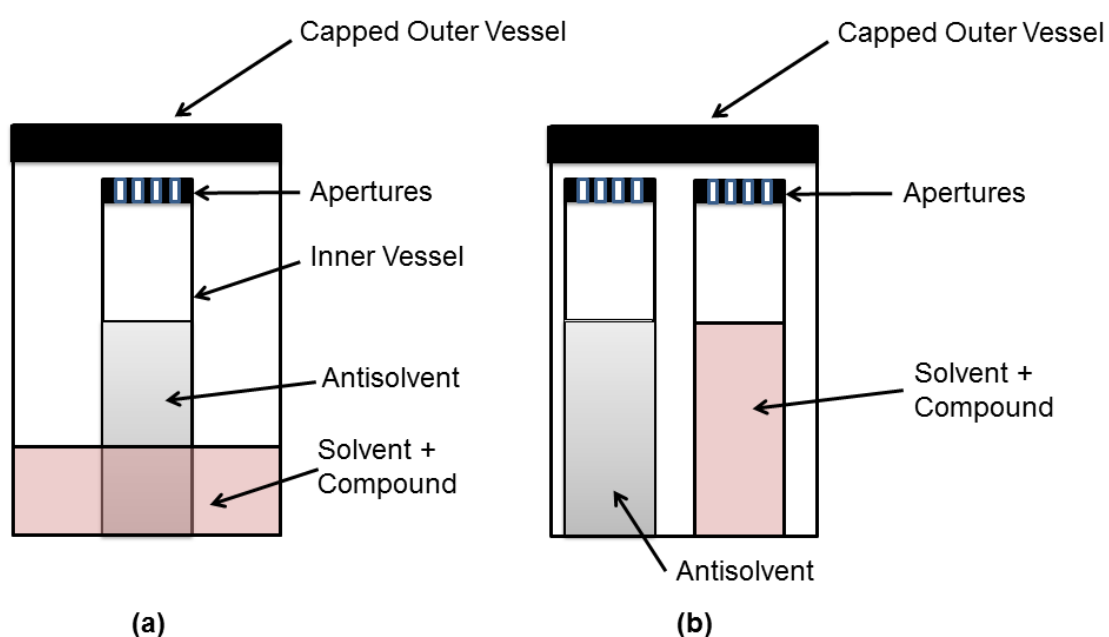


Figure 2.2: Set up of vapour diffusion cells

2.1.2 Melt Crystallisation

This method is suitable for the crystal growth of compounds (e.g. organic) with relatively low melting points. A limitation of the method is the fact that elevated temperatures can cause decomposition of the solids under study. A compound (or more) is mixed together and heated until they melt. Crystallisation is achieved during melt cooling.

2.1.3 Sublimation

The conversion of a solid compound directly into gaseous state without going through the liquid state is known as sublimation. In this method, the solid compound is heated above its temperature of vapourisation and the vapours formed pass to a cooled surface on which crystals form.⁶⁰

2.1.4 Synthetic methods used during this research

2.1.4.1 Solution Crystallisation

Most of the crystals presented in the present work were grown using solution crystallisation methods. Compounds were dissolved in water, ethanol or ethanol:water mixtures. The reaction mixtures were usually heated to 60-80 °C. In cases where compounds were sparingly soluble in the warm solvent, the solid compounds were ground prior to mixing with the solvent. This was found to improve solubility.

Experiments involving ligand coordination to transition metals were usually performed without adjusting the pH of the system. However, in cases where deprotonation of the ligand was not achieved, 0.1M NaOH solution was added drop-wise to achieve dissolution. Reactions were performed either by adjusting the pH of the entire reaction mixture or by adjusting the pH of the ligand solution separately and subsequently adding this solution drop-wise to the transition metal solution.

2.1.4.2 Reflux

When dissolution challenges persisted during solution crystallisation, the reaction mixture was heated under reflux. The duration of reflux varied depending on the reagents present in the mixture. Upon completion, the reaction vessel was wrapped with aluminium foil and left unperturbed to cool down to room temperature. In other instances, the reaction vessel was left immersed in the oil bath so that the cooling could be further slowed down.

2.1.4.3 Recrystallisation from water

Methanolic or ethanolic solutions were used for growing crystals containing hydrogen-bonded networks of DNA bases with transition metals. The reaction mixture was left to cool to room temperature overnight. The mixture was subsequently filtered and the powder obtained was dissolved in water. Slow solvent crystallisation from water produced crystals.

2.2 Structure Determination

2.2.1 Crystallography

2.2.1.1 Unit Cell and Crystal Systems

A unit cell is defined as the fundamental building block and the repeat unit of a lattice. One unit cell is related to its neighbouring unit cells by translation. Conventionally, the unit cell can be defined by its parameters, a , b , c referring to the unit cell lengths and α , β , γ referring to the interaxial angles. (Figure 2.3)

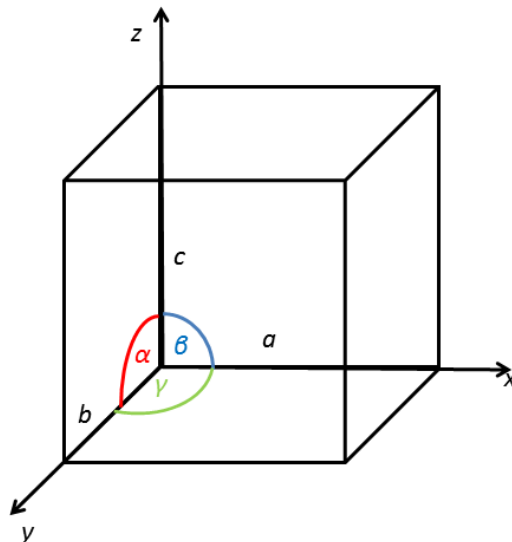


Figure 2.3: Six unit cell parameters used to define a general unit cell

There exist seven crystal systems, which are defined by the minimum symmetry element present. The symmetry elements impose restrictions and dictate the shape of the unit cell in a crystal system. Therefore, it is important to note that the shape of a unit cell arises due to symmetry and not *vice versa*. Table 2.1 presents the seven crystal systems and their essential symmetry element.

Table 2.1: Seven crystal systems

Crystal System	Unit Cell Parameters	Essential Symmetry Element
Cubic	$a = b = c; \alpha = \beta = \gamma = 90^\circ$	Four 3-fold rotations axes
Tetragonal	$a = b \neq c; \alpha = \beta = \gamma = 90^\circ$	One 4-fold rotation axis
Orthorhombic	$a \neq b \neq c; \alpha = \beta = \gamma = 90^\circ$	Three mutually \perp 2-fold axes or mirror planes
Hexagonal	$a = b \neq c; \alpha = \beta = 90^\circ; \gamma = 120^\circ$	One 6-fold rotation axis
Trigonal	$a = b \neq c; \alpha = \beta = 90^\circ; \gamma = 120^\circ$	One 3-fold rotation axis
Monoclinic	$a \neq b \neq c; \alpha = \gamma = 90^\circ; \beta \neq 90^\circ$	2-fold rotation axis or mirror plane
Triclinic	$a \neq b \neq c; \alpha \neq \beta \neq \gamma \neq 90^\circ$	None

2.2.1.2 Lattice Types

A lattice is a regular repeating array of points in space, whereas the 'basis' is an atom or a group of atoms. Placing the basis on every lattice point gives rise to the crystal structure. There are four lattice types which are classified as: primitive (*P*), body centred (*I*), face centred (*F*) and C-centred (*C*).

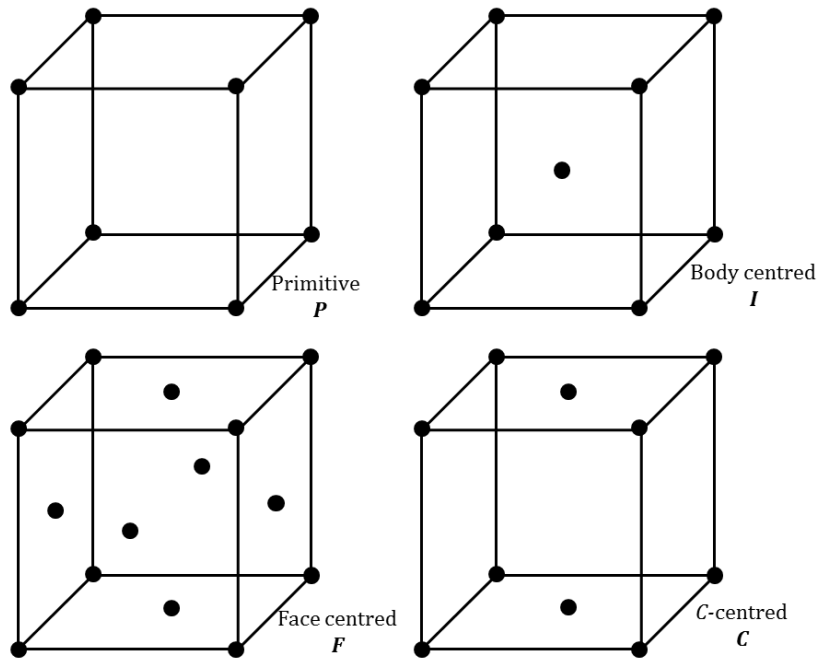


Figure 2.4: Illustration of the four lattice types showing the relationship between lattice points

Figure 2.4 depicts a schematic representation of the four lattice types. The primitive unit cell contains a single lattice point at (x, y, z) . Each lattice point is related to others by a translation of one unit along the unit cell axes a, b and c .

The body centred lattice is similar to the primitive lattice with the addition of another lattice point. The lattice points are located at (x, y, z) and $(x + \frac{1}{2}, y + \frac{1}{2}, z + \frac{1}{2})$. The face centred unit cell has lattice points at (x, y, z) and $(x, y + \frac{1}{2}, z + \frac{1}{2})$, $(x + \frac{1}{2}, y, z + \frac{1}{2})$ and $(x + \frac{1}{2}, y + \frac{1}{2}, z)$.

A C-centred lattice contains lattice points at (x, y, z) and $(x + \frac{1}{2}, y + \frac{1}{2}, z)$. This unit cell contains two lattice points.

Combining the seven crystal systems with the four lattice types generates the 14 Bravais lattices named after Auguste Bravais and shown in Table 2.2.

Table 2.2: The 14 Bravais lattices

Crystal System	Bravais Lattice
Cubic	<i>P, F, I</i>
Tetragonal	<i>P, I</i>
Orthorhombic	<i>P, C, F, I</i>
Hexagonal	<i>P</i>
Trigonal	<i>P</i>
Monoclinic	<i>P, C</i>
Triclinic	<i>P</i>

2.2.1.3 Symmetry Analysis

A molecule is regarded as symmetrical if upon movement it is indistinguishable from its initial orientation. This movement is known as the **symmetry operation** and includes either a rotation, reflection or a translation. On the other hand, the geometrical entity with respect to which the symmetry operation is performed represents the **symmetry element**.⁶⁵

There are two symmetry groups within which molecules can be classified and these are known as the **point-symmetry** and **the space-symmetry**. A molecule is said to have a point-symmetry only if the symmetry operation leaves one point within the molecule unchanged or fixed. For example, rotation of an octahedral molecule by a 180° about z would leave two bonds on the z-axis unchanged or fixed. Space-symmetry, on the other hand, arises as a result of combining a point-symmetry operation with a translation. Space-symmetry leaves no point within the molecule fixed because the entire molecule moves an equal distance.

2.2.1.4 Point Symmetry Operations

n-fold rotation

In this symmetry operation, a rotation of $360^\circ/n$ leaves the properties of the surrounding space unchanged. Here, n refers to the order of the axis and can take values 1, 2, 3, 4 and 6. For example, for $n = 4$, a 4-fold rotation rotates the molecules by 90° . If the order of the axis is $n = 0$, this implies a 360° rotation which is referred to as the identity operation.

n-fold rotoinversion

In this symmetry operation, a rotation of the order n is combined with inversion through a point whereby an atom at positions x, y, z is mapped onto $-x, -y, -z$. A rotoinversion is denoted as \bar{n} and it can take values $\bar{1}, \bar{2}, \bar{3}, \bar{4}, \bar{6}$. A one-fold symmetry operation $\bar{1}$ is called the centre of symmetry. It is imperative to distinguish between a pure rotation and a rotoinversion in the sense that a pure rotation converts a right-handed molecule only to right-handed molecules, whereas applying successive rotoinversion operations converts a right-handed molecule to a left-handed molecule.

Mirror plane

This operation is denoted with the symbol m . A mirror plane is equivalent to a two-fold rotation axis $\bar{2}$ perpendicular to this plane.

2.2.1.5 Space Symmetry Operations

As stated previously, the combination of point-symmetry operations with translational operations generates the space-symmetry operations, which are discussed below.

n-fold screw axis: A screw axis combines a pure rotation with a translational operation and is also referred to as a rototranslation. This symmetry operation is given the symbol m_n , where n refers to the rotation component and n/m refers to the translational component. Therefore, a rotation of $360^\circ/n$ is followed by a translation along the rotation

axis by a fraction of n/m . For example, a 2_1 screw axis implies that a molecule will undergo a 2-fold rotation (180°), which is then followed by a translation of $\frac{1}{2}$ parallel to the axis of rotation. This operation is depicted in Figure 2.5.

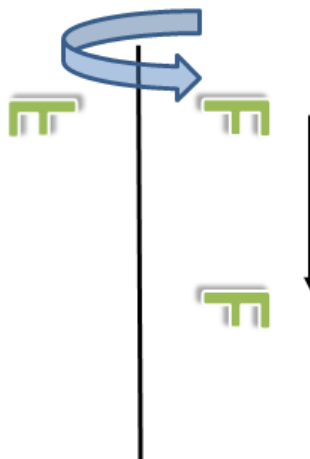


Figure 2.5: 2_1 screw axis

Glide plane: Combining a mirror plane with a translation gives rise to a glide plane. A glide plane involves a translation of $\frac{1}{2}$ along an axis followed by a reflection along to the same axis. Depending on which axis the operation takes place it can be called an *a*-glide, *b*-glide and a *c*-glide. A diagonal glide plane between two axes is called an *n*-glide.

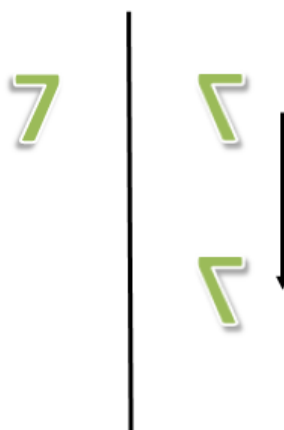


Figure 2.6: Glide plane

2.2.1.6 Miller Indices

Miller indices are used to identify a parallel set of planes.⁶⁶ A lattice plane cuts the crystallographic axes x, y and z at $1/h, 1/k$ and $1/l$. If a lattice plane cuts x, y and z at $(1, \frac{1}{2}, \frac{1}{3})$, its Miller indices will be (123) . This relationship shows that the Miller indices are obtained by taking the reciprocal of the crystallographic axes. Crystallographic planes oriented parallel to either x, y , or z can be defined by $(0kl), (h0l)$ or $(hk0)$, respectively. Similarly, planes parallel to the faces A, B and C take the values $(h00), (0k0)$ and $(00l)$, respectively.⁶⁷

2.2.1.7 Space Groups

There are 230 ways that are compatible with geometrical requirements in which one can combine rotations, rotoinversions, screw axis and glide planes. These combinations generate the 230 space groups.

Giacovazzo *et al.*⁶⁷ define a space group as “a set of geometrical symmetry operations that take a three-dimensional object to itself”. Point symmetry operations can be combined in 32 ways and this generates the 32 point groups. These points groups when combined with the 14 Bravais lattices give rise to the 73 symmorphic space groups. Combining the 73 symmorphic space groups with space symmetry generates the 230 space groups.

2.2.2 X-ray Diffraction

The discovery of X-rays was made by Wilhelm Conrad Röntgen in 1895 and he referred to them as X-rays.⁶⁸ The interaction of X-rays with matter has been crucial to the development of various modern structure determination techniques. X-rays interact with electrons and the scattering of X-rays from electrons is referred to as Thomson scattering. X-rays can interact with the contents of a crystal because their wavelengths lie in the region $0.1-100 \text{ \AA}$, which also corresponds to the same order of molecular bond distances in the typical range $0.8-3.0 \text{ \AA}$.⁶⁹

X-ray diffraction experiments can be carried out on single crystals and on polycrystalline materials (powders). This analytical technique utilises X-rays to identify the arrangements of molecules, atoms and ions in a crystal form. It has been regarded as the only analytical technique that enables full understanding of the molecular structure of a compound in the solid crystalline state.⁶⁹ Single-crystal X-ray diffraction enables absolute structure determination by identifying the arrangement of atoms in a crystal.

On the other hand, X-ray powder diffraction is suitable for the characterisation of polycrystalline materials and provides information on phase purity or presence of more than one phase in the powder mixture.

While other structure determination techniques provide information about the chemical structure of a compound, single-crystal X-ray diffraction is the only technique that provides information on the bond length and interatomic and intermolecular distances of the compound.

2.2.2.1 Generation of X-rays

X-rays are a particular type of electromagnetic radiation. They are produced when rapidly moving electrons are stopped by a solid target and their kinetic energy is converted into radiation. A high voltage (40 kV) is applied to a metal filament, which accelerates the electrons towards a metal target (anode). As the electrons penetrate the metal target, their velocity is decreased due to collisions and the energy loss as a result of this deceleration is converted to continuous X-ray emission. This is commonly referred to as Bremsstrahlung radiation. Apart from continuous X-ray radiation, there is also characteristic radiation. When the metal target is bombarded by an energetic beam of electrons, these electrons collide with and remove the K-shell electrons from the metal target - in this way creating holes. Subsequently, electrons from the L-shell of the target decay to fill the holes in the K-shell and this gives rise to X-rays.⁷⁰

The energy of the emitted X-rays is equal to the difference between the upper and lower energy levels of the electron that filled the hole of the K-shell. Since the energy levels of K and L differ by only one quantum level (K being $n = 1$ and L being $n = 2$) the transition is denoted as α lines.

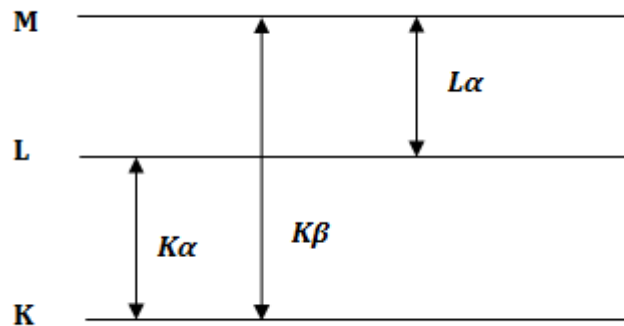


Figure 2.7: Energy levels of the metal target and the denomination of emissions

In the example above the transition occurred by filling a hole in K-shell and this is conventionally described as $K\alpha$ lines. In addition, if the hole in the K-shell was filled with the transition of an electron from the M-shell ($n=3$) the denomination would be $K\beta$ lines, as β signifies a quantum level difference of two. Schematic representation of these transitions is shown in Figure 2.7. Given that the energy released during this transition corresponds to a specific target metal and the specific electron shell within the target metal, this energy is called the characteristic X-ray. Figure 2.8 presents the characteristic radiation of an X-ray generator.

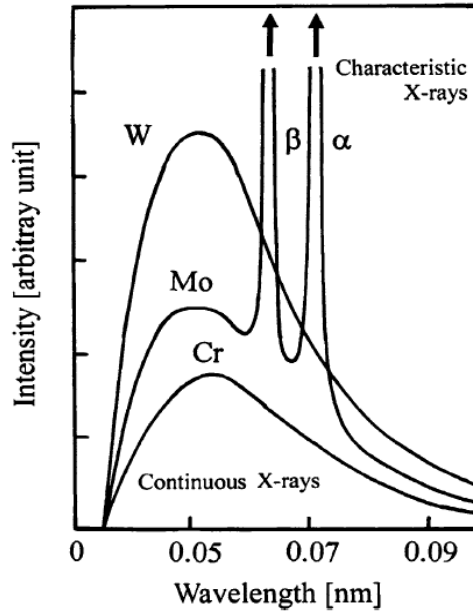


Figure 2.8: Representation of the X-ray spectrum⁷¹

It should be stressed that characteristic X-rays can be generated only in the condition that the applied voltage is high enough to accelerate electron such that they have sufficient energy to eject an electron from the K-shell.⁷¹ Quantum levels $n = 2$ or higher lead to multiple energy levels which cause α and β transition to split into very closely spaced lines at high resolution. This implies that $K\alpha$ at high resolution can be resolved as $K\alpha_1$ and $K\alpha_2$ occurring at different wavelengths which are close to each other. However, at low resolutions the overall $K\alpha$ is calculated as the weighted average of $K\alpha_1$ and $K\alpha_2$ by using Equation 2.1:

Equation 2.1

$$\lambda(\text{average } K\alpha) = \frac{[2(\lambda(K\alpha_1)) + (\lambda(K\alpha_2))]}{3}$$

Crystals of strongly absorbing materials are usually analysed with molybdenum as the metal target (anode). A weighted average for MoK α can be determined as shown in Table 2.3.

Table 2.3: Characteristic X-ray wavelengths for molybdenum

Type of radiation	Wavelength (Å)
MoK α_1	0.70932
MoK α_2	0.71354
average K α	0.71703

2.2.2.2 Diffraction and Bragg's Law

Diffracted beams are observed only when the incident X-rays and the scattered X-rays from the crystal have constructive interference. This implies that the incident and scattered rays must be completely in phase. Such geometrical condition is crucial for observing the diffracted beams and is known as Bragg's law.⁶⁶ According to Bragg's law, the difference in the path lengths between scattered and incident X-rays must be an integer number of wavelengths and is expressed by Equation 2.2:

Equation 2.2

$$2d\sin\theta = n\lambda$$

where θ refers to the Bragg angle or the diffraction angle, n is the order of diffraction and is usually taken as unity, λ corresponds to the wavelength of the X-rays and d is interplanar spacing.⁶⁶

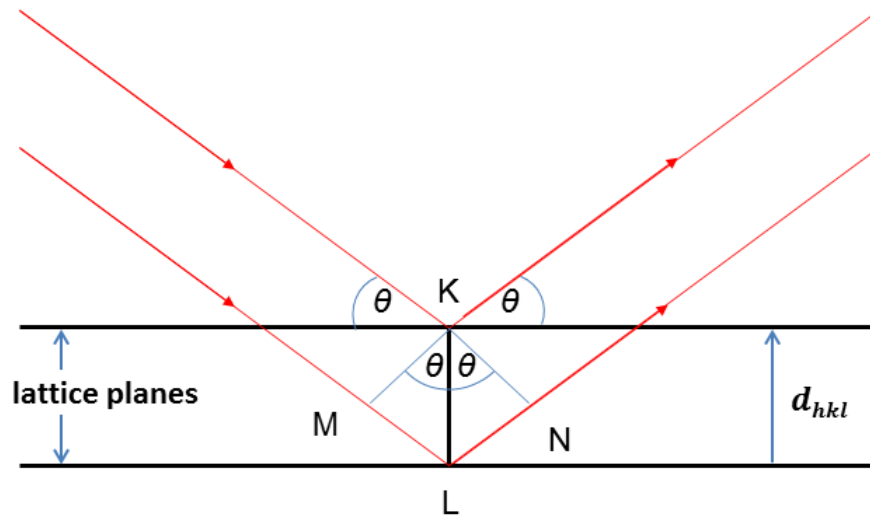


Figure 2.9: The Bragg condition for X-ray diffraction from a crystal

As it can be seen from Figure 2.9, the angle at which the incident X-ray (between point M on the figure and the plane normal L) collides with the crystal is denoted as θ . This angle is equal to the angle occurring between the plane normal and the diffracted X-ray (between plane normal L and point N)⁷¹ and is given by the expression:

Equation 2.3

$$LM + LN = n\lambda \text{ and } \sin \theta = LM/d$$

The condition for obtaining constructive interference is satisfied when the path difference is an integer number of wavelengths.

For a cubic unit cell the relationship between interplanar spacing (d) and hkl is given by the following expression:

Equation 2.4

$$\frac{1}{d^2} = \frac{h^2 + k^2 + l^2}{a^2}$$

2.2.2.3 Diffraction Intensities and the Structure Factor

Each scattered X-ray may be thought of as arising from a set of planes defined by hkl and has intensity denoted I_{hkl} .⁶⁹ This intensity is proportional to the square of the structure factor (F_{hkl}).

In general, the structure factor is a complex number and it contains two pieces of information: the amplitude and the phase shown in the Argand plane. (Figure 2.10). The length of the vector corresponds to the amplitude of the wave and the inclination of this vector on the horizontal (real) axis represents the phase angle.⁷¹ The summation of all scattered waves by all atoms in the unit cell from a given plane gives the resultant wave.

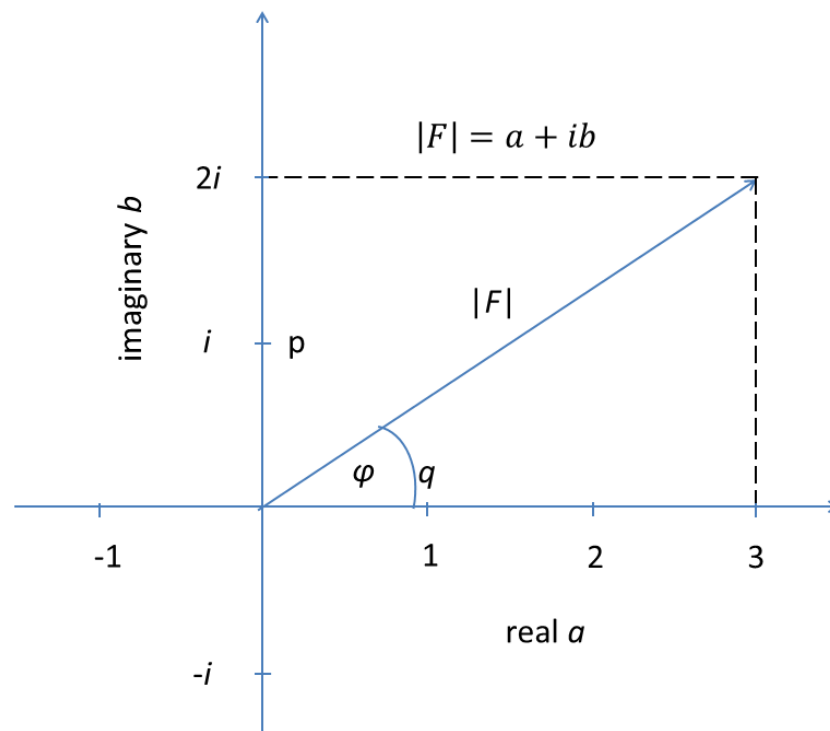


Figure 2.10: Argand diagram representing wave behaviour by complex number

It is evident from Figure 2.10 that the structure factor, F is a complex number defined by a and b as the real components and i as the imaginary component. This relationship is given by the equation below:

Equation 2.5

$$F = a + ib$$

The relationship of a and b with the magnitude $|F|$ is given by:

Equation 2.6

$$a = |F|\cos\phi$$

Equation 2.7

$$b = |F|\sin\phi$$

Using Euler's law, $(\cos\phi + i\sin\phi) = e^{i\phi}$, the structure factor equation can be simplified to:

Equation 2.8

$$F = |F|e^{i\phi}$$

Each wave with its amplitude and phase represents the forward Fourier transform of the crystal structure and is given by the following mathematical relationship:

Equation 2.9

$$F_{hkl} = \sum_{j=1}^N f_j \exp[2\pi i(hx_j + ky_j + lz_j)]$$

where f_j refers to the atomic scattering factor for atom j , defined by coordinates x_j, y_j, z_j , Miller indices are represented by h, k, l and N being the number of atoms in the unit cell. This equation shows that the structure factor is independent of the size and the shape of

the unit cell (refer to the 7 crystal systems). It, however, demonstrates that the structure factor is related to atomic positions within the unit cell.⁷¹

2.2.2.3.1 Structure Factor Extinction Rule for a primitive Cell

A primitive unit cell lattice has points at x, y, z . For a primitive lattice there are no extinctions due to the lattice.

2.2.2.3.2 Structure Factor Extinction Rule for a Body-centred lattice

A body-centred lattice has lattice points at (x, y, z) and $(x + \frac{1}{2}, y + \frac{1}{2}, z + \frac{1}{2})$. Using Equation 2.9, the following expression will be obtained:

Equation 2.10

$$\begin{aligned}
 F_{hkl} &= \sum_{j=1}^N f_j \exp[2\pi i(hx_j + ky_j + lz_j)] \\
 &= f_j \exp[2\pi i(hx + ky + lz)] + \exp[2\pi i\left(\left(hx + \frac{1}{2}\right) + \left(ky + \frac{1}{2}\right) + \left(lz + \frac{1}{2}\right)\right)] \\
 &= \sum_{j=1}^N f_j \exp[2\pi i(hx + ky + lz)] (1 + \exp[\pi i(h + k + l)])
 \end{aligned}$$

This proves that in a body centred lattice, if the sum of $h + k + l = \text{odd}$, the intensity is zero due to destructive interference of the waves. On the other hand, when $h + k + l = \text{even}$ there will be reflections observed because the condition for constructive interference is satisfied.

2.2.2.3.3 Structure Factor Extinction Rule for *F*-centred lattice and C-centred lattice

Reflections from a face-centred lattice are only observed when h, k, l are all odd or all even. Reflections from a C-centred lattice are only observed when $h + k + l = \text{even}$. If $h + k + l = \text{odd}$, destructive interference would occur and therefore no reflections would be observed.

2.2.2.3.4 Summary of Rules

Lattice Type	Systematic Absence Condition
P	None
I	$h + k + l \neq 2n$
F	$hkl \neq$ all odd or all even
C	$h + k \neq 2n$

2.2.3 Single-Crystal X-ray Diffraction

2.2.3.1 Data Collection

A Stoe IPDS II diffractometer which operates with Mo $K\alpha$ radiation was used for collecting single crystal data. Unless stated otherwise, the data were collected at 150 K. The cooling of crystals was achieved using an Oxford Instruments nitrogen cryostream. The design of a typical diffractometer is given in Figure 2.11.

There are three main components in the set-up of the diffractometer, namely the X-ray source, sample holder and the detector.

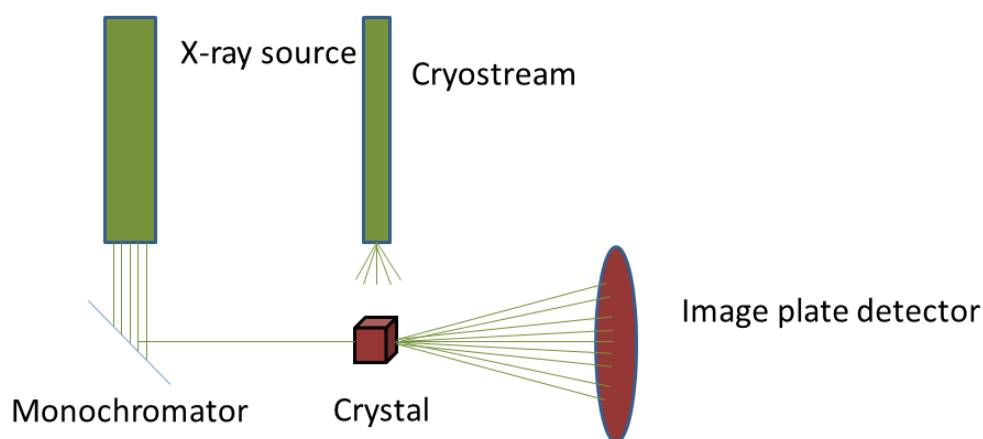


Figure 2.11: Schematic diagram of a single-crystal X-ray diffractometer

2.2.3.2 Data Collection at Low Temperatures

The quality of diffraction data depends both on the quality of the crystal under study and the temperature at which the data are collected. Collecting diffraction data at room temperature is usually associated with large atomic displacement parameters due to the thermal vibration of the atoms. The magnitude of thermal motion rises with increasing temperature. Assuming that the thermal motion of each atom is equal in all directions (isotropic motion), any decrease in the scattering intensity is directly linked to an increase in scattering angle.

In the isotropic case, there is only one parameter to be taken into account, commonly denoted as B . The relationship between B and the atomic scattering factor is expressed as:

Equation 2.11

$$f = f_{rest} \exp\left(\frac{-B \sin^2 \theta}{\lambda^2}\right)$$

where f refers to the scattering factor of the atom undergoing isotropic motion and f_{rest} is the atomic scattering factor at rest. It should be noted that B is related to the root-mean-square vibration amplitude u^2 by the following expression:

Equation 2.12

$$B = 8\pi^2 u^2$$

Low temperature data collection reduces the extent of the atomic vibrations.⁷² Typical temperatures are 100 – 200 K and this reduces the value of B by a factor of 2 or 3 compared to the typical value of 4\AA^2 when at room temperature.⁶⁵

However, that the assumption for isotropic thermal motion is not a realistic one, because the environment of the atoms in a crystal is not isotropic. As a result, an anisotropic model with six parameters is adopted and the exponential part of Equation 2.12 is modified to include the six parameters:

Equation 2.13

$$\exp -(b_{11}h^2 + b_{22}k^2 + b_{33}l^2 + b_{12}hk + b_{23}kl + b_{31}hl)$$

There are other advantages associated with collection data at low temperatures. For example, low temperature experiments help in retaining the crystallinity of the sample. In addition, highly unstable crystalline materials which are prone to decay can be stabilised temporarily at a low temperature in order to collect data.

2.2.3.3 Fourier Syntheses

The electron density of a crystal structure can be obtained from the diffraction pattern. A Fourier transform implies that in order to obtain the electron density in the unit cell, one has to add up all the scattered X-rays in the form of the structure factor. As determined previously, the structure factor F_{hkl} is a complex number consisting of the amplitude and the phase.

The amplitude of the wave is derived from the intensities in the diffraction pattern; however, the information about the phases of the individual reflections is lost. It is precisely the recovery of the phase information that constitutes the solution of a crystal structure. The electron density at any point x, y, z (ρ_{xyz}) within the unit cell is expressed as follows:

Equation 2.14

$$\rho_{xyz} = \frac{1}{V} \sum_{hkl} F_{hkl} \exp[-2\pi i(hx + ky + lz)]$$

Where V is the volume of the unit cell. The summation of structure factors is performed over all hkl values. It should be noted that the units of the structure factor in Equation 2.9 are expressed in electrons, whereas the electron density is expressed in electron per cubic Angstrom ($e^-/\text{\AA}^3$).

2.2.3.4 The Phase Problem and Structure Solution

Wave recombination depends on three factors associated with each wave:

- a) the direction of the wave – identified by hkl of the crystal plane diffracting
- b) the amplitude of the wave – deduced by the intensity of the wave (shown above)
- c) the phase – which is lost information. This is known as the phase problem.

Two most commonly used methods for solving a crystal structure are known as the direct methods and the Patterson method. It should be noted that crystal structure solution using direct methods requires prior knowledge of the chemical composition of the crystal. On the other hand, Patterson methods are most suitable for solving crystal structures which have a heavy atom present. For the purposes of this thesis, both direct and Patterson methods were used depending on the chemical composition of the crystal under study.

2.2.3.4.1 Direct Methods

Direct methods attempt to derive an approximate set of phases from which one can calculate the electron density of the crystal. Direct methods heavily rely on the fact that structural information is contained within the intensities of reflections and that the electron density in a crystal cannot take negative values. In non-centrosymmetric structures, the phase angle can take values between 0 and 2π , whereas in centrosymmetric systems phases can only take two values, either 0 or π .⁷³ There are constraints which limit the values that the phase angle can take. Section 2.2.3.3 demonstrated that the electron density is related to structure factors by a Fourier transform. Therefore, applying constraints on the electron density will impose constraints on the structure factor. The electron density in any real crystal is constrained to positive values only and therefore only phases calculated from positive electron density are taken into consideration.⁶⁵

2.2.3.4.2 The Patterson Method

The Patterson method omits the phases altogether and instead a Patterson map is calculated from a summation of the amplitude $|F|^2$ of each diffracted beam. Ignoring the phases essentially implies replacing the complex structure factors by multiplying them with their complex conjugate. Such operation of multiplying a complex number by its complex conjugate yields a real number due to the cancelling out of the imaginary parts.⁷⁴

In doing so, the Patterson function simplifies to the real *cosine* term and is given by:

Equation 2.15

$$P_{uvw} = \frac{1}{V} \sum_{hkl} |F|^2 \cos 2\pi(hu + kv + lw)$$

The maxima in the Patterson function at a point u, v, w do not represent the individual atomic positions. Instead, they correspond to vectors between pairs of atoms. The Patterson space is defined by u, v, w and it corresponds to a vector between a pair of

atoms in the crystal located at x_1, y_1, z_1 and x_2, y_2, z_2 . Based on this notation, a Patterson map will have a maximum at $u_1 = x_1 - x_2$; $v_1 = y_1 - y_2$; $w_1 = z_1 - z_2$.

2.2.3.5 Structure Refinement

Resolving the phase problem and solving the crystal structure represent only half of the story in crystal structure determination. The data obtained from the model structure should be checked against the experimentally observed data in order to see the extent of agreement between the two. The process of improving the parameters of the model structure in order to achieve the best fit between the observed and calculated data is referred to as refinement.⁷⁵

During the refinement cycle, the model structure is successively improved in order to improve the fit of the model to the data observed from the diffraction pattern. However, a refinement is considered to have converged if there is almost negligible shift in the parameters between the last two cycles.⁶⁵

The quality of the fit is monitored by the R -value expressed as follows:

Equation 2.16

$$R = \frac{\sum(|F_o| - |F_c|)}{\sum |F_o|}$$

Clegg *et al.*⁶⁴ define parameters as the numerical descriptors of a model structure. Three sets of descriptors are adjusted during the refinement process and they are:

- a) atomic coordinates, x, y, z
- b) atomic displacement parameters, where each isotropic atom has one atomic displacement parameters (U), whereas anisotropic atoms have six U values.
- c) scale factor, which is used to compare the observed and the calculated square structure factors.

2.2.4 X-ray Powder Diffraction

Powder samples contain a large number of small crystallites, which adopt all possible orientations in a random order. Contrary to single crystal analysis where only one crystal is involved in diffraction, all of the polycrystallites in powder diffraction give rise to diffraction data, producing cones of diffraction⁷⁶ as shown in Figure 2.12.

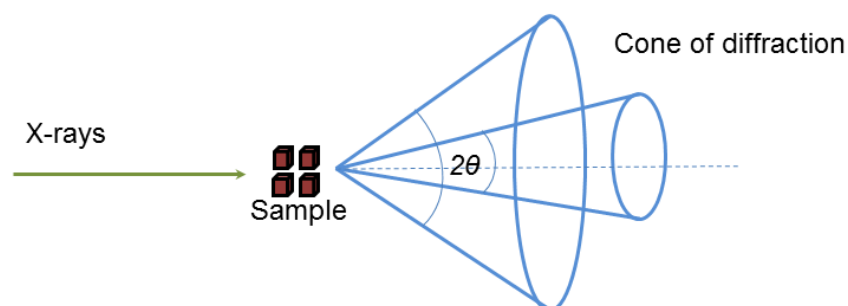


Figure 2.12: Scattering from a polycrystalline sample

The main distinguishing feature between powder and single crystal diffraction is that powder data are one-dimensional compared to the three-dimensional nature of the single crystal data. Such compression of three-dimensional data into one dimension is associated with a considerable loss of structural information.⁷⁶ However, the diffraction pattern of any material provides two important pieces of structural information. Peak positions provide information on the size of the unit cell and the crystal system, whereas atomic positions are determined by peak intensities.

2.2.4.1 Phase Identification

Powder diffraction is a powerful technique in determining sample composition and provides information on the homogeneity of the bulk material.⁷⁶ The set of peaks obtained from a powder are compared to the existing database of compounds in order to understand their composition. This is especially useful when crystallisation reactions fail to produce crystals and instead powdered samples are isolated. In these cases, performing

powder diffraction can provide information on the competing reactions that might have taken place. The conclusions drawn from interpreting the powder pattern can be invaluable in the subsequent steps of experimental design and method development.

In the present thesis, powder diffraction was used to determine whether the crystal structure obtained from the single crystal was representative of the bulk. Crystals were filtered from the supernatant, allowed to dry at ambient conditions and were subsequently ground to a fine powder suitable for powder diffraction. Samples were mounted on the sample holder and were analysed using Cu K α -radiation. The patterns obtained were compared to the simulated patterns from single crystal.

2.3 Other Analytical Techniques

2.3.1 Infrared Spectroscopy

The interaction of infrared radiation with matter is explained in terms of vibrations occurring within a molecule. Molecular vibrations have the energy that corresponds to that of the infrared region in the electromagnetic spectrum. Functional groups in organic molecules can be identified by characteristic vibration frequencies occurring only for that functional group.⁷⁷ Such interaction of molecules with infrared radiation provides a very important analytical technique for identifying the chemical composition of a sample. Infrared spectroscopy is a versatile technique in that it can be used for analysing solid, liquid and gaseous samples.

2.3.1.1 Infrared Absorption

The selection rule for infrared spectroscopy stipulates that the electric dipole moment of the molecules must change during a vibration. Therefore, a heteronuclear diatomic molecule is considered to be IR-active because the dipole moment of this molecule changes as the bond between the two atoms expands and contracts. Conversely, a

homonuclear diatomic molecule is considered to be IR-inactive if the dipole moment of the molecule is zero regardless of expansion and contraction of the bond.⁷⁸

2.3.1.2 Molecular Vibrations

The number of vibrational modes present in a molecule varies largely by the complexity of the molecule. However, regardless of the complexity of the molecule, most of the molecular vibrations can be assigned to certain functional groups. These are called the localised vibrations and include: stretching and bending. Stretching refers to changes in the bond length between two atoms, whereas bending involves changes in bond angles. Stretching vibrations can either be symmetrical or asymmetrical. Bending vibrations can be divided into scissoring, rocking, twisting and wagging.

2.3.2 Thermogravimetric Analysis

Experimental methods which measure changes in the physical and chemical properties of a system at elevated temperatures are known as thermal analyses. One such method is thermogravimetric analysis, which measures changes in the weight of a material as a function of increasing temperature. This analytical technique requires two pieces of instrumentation: a microbalance and a furnace which operates a linear increase of temperature with time.⁷⁹ The sample is introduced in the microbalance which is placed inside the furnace. A temperature programmer controls the operating temperature and the heating rate. The environment of the sample is controlled by a sample purge gas. The choice of atmosphere is very important and it depends on the type analysis. Nitrogen atmosphere is used in order to prevent the oxidative reactions that may take place between the material under study and air.

Thermogravimetry is a widely used technique in the analysis of solid materials in order to understand their decomposition and structural stability. Compositional analysis can be performed in order to decompose or remove components of the material and analyse at what temperature the decomposition takes place. This method is particularly useful for

investigating the dehydration of hydrated materials. It can provide information on the nature of water loss. This could relate to regular, nebulous, single stage or multiple stage water loss. It is also possible to decipher the loss of solvents, decarboxylation, oxidation and partial and full decomposition.⁷⁹

Chapter 3:
Multicomponent Crystals: Salts, Co-crystals and
Hydrates

3.0 MULTICOMPONENT CRYSTALS: SALTS, CO-CRYSTALS AND HYDRATES

3.1 Introduction

Solid state chemistry is focused upon the synthesis, structural aspects and the properties of solid materials.⁸⁰ Multicomponent crystals are organic materials which comprise two or more components. Friscic and Jones⁸¹ divide multicomponent crystals in the following groups: hydrates or solvates, salts and co-crystals. When two or more molecules crystallise together, the identity of the solid material obtained is largely dependent on the way these molecules interact with one another. Inclusion of a solvent molecule yields a solvate, whereas inclusion of water generates a hydrate. Some of these forms contain only solid materials at ambient conditions. However, the identity of the solid differs if crystallisation is associated with proton transfer. In cases where there is proton migration from acid to the base, the resulting solid material is known as a salt. Crystallisation of two or more molecules wherein all components are incorporated in their neutral form generates a co-crystal. Figure 3.1 gives a schematic representation of the solid forms mentioned above.

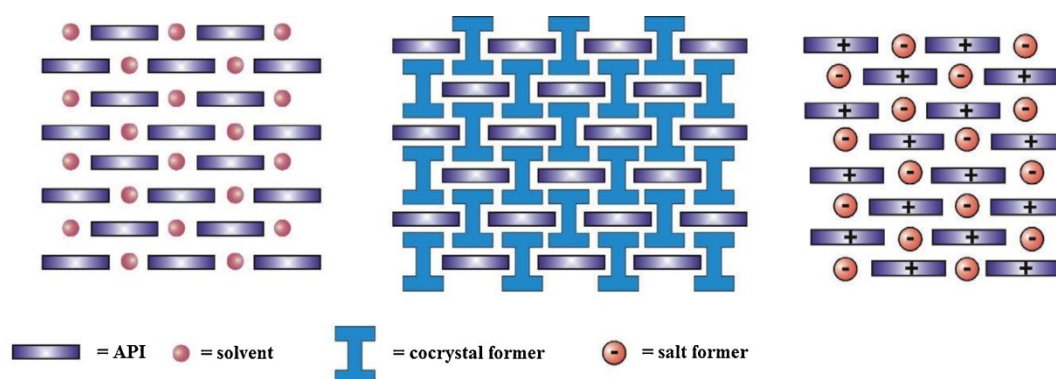


Figure 3.1: Classification of solid forms by Friscic and Jones⁸¹ (Extract from *Journal of Pharmacy and Pharmacology*, 2010)

3.2 Definition of a co-crystal

In a highlight published in 2005, Åakeroy *et al.*⁸² discussed how covalent synthesis has developed enormously over the years. Åakeroy attributes this development to the ability of organic chemists to establish “*reproducible links between molecular structure, reactivity and reaction pathways through systematic studies of innumerable organic reactions*”.⁸² He argues that this has been pivotal to the construction of novel and diverse molecules of different complexity and use.

While this is the case in classic organic synthesis, literature reports as well as the experience and knowledge obtained from the present thesis reveal that supramolecular synthesis lacks the same level of finesse present in organic synthesis. Thus, it would be correct to say that despite the tangible progress made in crystal engineering, Maddox’s¹ statement about predicting crystal structure is pertinent even to this day. The development of this area requires further research in understating the link between molecules and their self-assembly at a supramolecular level.

Although known to scientists since the 19th century and encountered many times ever since, co-crystals remain an area of solid state chemistry where there is considerable debate in relation to the terminology used to describe these species.⁸³ There continue to be disputes as to what precisely constitutes a co-crystal. Indeed, claims of Zawrotko *et al.*⁸⁴ stating that “*less than 1% of the structurally characterised organic molecules are co-crystals*” confirm that co-crystals represent a new opportunity for the design of new molecular structures.

In the absence of a widely accepted and acknowledged definition of co-crystals, Zawrotko *et al.* proposed a more restrictive definition, which still remains relatively broad. He stated that “*a co-crystal is a multiple component crystal in which all components are solid under ambient conditions when in their pure form. These components co-exist as a stoichiometric ratio of a target molecule or ion and a neutral molecular co-crystal former.*”

Furthermore, Åakeroy *et al.* contributed to the narrowing down of this broad definition by excluding solvates and hydrates. For the purposes of the present research work, further narrowing down of the definition is required in order to clearly define the meaning of the word co-crystal. As a result, from this point onwards the term co-crystal will be used to refer only to compounds designed from neutral organic molecules, which are solids at ambient conditions. This implies that ions, inorganic/organic hydrogen bonding networks, hydrates and solvates are excluded from this definition.

3.3 Distinction between salts and co-crystals

3.3.1 The Effect of Proton Transfer

Both co-crystals and salts are categorised as multicomponent crystals, which in turn represent two or more components associated through intermolecular interactions.⁸⁵ However, this does not suggest that salts and co-crystals are the same thing. On the contrary, there is a subtle difference between these two species. From a chemical perspective, the distinction between a salt and a co-crystal is made by analysing whether proton transfer has taken place from an acid to a base.⁸⁵ For a multicomponent crystal to qualify as a co-crystal the molecules need not be modified from a covalent perspective.⁸⁶ Friscic and Jones⁸¹ refer to the process of co-crystallisation as a non-covalent derivatisation. Etter and co-workers argued that formation of a salt or co-crystal can be predicted by examining the pK_a difference between the two components.⁸⁷ If this difference is large enough then the acid-base pairs will yield salts rather than co-crystals.⁸⁷

Equation 3.1*

$$\Delta pK_a = pK_a(\text{base}) - pK_a(\text{acid})$$

* The pK_a of the base refers to the pK_a of the protonated base. It is given by the following equation: $BH^+ + H_2O \rightleftharpoons B_{(aq)} + H_3O^+$

Bhogala *et al.*⁸⁸ provide more restrictive cut-off points by presenting three scenarios between pyridine bases and carboxylic acids: $\Delta pK_a < 0$ yields neutral O—H \cdots N hydrogen bond and therefore a co-crystal; $0 < \Delta pK_a < 3.75$ generates hydrogen bonds with an intermediate character O—H \cdots N/ N⁺—H \cdots O⁻; and finally $\Delta pK_a > 3.75$ results in N⁺—H \cdots O⁻ and therefore a salt.

3.3.2 The Continuum Between Salts and Co-crystals

This form of distinction between co-crystals and salts is generally acceptable given that a vast majority of acid-base complexes lie within the ΔpK_a ranges of less than 0 or more than 3.75. However, problems surface when tackling the region in between the two extremes. Childs *et al.*⁸⁵ argue that having an organic base and an organic acid interacting in order to deposit a crystalline solid does not necessarily mean that a salt is obtained. Instead, evaluations on the location of the proton should be conducted in order to resolve the identity of the solid. Should the proton reside on the base, then it is evident that proton transfer has taken place and therefore a salt is obtained. Likewise, if the proton is attached to the acid, then there has been no acid-base reaction and therefore the crystalline solid constitutes a co-crystal.

Utilisation of pK_a can enable predictions with regards to the ionisation or non-ionisation of final product, but one factor should be taken into account because pK_a values usually describe equilibrium phenomena occurring in solution rather than in the solid state. It, therefore, transpires that when referring to the pK_a values with respect to solid state systems, this concept is being used for a system, to which it does not correspond or apply strictly. Consultation of literature could assist in explaining as to why pK_a values are good predictive tools at $\Delta pK_a < 0$ or $\Delta pK_a > 3.75$, but fail to provide the same accuracy and sophistication when concerned with the region of $0 < \Delta pK_a < 3.75$.

Childs *et al.*⁸⁵ stated that the extent of proton transfer in solid state can be determined from single crystal X-ray diffraction by evaluating:

- 1) Proton location
- 2) Bond length of the carboxylic acid group
- 3) Bond angles

The discussions below will seek to explain in detail the three aforementioned points and their implications in identifying a multicomponent crystal as a co-crystal or a salt.

3.3.3 The Shared Proton – Co-crystal or Salt?

In an attempt to probe the continuum between co-crystals and salts Li *et al.*⁸⁹ focused on the interaction between a carboxylic acid and a base containing several functional groups such as: acetamide, quinazoline, methylpyridine and amine. Carboxylic acids utilised were maleic acid with $pK_a = 1.91$, malonic acid with $pK_a = 2.85$ and succinic acid with $pK_a = 4.21$. The aim of the investigation was to identify the nature of the multicomponent crystal produced.

Based on the pK_a values it was difficult to determine whether the solid deposition of the malonic acid and the organic base system (shown in Figure 3.3) was a co-crystal or a salt due to the reported ΔpK_a being 2.09. Such value falls within the 0 – 3.75 range and therefore determining whether proton transfer has occurred is not as straightforward. As a result, the research group conducted single crystal X-ray investigations and designed the so-called three proton transfer states diagram.

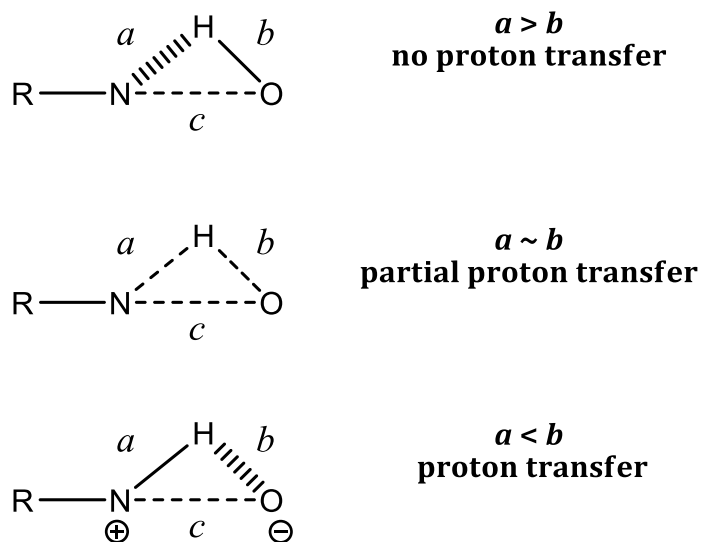


Figure 3.2: Three phases of proton transfer between a basic nitrogen and a hydroxyl fragment of a carboxylic acid. Denominations a , b and c refer to N-H, O-H and N-O distances, respectively⁸⁹

The most intriguing feature of this three state diagram is the introduction of the idea of a “shared proton” between the hydrogen bond donor and acceptor. The researchers attributed such behaviour to the narrow $\Delta pK_a = 0 - 3.0$ and therefore alluded to the existence of an alternative state. This state is different to the two cases for identifying a salt and a co-crystal. It is evident from Figure 3.2 that when the relationship between the bond lengths is $a > b$ then the multicomponent crystal is identified as a co-crystal, whereas when the reverse $a < b$ is applicable, then the formation of a salt prevails. Remarkably, however, Li *et al.*⁸⁹ reported a case of partial proton transfer between N—H—O, where the acceptor-hydrogen distance was recorded as 1.431 Å, which was argued to be less than the expected, 1.5 - 2.2 Å corresponding to a strong hydrogen bond. This is shown in Figure 3.3.

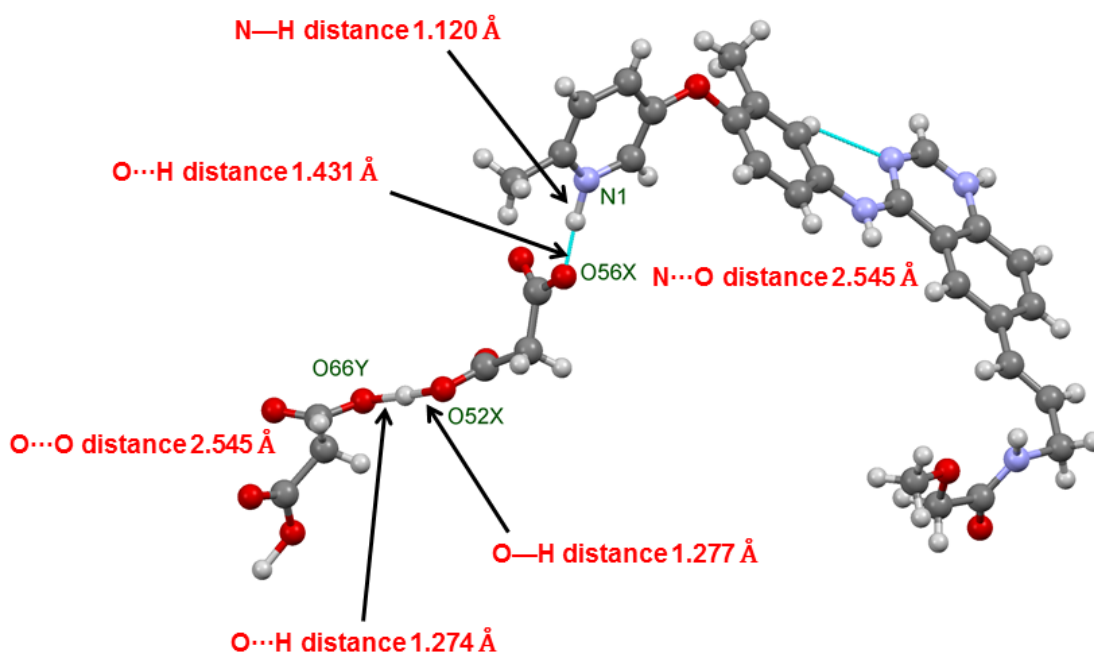


Figure 3.3: Malonate salt of a cancer drug with hydrogen bonds containing shared protons as described by Li *et al.*⁸⁹ (errors on distances were not cited in the original publication)

The research work also pointed out that the N1⁺—H bond length (shown in blue in Figure 3.3) was 1.120 Å which was regarded longer than the usual N—H bond length of 1.009 Å. In addition, Li *et al.*⁸⁹ also stated that upon X-ray examination the O...N distance was found to be 2.454 Å. They argued that this distance is short and concluded that the hydrogen atom between the pyridine nitrogen and the carbonyl oxygen N²⁺H...O56X—C54X is shared between the donor and the acceptor giving rise to a partially transferred proton N^{δ+}...H...O^{δ-} resembling a zwitterion. As a result, Li *et al.*⁸⁹ noted that the structure shown in Figure 3.3 cannot be simply described as a salt or a co-crystal because the hydrogen atom does not show tendency of favouring the donor or the acceptor.

What is important to address is whether the identity of the crystalline solid (salt or co-crystal) will change the properties of the crystal. In other words, would the properties of a solid be the same if we compare two crystals with the same components and the only difference between the two is the position of the proton classifying one crystal as a salt

and the other as a co-crystal? This question should be tackled by taking into account the two molecules involved in the reaction. However, proton migration can alter the hydrogen bonding in the structure considerably and this may be associated with changes in crystal packing and thus affect the properties.

3.3.4 Examination of Carboxylic/Carboxylate Bond Lengths

Bond length examinations for identifying a complex as a salt or co-crystal were conducted by Childs *et al.*,⁸⁵ who investigated the interaction between 2-aminopyridine and various carboxylic acids from the CSD.¹³ Analysis of the crystal structures revealed a trend relating to the C—O distance in the carboxylic groups. They argued that salt formation is associated with similar C—O bond lengths in the carboxylic acid groups with a $\Delta D_{C-O} < 0.03 \text{ \AA}$, whereas co-crystal formation was reported to contain distinctively different distances and $\Delta D_{C-O} > 0.08 \text{ \AA}$. ΔD_{C-O} is defined as follows: $\Delta D_{C-O} = [d(C - O) - d(C = O)]$.

Similar arguments were also put forward by Åakeroy *et al.*⁹⁰, who stated that if a co-crystal is formed then the C—O bond lengths in a carboxylic acid should be different, whereby one value corresponds to the C=O and the other to C—O(H) covalent bonds. Furthermore, Childs *et al.*⁸⁵ probed the C—O bond lengths and compared it to the ΔpK_a . His research group suggested that there is a correlation between C—O bond lengths and ΔpK_a in the complexes of phenols. He argued that shorter C—O bond lengths at higher ΔpK_a indicate salt formation, whereas longer C—O bond lengths with lower ΔpK_a imply co-crystal formation.

3.3.5 Bond Angle at the Site of Protonation

Inspection of proton transfer can also be achieved by scrutinising the bond angles of the protonated atom in the base. In an effort to understand nucleobase interactions, crystals between the adeninium and cytosinium cations and the sulphate anion were investigated by Cherouana *et al.*⁹¹ who presented the impact of protonation on the bond angle. They

claimed that protonation is associated with an increase in the bond angle at the site of protonation.

A similar claim was also made earlier by Hingerty *et al.*⁹² in 1981, who stated that the protonation of adenine was characteristic as it is associated with a change in the internal bond angle of the purine. Cherouana *et al.* crystallised adeninium dinitrate monohydrate and stated that the change in the bond angles were directly linked with the degree of protonation of adenine. An increase in the angle between C2—N1—C6 was observed when adenine was protonated to become adeninium. The bond angle between C2—N1—C6 in adeninium was reported to be 123.35°. This value agrees with other adeninium salt structures.

Table 3.1 shows the comparison in bond angles between C2—N1—C6 in various adeninium salts.

Table 3.1: Comparison of C2—N1—C6 bond angle in adeninium salts⁹²

Salt	C2—N1—C6 (°)
Adenine hydrochloride hemihydrates	123.5(4)
Adenine hydrobromide hemihydrate	124.3(4)
Adeninium hemisulphate hydrate	123.0(4)
Adeninium phosphate	123.6(5)
Adeninium dinitrate monohydrate	123.8(2)

It is evident that the bond angles of the compound reported by Hingerty *et al.* agree with those reported for other compounds of adenine salts. This trend will be compared to compounds synthesised as part of the thesis. The concluding remarks of Hingerty *et al.* were also previously put forward by Langer *et al.*⁹³, who stated that protonation at N1 site of adenine leads to a change in bond angles of all nitrogen atoms in the six-member

aromatic ring. Observations of bond angles were also made by Åakeroy *et al.*⁹⁰, who argued that a narrow range 118.1 – 119.1° is indicative of non-ionised pyridine units.

In a related work focusing on the increase in bond angles in purines upon protonation, Singh⁹⁴ investigated this behaviour. The investigation involved compiling a library of six-membered heterocyclic compounds reported in *Acta Crystallographica* since 1948. Upon comparing a plethora of compounds in the library, Singh reported that the X—N1—Y mean angle of the protonated nitrogen was $125 \pm 0.2^\circ$, whereas the same mean angle with no attachments on the nitrogen was found to be $115.7 \pm 0.2^\circ$. The reported average bond angle difference of 9.3° is substantial. Based on this observation, Singh claimed that heterocyclic nitrogen angles which lie in the range $125 \pm 3^\circ$ indicate the attachment of a hydrogen bond to the nitrogen, whereas if the heterocyclic nitrogen angles lie in the range $116 \pm 3^\circ$ it implies that there are no hydrogen atoms attached to the nitrogen.

3.4 Structural Cohesion in Guaninium Sulphate Hydrate

3.4.1 Introduction

Water is frequently found within crystal structures. Gillon *et al.*⁹⁵ attribute this to its small size and multidirectional hydrogen bonding capability. Inclusion of water molecules in the crystal structure can occur in three different forms: an isolated lattice hydrate, a channel hydrate, or an ion-coordinated hydrate.⁹⁶ Channel hydrates contain open channels within the crystal lattice into which water may enter and reside. A common feature of channel hydrates is the ability to exist in a number of hydration states dependent on the relative humidity of the environment.⁹⁷ From a pharmaceutical perspective, it has been estimated that one third of all pharmaceutical formulations on the market occur in hydrate forms.⁹⁸ Channel hydrates are frequent in a wide range of molecules, for example, in caffeine.⁹⁹⁻¹⁰¹

From a supramolecular chemistry point of view, the architecture and molecular mobility of the nucleic acids is closely linked to the rapid making and breaking of the hydrogen bonds between nucleobases. As a result, the synthesis of co-crystals of nucleobases or nucleobase salts is useful in examining the hydrogen bond functionality of these crucial building blocks of DNA. Within a considerable number of crystal structure reports^{91, 102-108} of DNA bases, hydrogen bonding is regarded as the master-key of structural cohesion. Guanine is one of the two purine bases of DNA. It has many sites for hydrogen bonding and this makes it an attractive candidate as a building block in crystal engineering. It has an equal number of hydrogen-bond donor (N1, N2, N7) and acceptor sites (O6, N3, N9) as illustrated in Figure 3.4.³³

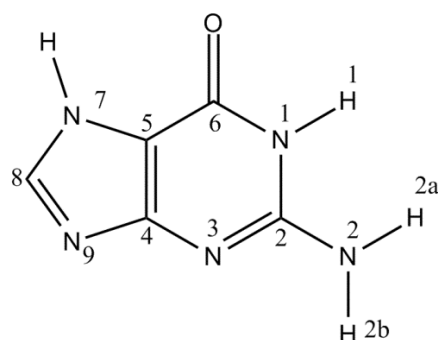


Figure 3.4: Hydrogen bond functionality of guanine

A structure focusing on the hydrogen bonding of a protonated guanine molecule was reported by Cherouana *et al.*¹⁰³ who studied the interaction of guanine with sulphuric acid. It was reported that guaninium sulphate monohydrate ((GH₂)SO₄·H₂O) adopts the centrosymmetric space group *P*2₁/*c* and contains [GH₂]²⁺ cations surrounded by water and the sulphate anion. The guanine moiety in this structure is doubly protonated and this blocks the formation of any homosynthon in guanine cations. Instead, the structure is stabilised by hydrogen bonds between the cation, anion and water, which assemble in layers.

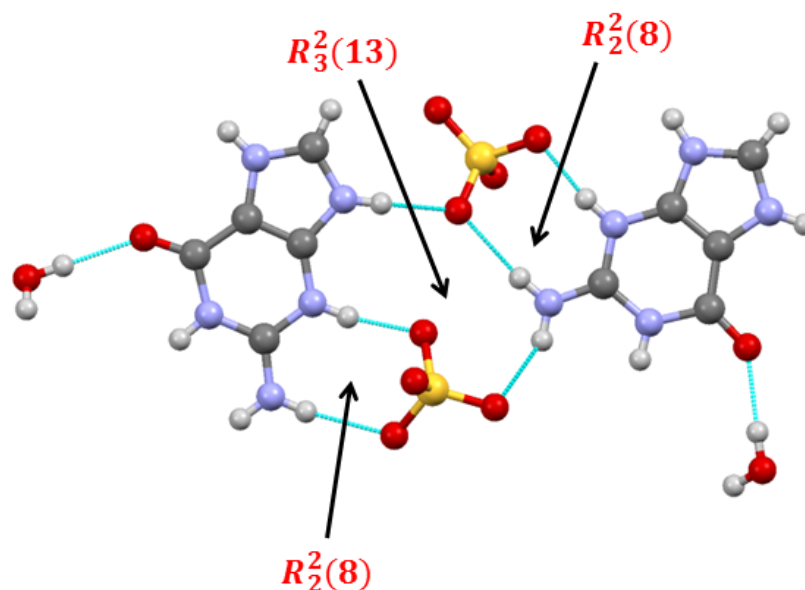


Figure 3.5: Hydrogen-bonding in ((GH₂)SO₄·H₂O)

As it can be seen from Figure 3.5, guaninium forms a $R_2^2(8)$ heterosynthon with the sulphate anion. The hydrogen bond donors involved are the N—H from the amine group and the N—H from the protonated endocyclic nitrogen. In addition, the structure is sustained by an additional hydrogen bonding motif in the form of a $R_3^2(13)$ heterosynthon between two guaninium cations and two sulphate anions.

A different hydrogen bonding motif was observed in the methylguaninium nitrate crystals grown by Kozma *et al.*¹⁰⁹ In this structure, methylguaninium cations are stabilised by nitrate anions. Such interaction leads to the formation of methylguaninium ribbons which are sustained by two distinct hydrogen bonding $R_2^2(8)$ homosynthon (Figure 3.6: highlighted in pink and in blue). Interactions between parallel ribbons generate two-dimensional sheets.

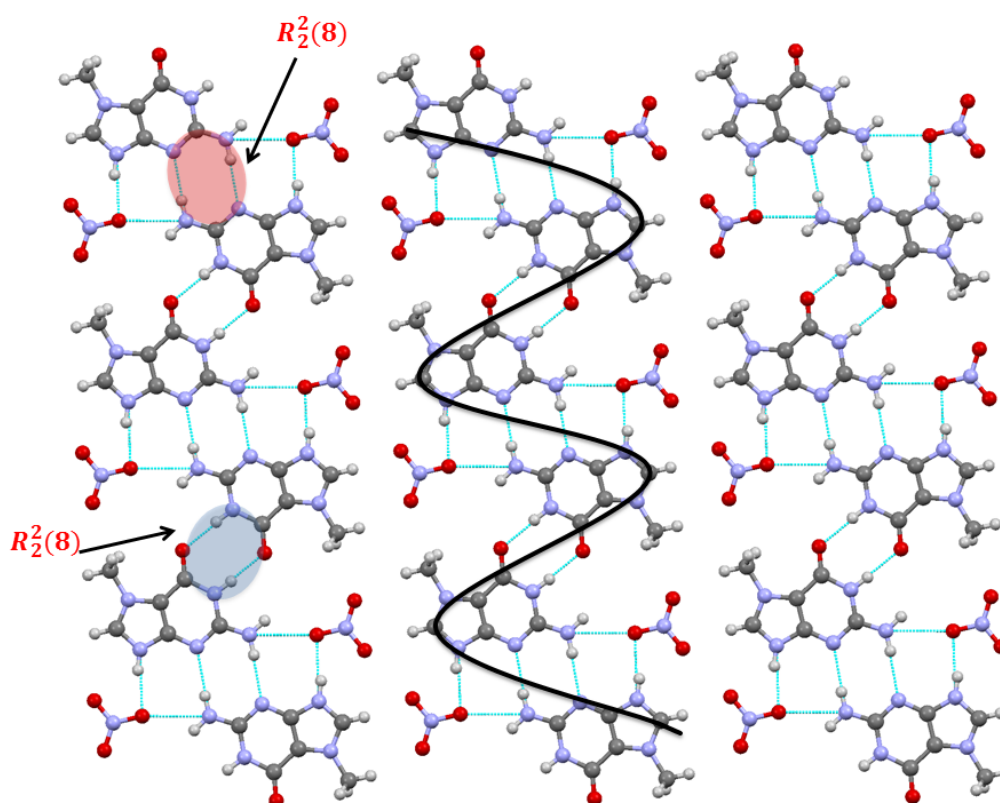


Figure 3.6: Guaninium ribbons in methylguaninium nitrate

The objective of the work described here was to further probe the hydrogen bonding capability of guaninium under mildly acidic conditions in the presence of anions capable of acting as hydrogen-bond acceptors. Monoprotonation, for example, would leave the other endocyclic nitrogen in guanine available to act as a hydrogen bond acceptor and it would therefore enable hydrogen bonding between cations.

Herein, the synthesis and crystal structure of *bis*(guaninium) sulphate hydrate, $(\text{GH})_2\text{SO}_4 \cdot 2.5\text{H}_2\text{O}$ is discussed. The thermal behaviour of this phase is reported and its dehydration to form the crystalline phases $(\text{GH})_2\text{SO}_4 \cdot 1.5\text{H}_2\text{O}$ and $\text{G}(\text{GH})_3(\text{SO}_4\text{H})(\text{SO}_4)$ is described. Dehydration is shown to be associated with limited structural change.

3.4.2 Experimental

3.4.2.1 Single Crystal Preparation

Synthesis of *bis*(guaninium) sulfate hydrate: Guanine (0.13513 g, 1 mmol) and sulphuric acid (3 mmol) were dissolved in boiling water (30 mL). The solution was allowed to cool to room temperature and the water allowed to evaporate slowly at room temperature. Colourless needle-like crystals were obtained after approximately seven days.

3.4.2.2 Infra-red (IR) Spectroscopy and Thermogravimetric Analysis (TGA)

TGA and IR Analysis: FT-IR spectra were collected from samples prepared as KBr disks (1:20 dilution) using a Perkin Elmer FT-IR Spectrometer Spectrum RX1. The thermogravimetric behaviour of the compound was investigated using Mettler Toledo TGA/DSC 1. Samples were loaded in 70 μL alumina pans and heated at a ramp rate of 10 $^\circ\text{C}/\text{min}$ under a flow of nitrogen gas.

3.4.2.3 Single Crystal X-ray Diffraction Measurements

Single crystal X-ray diffraction data were collected in series of ω -scans using a Stoe IPDS2 image plate diffractometer utilising monochromated Mo radiation ($\lambda = 0.71073 \text{ \AA}$). Standard procedures were employed for the integration and processing of the data using X-RED.¹¹⁰ Samples were glued to the tip of a glass fibre and mounted on a goniometer. Temperature control of the crystal was undertaken using an Oxford Instruments nitrogen gas cryostream.

Structures **1a** and **1b** were solved using direct methods incorporated within SHELXS-97.¹¹¹ Completion of structures was achieved by performing least squares refinement against all unique F^2 values using SHELXL-97.¹¹¹ All non-H atoms were refined with anisotropic displacement parameters. Location of hydrogen atoms was achieved by using difference Fourier maps. Chemically sensible restraints were applied to O-H bond lengths and H-O-H bond angles.

Structure **1c** was solved using Superflip¹¹² implemented within Jana2006.¹¹³ The structure was refined within SHELXL-97. Diffraction data were not observed beyond $2\theta \approx 36^\circ$ and only data below this angular limit were employed in final refinements. Sensible restraints were applied within each moiety to minimise the number of refined parameters; all hydrogen atoms were placed with a riding model.

3.4.3 Results and Discussion

3.4.3.1 Crystal structure of $(\text{GH})_2\text{SO}_4 \cdot 2.5\text{H}_2\text{O}$, (**1a**)

Colourless crystals of bis(guaninium) sulfate 2.5 hydrate, **1a**, with well-developed faces were obtained by slow evaporation of water from an aqueous solution of guanine in sulphuric acid.¹¹⁴ Single crystal X-ray analysis showed that **1a** crystallises in the triclinic crystal system in the space group $P\bar{1}$ with unit cell volume 849.8(3) Å³. The asymmetric unit of **1a** is illustrated in Figure 3.7¹¹⁵ and contains two guaninium cations, a single sulphate anion, and 2.5 molecules of water. Satisfactory chemical analysis data were obtained for **1**. The structure contains intricate hydrogen bonding between guaninium cations, sulphate anions and the water molecules.

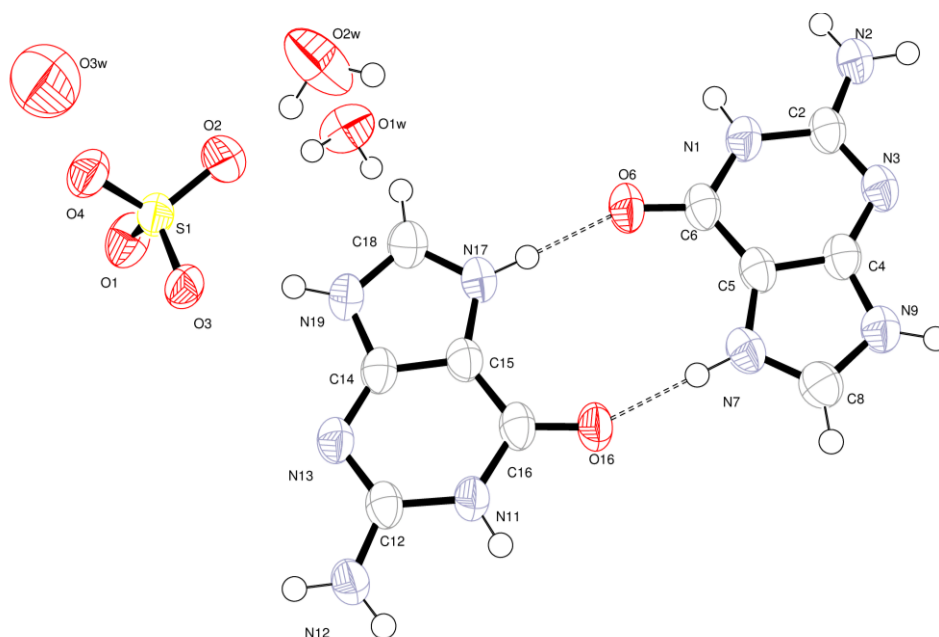


Figure 3.7: Asymmetric unit of (1a**) with atoms drawn as 70 % probability ellipsoids. Dashed lines indicate hydrogen bonds between guaninium cations within the asymmetric unit**

Guaninium cations interact with each other *via* hydrogen bonding and thus they form hydrogen-bonded tapes. These tapes are held together by two different hydrogen-bonding motifs that may be described using the Graph Set Notation.³² The tapes contain $R_2^2(10)$ and $R_2^2(8)$ homosynthon.³¹ Figure 3.8 depicts the $R_2^2(10)$ embrace. This homosynthon was described by Watson¹¹⁶ as the mode by which guanine forms hydrogen bonds to itself. It is formed by hydrogen bonds between N7—H7...O16 of length 2.718(3) Å (N7...O16 distance) and between N17—H17 and O6 of length 2.709(3) Å (N17...O6 distance). The tapes are generated by a two further centrosymmetric $R_2^2(8)$ embraces between crystallographically equivalent guaninium cations generated by symmetry. The two $R_2^2(8)$ embraces are each composed of a symmetry equivalent pair of N—H...N hydrogen bonds: the first synthon is sustained by a pair of N2—H2A...N3ⁱ ($i = -x-2, -y+2, -z$) hydrogen bonds with N...N distance 2.995(3) Å; the second synthon comprises a pair of N12—H12A...N13ⁱⁱ ($ii = -x+1, -y, -z$) hydrogen bonds with N...N distance 2.987(3) Å.

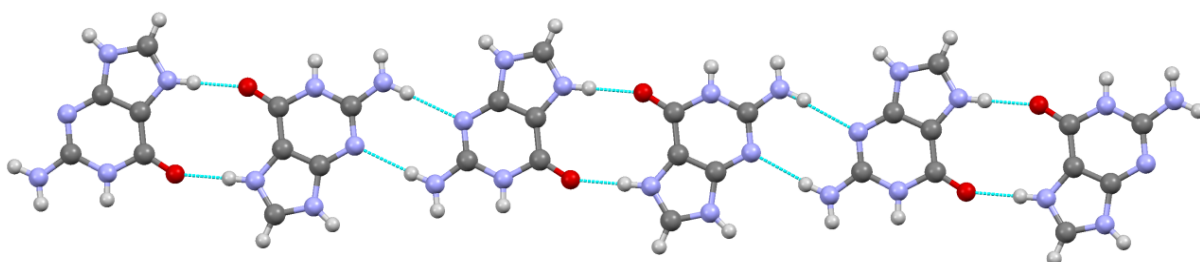


Figure 3.8: The hydrogen-bonded tape within (1a)

The tapes of guaninium cations are stacked in the [2 3 0] direction. The mean plane separation between the guaninium cations is 3.09(4) Å. The centroid to centroid distance was calculated as 4.8521 (10) Å. Sulphate anions lie between the stacks forming hydrogen bonds. Each sulphate acts as a hydrogen bond acceptor to two guaninium cations in adjacent tapes. The cation-anion hydrogen bonding interactions have the following N...O distances are 2.674(3) Å and 2.764(3) Å. (Figure 3.9)

The sulphate anion interacts with an additional guaninium from another stack wherein the N \cdots O distance is 2.656(3) Å, and to a pair of water molecules (O \cdots O distances are 2.718(3) Å and 2.741(5) Å).

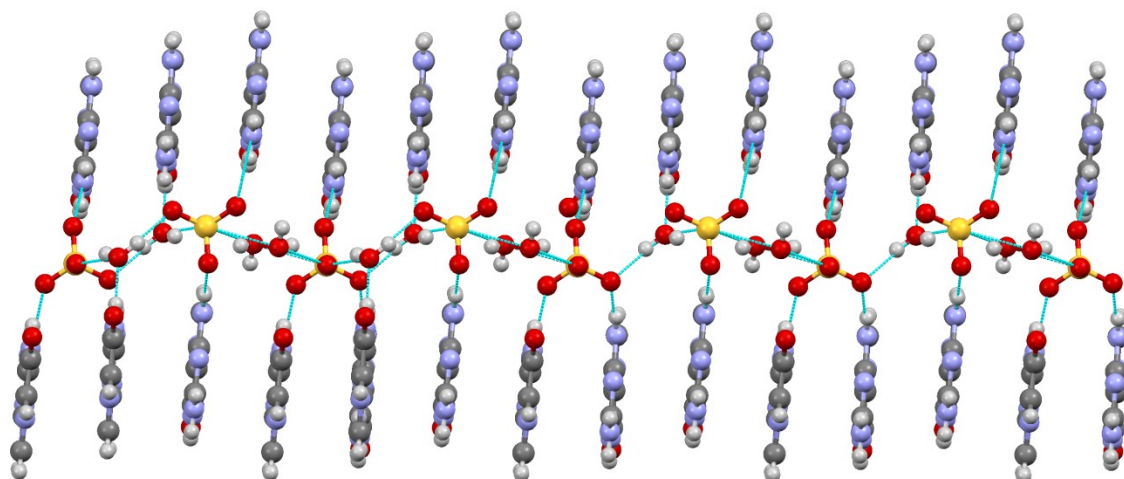


Figure 3.9: Depiction of hydrogen bonding between cations and anions in (1a)

This type of arrangement of guaninium cations and sulphate anions creates channels running parallel to the [100] direction. These channels accommodate 2.5 water molecules per formula unit as shown in Figure 3.10. The space occupied by the water in this structure is 10.6 % of the total crystal volume. Two water molecules (O1W and O2W) have been located with precision and hydrogen atoms assigned from difference Fourier maps. Structural refinements indicated that O2W is disordered over two positions related by the inversion centre, but it was possible to assign the positions of hydrogen atoms attached. However, the third water molecule (O3W) could not be located precisely and hydrogen atoms were not apparent in final difference Fourier maps.

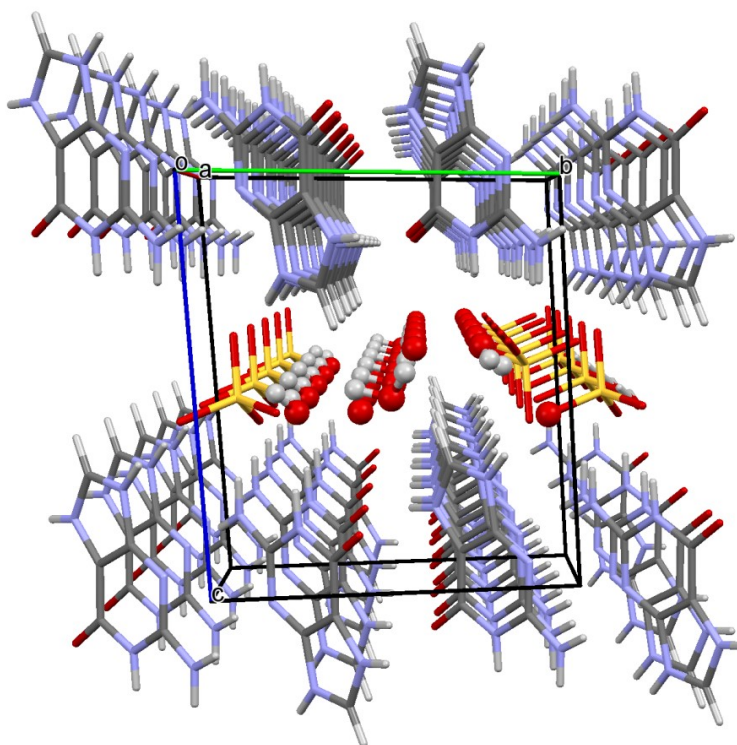


Figure 3.10: View of (1a) down [010] to show location of water molecules within channels.

The water molecules occupy positions within the channels to maximise favourable hydrogen-bonding interactions. Hydrogen bonding parameters are shown in Table 3.2. The first water molecule (O1W) acts as a hydrogen bond donor forming the following hydrogen bonds: O1W—H1AW...O2 of length 2.718(3) Å and O1W—H1BW...O1 of length 2.757(3) Å (O...O distances), and also acts a hydrogen bond acceptor: N1—H1...O1W of length 2.709(3) Å (N...O distance). The second water molecule (O2W) forms two hydrogen bonds: O2W—H2AW...O3W of length 3.088(7) Å and O2W—H2BW...O2 of length 2.741(5) Å (O...O distances). The water molecule centred on O3W does not display short O...O or O...N distances suggestive of hydrogen bonds. Instead O3W is 2.942(9) Å from a symmetry equivalent O3W, and the other shortest O...O distances for this atom are all greater than 3.06 Å in length. Similarly there are no O...N distances suggestive of hydrogen bonds. The lack of hydrogen bonding to localise O3W explains the relatively large displacement parameter of this atom and also the difficulty in locating hydrogen atoms for this water molecule.

Table 3.2: Hydrogen bonds within bis(guaninium) sulfate 2.5 hydrate, 1a

D-H	A	d (D-H) (Å)	d (H...A) (Å)	d (D...A) (Å)	<D-H...A (°)
O1W-H1AW	O2	0.924(17)	1.838(17)	2.718(3)	158(3)
O1W-H1BW	O1 ⁱ	0.907(15)	1.866(18)	2.757(3)	167(3)
O2W-H2AW	O3W ⁱⁱ	0.901(18)	2.332(18)	3.088(7)	141(2)
O2W-H2BW	O2	0.89(2)	1.93(3)	2.741(5)	150(5)
N1-H1	O1W ⁱⁱⁱ	0.88	1.83	2.709(3)	176.82
N2-H2A	N3 ^{iv}	0.88	2.117	2.995(3)	175.6
N2-H2B	O2 ⁱⁱⁱ	0.88	2.381	3.076(3)	136.1
N7-H7	O16	0.88	1.838	2.718(3)	179.56
N9-H9	O1 ^v	0.88	1.801	2.674(3)	170.94
N11-H11	O4 ^{vi}	0.88	1.937	2.764(3)	156.03
N12-H12A	N13 ^{vii}	0.88	2.173	3.045(3)	170.45
N12-H12B	O4 ^{vi}	0.88	2.24	2.987(3)	142.55
N12-H12B	O3 ^{vii}	0.88	2.331	2.832(3)	116.16
N17-H17	O6	0.88	1.829	2.709(3)	177.31
N19-H19	O3	0.88	1.788	2.656(3)	168.52

i = -x, -y, -z+1; ii = -x, -y+1, -z+1; iii = -x-1, -y+1, -z+1; iv = -x-2, -y+2, -z; v = x-1, y+1, z-1; vi = x, y, z-1; vii = -x+1, -y, -z

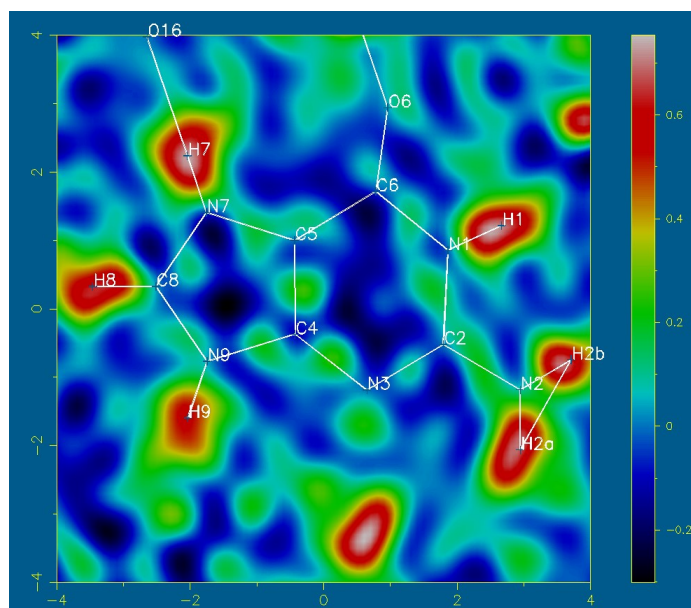


Figure 3.11: Difference Fourier map for guaninium 1

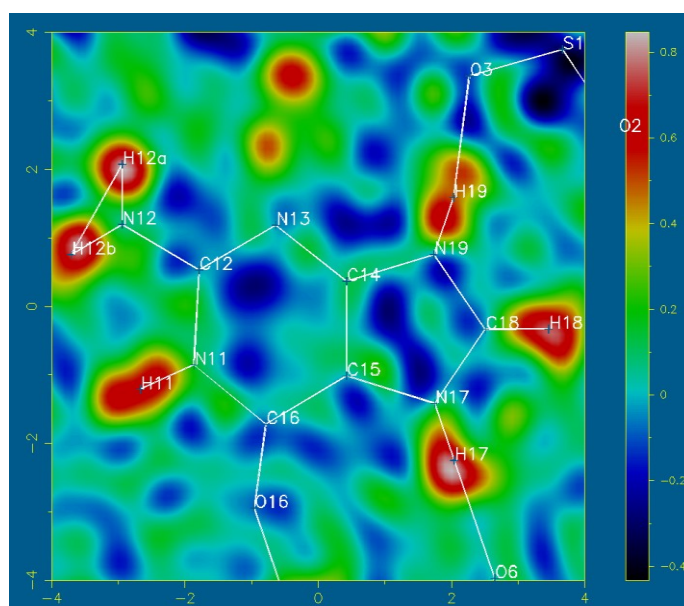


Figure 3.12: Difference Fourier map for guaninium 2

Figure 21 and 22 show that guaninium undergoes a [1H, 9H] protonation in both cases and the hydrogen atoms have been assigned correctly.

Sample purity for **1a** was determined by grinding the single crystals into a fine powder and collecting powder diffraction data. Subsequent powder X-ray analysis revealed that the selected single crystal is representative of the bulk sample and there is only one phase present. This is illustrated in Figure 3.13.

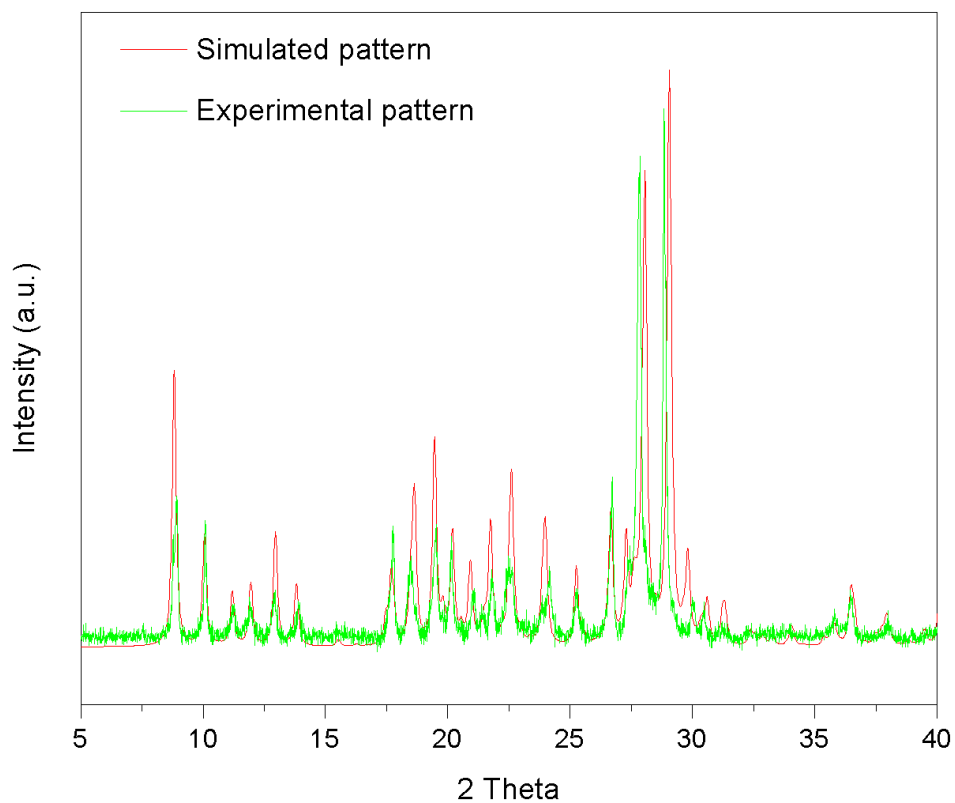


Figure 3.13: Overlay of simulated and experimental patterns showing the presence of a single phase

3.4.3.2 Relationship of (1a) to previous compounds

The compound $(\text{GH})_2(\text{HPO}_4) \cdot 2.5\text{H}_2\text{O}$ which was reported by Low *et al.*¹¹⁷ is isomorphous with the sulphate analogue described in this thesis. Low *et al.* give a rather brief structural description of the hydrogen phosphate phase and do not describe the thermal behaviour of this compound.

The structure of $(\text{GH}_2)\text{SO}_4 \cdot \text{H}_2\text{O}$ reported by Cherouana *et al.*¹⁰³ contains the diprotonated guaninium cation, $[\text{C}_5\text{H}_7\text{N}_5\text{O}]^{2+}$. The extra proton means that this ion only acts as a hydrogen bond donor through the protonated nitrogen atoms and this removes the possibility for the formation of chains of hydrogen-bonded guaninium cations. The compound $(\text{GH}_2)\text{Cl}_2$, reported by Matkovic-Calogovic *et al.*¹¹⁸, contains one symmetry-unique $\text{N}-\text{H} \cdots \text{O}$ hydrogen bond between guaninium cations and six unique $\text{N}-\text{H} \cdots \text{Cl}$ hydrogen bonds.

However, in structures that contain the singly protonated guanine, $[\text{C}_5\text{H}_6\text{N}_5\text{O}]^+$, there is much greater tendency for hydrogen bonding between cations. For example, $(\text{GH})\text{HPO}_3\text{H} \cdot 2\text{H}_2\text{O}$ ¹¹⁹ contains pairs of cations held by $R_2^2(8)$ embraces each composed of a symmetry equivalent pair of $\text{N}-\text{H} \cdots \text{N}$ hydrogen bonds. These pairs of cations are further linked into tapes by pairs of water molecules that form $R_4^4(14)$ embraces.

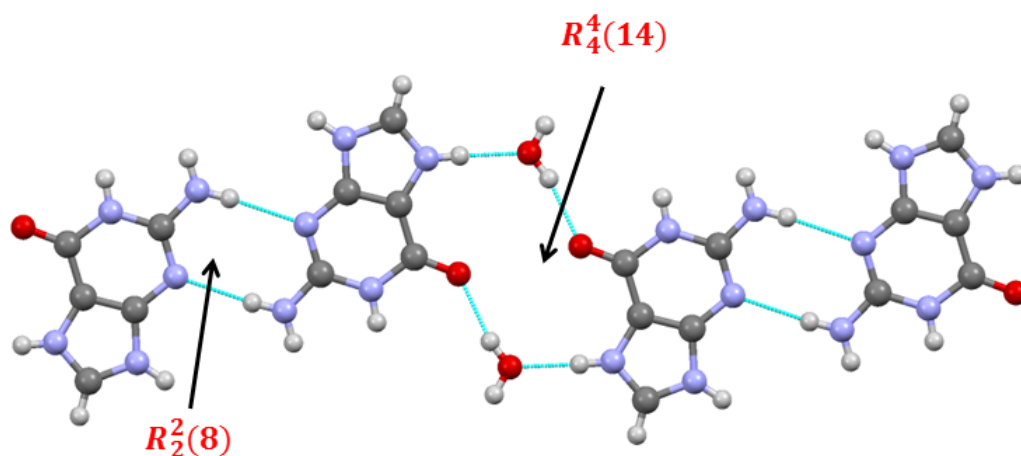


Figure 3.14: Cation interactions in the singly protonated guaninium salt.¹¹⁹

Similarly, guaninium chloride¹²⁰ contains hydrogen bonding dimers of guaninium cations held together by a $R_2^2(8)$ embrace. Around this dimer there are further hydrogen bonds to water and chloride. The structure of **1a** is thus similar to others that contain the $[\text{GH}]^+$ ion in the way that it contains hydrogen bonds between these cations and also anions.

3.4.3.3 IR spectrum and thermal behaviour of (1a)

The FTIR spectrum of **1a** demonstrated several bands arising from guaninium. N—H stretches in the region $3450\text{--}3550\text{ cm}^{-1}$ are present along with bands associated with the C=O and C=N bonds in guaninium. There is a notable broad band due to sulphate around 1160 cm^{-1} and others in the fingerprint region characteristic of this anion.

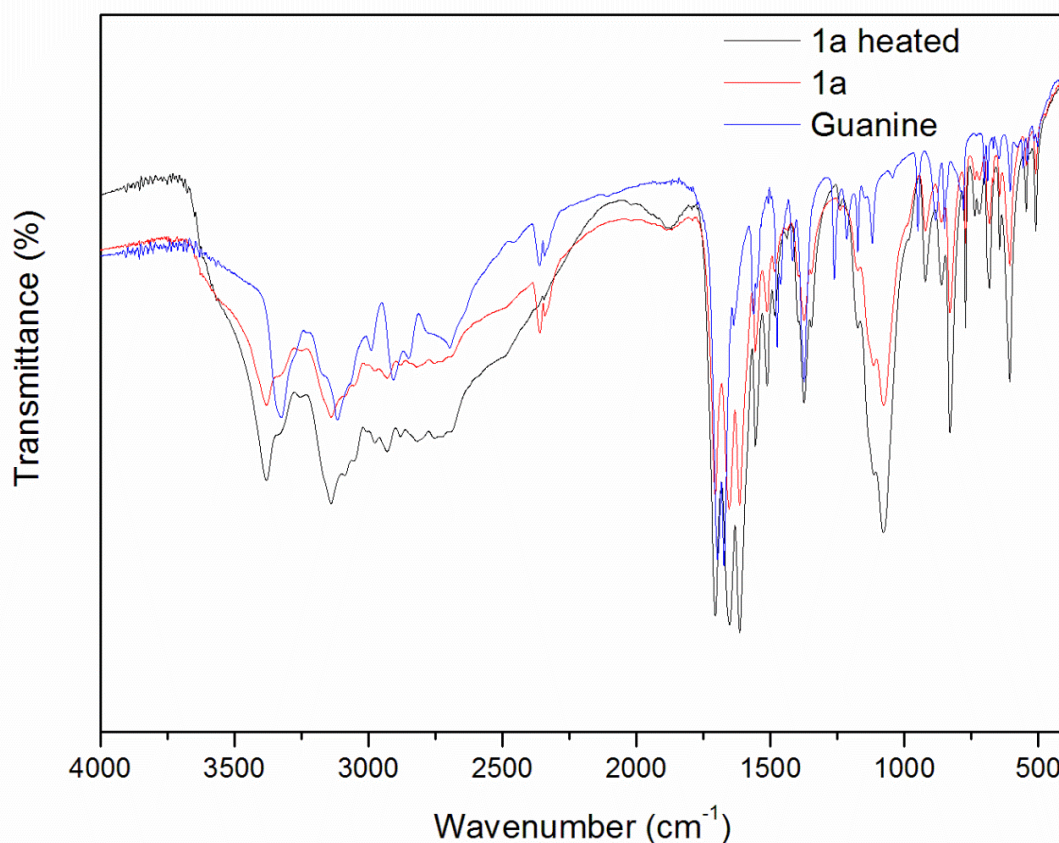


Figure 3.15: FTIR Spectrum of the 1a and guanine

For **1a** there is a very broad band centred approximately near 3300 cm^{-1} which can be assigned to the water within the structure. Upon heating to $200\text{ }^{\circ}\text{C}$ for a period of 1 h this band has greatly diminished in intensity. This observation and the structural features present (hydrogen bonded tapes and water contained within channels) suggested that it might be possible to remove water from the structure with limited structural rearrangement. Thermogravimetric data for **1a** are shown in Figure 3.16 and reveal that the compound begins to lose some water at a temperature of *circa* $45\text{ }^{\circ}\text{C}$ upon heating, with the majority of the water being completely removed by $150\text{ }^{\circ}\text{C}$. There is a loss of *ca.* 7.5 % mass from room temperature to $150\text{ }^{\circ}\text{C}$ which is rather lower than the 10.1% expected for the complete loss of 2.5 equivalents of water. This suggests that some water was lost from the structure at room temperature in the short time before examination by TGA. This is consistent with the observation of rather nebulous hydrogen bonding to O3W.

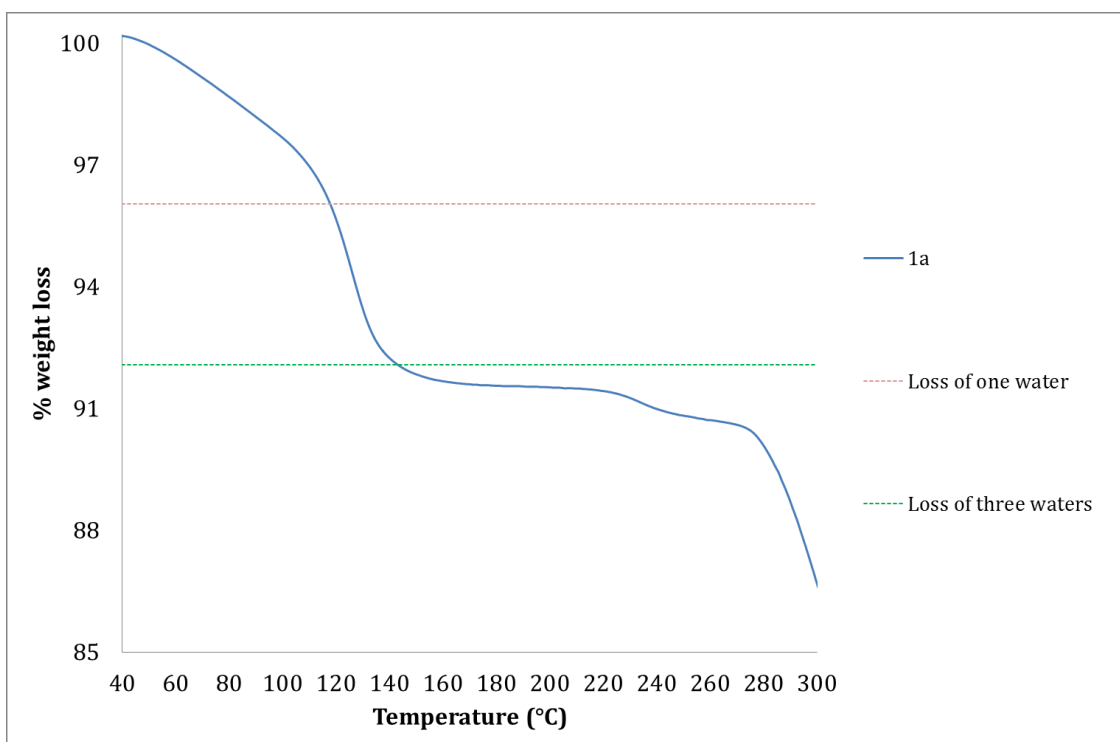


Figure 3.16: Thermogravimetric data for 1a

A crystal of **1a** was heated in an oven at 60 °C for 15 hours before examination by X-ray diffraction. After routine data collection, the structure obtained (**1a'**) was extremely similar to **1a**, except that there was an increase in the displacement parameter of O3W. For **1a** $U_{eq}(O3W) = 0.114$ and for **1a'** $U_{eq} = 0.1320$. This can be interpreted as loss of approximately 10% of O3W during this heating regime.

3.4.3.4 Partially dehydrated form, (**1b**)

To explore the persistence of water within the structure upon more vigorous heating and to determine whether the structure could undergo partial dehydration and retain crystallinity, a suitable crystal was selected for variable temperature X-ray diffraction measurements. The crystal was heated to 395 K for 2 minutes and then cooled down to 120 K. No change in unit cell volume was observed from **1a**, hence the crystal temperature was then raised to 293 K. Thereafter, the crystal was heated to 395 K over a period of *ca.* 20 minutes (300 K h^{-1}) and finally cooled to 120 K. At this point there was a noticeable change in the unit cell volume from **1a** and a full data collection was undertaken. The unit cell volume of **1a** is $839.8(3) \text{ \AA}^3$, but following this heat treatment the observed cell volume was $837.9(3) \text{ \AA}^3$. It should be noted that while exposure to such harsh conditions and rapid changes in temperature led to an increase in the mosaic spread of the crystal, it did not damage it significantly.

Subsequent data collection and structure solution revealed a partially dehydrated structure, **1b**. Unexpectedly, the X-ray structure analysis showed that only one water molecule (O3W) had been lost from the structure to generate a solid with composition $(\text{GH})_2\text{SO}_4 \cdot 1.5\text{H}_2\text{O}$. The compound is isomorphous with **1a**; it contains extended tapes of guaninium cations that are held into stacks by hydrogen bonding to sulphate and between these stacks there exist channels that contain water.

However, structure **1b** differs from **1a** in that it lacks one water molecule, the loosely held water centred on O3W as shown in Figure 3.17. The liberation of one water molecule (O3W) from the channels confirms that O1W and O2W are more tightly bound *via* hydrogen bonding than O3W and therefore they remain present in the channels, while the weakly bound O3W is driven out of the channel. A comparison of **1a** and **1b** is shown in Figure 3.18.

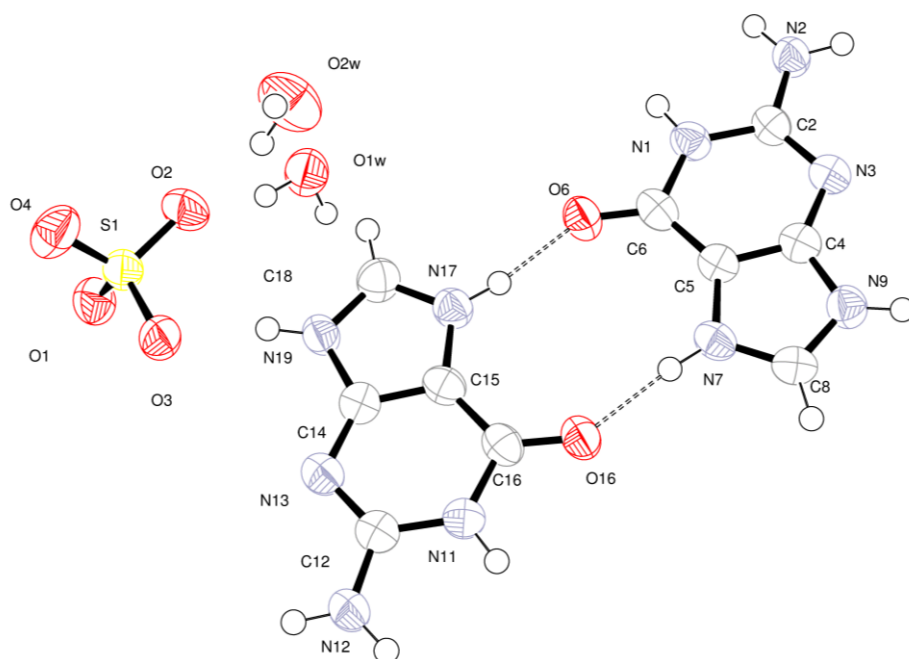


Figure 3.17: Asymmetric unit of (1b) with atoms drawn as 70 % probability ellipsoids. Dashed lines indicate hydrogen bonds between guaninium cations within the asymmetric unit.

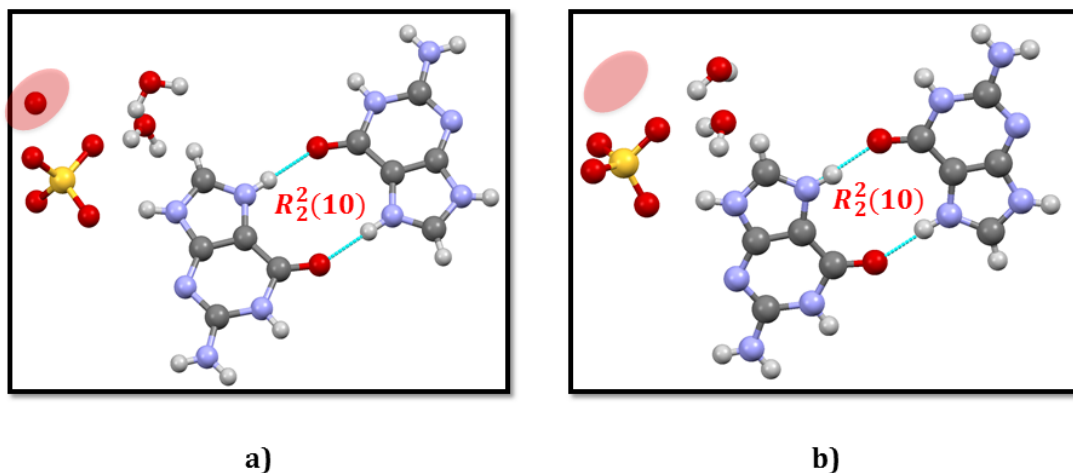


Figure 3.18: Comparison between structures; a) fully hydrated structure (1a); b) partially dehydrated structure (1b). The pink circles show the difference between the two structures. Cations in both (1a) and (1b) interact with each other by forming the same hydrogen-bond dimer

3.4.3.5 Fully dehydrated form (1c)

Following the successful partial dehydration of **1a** to generate **1b**, further attempts were made to achieve full dehydration in order to investigate the structural effect on the crystal. A suitable crystal was selected for X-ray examination and it was held at a temperature of 395 K for 10 minutes and data were collected after cooling the crystal to 120 K.

A significant degradation in the crystal quality was observed in the diffraction images following heating. The sample scattered X-rays very poorly and it proved to be very challenging to study. However, within a reasonable experimental time (53 h), it proved possible to collect *ca.* 95% of the unique reflections from the crystal (to 36° in 2θ) and these proved sufficient to solve and refine the structure. The fully dehydrated structure obtained by this route, **1c**, has formula $G(GH)_3(SO_4H)(SO_4)$.

Although the crystal was very weakly scattering, the structure solution gives valuable chemical information: the removal of the water leaves empty channels but there are subtle changes in hydrogen bonding of the resultant material. Dehydration is associated with two important changes in the structure:

a) the unit cell approximately doubles in volume and

b) the location of protons within the structure changes.

Protons were placed at positions consistent with short O—H···O, N—H···O, and N—H···N hydrogen bonds. In particular, there is close approach of two sulphate units so that one O···O distance is 2.455(13) Å. This strongly suggests the presence of a proton and an intermolecular hydrogen bond between SO₄²⁻ and SO₄H⁻.

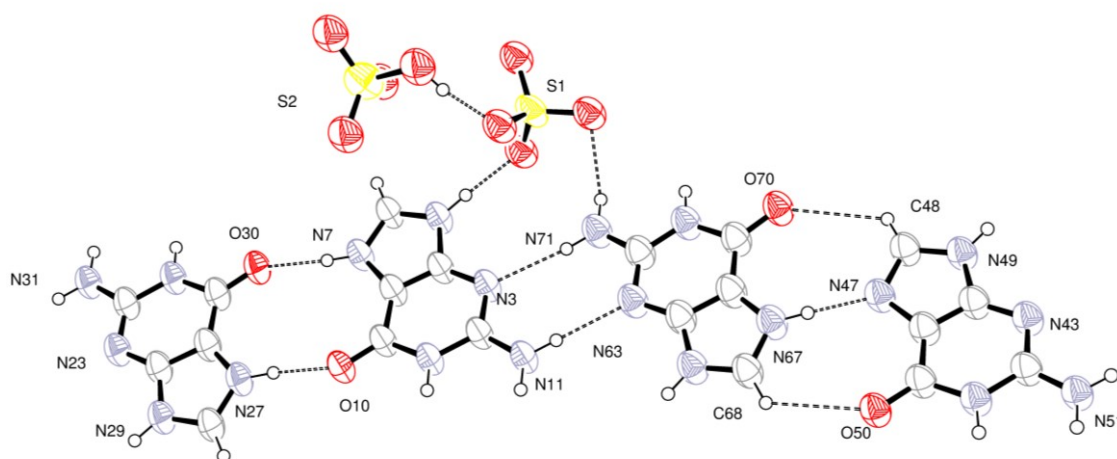


Figure 3.19: Representation of the asymmetric unit of (1c) with atoms drawn as 50 % probability ellipsoids. Dashed lines indicate hydrogen bonds.

Three of the four independent guanine molecules are singly protonated and one is unprotonated. This change in protonation between **1a** and **1c** leads to different hydrogen bonding chains in **1c**: a single type of tape is present but the repeat unit comprises three GH⁺ ions and one G molecule. The tapes have a repeat unit that encompasses four different

hydrogen-bonding motifs. The graph set notation for these is one $R_2^2(10)$ and three distinct $R_2^2(8)$ as shown in Figure 3.20.

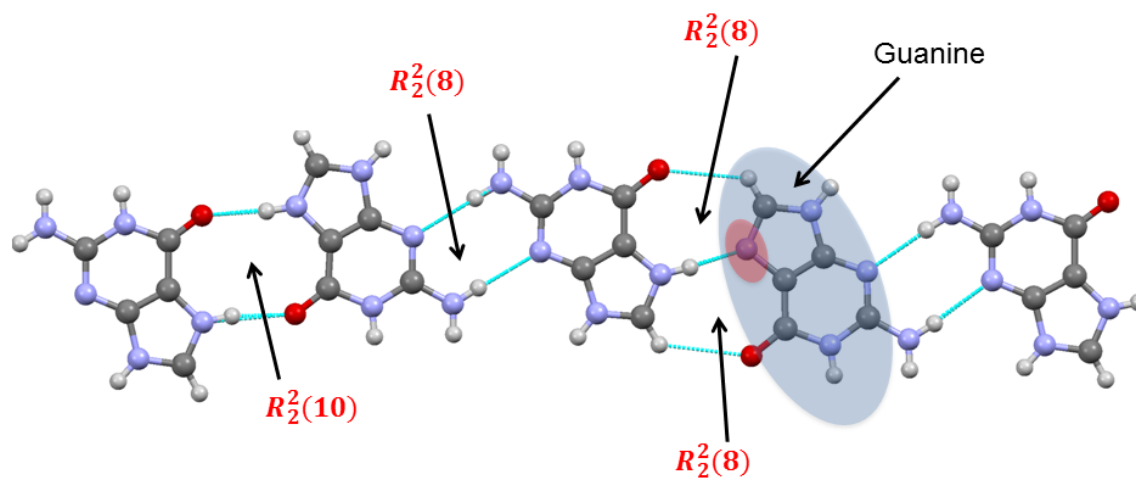


Figure 3.20: Different hydrogen bonding in the fully dehydrated form (1c). Highlighted in pink is the unprotonated imidazole nitrogen.

The tapes are arranged in stacks similar to **1a** at a separation of 3.181(17) Å. Between them lie the sulphate and hydrogen sulphate anions, forming hydrogen bonds between adjacent tapes within a stack and between adjacent stacks. The structure is similar to **1a** in that there are channels within the structure that run parallel to [100] at positions (0,0) and (0.5, 0.5) in parallel to *a*-axis. However, in **1c** these channels are not occupied by water and these voids extending through the structure constitute 8.1 % of the total volume. This void space is bounded primarily by the oxygen atoms of the sulphate anion. (Figure 3.21)

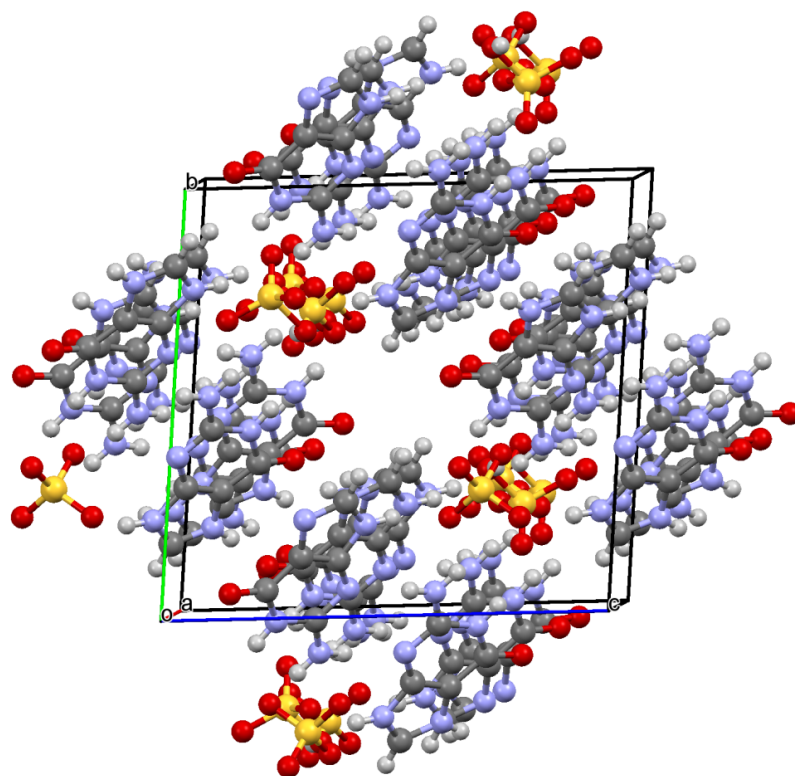


Figure 3.21: View of 1c down [010]. Vacant channels extend parallel to a at positions $(0,0)$ and $(\frac{1}{2}, \frac{1}{2})$ parallel to yz -axis

3.5 Co-crystallisation of DNA bases with 1,10-phenanthroline

3.5.1 Introduction

The physical properties of molecular solids are inextricably linked with the arrangements of individual molecules in the crystal.¹²¹ Any change in the overall crystal structure, for example, the inclusion of a water molecule or proton migration, causes changes in the intermolecular interactions in the crystal. Such alteration in the intermolecular interactions and the crystal packing normally results in a change in physical properties. A promising route to improving physical properties of a solid is co-crystallisation of a given compound with another neutral compound which is a solid at ambient conditions.

Crystal engineering^{2,3} may be defined as the intelligent design of crystalline solids through control of intermolecular interactions. Within this field co-crystals have gained attention due to the interest in modifying the physical properties of one compound by its inclusion within a co-crystal.¹²² For example, in the pharmaceutical industry co-crystallisation has shown potential to alter the solubility, bioavailability, dissolution, and physiochemical stability of active pharmaceutical ingredients (APIs).¹²³ Drug candidates that display poor solubility present a major challenge in the pharmaceutical industry and hence many APIs are prepared as hydrates or salts. However, co-crystallisation is also an important area to explore for the improvement of properties.

A classic example is the case of sildenafil or Viagra, which was initially used for addressing angina, high blood pressure or pulmonary hypertension, but was subsequently targeted for treating erectile dysfunction. In the Viagra formulation, the active ingredient sildenafil is present as a citrate salt, which is only moderately soluble.⁸⁴ However, a remarkable increase in solubility has been observed when sildenafil was co-crystallised with acetylsalicylic acid.¹²⁴

Similarly, co-crystallisation of melamine with cyanuric acid has a profound effect on solubility. Toxicological studies of both melamine and cyanuric acid showed no effect on the kidney function of cats fed on melamine and cyanuric acid individually.¹²⁵ However, intratubular precipitation of highly insoluble co-crystals of melamine:cyanuric acid causes acute renal failure in cats.

When it comes to co-crystallisation reactions, DNA nucleobases are good candidates for co-crystallisation because of their versatile hydrogen bonding functionality.^{91, 102-108} Co-crystallisation of DNA bases has been demonstrated for a wide range of commercially available co-formers including other DNA bases, carboxylic acids, or N-donor bases.^{104, 126}

A survey of the Cambridge Structural Database¹³ (CSD version 5.35, November 2013) shows that nucleobases can display a range of different hydrogen bonding motifs. A good example of this flexibility is the base pairing between DNA bases which can follow either the Watson-Crick³⁵ or Hoogsteen³⁶ modes of hydrogen bonding. However, structures involving cytosine frequently display hydrogen-bonded chains of molecules as shown Figure 3.22.

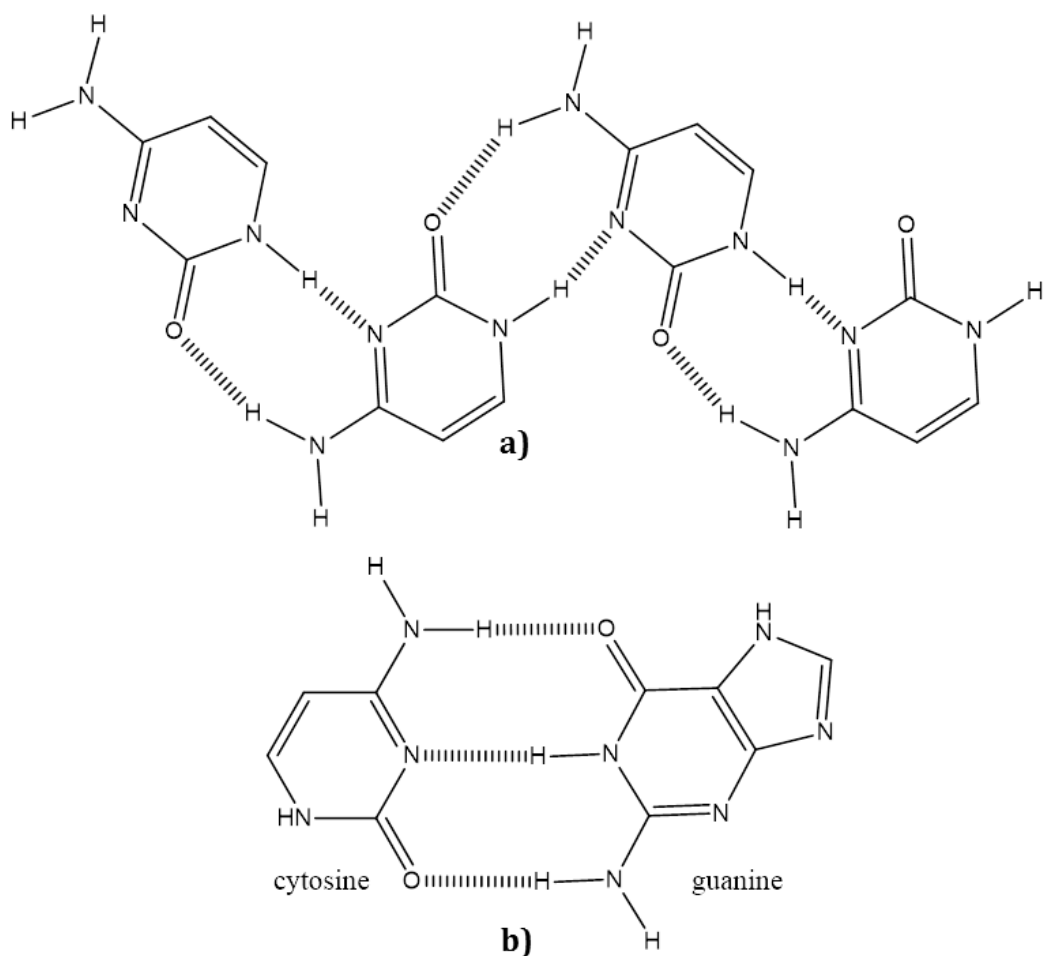


Figure 3.22: Comparison of synthons: a) synthon formation between two cytosine molecules; b) synthon formation between G:C. Dashed lines represent hydrogen bonds.

Cytosine is pyrimidine derivative and is one of the four DNA and RNA bases. It exhibits a versatile hydrogen bonding functionality owing to its hydrogen donor and acceptor sites. As it can be seen from Figure 3.23, cytosine has an uneven functionality of acceptor and donor sites. The carbonyl oxygen and the endocyclic nitrogen act as two hydrogen bond acceptors, whereas the N—H group and the amine group act as 3 hydrogen bond donors.

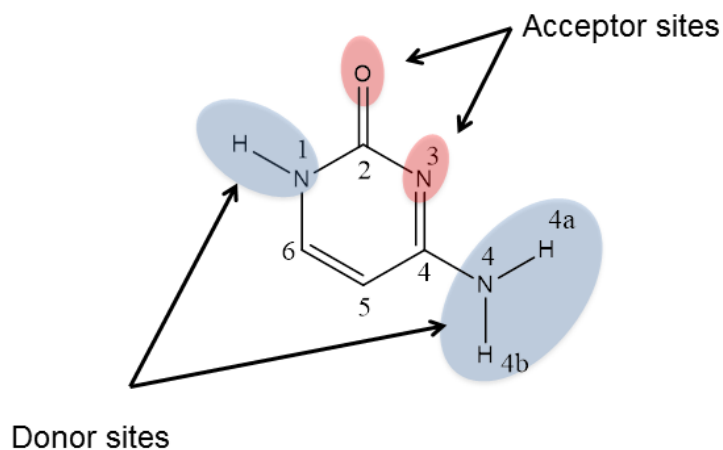


Figure 3.23: Structure of cytosine

The CSD was searched for crystals containing cytosine or its derivatives. The search was carried out using the software ConQuest⁶² and the following three filters were applied: “only organics”, “no ions” and “3D coordinates determined”. The search revealed only 51 entries with cytosine or halide substituents of cytosine. Majority of these entries were cytosine co-crystals grown with carboxylic acids, but it was noticed that no co-crystals were found with aromatic N-donor compounds. This was also the case with adenine compounds.

The objective of the study presented below is to understand and exploit the hydrogen bonding interactions of DNA bases with 1,10-phenanthroline (1,10-phen). The study seeks to explore whether the hydrogen bond acceptor properties of 1,10-phen would make it a suitable co-former. Experimental studies ran parallel to crystal structure predictions. Crystal structure determinations and crystal structure predictions are presented and the differences rationalised.

3.5.2 Experimental

3.5.2.1 Co-crystal screening

In order to explore the formation of co-crystals between DNA bases and the 1,10-phen, we employed solid-state neat grinding¹²⁷ methods described in literature.¹²⁸ Binary mixtures of 1,10-phenanthroline hydrate (0.1982 g, 1 mmol) with DNA bases [Cytosine (0.111 g, 1 mmol)/Adenine (0.135 g, 1 mmol)/Thymine (0.126 g, 1 mmol), Guanine (0.151 g, 1 mmol)] were prepared. These were transferred to a 12 mL jar and milled for 1 hour under neat condition in a Retsch PM 100 ball mill. Two stainless steel balls of 10mm diameter were used for milling.

3.5.2.2 Single Crystal Preparation

1,10-phenanthroline hydrate (0.1982 g, 1 mmol) and the DNA base [Cytosine (0.027 g, 0.25 mmol); Adenine (0.034 g, 0.25 mmol); Thymine (0.032 g, 0.25 mmol); Guanine (0.038 g, 0.25 mmol)] were dissolved in 50% ethanol:water (20mL) and stirred for 10 min with gentle heating. The solution was allowed to evaporate slowly at room temperature.

3.5.2.3 Infra-red (IR) Spectroscopy

FT-IR spectra were collected from samples prepared as KBr disks (1:20 dilution) using a Perkin Elmer FT-IR Spectrometer Spectrum RX1.

3.5.2.4 Single Crystal X-ray Diffraction Measurements

Routine single crystal data collection was performed and temperature during the diffraction experiment, which was set to 100 K. All non-H atoms were refined with anisotropic displacement parameters. Location of hydrogen atoms was achieved by using difference Fourier maps.

3.5.2.5 X-ray Powder Diffraction

Relatively high resolution X-ray powder diffraction data were collected from intimately ground samples mounted on a PANalytical Empyrean diffractometer operating with

Cu $K\alpha_1$ radiation and a PIXCel detector. Rietveld¹²⁹ refinement was carried out within the GSAS¹³⁰ suite of programs. The background was fitted using a 6-term shifted Chebyshev function. The unit cell parameters and a zero point error were refined. A single Gaussian peak shape parameter was refined. No atoms positions were refined; a single isotropic displacement parameter was refined for all non-H atoms and $U_{\text{iso}}(\text{H})$ was set to 0.05 \AA^2 .

3.5.3 Results and Discussion

3.5.3.1 Co-crystal screening and PXRD analysis

It was predicted that all four DNA bases, adenine, cytosine, thymine and guanine might form co-crystals with 1,10-phenanthroline. This hypothesis was based on the hydrogen bond donor sites present in all these bases that would enable them to interact with the basic nitrogens of 1,10-phenanthroline, forming $\text{N}-\text{H}\cdots\text{N}(\text{pyridyl})$ interactions. However, the results of the screening experiments suggest that not all DNA bases do form co-crystals with 1,10-phenanthroline. X-ray powder diffraction data collected from the product of milling cytosine with 1,10-phen is shown in Figure 3.24. It is clear that characteristic peaks of cytosine and 1,10-phen hydrate are no longer present in the pattern. For example, no major feature exists in the region around $2\theta = 20^\circ$ in the product unlike patterns of each starting material. Therefore, milling generated a new phase labelled **cyt:phen**.

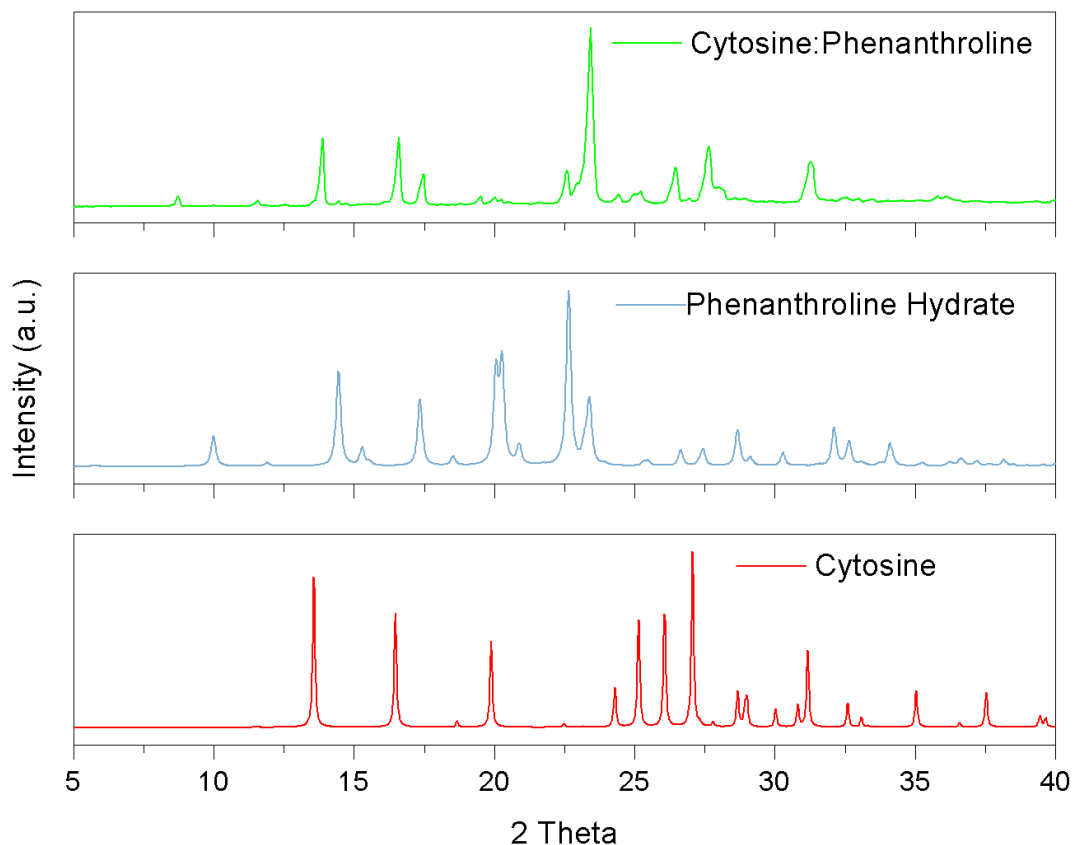


Figure 3.24: Simulated X-ray powder diffraction patterns of cytosine and 1,10-phenanthroline hydrate, and experimental pattern obtained after milling their mixture.

For the other DNA bases, evidence that co-crystallisation has occurred with 1,10-phen is much weaker. This is because the powder patterns yield insufficient evidence of such phase transformation. Little evidence of partial phase transformation was observed on the co-crystallisation experiment between adenine and 1,10-phenanthroline. (Figure 3.25.) These findings suggest that the pattern of the product is simply a mixture of the two starting materials.

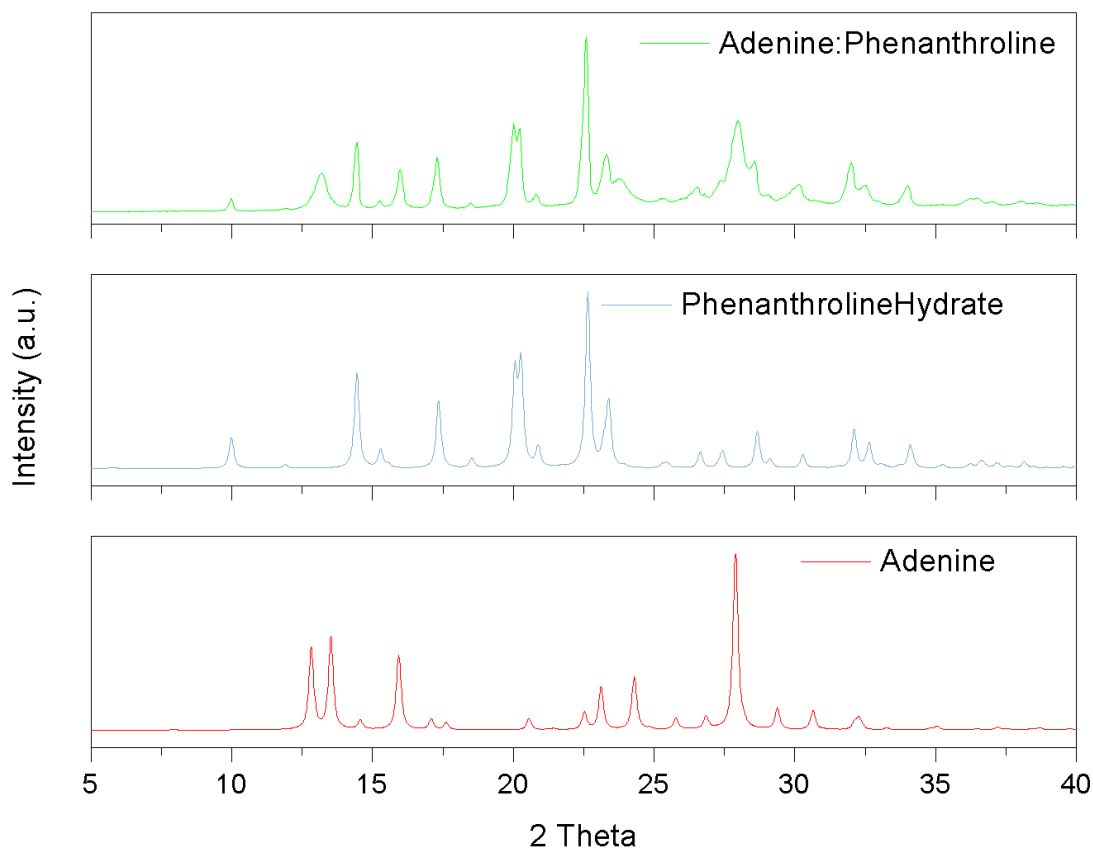


Figure 3.25: X-ray patterns from co-crystallisation of adenine and 1,10-phenanthroline

Figure 3.26 shows X-ray powder diffraction pattern collected from the solid product of milling thymine with 1,10-phen. Careful inspection shows the sample that has been ground closely resembles a mixture of thymine and 1,10-phen hydrate. However, the emergence of small feature in the region $2\theta = 8 - 12^\circ$ suggest a new phase may be emerging. Protracted grinding of this mixture did not yield a co-crystal and the pattern obtained was the same as the one in Figure 3.26.

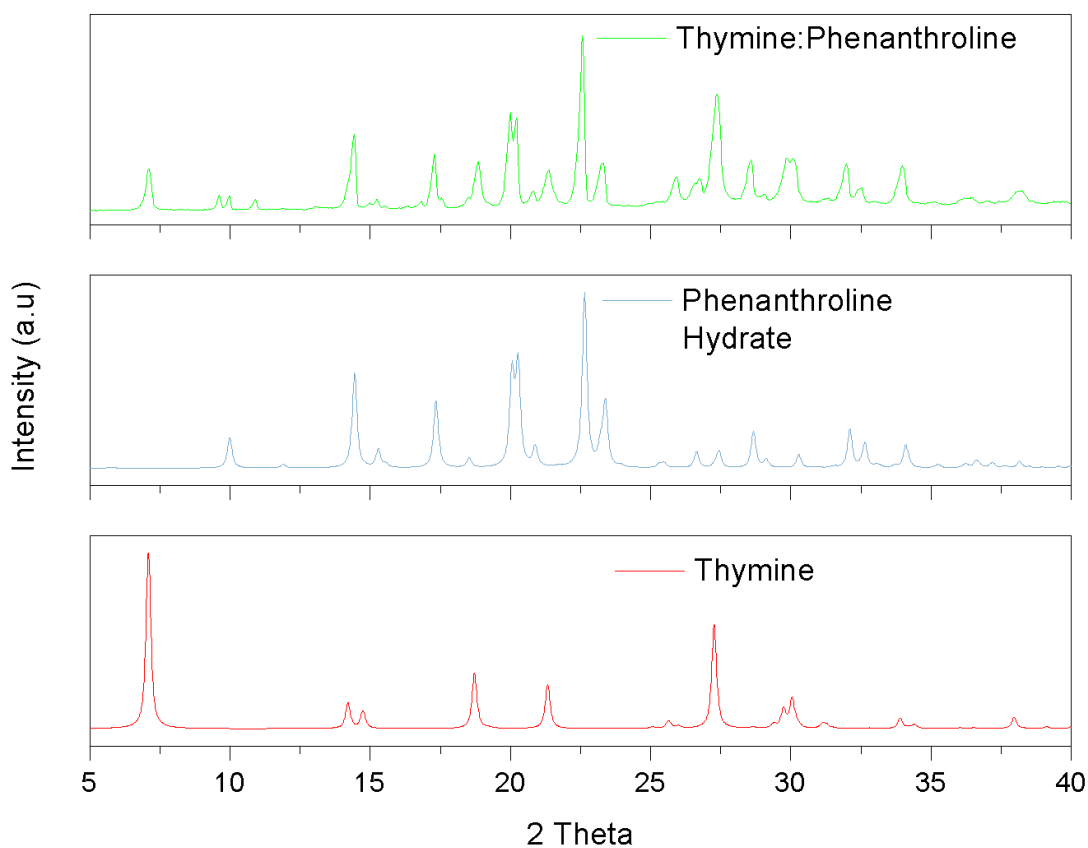


Figure 3.26: X-ray patterns from co-crystallisation of thymine and 1,10-phenanthroline

Finally, the results of the co-crystallisation between guanine and 1,10-phenanthroline are shown in Figure 3.27. The pattern of the milled product bears a close resemblance to that of 1,10-phen hydrate but there are extra features that do not appear to be consistent with pure guanine such as the broad peak at $2\theta = 27^\circ$, shoulder at $2\theta = 14^\circ$ and disappearance of guanine peaks at $2\theta = 13, 13.8$ and 16.2° . Similar to the case of thymine, protracted grinding did not produce a co-crystal.

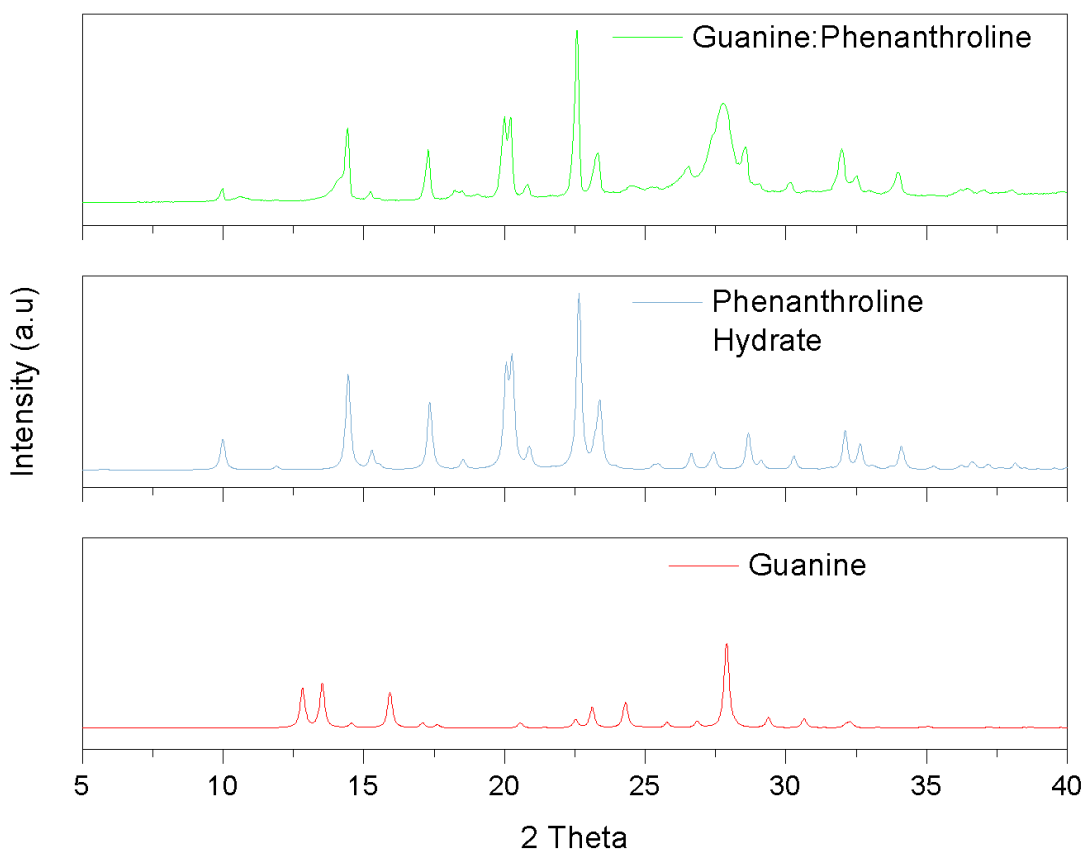


Figure 3.27: X-ray patterns from co-crystallisation of guanine and 1,10-phenanthroline

3.5.3.2 Evaluation of the results from co-crystal screening and solution crystallisation

The initial screening reactions by milling demonstrated a new **cyt:phen** phase had formed. We were able to use solution methods to grow crystals from a mixture of cytosine and 1,10-phen hydrate. It proved possible to solve the structure by routine single-crystal X-ray methods.

Screening experiments of 1,10-phen hydrate with adenine, thymine and guanine, respectively suggested that co-crystallisation has been unsuccessful. Remarkably, the only reaction which afforded single crystals is the reaction of cytosine with 1,10-phen hydrate,

which is consistent with the formation of a new phase upon milling these two starting materials together.

3.5.3.3 Structure of (cyt:phen)

Colourless crystals were obtained by simple solvent evaporation and were determined to be $(C_4H_5N_3O)_2 \cdot (C_{12}H_8N_2)_2$. This phase **cyt:phen** crystallises in the monoclinic space group $P2_1/c$ with a unit cell volume = 2722.99(5) Å³. The asymmetric unit contains two crystallographically independent cytosine molecules and two crystallographically independent 1,10-phenanthroline molecules (*i.e.* $Z' = 2$) as depicted in Figure 3.28.

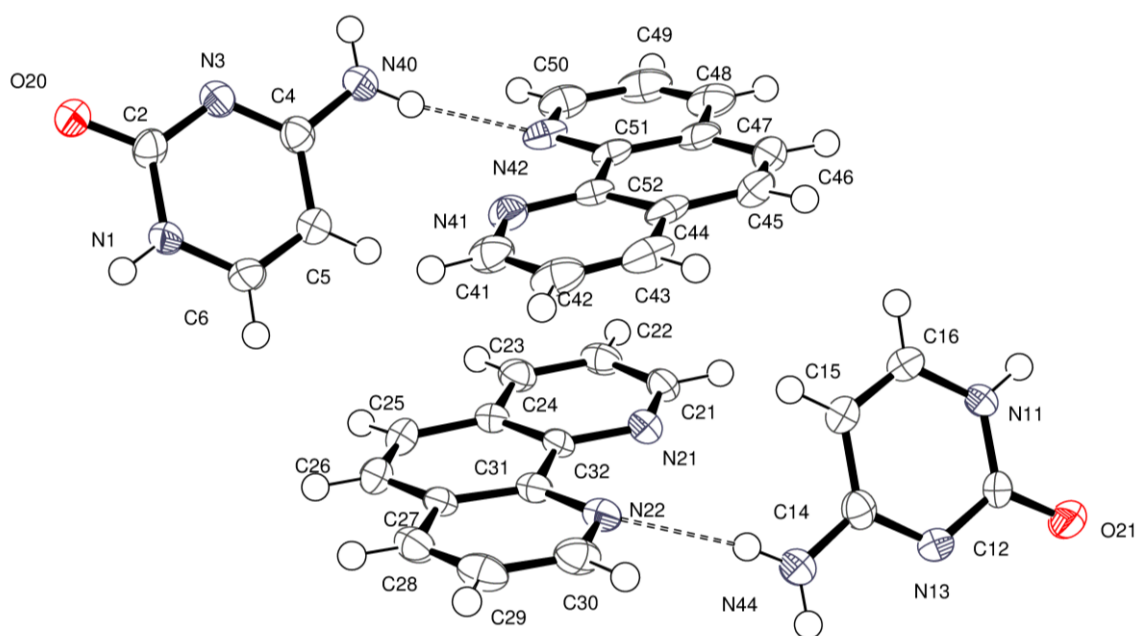


Figure 3.28: Asymmetric unit of cyt:phen. Atoms are drawn as 70% probability ellipsoids. Dashed lines represent N—H...N hydrogen bonds

Chemically sensible criteria were imposed while analysing and identifying the hydrogen bond patterns in the structure. These include: all donors should have a covalent bond with a hydrogen atom, the hydrogen bond acceptors should possess a lone pair of electrons capable of forming hydrogen bonds, and the D—H···A angle $> 90^\circ$, as classified by Jeffrey.³³

Each of the two independent cytosine molecules forms a zigzag hydrogen-bonded chain that extends parallel to the crystallographic *b*-axis. Chain 1 is composed only of the first cytosine molecule and likewise the second crystallographically-independent cytosine is only found in chain 2. The chains are very similar and are sustained by pairs of $R_2^2(8)$ embraces between symmetry-related cytosine molecules. (Figure 3.29)

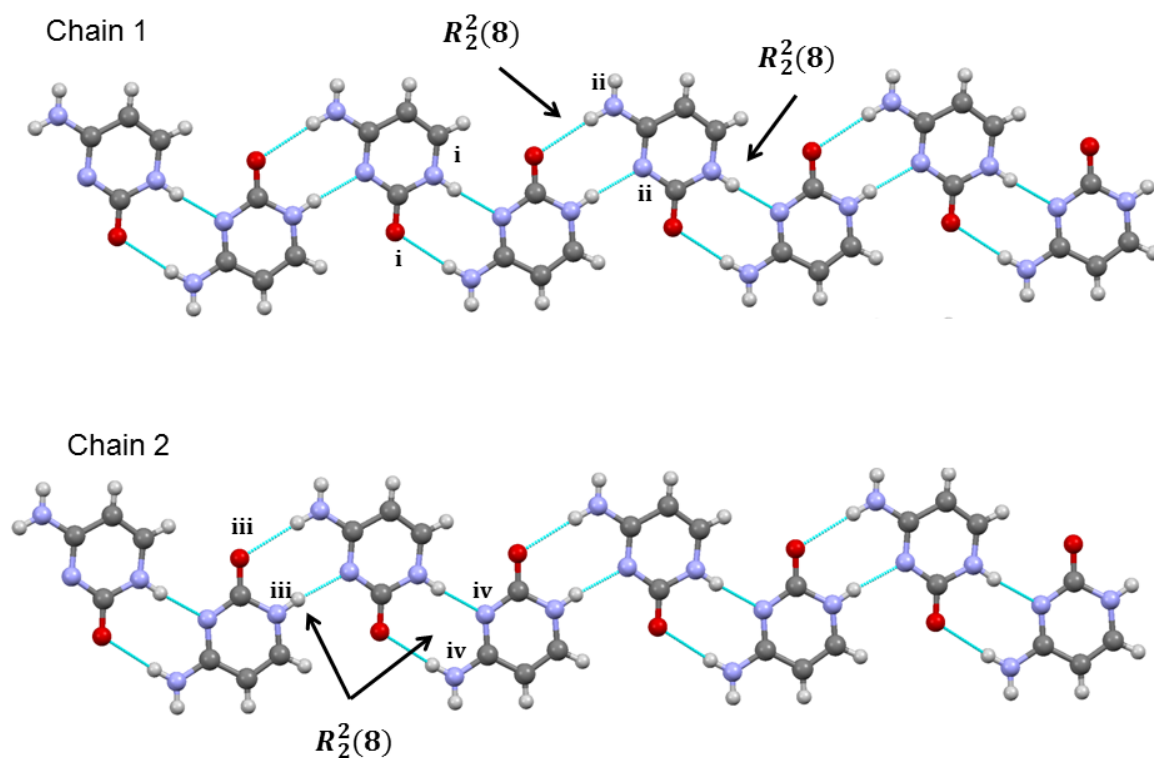


Figure 3.29: Chains formed by each crystallographically-independent cytosine. $R_2^2(8)$ homosynthon is generated with symmetry equivalent counterparts of each cytosine with the following symmetry operations: $i=(-x, y-0.5, -z+1.5)$; $ii=(-x, y+0.5, -z+1.5)$; $iii=(-x+1, y-0.5, -z+0.5)$; $iv=(-x+1, y+0.5, z-0.5)$.

The two symmetry-independent 1,10-phen molecules are arranged approximately parallel. The phenanthroline molecules are stacked along the crystallographic *b*-axis but they are inclined at an angle 46.175° to *b*. Within this π -stack the distances between π -systems alternate between mean plane separation 3.38 (7) Å and 3.28 (8) Å. The centroid to centroid separation was recorded as 3.9496 (19) Å and 3.579 (19) Å. These separations are suggestive of a moderately strong interactions between the two π -systems. This pair of 1,10-phen molecules are part of an extended π -stack that is parallel to *b*-axis. The structure is thus divided into two structural elements: the hydrophilic part comprising hydrogen-bonded chains and the hydrophobic part comprising π -stacked aromatic molecules. (Figure 3.30 and Figure 3.31)

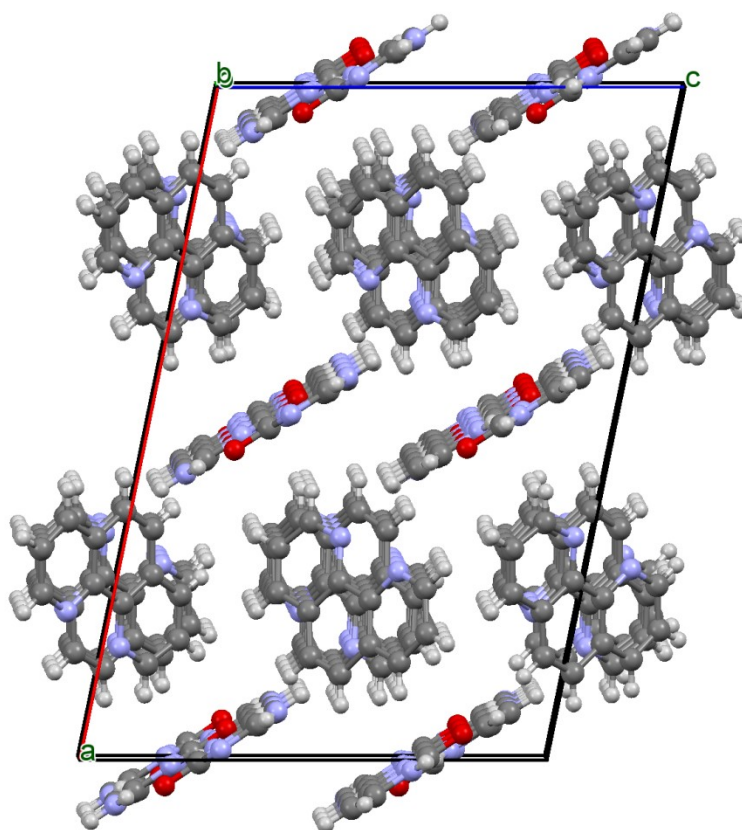


Figure 3.30: View of cyt:phen just off [010] direction illustrating infinite chains of cytosine and stacking of phenanthroline molecules

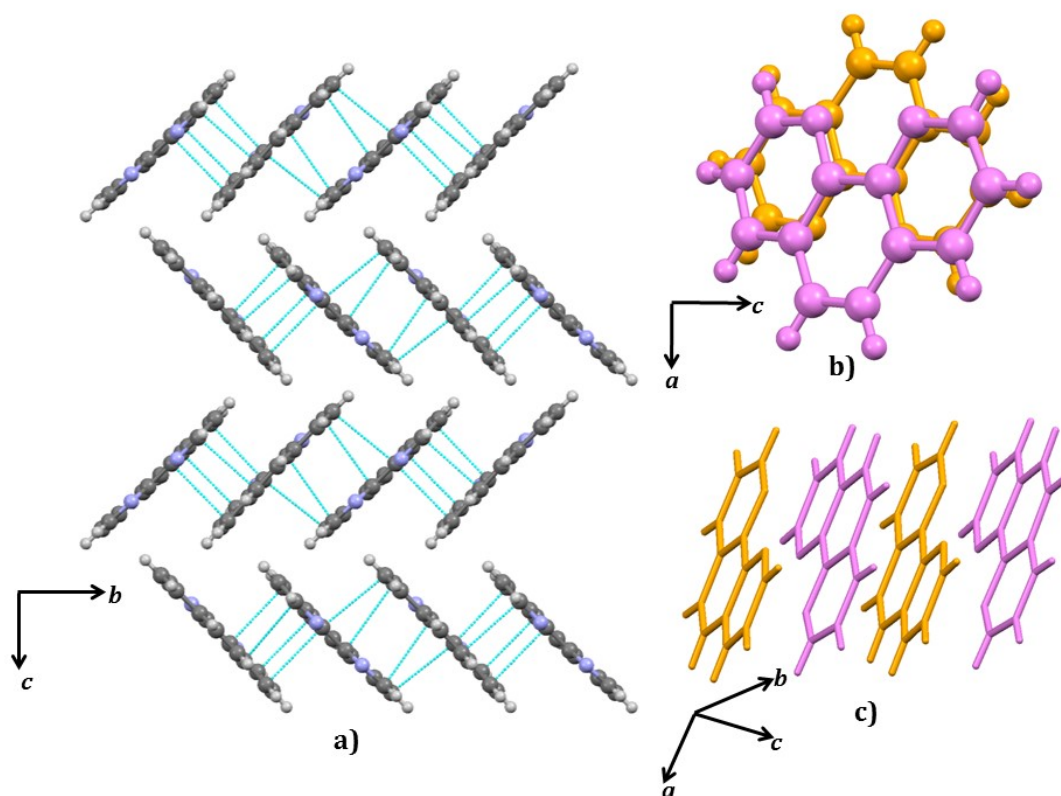


Figure 3.31: The stacking of phenanthroline: a) packing of phenanthroline viewed from *a*-axis inclined at an angle 46.175° to *b*; b) π - π stacking of 1,10-phenanthroline; c) stacking of each molecule with its symmetry generated counterpart

There are classical and non-classical hydrogen bonds between the hydrogen-bonded chains and the 1,10-phen π -stacks. As shown in Figure 3.28, each 1,10-phen acts as a hydrogen bond acceptor to a cytosine. Close examination of the structure reveals the presence of a weak hydrogen bond between cytosine and 1,10-phen molecule in the asymmetric unit. The interaction arises between C50—H50(aromatic)⋯N3(endocyclic). The donor acceptor distance and the angle of this interaction are in compliance with the classification provided by Jeffrey.³³ The distance was recorded as 3.511(4) Å and the angle was observed to be 150.5° . Full details of the hydrogen bonding present are shown in Table 3.3.

Table 3.3: Hydrogen bonding in cyt:phen

D-H	A	d (D-H) (Å)	d (H...A) (Å)	d (D...A) (Å)	<D-H...A (°)
N1-H1	N3 ⁱ	0.86	1.94	2.792(3)	171.9
N40-H40A	O20 ⁱⁱ	0.86	2.24	3.094(3)	170.4
N40-H40B	N42	0.86	2.16	3.012(3)	169.4
C5-H5	N41	0.93	2.66	3.206(3)	118.1
N44-H44A	O21 ⁱⁱⁱ	0.86	2.26	3.116(3)	174.7
N44-H44B	N22	0.86	2.22	3.072(3)	168.9
C15-H15	N21	0.93	2.63	3.147(3)	115.4
N11-H11	N13 ^{iv}	0.86	1.94	2.798(3)	173.5
C50-H50	N3 ^v	0.93	2.67	3.511(4)	150.5

ⁱ [-x+1, y-0.5, -z+1.5]; ⁱⁱ [-x, y+0.5, -z+1.5]; ⁱⁱⁱ [-x+1, y-0.5, -z+0.5]; ^{iv} [-x+1, y+0.5, -z+0.5];

^v [-x, -y+2, -z+1];

3.5.3.4 Phase Purity and Rietveld Fitting

X-ray powder diffraction was used to determine whether the single crystal examined was representative of the phase obtained by ball milling. Data were collected from 1:1 mixture of cyt:phen that had been milled for 1 hour. A partial Rietveld fit was performed by Dr Timothy J. Prior and is shown in Figure 3.32. The initial model employed to fit the observed data was the structure determined from the single crystal at 100 K. Following refinement of the model, it is clear that the quality of fit to the observed data is good, as shown by R_p of 0.0918 for all data. There is no evidence for other crystalline phases present. It would be possible to improve the fit further by imposing appropriate restraints on the model and refining atom positions, but this would be very time-consuming given the complexity of the model. The fit shown in Figure 3.32 demonstrates clearly that the **cyt:phen** co-crystal can be obtained pure by ball-milling of the two components and demonstrates the solution and ball-milling techniques produce the same co-crystal.

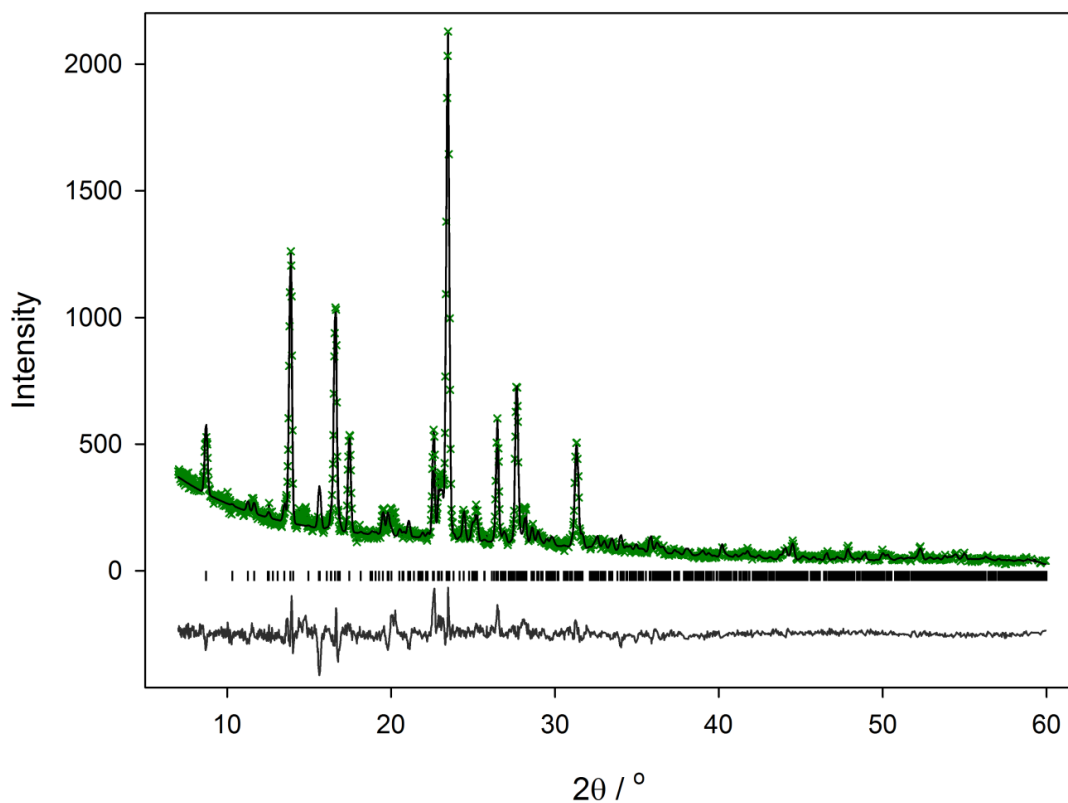


Figure 3.32: Observed (×), calculated (line), and difference (lower line) X-ray powder diffraction profiles for cyt:phen at room temperature; tick marks indicate positions of allowed reflections from the $K\alpha_1$ diffraction.

The synthesis of **cyt:phen** by ball-milling was entirely reproducible. Experiments to prove the extent of reaction as a function of milling time were undertaken. After 30 minutes grinding there is little evidence of a transformation to the co-crystal, but 60 minutes grinding is sufficient to effect a full transformation. A comparison of patterns obtained from mixing reagents and 30 minutes milling is shown in Figure 3.33.

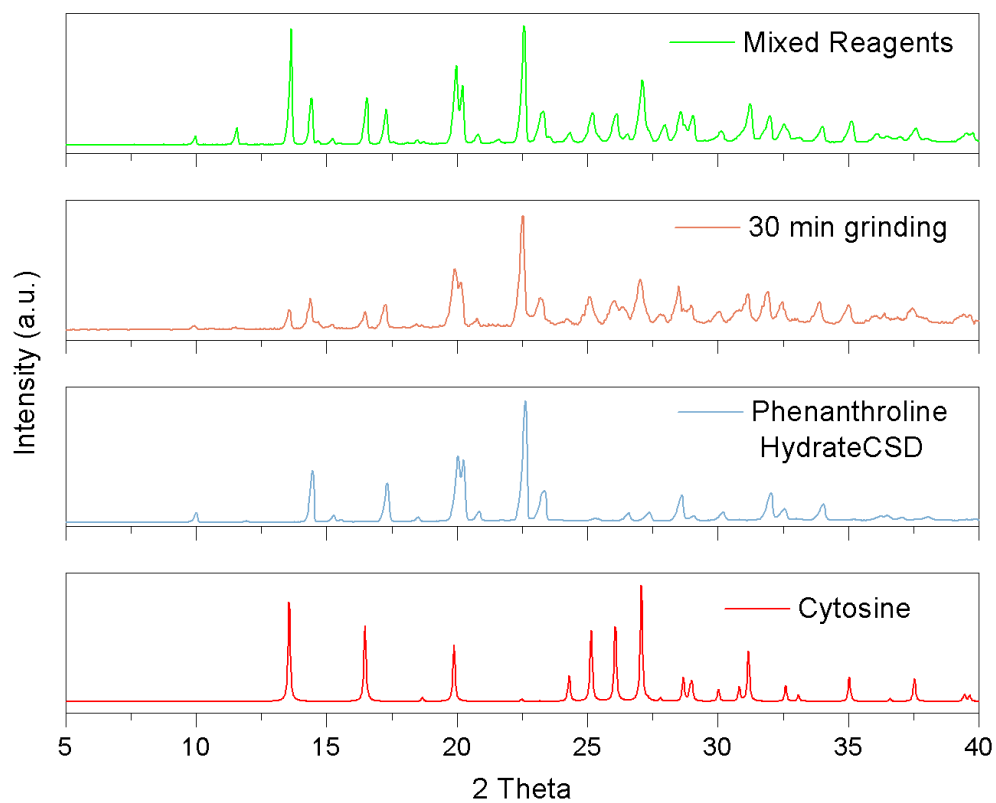


Figure 3.33: Patterns from mixing reagents, 30 min milling and starting materials

3.5.3.5 Rationalisation of Co-crystallisation and Crystal Structure

Prediction

In order to rationalise why co-crystals are obtained with cytosine and 1,10-phen, but the same reaction does not produce co-crystals with other DNA bases (adenine, guanine, thymine), it was decided that these systems should be probed further by trying to understand the energetic aspects of co-crystallisation.

Energy landscapes for all four systems were calculated using established techniques from crystal structure prediction. This work was conducted in collaboration with the research group of Prof. Graeme Day in the University of Southampton. Calculations included lattice energies for all four DNA bases separately, lattice energies of DNA bases with 1,10-phen and lattice energies of co-crystals of each DNA base with 1,10-phen. Crystal structure prediction was implemented by using $Z'=1$. The results obtained from these calculations are pivotal to explaining why **cyt:phen** co-crystallises successfully, whereas other DNA bases remain as a mixture of the two starting materials.

Table 3.4: Energy landscapes for co-crystallisation of DNA bases with 1,10-phen

Energies (kJ/mol)	Adenine	Cytosine	Guanine	Thymine
E(Latt) expt	-135.126675	-124.562759	-161.2967	-113.7615
+ Phenanthroline	-227.079295	-216.515	-253.24932	-205.7141
Lowest ($Z'=1$) CSP	-218.5895	-225.257	-253.0200	-205.5188
Expt. Co-crystal	None	-226.064	None	None

Table 3.4 shows the energy landscapes for these systems. The lattice energy of adenine was calculated to be -135.13 kJ/mol, whereas the sum of adenine and 1,10-phen was calculated as -227.08 kJ/mol. CSP calculations revealed that the global minimum for the co-crystal in $Z'=1$ is -218.59 kJ/mol. This value is higher in energy by 8.48 kJ/mol compared to the sum of the energies of the precursors. Such a marked energy difference

clearly demonstrates that co-crystal formation is not favoured energetically and agree with the failure to form a co-crystal experimentally.

Calculations on guanine and thymine are especially intriguing. As far as guanine is concerned, Table 3.4 shows that its lattice energy was calculated to be -161.30 kJ/mol, whereas the lattice energies of guanine and 1,10-phen were calculated as -253.25 kJ/mol. Based on energy calculations, the co-crystal ($Z'=1$) is only 0.23 kJ/mol less stable than the sum of the energies of the precursors. It should be noted that these values are calculations of the estimated energies and are within experimental error. However, they may help in explaining the partial phase transformation upon milling the precursors for 1 h. However, it is evident that co-crystal formation is not favoured energetically and this explains why protracted grinding did not drive the reaction forward.

Calculations on thymine also reveal a small difference in energies between the co-crystal ($Z'=1$) and the sum of the energies of the precursors. The lattice energy of the two precursors was calculated as -205.71 kJ/mol, whereas the energy of the co-crystal ($Z'=1$) is -205.52 kJ/mol. It is evident that the two systems are almost equi-energetic with the energy of the precursors being more stable by 0.2 kJ/mol.

On the other hand, energy landscape calculations reveal a dramatic change in energy upon co-crystallisation of cytosine with 1,10-phen compared to the sum of the energies of the precursors. The sum of the energies was calculated as -216.51 kJ/mol, whereas the global minimum for the co-crystal ($Z'=1$) lies 8.74 kJ/mol lower in energy at -225.26 kJ/mol, showing that co-crystallisation is energetically preferred and would have been predictable.^{131 132 133}

The results are important in showing that in the case of cytosine there is a large, favourable energetic driving force for **cyt:phen** formation, which is approximately the same energetic amount that disfavors the formation of **ade:phen**. On the other hand, formation of **gua:phen** and **thy:phen** is disfavoured by a rather small energy barrier. The

results also demonstrate why many such systems fail to produce co-crystals despite predictions based on apparently favourable and robust hydrogen bonding interactions using synthon theory. Indeed, this emphasises Desiraju's quote that *"any way of minimising the free energy of the system is a respectable way"*²⁵, and that may be as pure single component crystalline phases

3.5.3.6 Relationship of (cyt:phen) to other cytosine containing compounds

Evaluation of the **cyt:phen** structure and other cytosine-containing structures in the CSD sheds light on the rather flexible and versatile hydrogen bonding displayed by this compound. Hydrogen bond patterns were firstly compared with those observed in organic salts of cytosine.

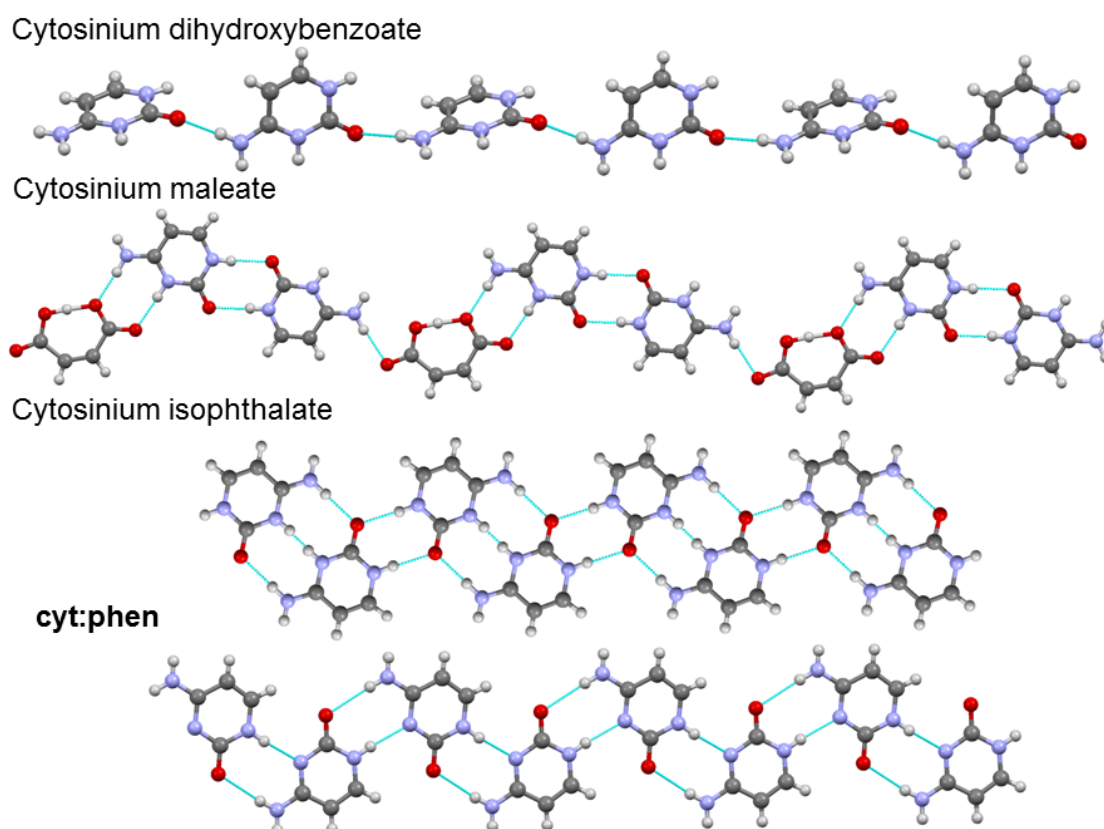
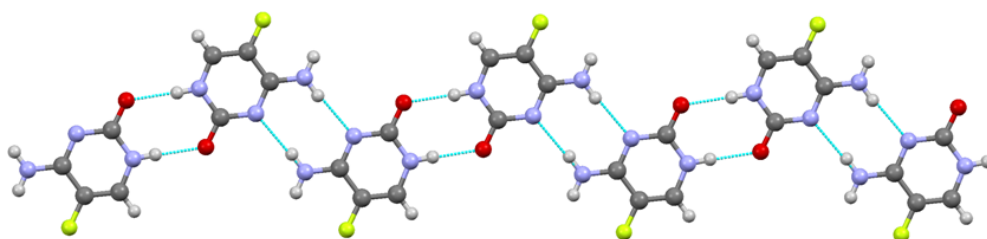


Figure 3.34: Representations of portions of crystal structures of cytosine and cytosinium compounds

It is evident from Figure 3.34 that in cytosinium dihydroxybenzoate the cytosinium cations interact with each other *via* only one hydrogen bond and the neighbouring molecules are tilted.¹³⁴ In cytosinum maleate, the cytosinium cations form pairs of hydrogen bonds which generate a $R_2^2(8)$ homosynthon.¹³⁵ In this case, the cytosinium ribbon is interrupted by the maleate anion, which forms a $R_2^2(8)$ heterosynthon with cytosinium on one side, and a single hydrogen bond on the other. Interestingly, the cytosinium ribbons in cytosinium isophthalate are held together *via* two distinct hydrogen bonding patterns. The first one is a $R_2^2(12)$ homosynthon and the second pattern is $R_2^2(8)$ homosynthon.¹³⁶ The latter is akin to the interaction observed in the **cyt:phen** structure.

Hydrogen bond patterns of **cyt:phen** were also compared to co-crystals of cytosine (or its derivatives) reported in literature and retrieved from the CSD. It was noticed that there are fewer co-crystals of cytosine or its derivatives compared to salt forms. Figure 3.35 depicts the hydrogen bonding between the reported 5-fluorocytosine:terephthalic acid and **cyt:phen**. The findings on cytosine hydrogen bonding from the present study are in agreement with the findings of da Silva and co-workers.¹³⁷

5-fluorocytosine:terephthalic acid



cyt:phen

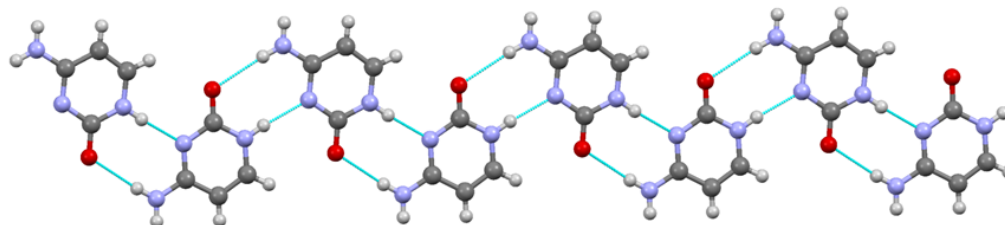
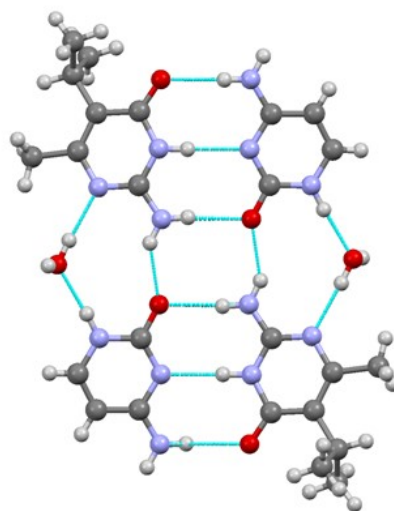


Figure 3.35: Representations of portions of crystal structures of the co-crystals 5-fluorocytosine:terephthalic acid and cyt:phen.

However, contrary to the cytosine ribbon obtained in the **cyt:phen** co-crystal, co-crystals of cytosine:5-isopropyl-6-methylisocytosine (herein referred to as co-former) display a different hydrogen bonding motif. In the structure reported by Radhakrishnan *et al.*¹³⁸ in 2014, cytosine is hydrogen bonded to the co-former *via* a similar motif to its base pairing with guanine in the DNA. It should also be noted that the G:C-like hydrogen bond between cytosine and its co-former is stabilised by hydrogen bonding to the adjacent molecules which generate a $R_4^2(8)$ heterosynthon.

Incorporation of water molecules in the crystal structure gives rise to further hydrogen bonding as shown in Figure 3.36. The water molecules act both as a hydrogen bond donor and as a hydrogen bond acceptor.

Cytosine:5-isopropyl-6-methylcytosine



cyt:phen

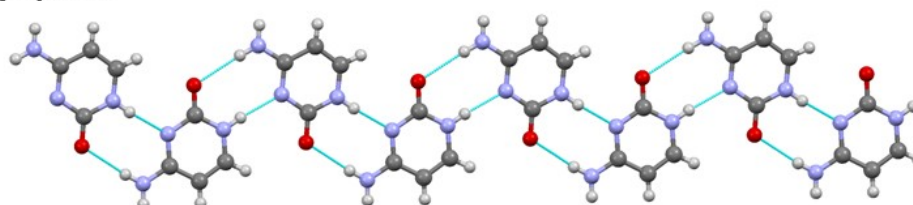


Figure 3.36: Comparison of (cyt:phen) with cytosine:5-isopropyl-6-methylisocytosine

Co-crystallisation of 5-fluorocytosine with 6-methylisocytosine (herein referred to as co-former) is perhaps the best example which demonstrates the versatility of hydrogen bonding in cytosine and its derivatives. The co-crystal isolated by Tutughamiarso and Egert¹³⁹ in 2012 displays intricate hydrogen bonding with 4 distinct motifs. As it can be seen from Figure 3.37, aside from the G:C-type hydrogen bonding between 5-fluorocytosine and its co-former, there are 3 other modes of hydrogen bonding in the structure. The $R_2^2(8)$ homosynthon between two 5-fluorocytosine molecules is analogous to the interaction observed in **cyt:phen**, whereby the ring is sustained via N—H···N and N—H···O interactions. However, the most striking feature of this structure is the formation of a large ring of hydrogen bonding which contains 46 atoms. The $R_8^6(46)$ heterosynthon between 5-fluorocytosine and its co-former leads to an open net arrangement.

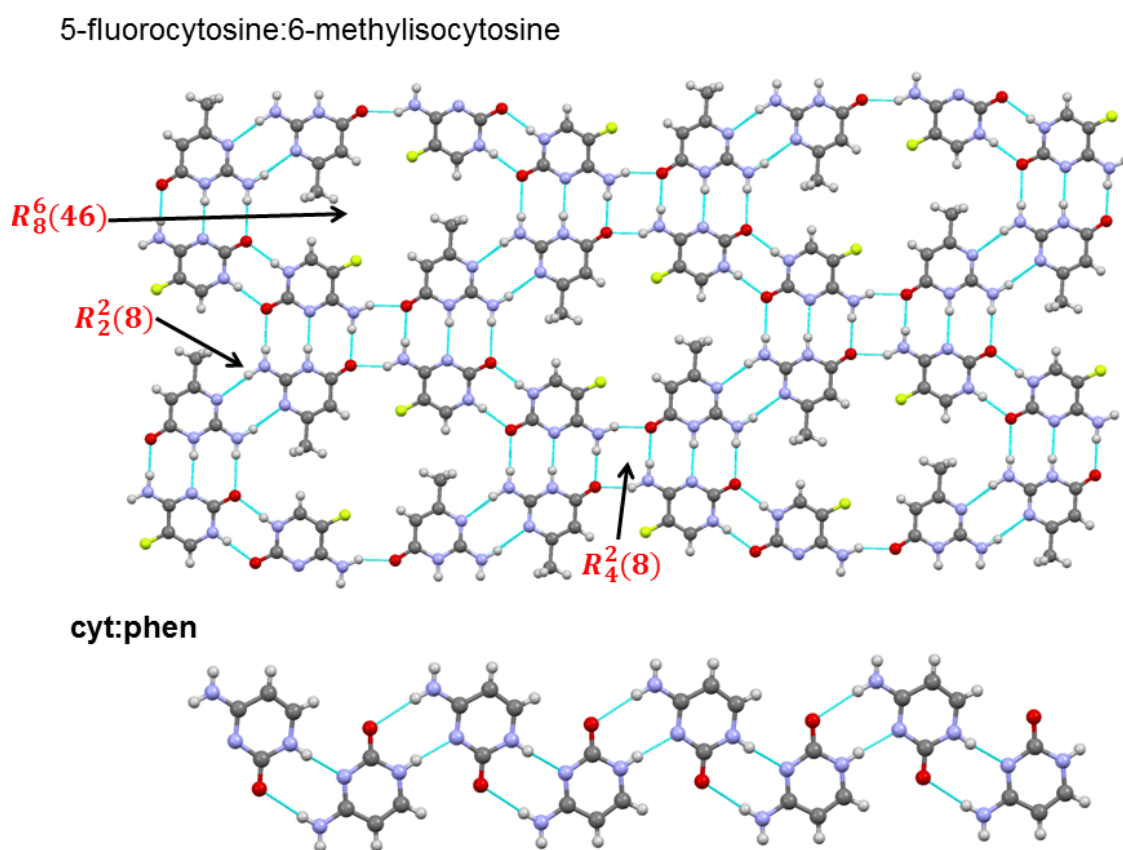


Figure 3.37: Comparison of (cyt:phen) with 5-fluorocytosine:6-methylisocytosine

3.5.3.7 Investigations on the cause of colour change

During co-crystal screening experiments *via* neat grinding, it was noticed that upon 1 h of grinding within the ball mill the samples changed colour to pink. This was an unexpected result given that both starting materials are white powders in their pure form.

A colour change to pink in **cyt:phen** upon grinding raised the question of a potential cross-contamination of the sample, but the pink colour persisted upon repeating the experiment. Inspection of milled **ade:phen**, **thy:phen** and **gua:phen** mixtures revealed that these powders remained white upon 1 h grinding. To investigate the colour change and to address its origin, further experiments were performed. Fitting of the milled powder pattern with the simulated pattern (Section 3.5.3.4) showed the presence of a single phase.

Initially, it was thought that the colour change to pink could be due to any source of contamination during the experiment. The stainless steel milling balls were suspected to be a possible source of contamination. Literature has lots of reports on the dark red powder obtained from the reaction of iron with 1,10-phenanthroline to give a $[\text{Fe}(\text{phen})_3]^{2+}$ complex known as ferriin.^{140, 141} In fact, 1,10-phenanthroline is used as a test for determination of iron content in various systems and the crystal structure of this complex in the presence of anions has been reported previously.¹⁴² The UV-spectrum of this complex has an absorption peak at *circa*. 511 – 518 nm, which is attributed to the metal-to-ligand charge transfer.¹⁴¹

Solid state UV spectroscopy was performed in order to understand whether the pink sample of **cyt:phen** is contaminated with this complex. The spectrum of the sample from 1 h neat grinding was analysed against a reference ($\text{Fe}(\text{phen})_3(\text{NCS})_2$) for comparison. In addition, a UV spectrum was also obtained from a solution of ferriin.

The results from the three UV analyses are plotted in Figure 3.38. Shown in red is the spectrum of $\text{Fe}(\text{phen})_3(\text{NCS})_2$ with the charge-transfer absorption peak occurring at

532 nm. The blue line is the spectrum of $\text{Fe}(\text{phen})_3(\text{NCS})_2$ in solution which has the absorption peak at 518 nm. The pink sample of **cyt:phen** is shown in green and its absorbs at 522 nm. All three samples absorb very close to each other in the same region. It is especially notable that the absorption of the ferrioin solution and the milled **cyt:phen** is very similar.

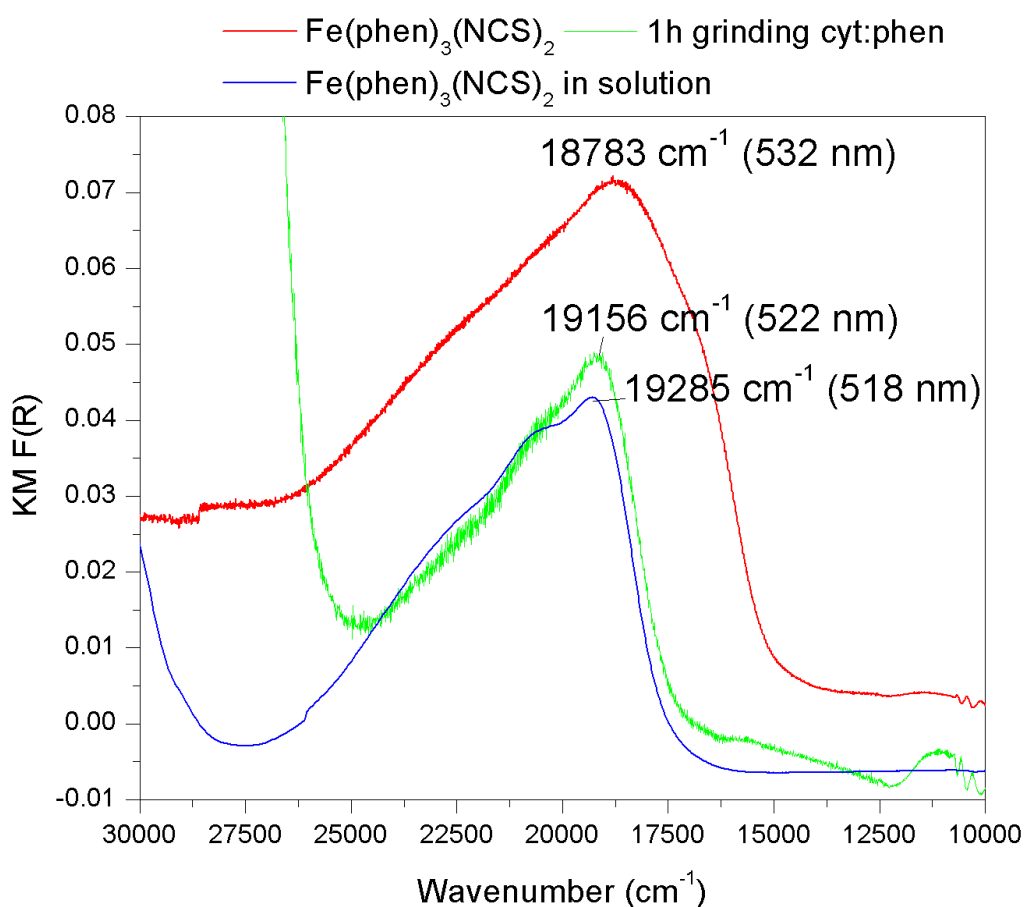


Figure 3.38: Solid state UV-Vis Spectra comparing ferrioin and cyt:phen

These results shown in Figure 3.38 demonstrate that reaction conditions during milling are sufficient for the stainless steel balls to react with mixtures that contain 1,10-phen. The other three DNA bases (adenine, guanine and thymine), which remained white upon 1 h milling with 1-phen, were investigated further. Protracted milling of these bases in the presence of 1,10-phenanthroline leads to a colour change in the sample from white to pink, which has been identified as the ferriox complex. However, in the case of **cyt:phen**, the emergence of this by-product does not interfere with structural studies, as shown by single crystal analysis.

Further analysis were performed on the the **cyt:phen** system in order to understand whether grinding outside a ball mill is associated with colour change. Grinding of cytosine and 1,10-phen for 1 h by hand in an agate pestle and mortar produces the identical phase transformation to that described for the **cyt:phen** mixture but without the emergence of a pink colouration. This result is shown in Figure 3.39.

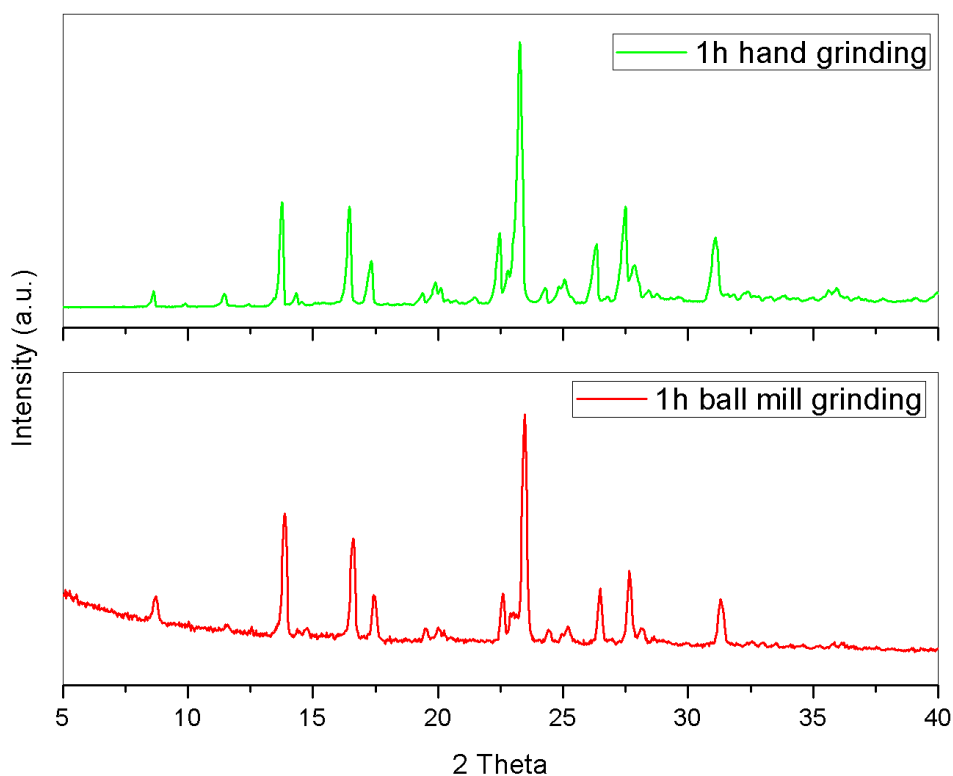


Figure 3.39: Comparison of (cyt:phen) patterns obtained from 1h hand grinding and 1h ball milling grinding

The formation of the iron-phenanthroline complex was also investigated using ICP analysis to determine iron levels in the sample. (Table 3.5)

Iron content was measured for four independent preparations:

A) milling of cytosine for 1h

B) milling of 1,10-phen for 1h

C) milling of a) and b) for further 1h together

D) gentle mixing of cytosine and 1,10-phen powder without grinding

Table 3.5: Iron content for different preparations

Independent preparations	Cytosine (1 h)	1,10-phen (1h)	Cytosine + 1,10-phen (1h)	Gentle mixing of cytosine + 1,10-phen
Fe content (ppm)	38.69	94.54	93.62	9.88

When ground separately, cytosine and 1,10-phen have different iron content levels. ICP analysis revealed that upon 1 h milling of cytosine the content of iron in the sample was 38.69 ppm and the sample had turned pale pink. The grinding of for 1,10-phen produced a pink coloured powder and subsequent ICP analysis revealed that the iron content was 94.54 ppm. When these two samples were mixed together and were further milled for 1 h, the iron content was determined to be 93.62 ppm. This sample was observed to be more intensely pink.

However, ICP results on the gently mixed cytosine and 1,10-phen (without any milling) showed that iron content was 9.88 ppm, which is remarkably lower compared to the other preparations. It should be noted that the gently mixed sample remained white.

This was also the case for the 1 h hand ground sample discussed previously. Given all these results, it can be concluded that the source of colouration emerges from the milling balls, which react with 1,10-phen to generate a ferriin complex. These findings, in conjunction with UV spectroscopy, provided sufficient evidence that the milling balls are the source of the pink colour. However, colouration does not interfere with the formation of a single phase co-crystal of **cyt:phen**, as demonstrated by X-ray powder diffraction. The large absorptivity of the ferriin complex implies that small amounts of this complex would be sufficient for the pink colour to emerge.

3.5.3.8 Critical Evaluation of Lee and Wang's Paper

During the CSD search for cytosine co-crystals, a wide variety of reported structures were studied and compared to the **cyt:phen** structure presented in this thesis. The paper of Lee and Wang¹²⁶ was one of the papers reviewed as part of this CSD search. However, closer examination of the structures contained therein revealed shortcomings in the original structure analysis. The key structural point is the existence of a $R_2^2(12)$ homosynthon between two cytosine molecules as shown in Figure 3.40. This was unexpected and close analysis shows it is incorrect.

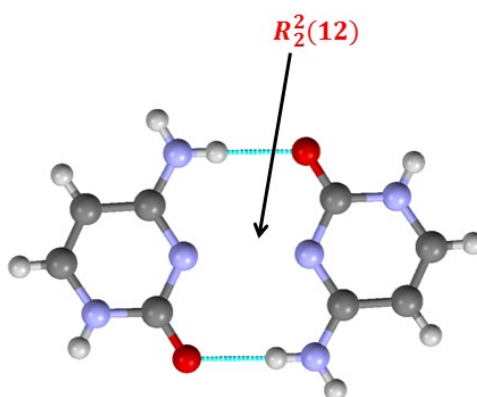


Figure 3.40: Unexpected homosynthon in cytosine systems

This section provides a critical analysis and evaluation of the results presented by Lee and Wang and addresses the flaws in structure determination. In this paper, the behaviour of cytosine with oxalic, malonic and succinic acid was studied. The multicomponent crystals obtained from the reaction of cytosine with these three dicarboxylic acids were assigned to be co-crystals. However, meticulous analysis of the structures reveals that this assignment is incorrect and does not yield sensible hydrogen bonding motifs.

Inspection of the monohydrate form of cytosine and oxalic acid reveals the presence of dubious hydrogen bonding between oxalic acid and water. Here, oxalic acid lies on a 2-fold rotation axis and the rest of the molecule is generated by symmetry. Inspection of the C—O distances in the carboxylic reveals that the difference between the two is 0.006 Å. According to Childs *et al.*⁸⁵, in structures which display a similarity in C—O bond lengths ($\Delta D_{C-O} < 0.03$ Å) the acid group is deprotonated indicating proton transfer to the base. Proton transfer manifests itself by increasing the internal angle of the endocyclic nitrogen at the site of protonation. Indeed, inspection of C5-N4-C8 and C1-N1-C2 bond lengths in cytosine shows that the angle is 121.77(3)° and 121.75(3)°, respectively. These values are very close to the angle in the protonated endocyclic nitrogen in cytosine which is 122.2(4)° and 122.1(4)°. These readings provide strong evidence of proton transfer from the acid to the base, which has not been accounted for by the researchers. This explains the incorrect hydrogen bonding between the oxalic acid and the water molecule, wherein two hydrogen atoms are in close proximity as shown in Figure 3.41.

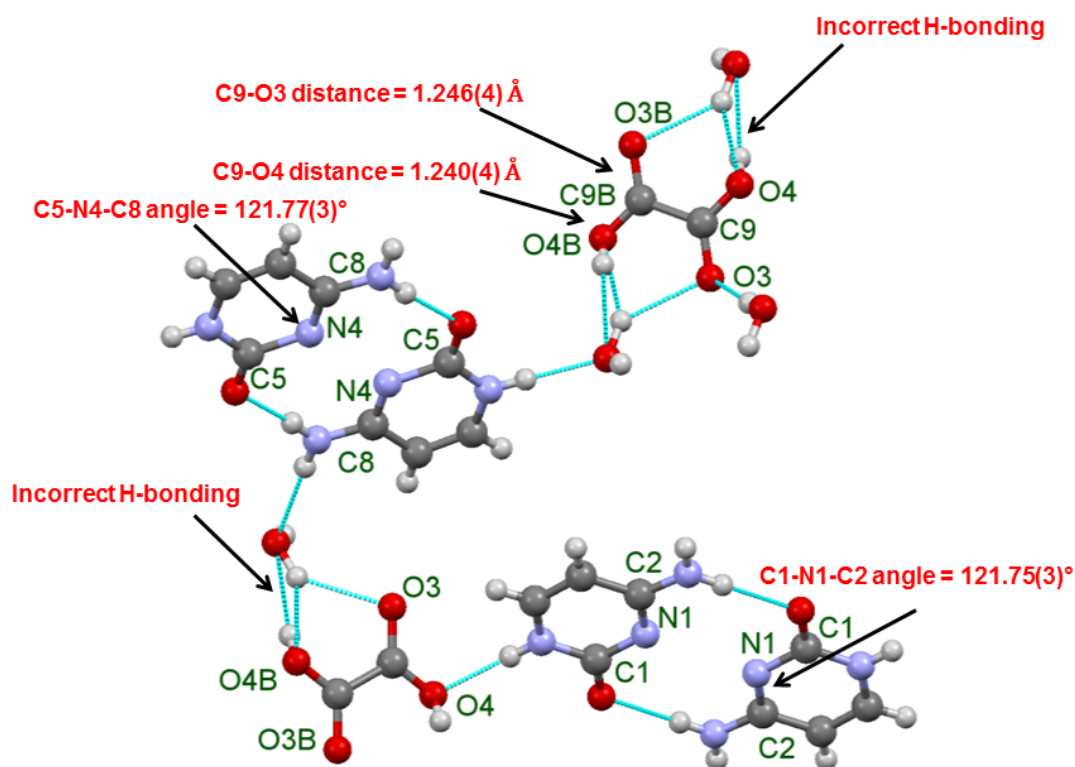


Figure 3.41: Hydrogen bonding and selected bond angles and distances in Lee and Wang's paper for cytosine and oxalic acid

The dimer obtained between two cytosine molecules is a result of the incorrect assignment of the proton position. Perumalla *et al.*¹⁴³ reported the existence of a cytosine:cytosinium duplex with triple hydrogen bonding where one of the cytosine moieties protonated. Protonation of cytosine in the structure of Lee and Wang would lead to such cytosine:cytosinium duplex and would be the correct depiction of the crystal which is a salt. Perumalla *et al.*¹⁴³ have correctly determined that cytosine and oxalic acid yield a salt. The same argumentation applies for the multicomponent crystal of cytosine with malonic acid. The third structure studied by Lee and Wang was that of cytosine with succinic acid.

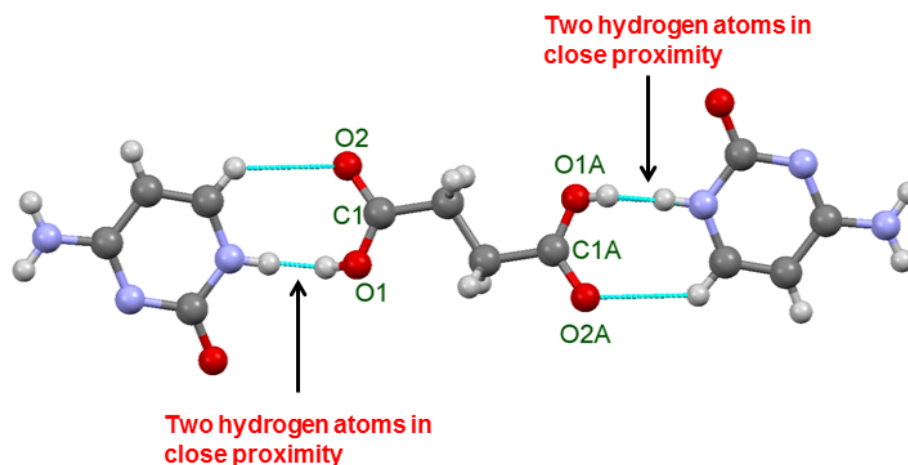


Figure 3.42: Incorrect assignment of proton location

Lee and Wang reported the existence of a heterosynthon between cytosine and succinic acid as shown in Figure 3.42. However, in this heterosynthon the hydrogen atom from cytosine and the one from succinic acid are in close proximity. This interaction is of the form D—H···H—A, which is unfavourable due to repulsion from the two hydrogens. Furthermore, it does not obey the rule of sharing one proton between the donor and the acceptor as stipulated by the definition for hydrogen bonding.³⁰ The reporting of this interaction in the structure is as a result of the incorrect assignment of the proton location. The multicomponent crystal in question is not a co-crystal but it is a salt. In this example, the difference in C—O distances is 0.54 Å, which once again lies between the 0.03 Å and 0.08 Å thresholds and therefore it is unclear whether salt or co-crystal has formed.

However, examination of internal nitrogen bond angles in cytosine C3-N1-C4 shows that the value is 121.67(15)°, which is similar to the 122.08(15)° of the other nitrogen in cytosine which is protonated. Values of this range are a characteristic of protonated nitrogen atoms in cytosine.^{136, 137, 144} In summary, all three structures reported in this paper are salts and not co-crystals. Identifying the structures as co-crystals explains the emergence of dubious hydrogen bonding.

3.6 Structure of Melaminium Nitrilotriacetate Trihydrate

3.6.1 Introduction

Melamine is an organic base which displays a pronounced tendency to form hydrogen-bonded architectures in combination with carboxylic acids. Many of these systems exhibit common structural features. In most cases, crystallisation of melamine with carboxylic acids leads to salt formation. This is associated with full proton transfer to form melaminium cations. These cations then interact with each other *via* hydrogen-bonding to form tapes composed of N—H \cdots N hydrogen bonds. The tapes have a tendency to assemble into π -stacks. Figure 3.43 shows the carboxylate group of terephthalic acid which forms a $R_2^2(8)$ with the melamine at the site of protonation.¹⁴⁵

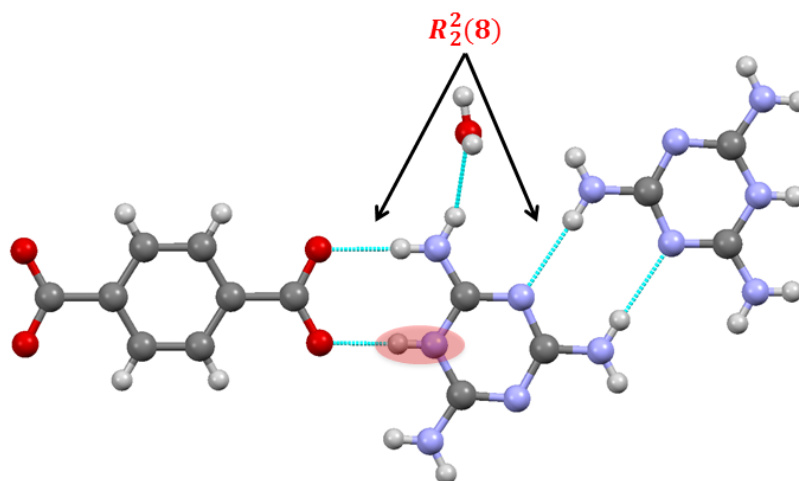


Figure 3.43: Illustration of hydrogen bonding in melamine salts. N—H \cdots N hydrogen bonds between melaminium cations and carboxylate:melaminium heterosynthon form $R_2^2(8)$. Site of melamine protonation is highlighted in pink

A wide range of organic salts of melamine are reported in the CSD. These include simple alkyl chain carboxylic acids¹⁴⁶ and dicarboxylic acids.^{147, 148} Melamine has also been successfully co-crystallised with phthalimide.^{149, 150} A particularly interesting structure is the one of melamine with phthalimide.

In this structure melamine uses its hydrogen bonding capacity fully by forming the maximum of nine hydrogen bonds. (Figure 3.44) This is not usually the case when

melamine interacts with carboxylic acids. The arrangement shown in Figure 3.44 is forms a planar sheet and the two molecules in the different sheets interact *via* π - π interactions in this way forming a stacked geometry.

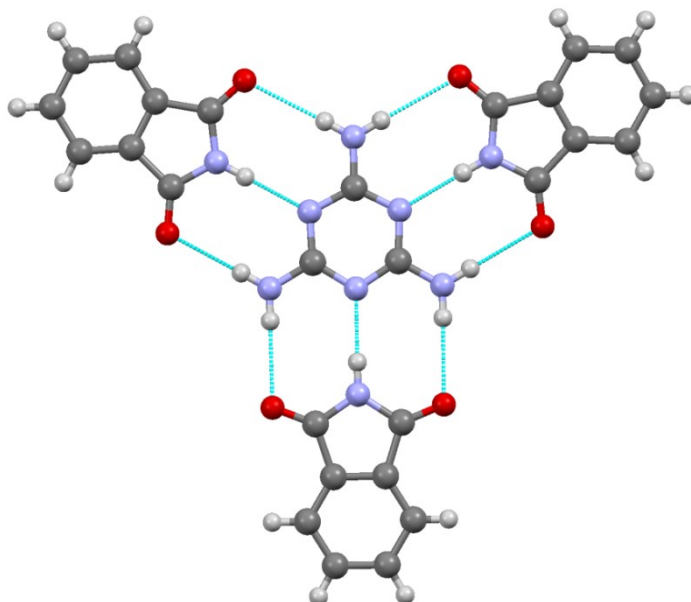


Figure 3.44: Melamine using all of its hydrogen bonding sites with phthalimide

While the interaction of melamine with monocarboxylic and dicarboxylic acids has been widely studied, a CSD survey revealed that tricarboxylic acid systems of this base are somewhat understudied. The objective of this study is to explore the effect of introducing multiple carboxylic acid groups with a flexible geometry. Nitrilotriacetic acid (**nta**) shown in Figure 3.45 was selected as a suitable acid for the study.

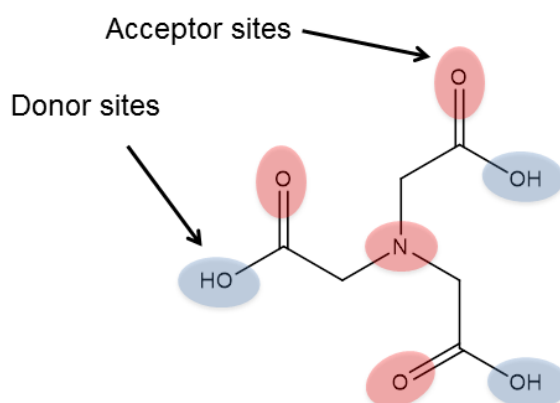


Figure 3.45: Structure and hydrogen bond functionality of NTA

3.6.2 Experimental

3.6.2.1 Single Crystal Preparation

Melamine (0.032g, 0.25 mmol) and nitrilotriacetic acid (0.048g, 0.25 mmol) were dissolved in 50:50 ethanol:water (20 mL) and stirred for 15 min. The solution was left unperturbed for slow solvent evaporation in suitably sized vials. After approximately 2-3 days, white needle-shaped crystals suitable for single crystal X-ray were isolated.

3.6.2.2 Single Crystal X-ray Diffraction Measurements

The crystal examined was found to be twinned by a 2-fold rotation about [100]. Two domains were identified from the diffraction data and both were used for integration. The structure was refined using all observed data using the HKLF5 formalism within *SHELXL97*. The relative amount of the two components was refined to be 0.5918: 0.4082 (14). Diffraction data were of reasonable quality to allow the location of hydrogen atoms in the structure using difference Fourier map.

3.6.2.3 TGA Study

The thermogravimetric data were collected using a Mettler Toledo TGA/DSC 1 instrument. Samples were loaded in 70 μ L alumina pans and heated at a ramp rate of 10 $^{\circ}$ C/min under a flow of nitrogen gas.

3.6.2.4 IR Spectroscopy

FT-IR spectra were collected from samples prepared as KBr disks (1:20 dilution) using a Perkin Elmer FT-IR Spectrometer Spectrum RX1.

3.6.3 Results and Discussion

3.6.3.1 Structure of Melaminium Nitrilotriacetate Trihydrate, $(\text{MH}^+)_2\text{nta}^{2-}\cdot 3\text{H}_2\text{O}$

$(\text{MH}^+)_2\text{nta}^{2-}\cdot 3\text{H}_2\text{O}$ crystallises in the triclinic space group $P\bar{1}$. The asymmetric unit shown in Figure 3.46 contains two crystallographically independent melaminium cations, the nitrilotriacetate anion and three crystallisation water molecules.¹⁵¹ The assignment of hydrogen bonding between different components was greatly facilitated by the identification of hydrogen atoms with final difference Fourier maps.

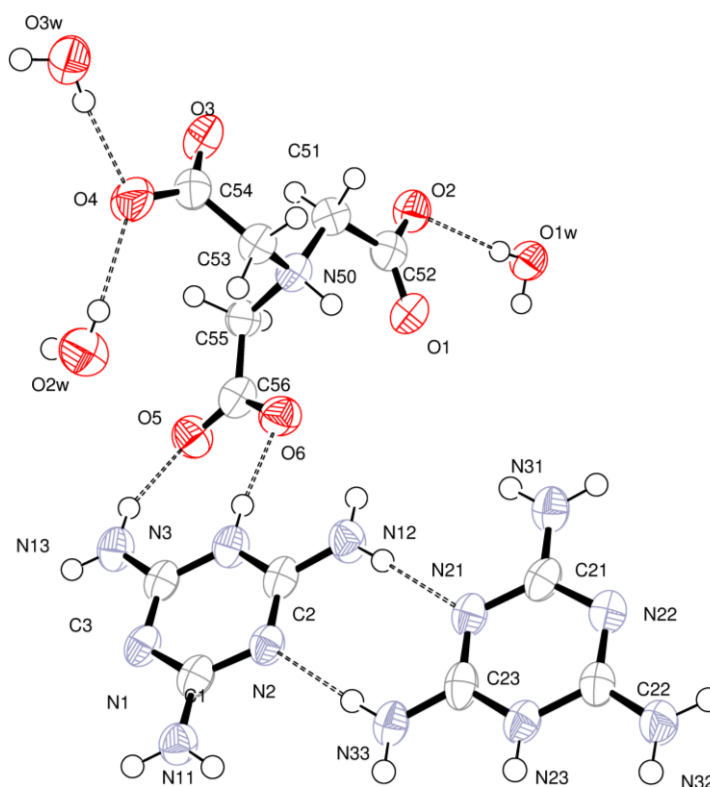


Figure 3.46: Asymmetric unit of $(\text{MH}^+)_2\text{nta}^{2-}\cdot 3\text{H}_2\text{O}$ with atoms drawn as 70% probability ellipsoids. Dashed lines represent hydrogen bonds.

Inspection of hydrogen atom locations reveals that crystallisation of this compound is associated with proton migration from acid to the base. The **nta** in the structure is triply deprotonated. Two carboxylic protons migrate to one of the endocyclic N atoms in each melamine generating two melaminium cations. In addition, there is an internal proton

transfer from the third carboxylic acid with the proton migrating to the central nitrogen in the **nta** moiety to generate the nitrilotriacetate zwitterion.

The two melaminium cations form hydrogen bonded tapes sustained by N—H···N interactions. This is a very common form of interaction with many other similar compounds. Pairs of N—H···N interactions between adjacent melaminium cations form embraces with graph set notation $R_2^2(8)$. There are two symmetry independent embraces of this type which assemble the melaminium cations into tapes that extend parallel to the crystallographic [010] direction as shown in Figure 3.47. These tapes are stacked parallel to the *a*-axis at a mean separation of $a/2$ (3.3559 (11) Å) and centroid to centroid separation 3.6230 (13) Å suggestive of π -stacking.

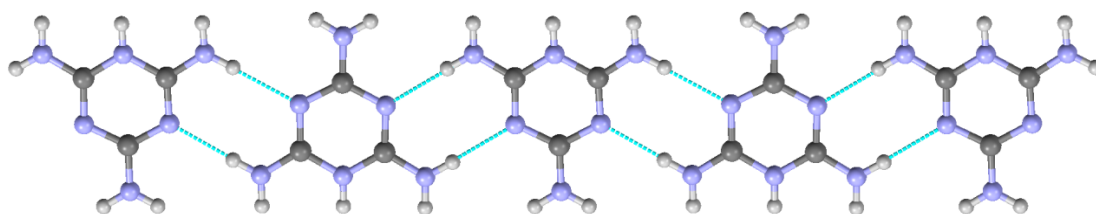


Figure 3.47: Infinite melaminium tapes held together by N—H(ammine)···N(endocyclic) hydrogen bonds

Melaminium tapes are stabilised by the nitrilotriacetate anions and the three water molecules. Each carboxylate acts as a hydrogen bond acceptor to amine groups of the melaminium cations. In this way the anions are involved in N—H···O hydrogen bonds between different cation tapes within the same stack and between different stacks. Water molecules provide further stabilisation and help knit together the cations and the anions. The interaction of O1W with the anions is particularly noteworthy as it plays a key role in crystal packing. It acts as a hydrogen bond donor and form O—H(water)···O(carboxylate) hydrogen bonds along the *a*-axis. Such interaction generates a $R_4^4(10)$ heterosynthon and it interconnects adjacent anions. The O···O distance is 2.856 (4) and the O—H···O angle is 172 (4)°. The interaction can be viewed in Figure 3.48.

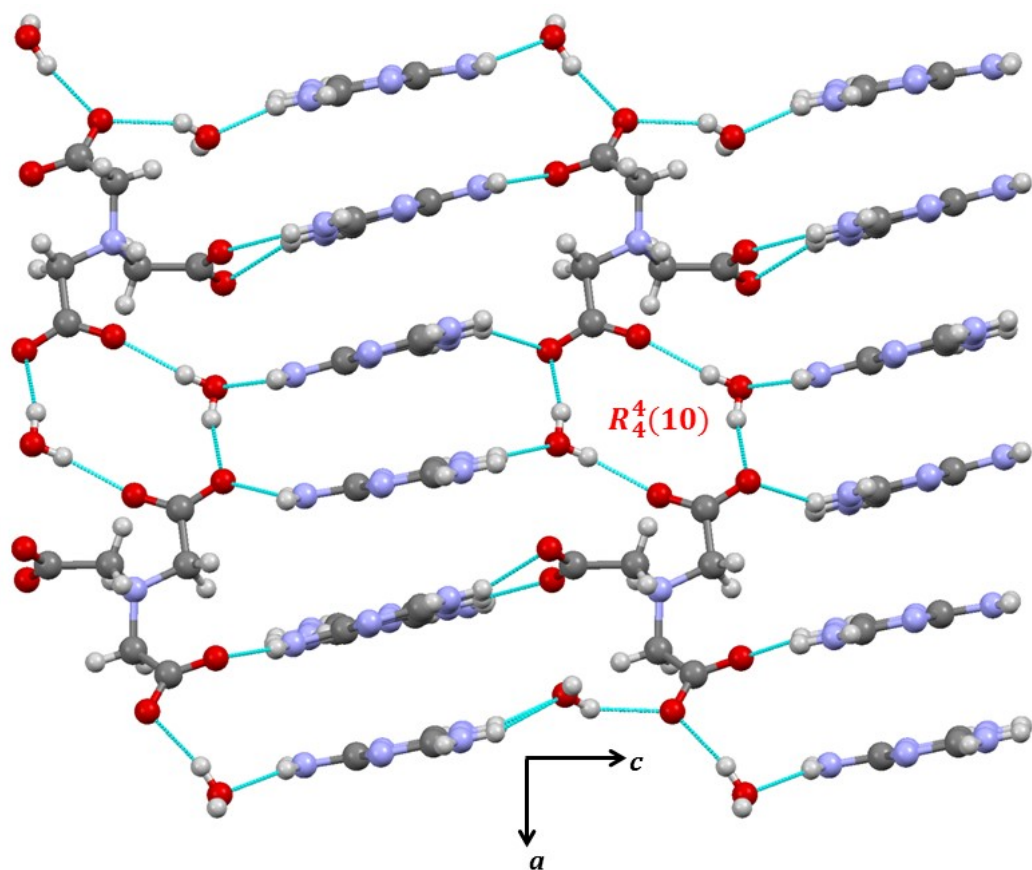


Figure 3.48: Stabilisation of the structure via $R_4^4(10)$ heterosynthon between adjacent anions and O3W

Table 3.6: Selected hydrogen bond parameters

D-H	A	d (D-H)/ (Å)	d (H···A) (Å)	d (D···A) (Å)	<D-H···A (°)
N3—H3	O5	0.88	2.6	3.296 (4)	136
N3—H3	O6	0.88	1.82	2.684(4)	166
N11—H11A	O3 ⁱ	0.88	2.18	3.042(4)	166
N11—H11B	O1W ⁱⁱ	0.88	2.13	2.989(4)	164
N12—H12A	N21	0.88	2.04	2.915(4)	174
N12—H12B	O2 ⁱⁱⁱ	0.88	2.25	2.904(4)	131
N12—H12B	O6	0.88	2.58	3.26(4)	135
N13—H13A	N22 ^{iv}	0.88	2.13	3.012(4)	176
N13—H13B	O5	0.88	2.03	2.87(4)	159
N23—H23	O2W ^v	0.88	1.94	2.793(4)	164
N31—H31A	O3W ^{vi}	0.88	2.06	2.87(4)	153
N31—H31B	O2 ⁱⁱⁱ	0.88	2.22	3.048(4)	157
N32—H32A	N1 ^{vii}	0.88	2.06	2.933(4)	173
N32—H32B	O3 ^{viii}	0.88	2.11	2.817(4)	137
N33—H33A	N2	0.88	2.09	2.973(4)	177
N33—H33B	O1W ⁱⁱ	0.88	2.19	2.85(4)	132
N50—H50	O1 ⁱⁱⁱ	0.93	2.28	2.969(4)	130
C55—H55A	O4 ^{ix}	0.99	2.55	3.47(5)	154
O1W—H1AW	O1 ^x	0.84(2)	2.02(2)	2.856(4)	172(4)
O1W—H1BW	O2	0.84(2)	1.98(3)	2.775(3)	157(4)
O2W—H2AW	O3 ^{xi}	0.83(2)	2.57(3)	3.265(4)	143(4)
O2W—H2AW	O4 ^{xi}	0.83(2)	2.38(3)	3.168(4)	159(4)
O2W—H2BW	O4	0.81(2)	2.08(2)	2.812(4)	150(4)
O3W—H3AW	O4	0.84(2)	1.95(3)	2.768(4)	163(4)
O3W—H3BW	O5 ^{xi}	0.83(2)	1.96(3)	2.773(4)	165(4)

ⁱ [x, y, z-1]; ⁱⁱ [x+1, y, z-1]; ⁱⁱⁱ [-x+1, -y+1, -z+1]; ^{iv} [x, y-1, z]; ^v [-x+2, -y+1, -z]; ^{vi} [-x+2, -y+1, -z+1]; ^{vii} [x, y+1, z]; ^{viii} [x, y+1, z-1]; ^{ix} [x, y, z+1]; ^x [x-1, y, z]; ^{xi} [-x, -y+1, -z+1]; ^{xii} [-x+2, -y, -z+1]

3.6.3.1 Proton transfer and its structural implications

The pK_a difference* between melamine and **nta** was calculated as 2.07. This value falls within the range which Child *et al.*⁸⁵ called the region of continuum between salts and co-crystals. Therefore, it was not straightforward to predict whether proton transfer would take place in this system. After successful structure solution and acceptable refinement the structure was examined for proton transfer. Indeed, there is strong evidence that proton transfer has occurred and that the obtained molecular crystal is a salt rather than a co-crystal.

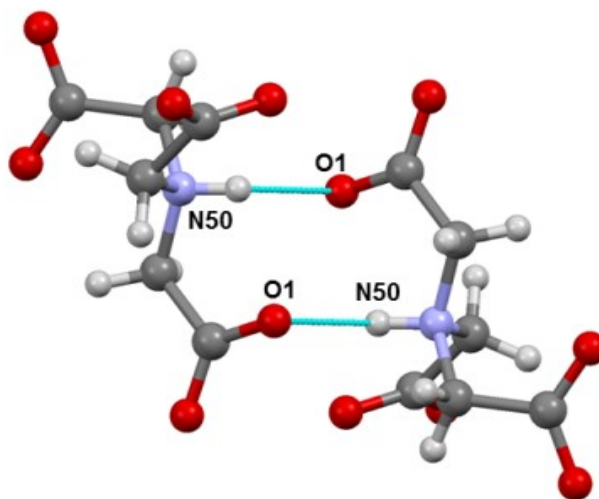


Figure 3.49: Anion-anion interaction via N—H...O hydrogen bonds

The zwitterion formed from the internal protonation in **nta** interacts *via* hydrogen bonding with itself *via* $-x + 1, -y + 1, -z + 1$ symmetry operator. The two anions interact with each other directly *via* N50—H50...O1 hydrogen bonds where N...O is 2.969(4) and the angle is 130° as shown in Figure 3.49 and Table 3.6. The relatively close approach of N50 and O1 suggests there is a proton present here. This was assigned from a difference map.

Inspection of the acid groups in **nta** revealed that all three of these groups have been deprotonated. The assignment of the carboxylates is consistent with the work of Childs *et al.*⁸⁵ who noted that a similarity in C—O bond lengths ($\Delta D_{C-O} < 0.03 \text{ \AA}$) is indicative of carboxylate rather than carboxylic acid. It was found that the C—O bond length difference satisfies the general rule presented by Childs *et al.*⁸⁵ for determining salt formation. For the three COO groups in the anion, the mean C—O bond length is 1.253 (3) \AA , but the deviations from equal values for the three pairs of C—O distances are 0.02, 0.008 and 0.003 \AA . These values are tabulated in Table 3.7.

Table 3.7: Carboxylate bond lengths and the difference in C-O for nitrilotriacetic acid

Carboxylate Bonds Involved	Bond Length / (\AA)	ΔD_{C-O} / (\AA)
C52 - O1	1.247(3)	0.02
C52 - O2	1.267(3)	
C54 - O3	1.247(3)	0.008
C54 - O4	1.255(3)	
C56 - O5	1.251(3)	0.003
C56 - O6	1.249(3)	

*please see Section 3.3.1 for the definition

Figure 3.50 shows the $R_2^2(8)$ heterosynthon between the cation and the anion. The proton fully resides on the base and the H3...O6 distance is 1.82 \AA . Despite being triply deprotonated there is only one symmetry unique cation-anion heterosynthon. The anion forms a heterosynthon with the first melaminium cation *via* N3—H3...O6 and N13—H13B...O5. The second melaminium cation does not form a $R_2^2(8)$ embrace at the site of protonation. Instead, it interacts with a water molecules *via* N23—H23...O2W hydrogen bond.

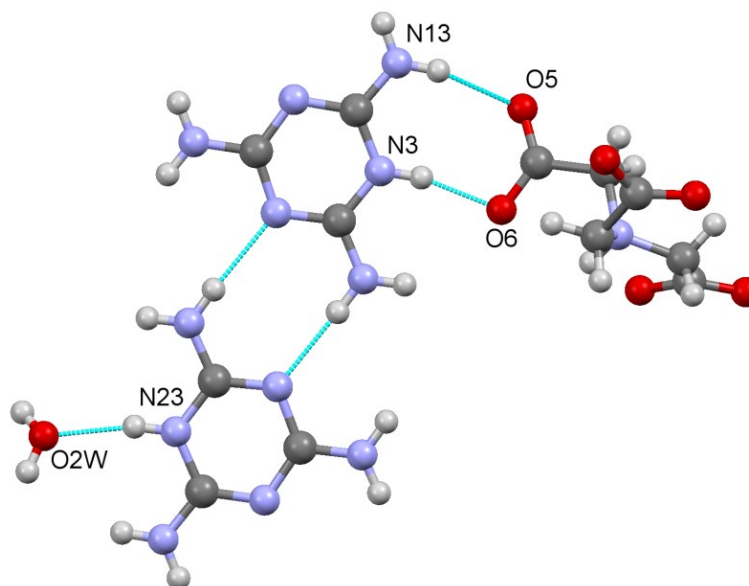


Figure 3.50: Carboxylate-melaminium interaction at the site of protonation

Further evidence for proton transfer can also be obtained by examining the bond angles at the site of protonation of both melaminium cations. There is a marked bond angle increase in the aromatic ring at the protonated nitrogen compared to the unprotonated endocyclic nitrogen atoms. These results are in agreement with the findings of Hingerty *et al.*⁹² who reported an increase in bond angle at the endocyclic nitrogen atoms upon protonation.

At the protonated N atoms of the triazine ring, the bond angles are 119.1 (2) and 119.3(2)° compared with the other C—N—C bond angles which have a mean of 115.8 (2) °. Fourier maps were also used to ensure correct assignment of hydrogen atoms in the structure. Figure 3.52 and Figure 3.53 depict the Fourier maps for the two symmetry independent cations.

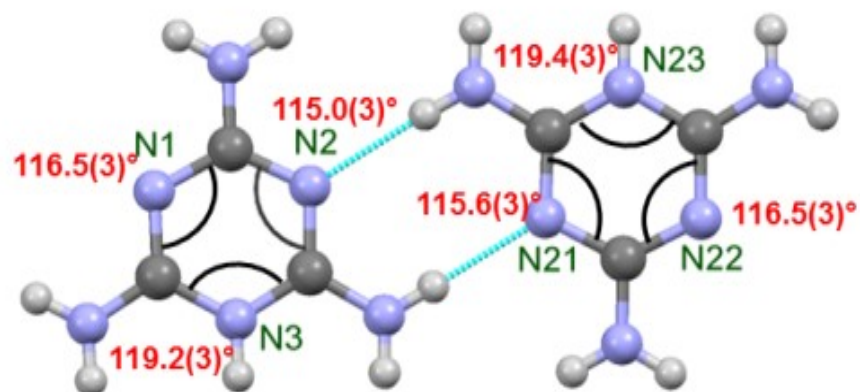


Figure 3.51: Comparison of C—N—C bond angles in the triazine ring

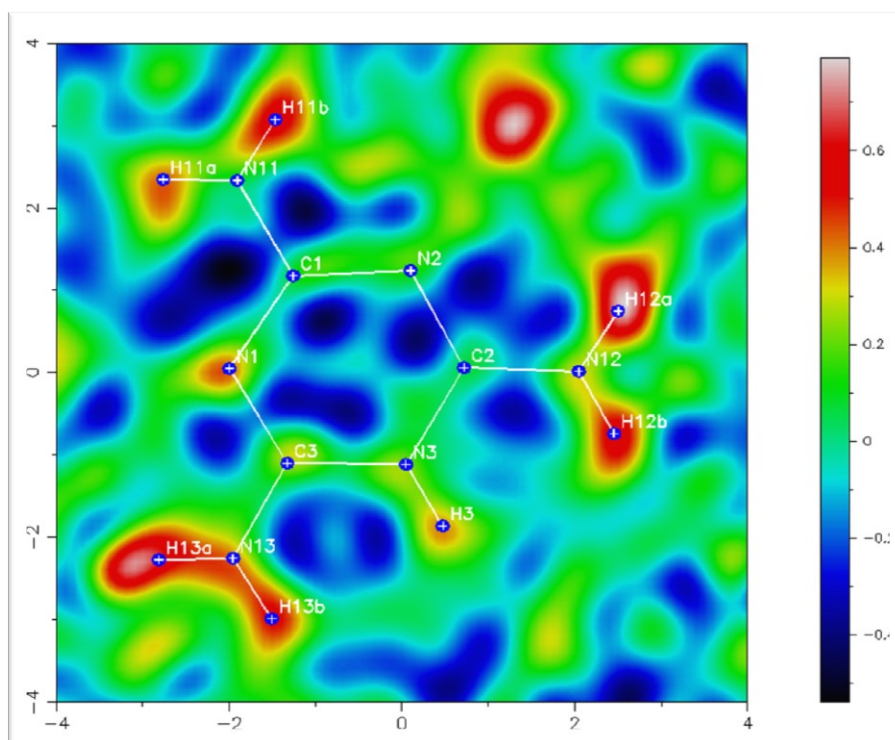


Figure 3.52: Fourier map showing the protonation of the first melamine moiety

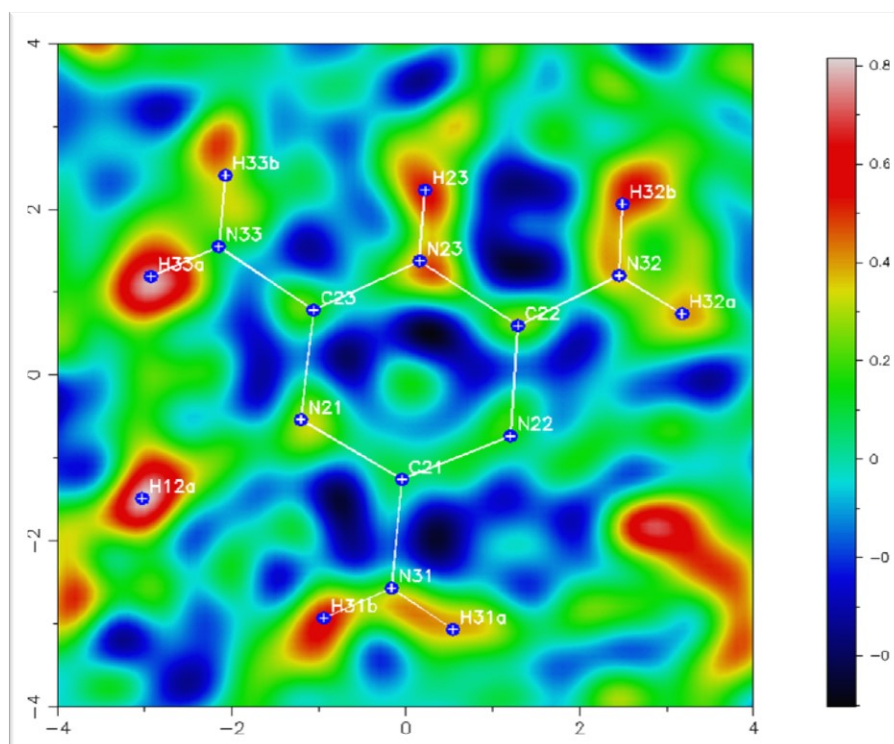


Figure 3.53: Fourier maps showing the protonation of the second melamine moiety

3.6.3.2 Confirmation of salt formation *via* IR Spectroscopy

IR spectroscopy has shown great potential in the identifying whether the multicomponent crystal is a salt or a co-crystal.¹⁵² Figure 3.54 shows the IR spectrum of $(\text{MH}^+)_2\text{nta}^{2-}\cdot 3\text{H}_2\text{O}$ and **nta**. Examination of the IR spectrum of $(\text{MH}^+)_2\text{nta}^{2-}\cdot 3\text{H}_2\text{O}$ (shown in green) reveals the presence of stretching frequencies in the region $1365 - 1615 \text{ cm}^{-1}$ which are characteristic of carboxylate anion.⁷⁷ The bands at $1370 - 1430 \text{ cm}^{-1}$ are characteristic of a symmetric COO^- stretching, whereas bands in the region $1540 - 1655 \text{ cm}^{-1}$ correspond to symmetric COO^- stretching. The band at 1722 cm^{-1} for **nta** is characteristic of carboxylic acids. A similar band appears in the spectrum of $(\text{MH}^+)_2\text{nta}^{2-}\cdot 3\text{H}_2\text{O}$ too. However, emergence of extra features in the region $1495 - 1680 \text{ cm}^{-1}$ demonstrates deprotonation of **nta**. These results are in agreement with single crystal analysis (protonation of two melamine moieties and an internal protonation of **nta**). Furthermore, C—O bond lengths in all three acid groups are 0.02, 0.008 and 0.003 Å, which fall within the threshold of salt formation and further confirms triple deprotonation.

The band at 3375 cm^{-1} arises due to NH_2 symmetric stretching from melamine, whereas the band appearing at 1611 cm^{-1} is attributed NH deformation of primary amines such as melamine.¹⁵³ The strong absorption at 1270 – 1337 cm^{-1} corresponds to the aromatic C—N stretching of melaminium.

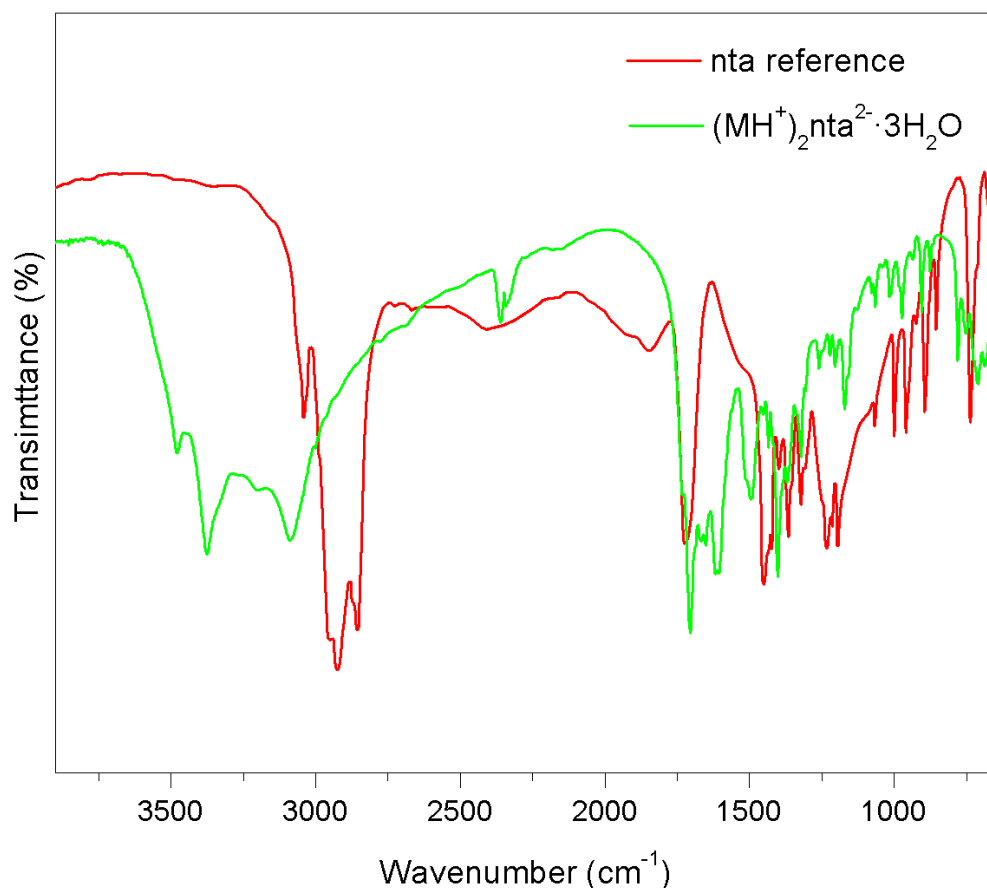


Figure 3.54: IR Spectrum of $(\text{MH}^+)_2\text{nta}^{2-}\cdot 3\text{H}_2\text{O}$

Table 3.8: Characteristic IR absorption for $(\text{MH}^+)_2\text{nta}^{2-}\cdot 3\text{H}_2\text{O}$

Functional Group	ν (cm^{-1})	Intensity
C—O	1365 – 1615	Medium, sharp
NH_2	3375	Medium, broad
N—H	1611	Strong, sharp
C—N	1270 – 1337	Medium, sharp

3.6.3.3 Thermal behaviour

The thermal behaviour of the crystal was investigated using thermogravimetric analysis. Inspection of the thermogram in Figure 3.55 reveals that the loss of water happens in an ill-defined manner. Water loss begins at 40° C and all the water is driven off *circa* 145 °C. The loss of one water molecule corresponds to 3.62% of the total sample weight, shown in pink dashed lines. However, it is evident from the thermogram that the first water molecule is lost without a clear step corresponding to weight loss. Figure 3.55 shows that at 135 °C there is a 7.25% weight loss (green dashed lines) and this corresponds to the loss of two water molecules. The loss of the third water molecules is expected at *circa* 142.5 °C, where the total weight loss would be 10.88%. It is clear from the thermogram that such loss takes place at a slightly higher temperature and all three water molecules are lost by 145 °C. At 230 °C the total weight loss is 19.3% but this could not be assigned to any moiety in the structure and upon heating above 230 °C the material starts to decompose.

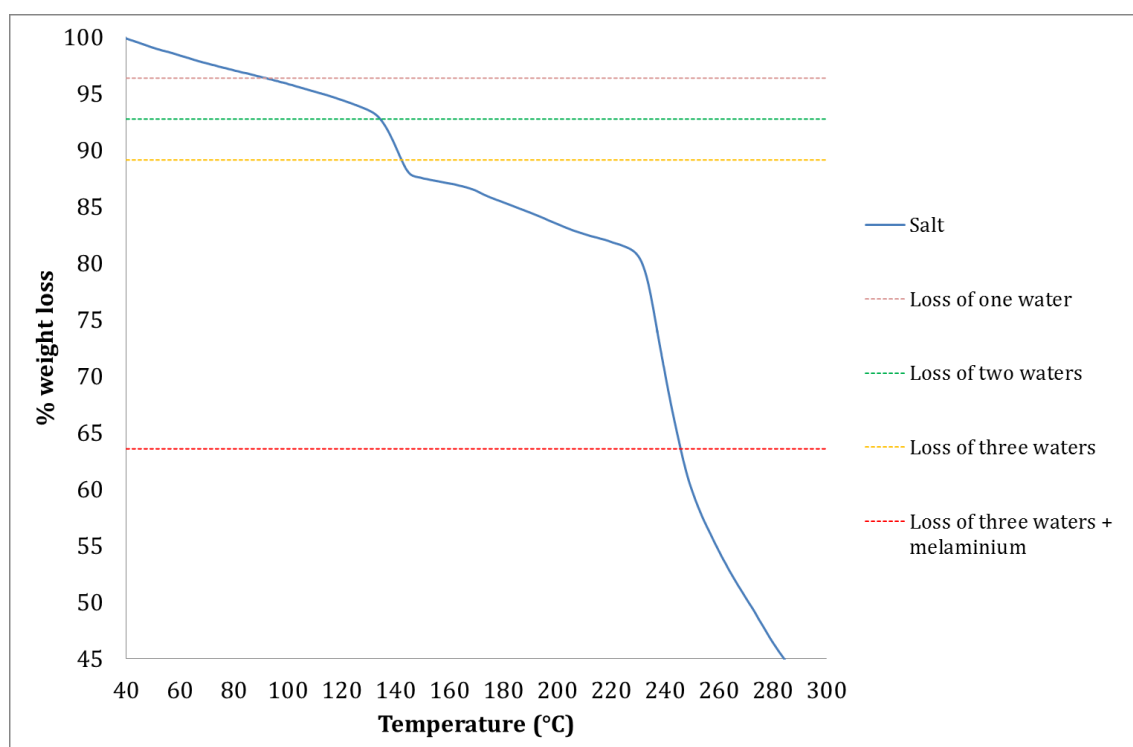
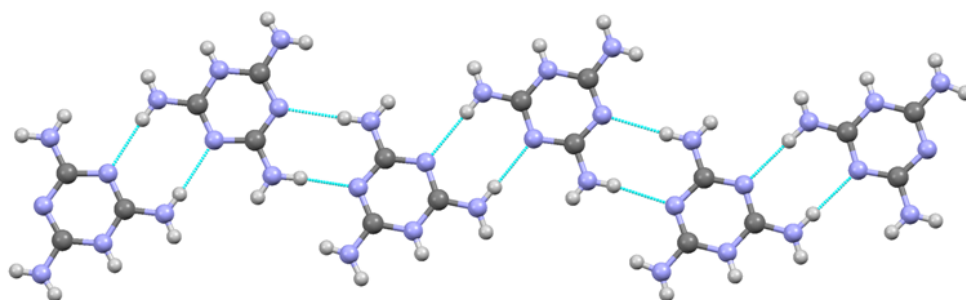


Figure 3.55: Thermogram of melaminium nitrilotriacetate trihydrate

3.6.3.4 Relationship to other melamine salts with tricabroxylic acids

The Cambridge Structural Database¹³ (CSD version 5.35, November 2013) was searched for similar compounds of melamine with tricarboxylic acids in order to compare their hydrogen bonding motifs with our structure. A particularly interesting example is the crystallisation of melamine with Kemp's acid as reported by Huczynski and co-workers.¹⁵⁴ In this structure, four crystallographically independent melaminium cations interact with each other *via* N—H···N hydrogen bonds, which is similar to what is observed in our case. However, the interaction of the cations in Huczynski's structure does not resemble the tapes formed in our crystal. Instead, the cations form zig-zag chains as shown in Figure 3.56.

Melaminium salt with Kemp's acid



Melaminium nitrilotriacetate trihydrate

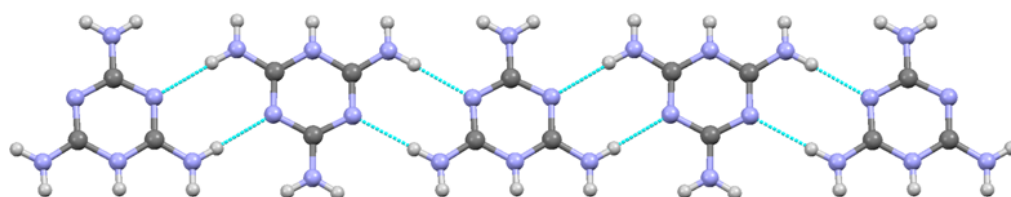


Figure 3.56: Comparison of cation interactions between two salts

Another notable difference between these two structures is the cation-anion interaction at the site of protonation. In the structure reported by Huczynski, three of the cations form a $R_2^2(8)$ dimer with the carboxylate group at the site of N atom protonation, whereas the fourth melaminium forms a N—H···O interaction with a water molecule. This is different

from our crystal because only one melaminium is hydrogen bonded to the anion forming a $R_2^2(8)$. The second symmetry independent melaminium does not form such embrace with the anion. It should also be noted that the melaminium tape observed in $(MH^+)_2nta^{2-}\cdot 3H_2O$ is the predominant set up in melaminium salts.

3.7 The missing carboxylic acid dimer due to competing hydrogen bonds in thymine acetic acid dihydrate

3.7.1 Introduction

During the research conducted for growing hydrogen-bonded networks of DNA bases or its derivatives, thymine acetic acid (**tac**) was used as a ligand. During these complexation reactions, white needle-shaped crystals were isolated as a by-product of the reaction. These crystals were studied *via* single crystal X-ray diffraction and subsequent structure solution revealed the emergence of a novel hydrate of **tac**. The molecule of **tac** contains the pyrimidine ring of thymine and the carboxylic acid functional group. Since the presence of this functional group in conjunction with the Watson-Crick³⁵ or Hoogsteen³⁶ could lead to intriguing architectures, this structure was explored further.

Despite being a commonly occurring synthon, the carboxylic acid dimer has been known to be absent in structures where crystal engineering would predict otherwise and a classic example is that of cubanecarboxylic acids.⁴⁵ These systems display a different type of carboxylic acid-carboxylic acid interaction in the solid state. This interaction is known as the carboxylic catemer and it replaces the commonly occurring carboxylic acid dimer. The carboxylic catemer interferes with the formation of the carboxylic acid dimer due to the involvement of C—H \cdots O hydrogen bonds.

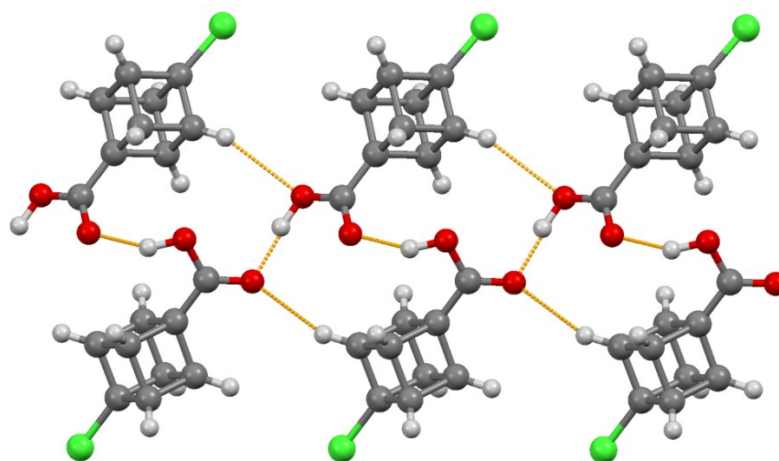


Figure 3.57: Hydrogen bonding motifs in 4-chlorocubanecarboxylic acid. The catemer inhibits the formation of the carboxylic acid dimer

Substituents such as carboxylic acids can add to the complexity of hydrogen bonding displayed by DNA and RNA bases.¹⁵⁵ Anhydrous and hydrated forms of carboxylic acid derivatives of DNA/RNA bases have been reported in literature.¹⁵⁶ The carboxylic group in these examples is unionised. Synthon theory and principles of crystal engineering suggest that the existence of the unionised form of this functional group would generate a carboxylic acid dimer⁸⁰ provided that there are no competing interactions. Examination of the CSD demonstrates that apart from competition from carboxylic acid catemer, the dimer has to compete with the Watson-Crick³⁵ or Hoogsteen³⁶ modes of hydrogen bonding between nucleobases with a carboxylic acid functionality.

Interestingly, the dominating interactions in these structures are the Watson-Crick³⁵ or Hoogsteen³⁶ modes of hydrogen bonding. These interactions are key to holding together the DNA double helix and may be the reason why they are favoured despite competition from carboxylic acid groups. This base-pair recognition is strong enough, and perhaps more energetically favourable, to discriminate the formation of the $R_2^2(8)$ carboxylic acid dimer. Instead, carboxylic groups interact *via* hydrogen bonding with acceptor groups in the pyrimidine or purine rings DNA/RNA bases.

An example of this behaviour can be seen in the structure of guanine acetic acid depicted in Figure 3.58.¹⁵⁵ As illustrated, the carboxylic acid group reacts with the guanine part of the molecule to form a $R_2^2(8)$ heterosynthon rather than the carboxylic acid dimer. It can also be seen that there is base-pair recognition in the purine moiety of the molecule. This resembles the Hoogsteen-type interaction seen in the guanine:cytosine recognition.

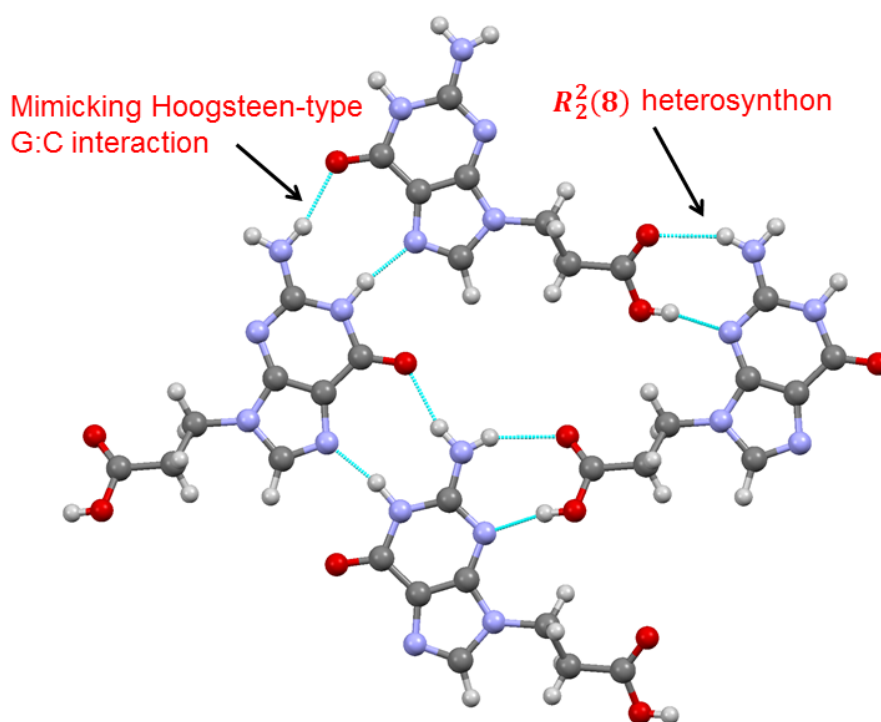


Figure 3.58: Hydrogen bonding in pure guanine acetic acid

The structure of anhydrous thymine acetic acid has been previously determined by Liu and co-workers.¹⁵⁷ The hydrogen bonding motifs in this crystal are in agreement with the trends discussed above. No carboxylic acid dimer is formed and the strongest interaction is hydrogen bonding *via* Watson-Crick sites in the pyrimidine rings of thymine.

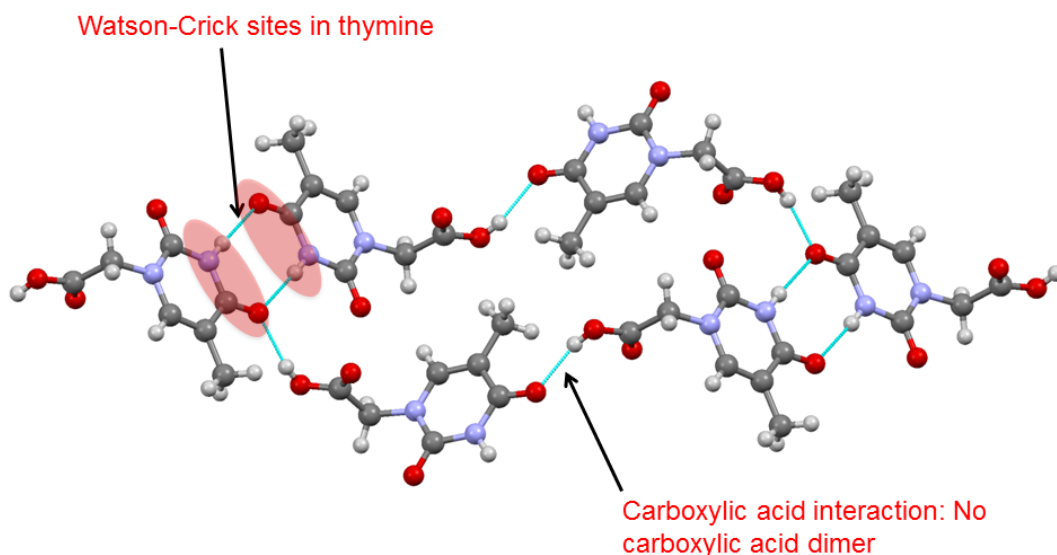


Figure 3.59: Hydrogen bonding in thymine acetic acid

3.7.2 Experimental

3.7.2.1 Synthesis of $\text{tac} \cdot 2\text{H}_2\text{O}$

Thymine acetic acid (0.046 g, 0.25 mmol), was dissolved in 50:50 ethanol:water (20 mL) by gentle heating. The clear solution obtained was left to slowly evaporate. Colourless single crystals suitable for X-ray diffraction were collected after approximately 1 week.

3.7.2.2 Single Crystal X-ray Diffraction

Standard procedures described previously were implemented for single crystal data collection.

3.7.2.3 Thermogravimetric analysis

The thermogravimetric behaviour of the compound was investigated using Mettler Toledo TGA/DSC 1. Samples were loaded in 70 μL alumina pans and heated at a ramp rate of 10 $^{\circ}\text{C}/\text{min}$ under a flow of nitrogen gas

3.7.3 Results and Discussion

3.7.3.1 Structure of $\text{tac}\cdot 2\text{H}_2\text{O}$

Thymine acetic acid dihydrate, hereafter $\text{tac}\cdot 2\text{H}_2\text{O}$ crystallises in the triclinic space group $P\bar{1}$. The asymmetric unit shown in Figure 3.60 contains one molecule of thymine acetic acid (**tac**) and two water molecules. As it can be seen from the asymmetric unit, the two water molecules are involved in hydrogen bonding with **tac**. The first water molecule acts as a hydrogen bond acceptor to the hydrogen atom of the carboxylic acid *via* $\text{O1}\cdots\text{H1}\cdots\text{O1W}$ (carboxylic). The second water molecules acts as a donor and forms a hydrogen bond to $\text{O2W}\cdots\text{H2WB}\cdots\text{O14}$ (carbonyl) hydrogen bonding with the carbonyl oxygen attached to the pyrimidine ring.

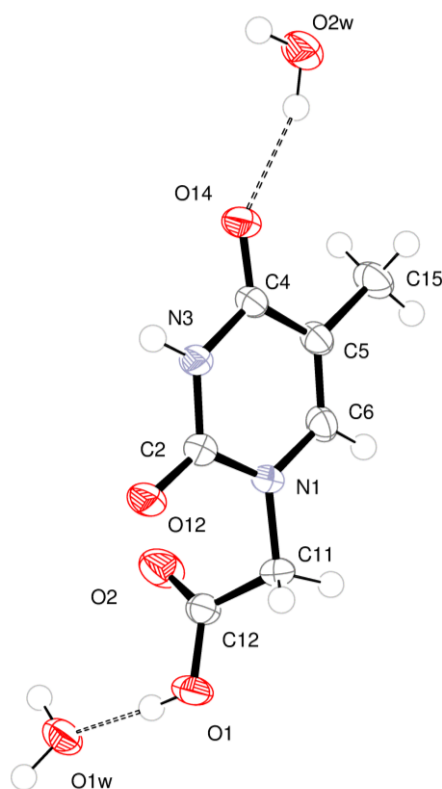


Figure 3.60: Asymmetric unit of $\text{tac}\cdot 2\text{H}_2\text{O}$ drawn at 75% ellipsoids. Dashed lines represent hydrogen bonds

The molecule of **tac** interacts with its symmetry equivalent counterpart *via* N—H...O hydrogen bonding at pyrimidine rings, thus generating a $R_2^2(8)$ homosynthon. (Figure 3.61 a). The interaction between two **tac** molecules *via* the pyrimidine rings resembles the urea dimer shown in Figure 3.61 b).

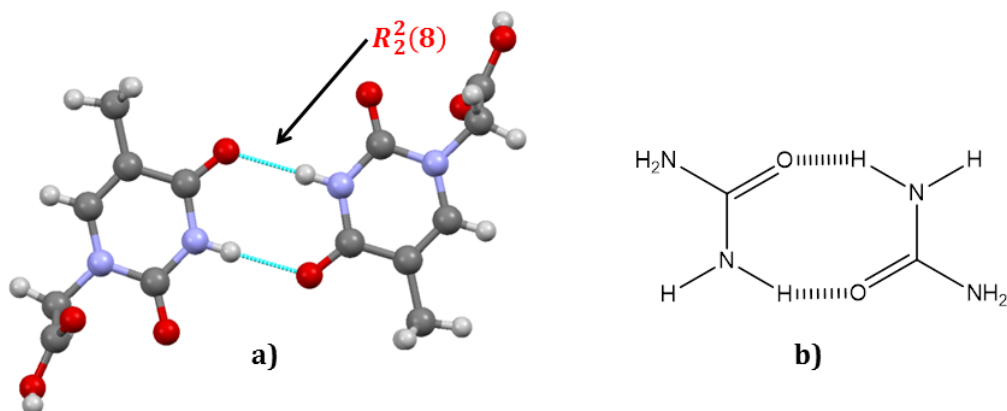


Figure 3.61: Pyrimidine-pyrimidine interaction in **tac resembling the urea-urea embrace**

Within the structure there is intricate hydrogen bonding. Water molecules are responsible for connecting adjacent **tac** molecules. Specifically, O1W facilitates the interaction of two carboxylic acid groups from different **tac** molecules. This water molecule acts simultaneously as a hydrogen bond donor and acceptor, thus generating a $R_4^4(12)$ heterosynthon with the carboxylic acid group as shown in Figure 3.62. The second water molecule, O2W further stabilises interaction between **tac** molecules. Figure 3.63 shows that O2W acts as a hydrogen bond donor to carbonyl oxygens from each pyrimidine ring and a hydrogen bond acceptor to O1W.

There is also some evidence of a potential π - π stacking of pyrimidine rings in **tac**. The adjacent layers stack parallel to *b*-axis and the mean plane separation was calculated to be 3.15 (2) Å. However, upon calculating the centroid to centroid separation (5.0805 (9) Å) it was concluded that this distance is outside the distance limit of what can be considered a π - π stacking interaction.

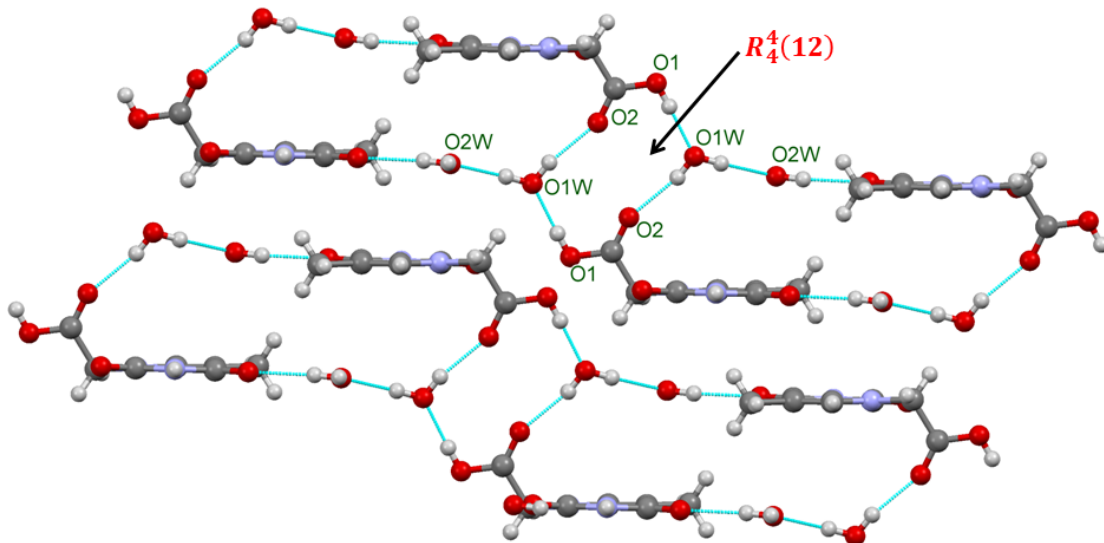


Figure 3.62: Crystal packing in tac•2H₂O

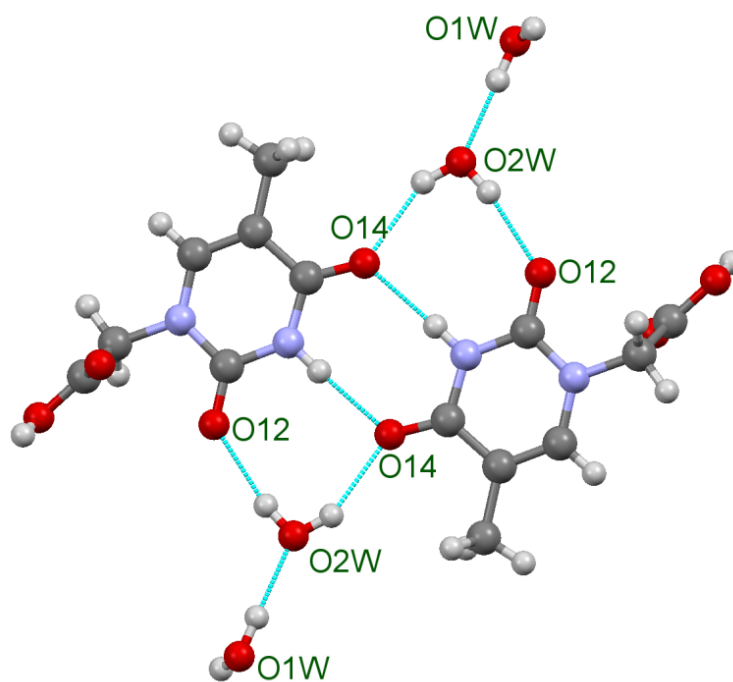


Figure 3.63: O2W provides further stabilisation to the interaction

3.7.3.2 The role of water molecules

The inclusion of two water molecules in this structure has major ramifications in hydrogen bonding compared to the motifs observed in **tac** anhydrous. A CSD analysis on the hydration of molecular crystals conducted by Gillon *et al.*⁹⁵ concluded that water seeks to maximise its hydrogen bonding capability in a crystal structure. Gillon *et al.* also reported that the most common environment for water is the one where it forms three hydrogen bonds: two *via* its hydrogen atoms and one *via* its oxygen. This conclusion is in agreement with what is observed in the present crystal. The overall effect of hydration in this system is that both waters act as bridges that stabilise the carboxylic acid and pyrimidine sites of **tac**. Both water molecules form three hydrogen bonds as depicted in Figure 3.62. O1W interacts with the carboxylic acid group, whereas O2W provides further stability to the Watson-Crick type interaction at the pyrimidine sites of **tac**.

Examination of the crystal structure shows that water molecules do not assist in the formation of the $R_2^2(8)$ carboxylic acid dimer. This finding is consistent with the reports of Prior and Sharp¹⁵⁸, who showed that antioxidant 2,3,4-trihydroxybenzoic acid dihydrate does not display the carboxylic acid dimer. Instead, they found that two acid molecules are linked to one another *via* two water molecules. This appears to be the case with **tac**•2H₂O too, where water inhibits dimer formation. However, hydration of **tac** is associated with an increase in the interaction between two carboxylic acid groups. Water molecule O1W allows the two carboxylic acid groups to interact with each other by acting as a bridge between the two and thus forming the $R_4^4(12)$ heterosynthon. This heterosynthon is one of several water-carboxylic interactions reported by Zaworotko's group.¹⁵⁹

Hydration of **tac** and the subsequent increase in the interaction between carboxylic acid groups replaces the carboxylic acid-pyrimidine interaction observed in the anhydrous form. Figure 3.64 compares the interaction of the carboxylic acid group between the two forms. It is evident that the anhydrous form does not display a carboxylic-carboxylic

interaction of any sort, but molecules interact with each other *via* carboxylic acid-pyrimidine interactions. The interaction between two carboxylic acids becomes more pronounced in the hydrated form owing to the stabilisation from water molecules.

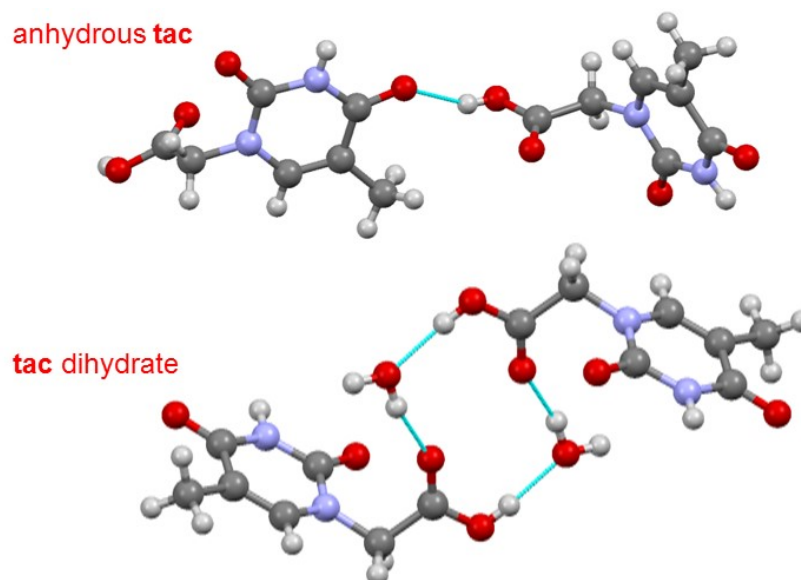


Figure 3.64: Comparison of the anhydrous and hydrated form

3.7.3.3 Carboxylic Acid Dimer vs tac-tac dimer

Assessment of the hydrogen bond table shows that the interaction which most closely approaches linearity is tac-tac interaction in pyrimidine rings. This interaction is strongly directing with an angle of 177.6° . The next interaction which approaches linearity is the water-carboxylic acid interaction $R_4^4(12)$ with an angle of 175.3° .

Given that crystals arise due to a trade-off between various types of interactions, it is fair to state that, for this system, the urea-urea like interaction is at the top of intermolecular bond hierarchy. This interaction diminishes the impact of other interactions, for example carboxylic acid dimer. Similar motifs were also reported in the case of orotic acid monohydrate, where carboxylic acid dimer is spared at the expense of the orotate-orotate homosynthon.¹⁶⁰

Although hydration helps in increasing acid-acid interactions by acting as a bridge, it is not sufficient to overcome the preference to form the urea-like dimer. This interaction can be seen as “interaction interference” *vis-à-vis* the carboxylic acid dimer. Similar interference to the carboxylic acid dimer is also observed in cubanecarboxylic acids, where the carboxylic catemer is formed.

Table 3.9: Hydrogen bond table for tac·2H₂O

D-H	A	d (D-H)/ (Å)	d (H...A) (Å)	d (D...A) (Å)	<D-H...A (°)
O1-H1	O1W	0.84	1.77	2.6080(13)	175.3
O1W-H1WA	O2W ⁱ	0.897(16)	1.863(16)	2.7596(12)	178.3(17)
O1W-H1WB	O2 ⁱⁱ	0.869(15)	1.942(15)	2.7769(12)	160.6(18)
O2W-H2WA	O14	0.884(16)	2.060(17)	2.8804(12)	154.0(16)
O2W-H2WB	O12 ⁱⁱⁱ	0.863(16)	1.992(16)	2.8450(13)	169.4(16)
N3-H3	O14 ⁱⁱⁱ	0.88	1.97	2.8491(13)	177.6
C6-H6	O1W ^{iv}	0.95	2.46	3.3268(16)	151.7

ⁱ [x+1, y, z-1]; ⁱⁱ [-x+2, -y, -z]; ⁱⁱⁱ [-x+2, -y+1, -z+1]; ^{iv} [-x+1, -y, -z];

3.7.3.4 Thermal Behaviour

The thermal behaviour of this crystal was investigated using thermogravimetric analysis. As shown in Figure 3.65, the loss of water follows a nebulous manner. Water loss begins soon after thermal treatment and removal of one water molecule corresponds to the loss of 8.17% of the total weight (shown in green dashed lines). The actual loss of this water molecules occurs at *circa.* 96 °C. The loss of the second water molecule corresponds to 16.35% of the total weight and is takes place *circa.* 215 °C (shown in red dashed lines). However, this water molecule is liberated slightly later when the temperature reaches approximately 180 °C. After the liberation of all waters there is a sharp drop in weight. This can be attributed to the decomposition of the crystal, which is completed as the temperature rises to above 240 °C.

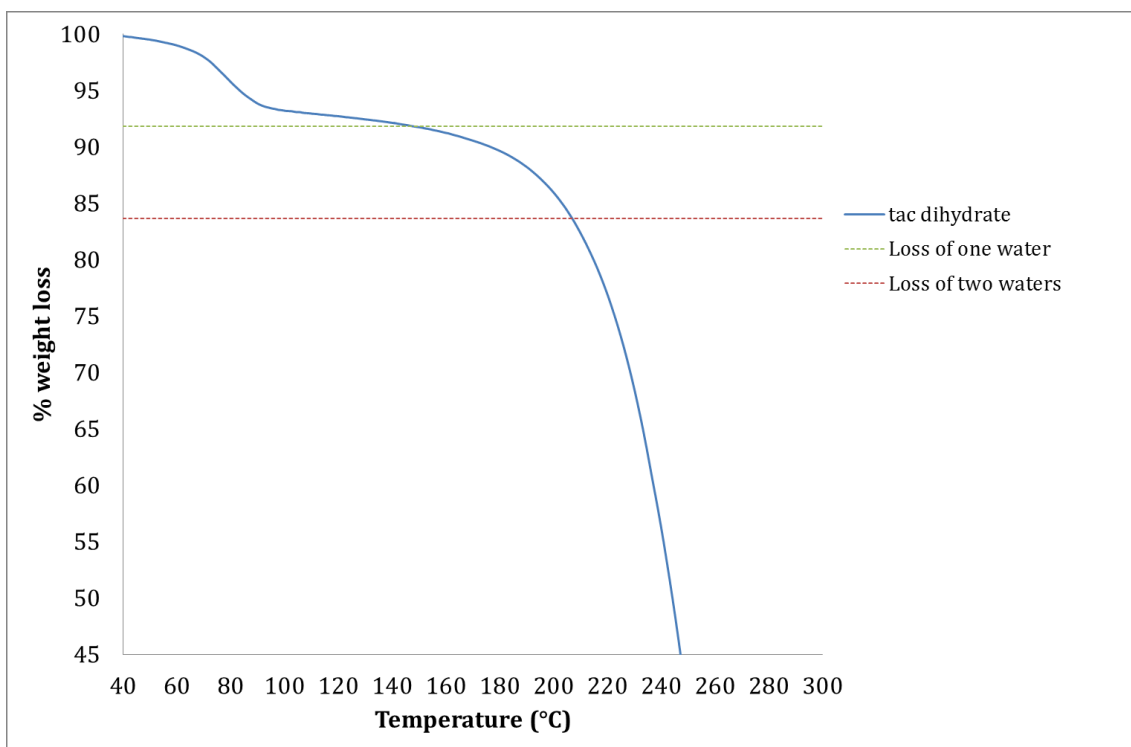


Figure 3.65: Thermal behaviour of tac•2H₂O

3.8 Co-crystallisation of Caffeine with 2-nitroterephthalic Acid:

3.8.1 Introduction

Aside from attempts to grow co-crystals with DNA bases, a wide variety of other similar organic compounds were utilised for co-crystallisation experiments. Co-crystallisation of caffeine with carboxylic acids is a particular area of interest since it can form co-crystals. Co-crystallisation reactions with caffeine have been reported to generate two distinct heterosynthons. Trask *et al.*¹²⁷ studied the co-crystals of caffeine with oxalic acid and reported the formation of a $R_2^2(7)$ heterosynthon. The interaction involves a non-classical C—H...O hydrogen bond from the caffeine to the carboxylic acid group as shown in Figure 3.66.

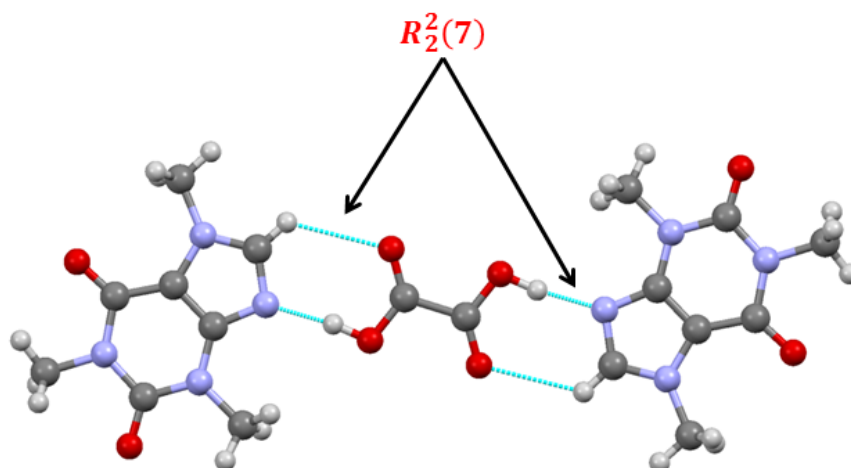


Figure 3.66: Heterosynthon formation in caffeine co-crystals

A different heterosynthon formation was reported by Bucar *et al.*¹⁶¹ who studied the co-crystallisation of caffeine with adipic acid. This interaction is the second most common heterosynthon encountered between caffeine and carboxylic acids. This is a $R_3^3(11)$ network generated by two synthons: $R_2^2(7)$ and $R_2^2(6)$ which is a characteristic of 1:1 caffeine carboxylic acid co-crystals.

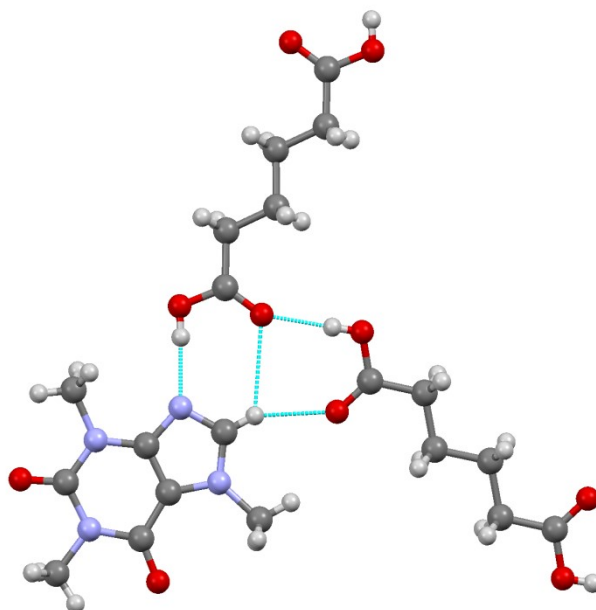


Figure 3.67: Second most common ($R_3^3(11)$) network based on ($R_2^2(7)$ and $R_2^2(6)$) synthons as observed in 1:1 caffeine:carboxylic acid co-crystals

Herein, a novel crystal structure of caffeine with 2-nitroterephthalic acid is presented. The co-crystal was grown by Patrick Heasman, a master level student working in the Prior Group. The author of this thesis has been involved in Patrick's research by providing guidance. The following structural analysis and discussion has been conducted by the author.

3.8.2 Experimental

3.8.2.1 Single Crystal Preparation

Caffeine (0.0970 g, 0.5 mmol) and 2-nitroterephthalic acid (0.1055 g, 0.5 mmol) were dissolved in a 50% methanol solution (20 mL). Needle shaped single crystal were obtained upon slow solvent evaporation.

3.8.2.2 Single Crystal X-ray diffraction measurements

Routine single crystal diffraction methods stipulated previously were employed for data collection.

3.8.2.3 IR Spectroscopy

FT-IR spectra were collected from samples prepared as KBr disks (1:20 dilution) using a Perkin Elmer FT-IR Spectrometer Spectrum RX1.

3.8.3 Results and Discussions

3.8.3.1 Structure of caf:2nitroTA

The reaction of caffeine with 2-nitroterephthalic acid produced needle shaped colourless crystals. Inspection of hydrogen atom locations shows that crystallisation is not associated with proton migration from acid to the base. Therefore, the multicomponent crystal obtained from this reaction was determined to be a co-crystal, hereafter referred to as **caf:2nitroTA**. This compound crystallises in the monoclinic space group $P2_1/n$. The asymmetric unit is comprised of one caffeine molecule and one 2-nitroterephthalic acid molecule as shown in Figure 3.68.

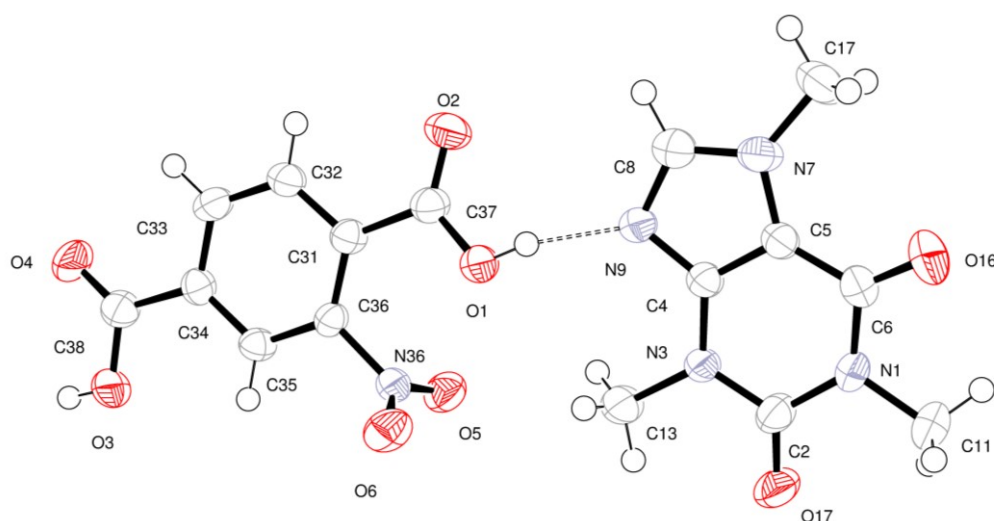


Figure 3.68: The asymmetric unit of caf:2nitroTA drawn as 70% probability ellipsoids

The carboxylic acid groups in 2-nitroterephthalic acid are involved in hydrogen bonding with caffeine. The first carboxylic acid forms a O—H(hydroxyl)⋯N(imidazole) with length 2.610(2) Å and angle 166.9°. The second carboxylic acid forms a O—H(hydroxyl)⋯O(pyrimidine) hydrogen bond with O⋯N distance 2.661(2) and O—H⋯N angle 170.1°. These interactions generate infinite tapes. A single tape is shown in Figure 3.70.

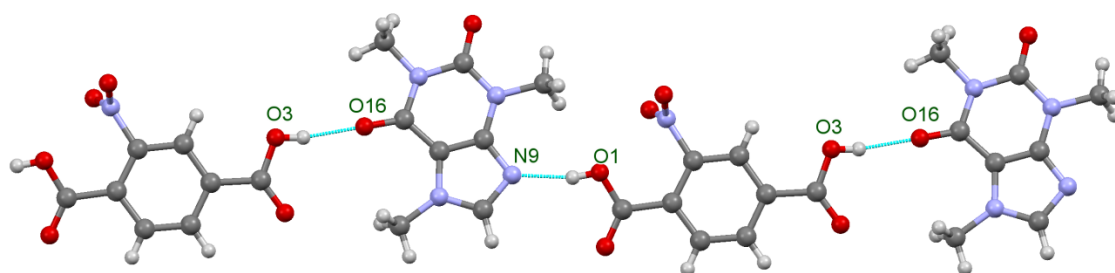


Figure 3.69: A single tape between caffeine and 2-nitroterephthalic acid

The $R_2^2(7)$ acid-imidazole heterosynthon formed in systems with caffeine and carboxylic acids is a common heterosynthon¹⁶¹, but it does not form in this structure. As a result, the C8 position in the imidazole ring of caffeine is available for hydrogen bonding forming a non-classical C—H(imidazole)⋯O(nitro) hydrogen bond (length 3.177(3) Å and angle 145.9(17)°) as shown in Figure 3.70. Crystal packing is shown in Figure 3.71.

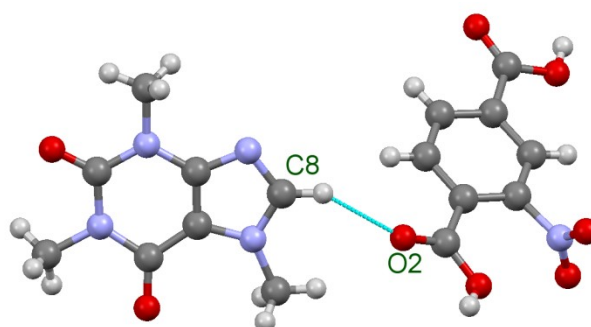


Figure 3.70: C—H⋯O hydrogen bond between caffeine and 2-nitroterephthalic acid

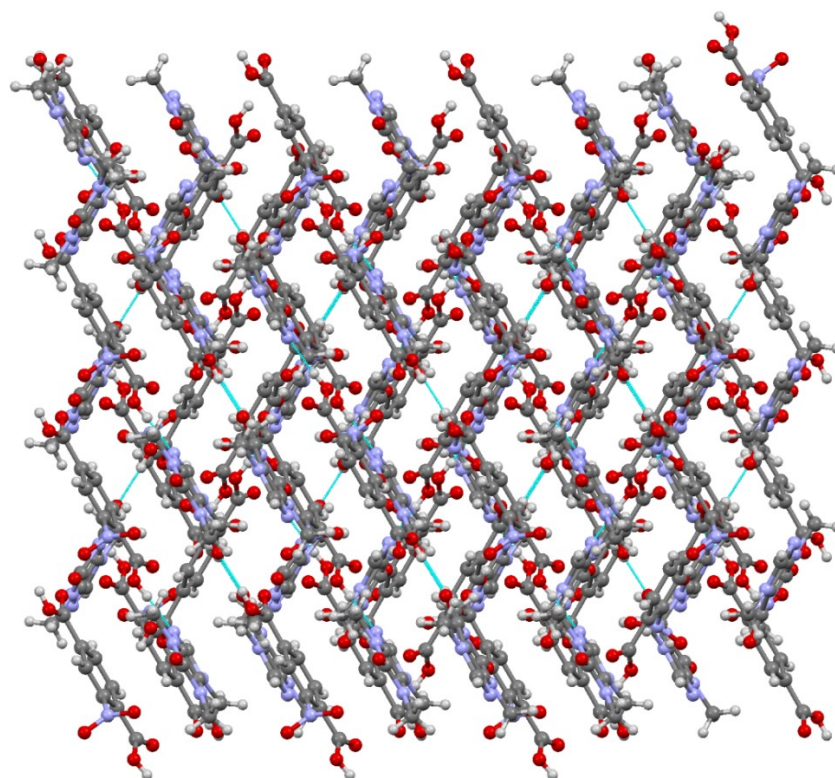


Figure 3.71: Crystal packing along *c*-axis

The structure contains another type of non-classical hydrogen bonding between C—H(aromatic)···O(carbonyl). Each of caffeine and 2-nitroterephthalic acid interact with each other *via* the C—H(aromatic)···O(carbonyl) and O—H(hydroxyl)···N(imidazole) to generate a ring as shown in Figure 3.72.

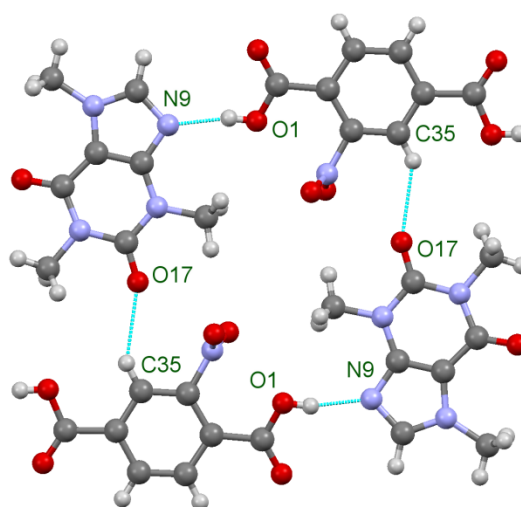


Figure 3.72: Classical and non-classical hydrogen bonds generating a ring between caffeine and 2-nitroterephthalic acid

3.8.3.2 Determination of co-crystal formation

Assignment of protons in the structure was achieved using Fourier maps. It is evident from Figure 3.73 that proton positions in both carboxylic acids have been correctly assigned and that the both acid groups are unionised.

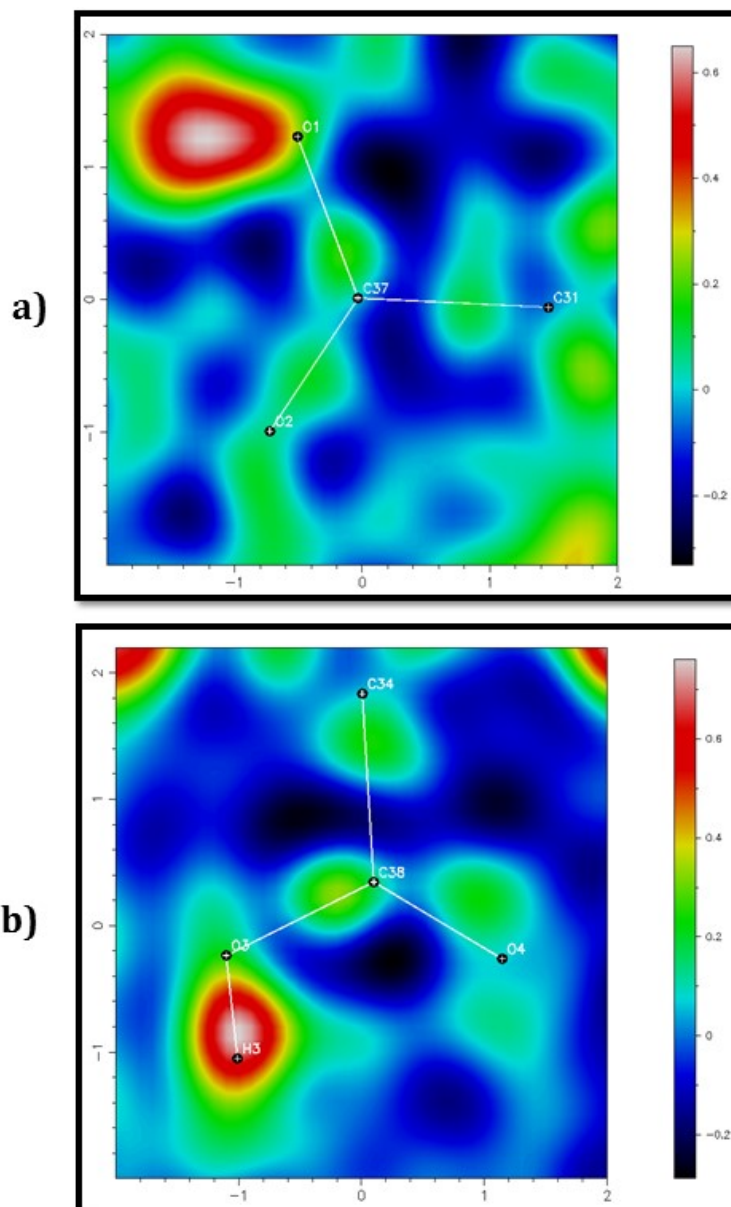


Figure 3.73: Fourier maps showing that the carboxylic acid group is unionised: a) proton location in the first carboxylic acid; b) proton location in the second carboxylic acid

Further evidence on the existence of the protonated carboxylic acid groups can be obtained upon inspection of the C—O lengths in the acid groups shown in Figure 3.74. Examination of C37—O1 (1.304(2) Å) and C37—O2 (1.216(2) Å) reveals that the length difference between the two is 0.09 Å. Likewise, examination of lengths of C38—O3 (1.330(2) Å) and C38—O4 (1.209(2) Å) reveals that the length difference is 0.12 Å. The bond angle at the endocyclic nitrogen site of the base can also assist in identifying whether proton migration has taken place (*i.e.* salt or co-crystal formation). Inspection of this site in caffeine reveals that the C4—N9—C8 bond angle is 102.71(19)°. This value is consistent with other caffeine co-crystals for example caffeine:adipic acid reported by Bucar *et al.*¹⁶¹ where the nitrogen angle is 103.94(9)°. The angle at the endocyclic nitrogen of **caf:2nitroTA** is lower than in systems where caffeine is protonated. Protonated caffeine systems experience an increase in this angle as observed in the chloride salt of caffeine. In this structure, reported by Mercer and Trotter¹⁶², the internal angle at the nitrogen site is 107.8 (3)°, which is larger than the angle in **caf:2nitroTA**.

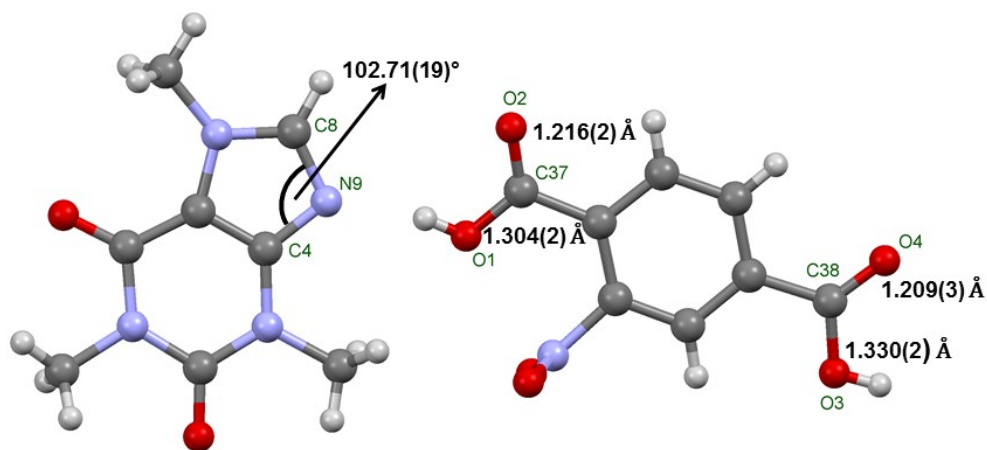


Figure 3.74: Determination of C—O distances in carboxylic acid and the C4—N9—C8 angle

Table 3.10: Hydrogen bond parameters for caf:2nitroTA

D-H	A	d (D-H)/ (Å)	d (H...A) (Å)	d (D...A) (Å)	<D-H...A (°)
O3-H3	O16 ⁱ	0.82	1.85	2.661(2)	170.1
O1-H1	N9	0.82	1.8	2.610(2)	166.9
C17-H17A	O2 ⁱⁱ	0.96	2.43	3.315(3)	152.3
C17-H17C	O2 ⁱⁱⁱ	0.96	2.55	3.267(3)	131.9
C13-H13B	O5 ^{iv}	0.96	2.64	3.527(2)	153.1
C8-H8	O2 ⁱⁱ	0.99(2)	2.31(2)	3.177(3)	145.9(17)
C35-H35	O17 ^{iv}	0.93	2.42	3.208(2)	142.8

ⁱ [x-1, y+2, z]; ⁱⁱ -x+2.5, y-0.5, -z+0.5]; ⁱⁱⁱ [x, y-1, z]; ^{iv} [-x+2, -y-1, -z];

3.8.3.3 Confirmation of co-crystal formation by IR spectroscopy

Examination of the IR spectrum also confirms the presence of neutral carboxylic acid groups. As shown in the spectrum Figure 3.75, there is a band near 1720 cm⁻¹ corresponding to the C=O absorption and a weaker band near 1280 cm⁻¹. Appearance of these bands indicates the presence of neutral carboxylic acids, which further confirms that crystallisation is not associated with proton transfer.¹⁶³ Although the unionised form is present in both acid groups, it is evident from the structure analysis that there is no dimer and therefore carboxylic acid dimer bands at 2500 – 2700 cm⁻¹ are not present. Strong bands at 1370 cm⁻¹ and 1540 cm⁻¹ as well as between 740-780 cm⁻¹ emerge as a result of the N=O stretching from the aromatic nitro group.¹⁵³ The IR findings are in accordance with the analysis on the C—O bond lengths in the acid groups, where no equalisation of bond length was observed, which would otherwise suggest deprotonation. In addition, IR results are also in agreement with the Fourier maps shown above and the data are conclusive that a co-crystal has been obtained.

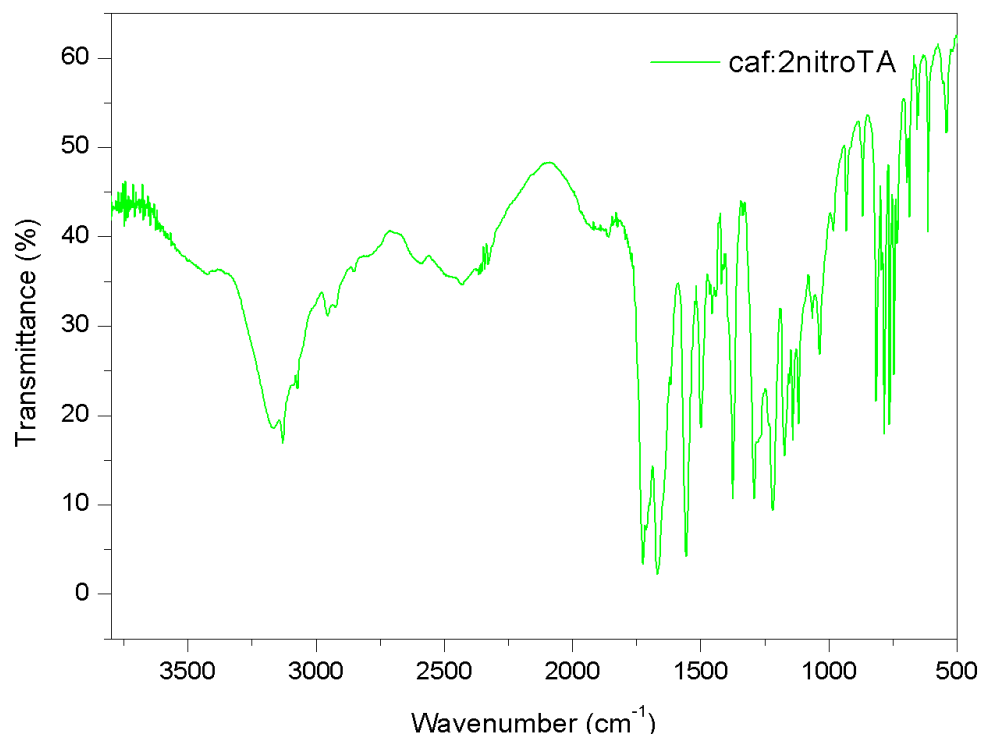


Figure 3.75: IR spectrum for caf:2nitroTA

Table 3.11: Characteristic IR absorption peaks

Functional Group	ν (cm ⁻¹)	Intensity
C=O	1280	Medium, sharp
C=O	1720	Strong, sharp
N=O	1370 - 1540	Strong, sharp
N=O	740 - 780	Medium, sharp
C—O	3050 - 3340	Strong, broad

3.8.3.4 Relationship to other compounds

The most remarkable difference between **caf:2nitroTA** and other structures reported in literature is the fact that neither of the two most commonly occurring heterosynthons are present in this co-crystal. Instead, there are O—H(hydroxyl)⋯N(imidazole) and O—H(hydroxyl)⋯O(pyrimidine) interactions between the base and the acid. The O—H(hydroxyl)⋯N(imidazole) is also observed in the caffeine co-crystal with isophthalic acid reported by Mahapatra *et al.*¹⁶⁴ However, Mahapatra's crystal contains caffeine-caffeine interactions which are not present in **caf:2nitroTA**.

3.9 Chapter Outlook and Conclusions

The results discussed in this chapter illustrate the complex nature of intermolecular interactions. This chapter primarily focused on designing and growing single crystal materials of DNA bases and their carboxylic acid derivatives with various other molecules. The objective of this study was to understand and examine the hydrogen bonding motifs and supramolecular synthons present in these systems. Initial experimental work showed that DNA nucleobases exhibit a poor solubility in aqueous media. To mitigate solubility challenges, we sought alternative routes of growing single crystals containing DNA bases. The alternative synthetic approaches included:

- 1) Altering the pH of the system where it was found that acidic and basic media improve the solubility of DNA bases. This approach afforded novel single crystal materials where the DNA base (guanine) was present in its protonated form as guaninium. The material obtained was a channel hydrate and it was possible to remove water partially and fully while retaining crystallinity.
- 2) Solution crystallisation of cytosine with 1,10-phenanthroline afforded good quality co-crystals. Co-crystallisation was also achieved upon milling the two starting materials for 1h at 300 rpm. There was found to be a correlation between phase transformation from grinding experiments and co-crystallisation using solution methods. Samples which did

not co-crystallise *via* milling were also found to be unsuccessful in yielding co-crystals *via* solution methods. Calculations on the energy landscape of these systems helped in rationalising these experimental results. It was concluded that for cytosine and 1,10-phenanthroline there is a favourable energetic driving force for co-crystallisation, whereas co-crystallisation of the other DNA bases with 1,10-phenanthroline was not energetically favoured.

3) Improvement in solubility was also achieved by utilising carboxylic acid derivatives of DNA bases. Specifically, thymine acetic acid was crystallised in its hydrate form and the structure was compared to its anhydrous form. It was found that hydration is associated with changes in the hydrogen bonding pattern, but the dominating interaction was the **tac-tac** hydrogen bonding at the pyrimidine rings.

In addition, the behaviour of melamine was studied in the presence of nitrilotriacetic acid and the behaviour of caffeine was studied in the presence of 2-nitroterephthalic acid. The former was characterised as a salt with two crystallisation water molecules, whereas the latter was characterised as a co-crystal.

In most cases the previously anticipated synthons were present in the crystal structures. This, however, does not imply that the behaviour of these molecules can be easily predicted. The situation is quite the opposite. Despite extensive research conducted on the hydrogen bonding of these molecules, it remains largely impossible to predict confidently which synthons will prevail in the crystal structure. This is because, as Dunitz notes, the predictive capacity of the synthon theory is limited and it only focuses on the hydrogen bonding between functional groups.

While it has proven to be a useful tool during experimental design over the three years of research, the limitations of the synthon theory have become evident from some of the results discussed in this thesis. For example, synthon theory was used to predict that thymine, adenine and guanine would form co-crystals with 1,10-phenanthroline. This was

based on the hydrogen bond donor and acceptor capabilities displayed by these bases, which would form robust synthons. However, none of these bases produced co-crystals with 1,10-phenanthroline, even though synthon theory suggested otherwise. This is because synthon theory steers away from energetic considerations and non-hydrogen bonding interactions, which are pivotal to the crystallisation process.

The results presented in this chapter show that self-assembly is driven in a way which maximises favourable hydrogen bonding interactions. But, other competing interactions, such as π - π stacking interactions, can play a role in stabilising crystal structures. Two interactions with the highest prevalence in DNA base crystals were found to be the Watson-Crick and Hoogsteen modes of hydrogen bonding. These investigations also shed light on the pivotal role of water molecules in stabilising crystal structures. Water molecules were found to provide structural cohesion by acting as hydrogen bond donor and acceptors, which bridge adjacent molecules in crystal structures. It was found that some water molecules are held more tightly *via* hydrogen bonding than others. As a result, partial and full dehydration was afforded in the channel hydrate of guaninium sulphate. Water was also found to increase the interaction between two carboxyl groups and replace the carboxylic acid-pyrimidine interaction in thymine acetic acid.

In conclusion, this chapter demonstrates that synthon theory cannot be used without taking into account energetic aspects of crystallisation. Where possible, these two concepts should be used in conjunction with one another, in order to successfully predict interactions in a crystal.

The chapter also highlights the importance of intelligently predicting favourable hydrogen bonding synthons by always considering other competing interactions which may not be hydrogen bonds. Lastly, the chapter contributes to establishing an understanding of hydrogen bonding and its role in stabilising crystals of DNA nucleobases or its derivatives.

Chapter 4:

Hydrogen-Bonded Networks Containing DNA

Nucleobases or Their Derivatives

4.0 HYDROGEN-BONDED NETWORKS CONTAINING DNA BASES OR THEIR DERIVATIVES

4.1 Introduction

Parallel to the development of organic crystal engineering, there has been extensive research on designing new molecular crystals by exploiting the coordination behaviour of transition metals. This sub-discipline of crystal engineering is now commonly referred to as inorganic crystal engineering. The potential of this field was noted by Dario Braga¹⁶⁵ in a perspective article in Dalton Transactions. Braga suggested that the stronger interactions of covalent character can be used alongside hydrogen bonding in these systems. He also noted that using the metal-ligand coordination bonds alongside the weaker forms of intermolecular interactions can afford novel supramolecular architectures of increasing complexity.

The similarities between organic and inorganic crystal engineering were highlighted by Desiraju¹⁶⁶ in his perspective article for Dalton Transaction in 2000. He argues that factors which govern and guide crystal packing in organic molecules bear the same importance in systems which contain metals. Furthermore, Desiraju states that the metal atoms in these systems are essentially isolated in the molecular cores, whereas the peripheries of these molecules (the ligands) are organic in nature and they are therefore crucial to packing. By focusing on the peripheral functional groups of ligands, Desiraju essentially takes a reductionist approach. He argues that crystal packing in these systems will be predominantly guided by the interactions of ligands, which follow the principles of organic crystal engineering.

Brammer¹⁶⁷ states that metal centres with their well-defined coordination geometries can serve as tools to orient the hydrogen bonding interactions on ligands. In other words, if the preferred geometry of a metal is, for example, tetrahedral, then its crystal packing

would be different from the case of an octahedral geometry because ligand orientation would necessarily be different. The validity of this claim can be confirmed if one considers that coordination bonds are stronger bonds than the strongest hydrogen bonding interactions. From a hierarchic perspective, once the stronger metal-ligand bonds are formed, the conditions are dictated for the formation of hydrogen bonds. In this way, the metal acts as a coordination centre which provides a template for the formation of a network sustained *via* hydrogen bonding.¹⁶⁸

4.2 Metal-Nucleobase Binding Motifs

Nucleic acids have a negative charge due to their phosphate groups and therefore seek stabilisation by a cation. Charge stabilisation can be provided from metal ions or protonated organic species. In a review discussing the multiplicity of metal-nucleic acid binding interactions, Lippert¹⁶⁹ divides these interactions into two groups:

1) a direct interaction

2) an indirect interaction

A direct interaction arises when the nucleic acids coordinate to the metal from their electron rich groups. A nucleic acid is comprised of the nucleobases, sugar group and the phosphate group. Binding to metals can take place *via* the oxygen atoms in the phosphate group, oxygen atoms in the sugar group or the electronegative atoms in the nucleobases.¹⁶⁹

According to Lippert, an indirect interaction is one between the nucleic acid and the ligands coordinated to the metal ion. Indirect interactions can be either *via* hydrogen bonding between water/amine ligands and the nucleic acid, or *via* π - π stacking interactions between the two.¹⁶⁹

4.2.1 Direct Metal-Nucleobase Interactions

Nucleobases contain oxygen and nitrogen in a range of geometries, which enable these bases to bind metal centres. Figure 4.1 depicts the multiplicity of metal binding exhibited by DNA bases, the atoms highlighted in red represent the sites which can bind to metals. It is evident that there are few possibilities for binding endocyclic nitrogen atoms or carbonyl oxygens. In addition, these bases can bind metals centres upon deprotonation at the endocyclic nitrogen atoms.¹⁷⁰

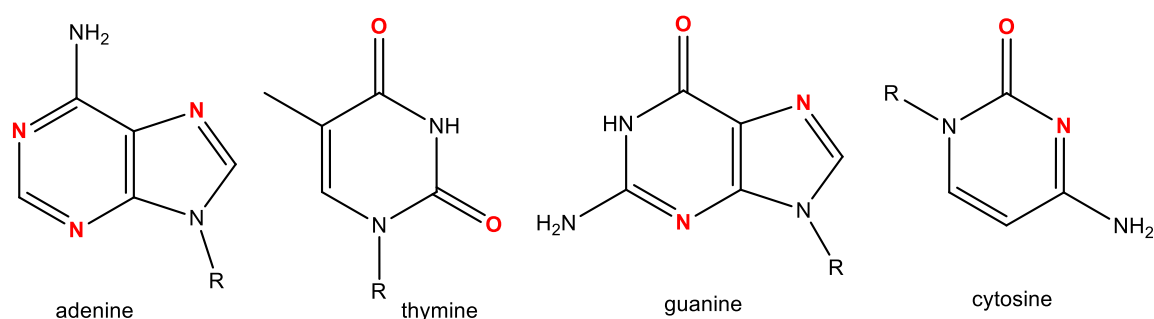


Figure 4.1: Metal binding sites in DNA nucleobases¹⁷⁰

Complexation with metals can alter the intermolecular interactions exhibited by nucleobases. If the site which binds the metal centre is normally a favourable site for hydrogen bonding *via* Watson-Crick³⁵ and Hoogsteen³⁶ interactions, then metallation could block the formation of such interaction. An alternative outcome of metallation could be the altering of the hydrogen bonding motif between bases.

4.2.2 Indirect Metal-Nucleobase Interactions

Apart from metal binding, the peripheral parts of nucleobases are capable of hydrogen bonding. Such capability enables the engineering of novel crystals whereby two nucleobases interact with one another through the metal ion. This concept of molecular design suggests that complexation of ligands with metal centres would generate building blocks. These building blocks would then interact *via* hydrogen bonding with other molecules that possess hydrogen bonding functionality to afford complex supramolecular structures. If one nucleobase is bound to a metal centre, its peripheral sites could be used for complementary base pairing with other nucleobases. This is especially useful given the poor solubility of DNA bases and the unsuccessful attempts in growing co-crystals. Therefore, the presence of a metal ion may facilitate the recognition between nucleobases. A classic example is the structure reported by Freisinger *et al.*¹⁷¹ where 1-methylcytosine is hydrogen bonded in a Watson-Crick fashion to the 9-methylguanine ligand bound to the platinum(II) metal centre. The structure depicted in Figure 4.2 demonstrates the ability of nucleobases to recognise one another upon metallation. Apart from the guanine-cytosine Watson-Crick interaction, there is a guanine interacting with a deprotonated guanine and in this way forming a triple hydrogen bond, which connects the two moieties.

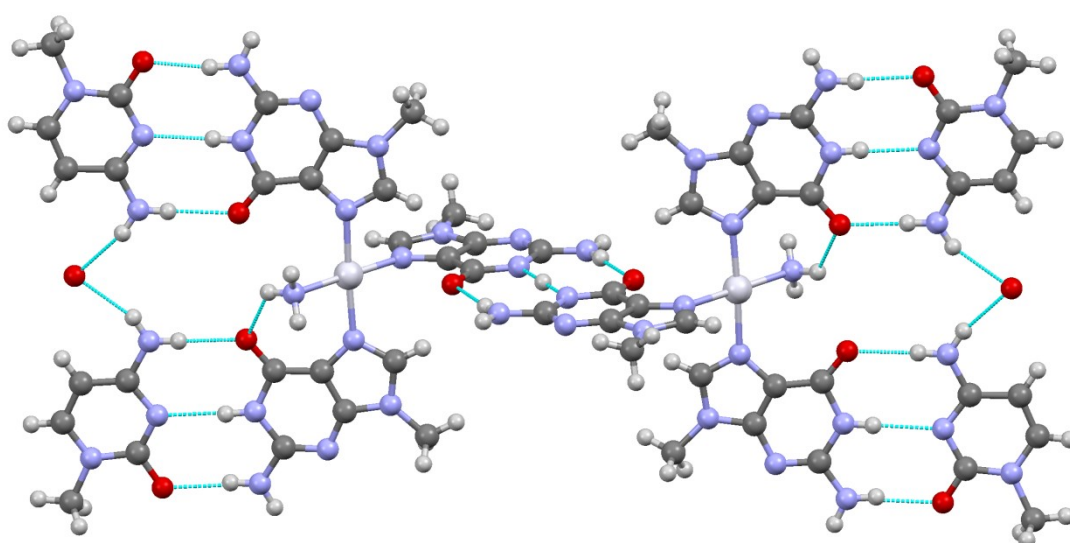


Figure 4.2: Hydrogen bonding of nucleobases through a metal centre¹⁷¹

One of the most striking effects of metal binding to nucleobases are the changes in basicity and acidity that take place in nucleobases. Metallation increases the acidity of the NH and NH₂ functional groups in nucleobases, while simultaneously causing a decrease in the basicity of the carbonyl oxygen atoms or endocyclic nitrogen atoms.¹⁶⁹ This was observed when the strength of Watson-Crick hydrogen bonding between the platinated guanine and the free cytosine was compared to that of the free 9-ethylguanine and cytosine.¹⁷² The strength of the former was noted to be greater than the latter owing to platination. This was attributed to the increase in acidity of the two sites N-sites in guanine, due to the electron-withdrawing effect of the metal. It was argued that such effect makes both the N-sites in guanine better hydrogen bond donors and this explains the increase in hydrogen bonding strength.

Similarly, it was argued that the hydrogen bonding capability of the carbonyl oxygen in guanine is weakened due to the same electron-withdrawing effect from the metal. Such effect would decrease the basicity of the carbonyl oxygen and therefore makes it a poorer hydrogen bond acceptor. However, Sigel *et al.*¹⁷² argued that the effects of having a poorer hydrogen bond acceptor are overruled by the presence of two N—H hydrogen bond donors in this system, whose donor capability is enhanced due to platination.

4.3 Recent Trends in Coordination Compounds with Nucleobases

The advantages of the rigid metal-ligand building block in stabilising DNA nucleobases have been extensively explored in the recent years in order to afford novel supramolecular architectures. A significant contribution during 2011-2013 comes from Castillo and co-workers, who studied copper paddle-wheel systems with adenine.¹⁷³⁻¹⁷⁵ In these systems, adenine acts as a bidentate bridging ligand to two copper metal centres. The novelty of these crystal structures is the emergence of a porous 3D framework, where the solvate molecules reside.

The role of adenine in self-assembly was also studied by Song *et al.*¹⁷⁶ in 2014. Adenine was used as an organic linker alongside cadmium(II) to synthesise three new MOFs which are distinct from one another both in terms of size and their structure. The unique structural features observed in these MOFs were attributed to adenine and its high number of nitrogen atoms capable of forming coordinate bonds.

An exhaustive review was published in 2012 by Patel *et al.*¹⁷⁷ who reviewed the metal binding modes of adenine in cationic, anionic and the neutral form. It was concluded that all forms adenine (including different tautomeric forms) display a rare degree of versatility as a ligand. While the anionic form was reported to promote the bridging capability of adenine, the neutral and cationic forms were found to participate in intricate hydrogen bonding. Similar findings on the metal binding versatility of guanine, thymine and cytosine were put forward in a 2014 review paper presented by Amo-Ochoa and Zamora.¹⁷⁸

4.4 Interaction of Nucleobases with Metal-Ligand Building Blocks

4.4.1 Introduction

Intermolecular interactions of nucleobases with a metal-ligand building block can take two possible forms: hydrogen bonding and π - π stacking or a combination of the two. However, the hydrogen bonding motifs displayed by nucleobases largely depend on the form in which they are incorporated in the crystal. Different motifs can arise depending on whether the nucleobase is protonated or not. Carboxylic acids are commonly employed in designing hydrogen bonded networks of DNA bases. For first row transition metals, usually two binding scenarios can arise: ligand binding to stabilise the charge on the metal ion; or binding to create metal-ligand anions which require stabilisation by a protonated base.

Dobrzynska *et al.*¹⁷⁹ reported a hydrogen bonded network of adenine in the presence of manganese (II) quinoline-2-carboxylate dihydrate. Here, the coordination complex is neutral (uncharged) and therefore the nucleobase is incorporated in its neutral form.

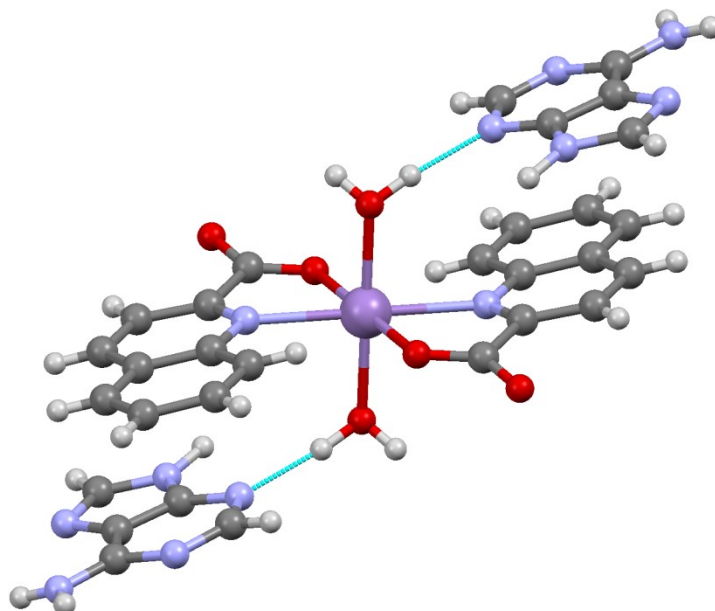


Figure 4.3: Hydrogen bonded network of adenine with manganese (II) quinoline-2-carboxylate

Two ligand molecules bind to the metal in a bidentate fashion *via* the endocyclic nitrogen and the deprotonated carboxylic acid group. The octahedral geometry is completed by two water molecules, which bind in a *trans* fashion at the metal. In addition, there are two neutral adenine molecules. It is remarkable to note that the interaction of the two adenine molecules generates a ribbon sustained by both Watson-Crick and Hoogsteen interactions.

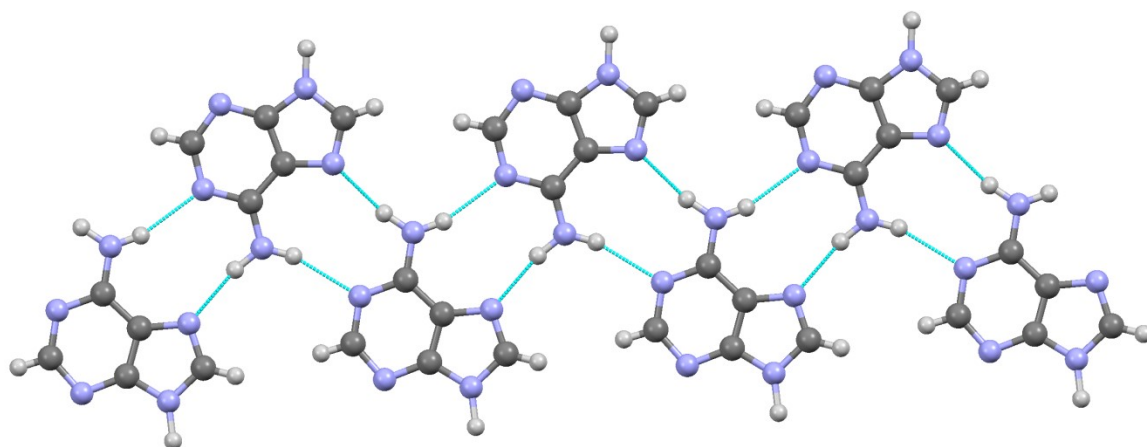


Figure 4.4: Adenine ribbon showing the presence of Watson-Crick and Hoogsteen interactions

Among other examples, Garcia-Teran *et al.*¹⁸⁰ reported that the complexation of oxalic acid with first row transition metals generates an anion, which is stabilised by protonated adenine species. The striking feature of these structures was the presence of adeninium in two different tautomeric forms, namely [1H, 9H] and [3H, 7H]. Despite protonation, the adeninium species interact with the oxalate moieties through their Watson-Crick sites, thus generating an $R_2^2(8)$ embrace. Garcia-Teran *et al.*¹⁸¹ also reported the assembly of protonated cytosine around the same metal-ligand complex. Similar to the adeninium case, cytosinium was reported to interact with oxalate *via* its Watson-Crick sites.¹⁸¹

Das *et al.*¹⁰⁶ reported that the use of 2,6-pyridinedicarboxylic acid is advantageous in engineering complex architectures where nucleobases are hydrogen bonded to the metal-ligand building block. They demonstrated the successful crystallisation of protonated cytosine and adenine by using 2,6-pyridinedicarboxylic acid with manganese (II), zinc (II), copper (II). The deprotonation of the two carboxylate groups and the lone pair of electrons on the nitrogen atom enable a tridentate binding to the metal centre. The metal-dipicolinate matrix provides the backbone which facilitates the interactions with the DNA bases.

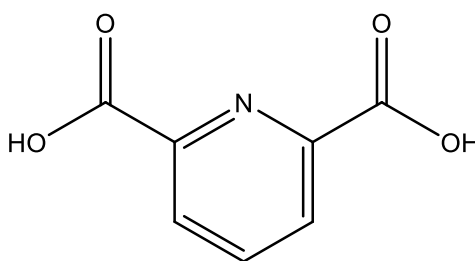


Figure 4.5: Structure of 2,6-pyridinedicarboxylic acid

The aim of the present study is to expand on the library of compounds presented by Das *et al.* by employing the same metal-ligand complex with other first row transition metals. The objective of this study was to investigate the behaviour of adenine and cytosine in the presence of nickel (II) and cobalt (II) and compare it with the structures reported by Das and co-workers. Furthermore, this study seeks to understand the hydrogen bonding motifs of guanine and thymine with the metal-ligand complex, which have been unexplored previously.

4.4.2 Experimental

4.4.2.1 Single crystal preparation

4.4.2.1.1 [1H, 9H AdH⁺][3H, 7H AdH⁺][Ni(dip)₂(H₂O)₃] and [1H, 9H AdH⁺][3H, 7H AdH⁺][Co(dip)₂(H₂O)₃]

Dipicolinic acid (0.334 g, 2 mmol) and nickel (II) acetate tetrahydrate (0.249 g, 1 mmol) or cobalt (II) acetate tetrahydrate (0.249 g, 1 mmol) were dissolved in methanol (20 mL) and stirred for 1h at 50 °C. A light green precipitate was obtained for nickel (II) and a dark red precipitate for cobalt (II). To the precipitate obtained, adenine (0.270 g, 2 mmol) dissolved in 15 mL of 1:1:1 methanol:ethanol:water was added in small portions with constant stirring. The reactions were left overnight at room temperature. The precipitate was filtered, dried. Crystallisation from Milli Q water was achieved over a period of few days. Light green block-shaped crystals with well-developed faces were isolated for the nickel complex, whereas red-brown block-shaped crystals with well-developed faces were isolated for the cobalt complex.

4.4.2.2 [1H CytH⁺]₂[Ni(dip)₂(H₂O)₃] and [1H CytH⁺]₂[Co(dip)₂(H₂O)₃]

The complexation of the metal and ligand was performed as per the method outlined above. To the precipitate obtained, cytosine (0.220 g, 2 mmol) dissolved in 10 mL of 50% methanol solution was added in small portions with constant stirring. The reaction was left overnight at room temperature. The precipitate was filtered, dried and crystallised from Milli Q water through slow solvent evaporation over few days. Light green block-shaped crystals with well-developed faces were isolated for the nickel complex, whereas red brown block-shaped crystals with well-developed faces were isolated for the cobalt complex.

4.4.2.3 [3H-cytosinium] Co(dip)₂] from methanol

Dipicolinic acid (0.334 g, 2 mmol) and cobalt (II) acetate tetrahydrate (0.249 g, 1 mmol) were dissolved in methanol (20 mL) and stirred for 1h at 50 °C. A dark red precipitate was obtained. To the precipitate obtained cytosine (0.220 g, 2 mmol) dissolved in 10mL of 50% methanol solution was added in small portions with constant stirring. A dark red solution was obtained and the reaction was left overnight at room temperature. Crystallisation was achieved through slow solvent evaporation from methanol over five days. Red brown plate-shaped crystals with well-developed faces were isolated.

4.4.2.4 Synthesis of thymine, uracil and guanine analogues

The complexation of the metal and ligand was performed as per the method outlined in Section 4.4.2.1.1.

To the precipitate obtained, thymine (0.252 g, 2 mmol), or uracil (0.224 g, 2 mmol) or guanine (0.302 g, 2 mmol) was dissolved in 10 mL of 50% methanol solution was added in small portions with constant stirring. The reaction was left overnight at room temperature. The precipitate was filtered, dried and crystallised from Milli Q water through slow solvent evaporation over few days.

The guanine mixture failed to dissolve during recrystallisation from Milli Q water, whereas the thymine mixture and uracil mixture produced a white precipitate upon cooling. The precipitate was determined as thymine monohydrate and uracil monohydrate.

4.4.2.5 Single crystal X-ray diffraction

Routine single crystal diffraction methods stipulated previously were employed for data collection.

4.4.3 Results and Discussion

4.4.3.1 Structure of $[1H, 9H \text{ AdH}^+][3H, 7H \text{ AdH}^+][\text{Co}(\text{dip})_2(\text{H}_2\text{O})_3]$

The metal-dipicolinato complex of protonated adenine crystallises in the monoclinic space group $P2_1/n$. This is the case for both the nickel(II) complex **(A)** and cobalt(II) complex **(B)**. Examination of **(A)** and **(B)** reveals that they are isomorphous; therefore, only the structure of **(B)** is discussed in detail. The asymmetric unit of **(B)** contains one bis-dipicolinato cobalt (II) complex wherein the ligand is coordinated in a tridentate fashion by two dipicolinato ligands giving rise to a distorted octahedral geometry. The ligand binds through its endocyclic nitrogen and two deprotonated carboxylate oxygen atoms. Two protonated adenine molecules and three molecules of water which complete the asymmetric unit as shown in Figure 4.6.

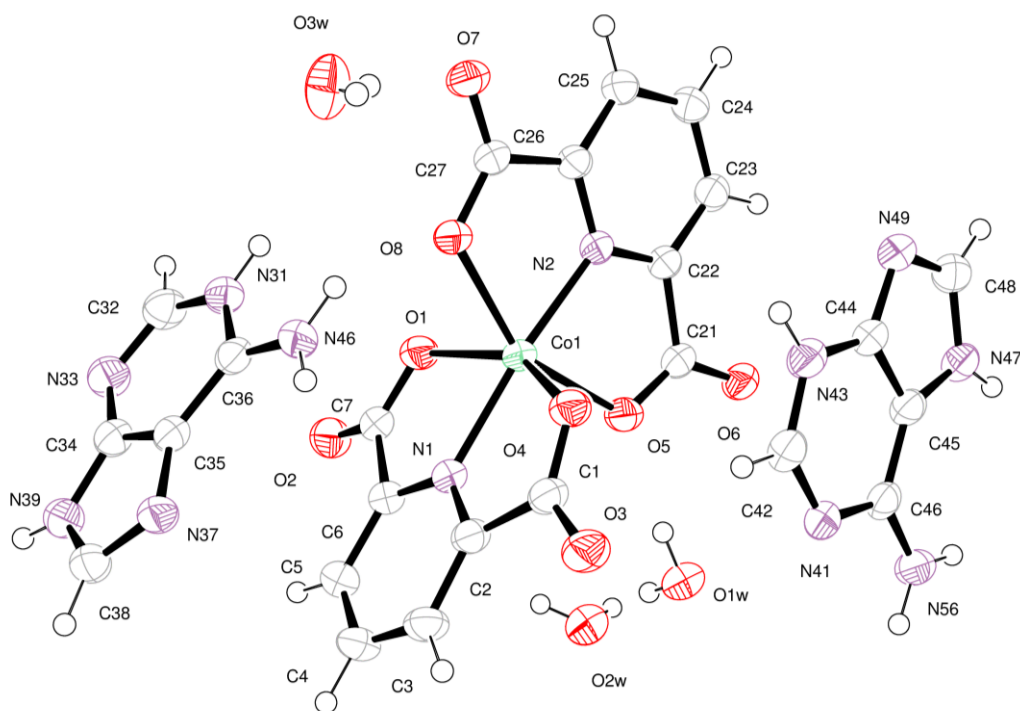


Figure 4.6: Asymmetric unit of compound (B) with atoms at drawn as 50% probability ellipsoids

Layers of alternating organic and inorganic species are linked *via* hydrogen bonding. This arrangement, depicted in Figure 4.7, represents the main feature of crystal packing in the structure. The organic layers comprise the two protonated forms of adenine, namely [1H, 9H AdH⁺] and [3H, 7H AdH⁺]. Figure 4.7 shows that [3H, 7H AdH⁺] cation is stabilised by the carbonyl oxygen, forming a $R_2^1(7)$ heterosynthon, whereas [1H, 9H AdH⁺] forms a single hydrogen bond to the carbonyl oxygen of the other dipicolinato moiety.

The difference in protonation allows the formation of cationic ribbons, which extend along the *c*-axis. The ribbons interact *via* hydrogen bonding to generate a $R_2^2(9)$ homosynthon. Cation interactions observed in this system are in accordance with those reported by Das *et al.*¹⁰⁶, who obtained similar structures with manganese (II) and copper (II) acetate. Rightly, Das *et al.* noted that the interaction between two protonated adenine molecules occurred at the Hoogsteen³⁶ edges of one of the protonated forms.

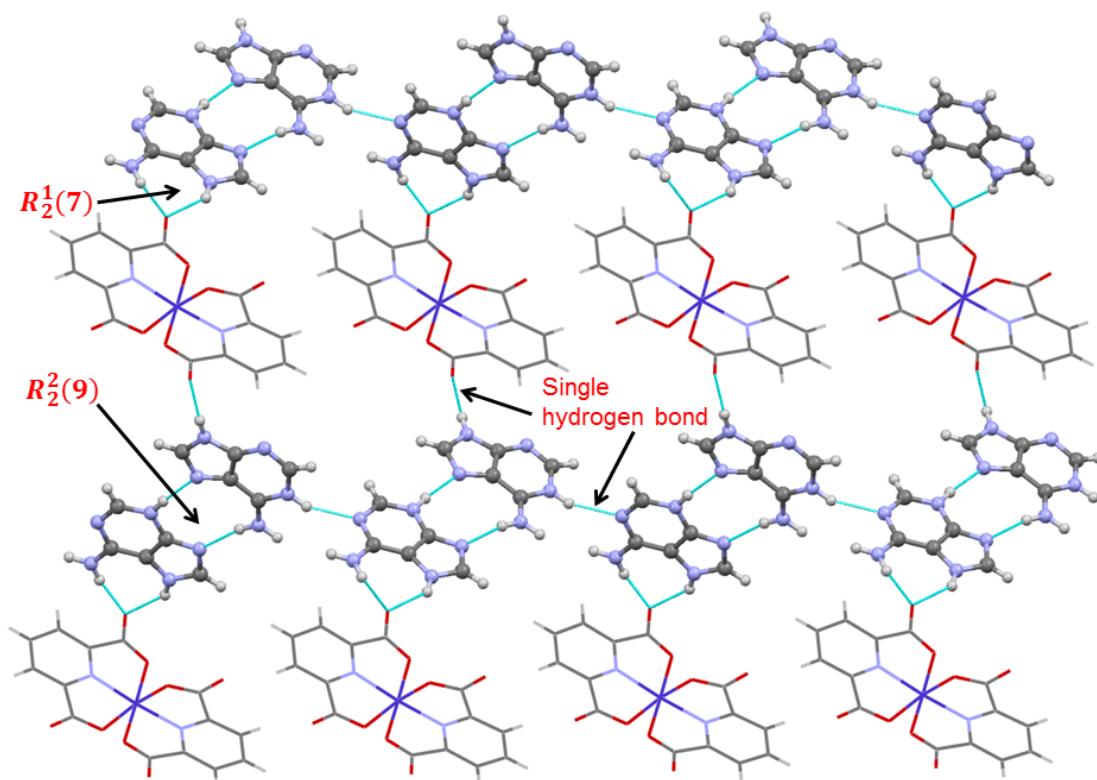


Figure 4.7: View of the alternating organic and inorganic layers along the *b*-axis. Water molecules omitted for clarity

The hydrogen bonding motifs displayed in this structure prompted further literature search in order to understand whether similar hydrogen bonding motifs between adenine (adeninium) molecules were reported elsewhere in other systems. Examination of hydrogen bonding motifs in adeninium shows that the $R_2^2(9)$ interaction present in the current structure expands the adeninium homosynthon reported by Thompson *et al.*⁵⁹, which is presented in Chapter 1, Section 1.7.5 of this thesis.

The $R_2^2(9)$ homosynthon is different from the $R_2^2(8)$ homosynthon observed between two adeninium molecules.⁵⁹ It takes place through the Hoogsteen edge of [1H, 9H AdH⁺] and the basal edge of [3H, 7H AdH⁺]. In addition to the $R_2^2(9)$ homosynthon, the cationic ribbons are involved in another N—H...N interaction between the [1H, 9H AdH⁺] and [3H, 7H AdH⁺]. In this interaction, [1H, 9H AdH⁺] acts as a hydrogen bond donor at its protonated nitrogen site N1 by interacting with the unprotonated N1 in [3H, 7H AdH⁺], which, in turn, acts as a donor. Anion-cation hydrogen bonding further ensures the structural cohesion in the ribbons.

Water molecules provide further stability to this structure by bridging adjacent anionic complexes as shown in Figure 4.8. All water molecules O1W, O2W and O3W are present in their most common environment of hydrogen bonding. These molecules form three hydrogen bonds: two *via* their hydrogen atoms and one *via* the oxygen.⁹⁵ Furthermore, O2W acts simultaneously as a hydrogen bond acceptor to O1W and twice as hydrogen bond donor to the carbonyl oxygen of the dipicolinato complex and O3W. On the other hand, O3W interconnects two adjacent dipicolinato moieties by acting as a hydrogen bond donor. Inspection of the structure revealed only a short contact between O1W and the cation (this interaction is not as visible in the viewing axis in Figure 4.8). The other two water molecules (O2W and O3W) are not involved in hydrogen bonding with any of the adeninium cations; they merely interact with the adjacent anionic moieties.

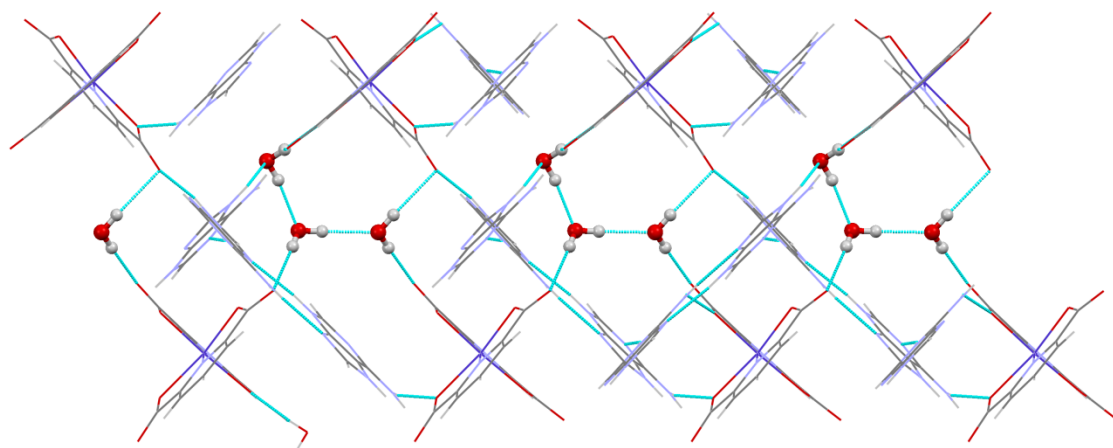


Figure 4.8: View of the crystal packing along the *c*-axis showing the role of water molecules in stabilising the structure

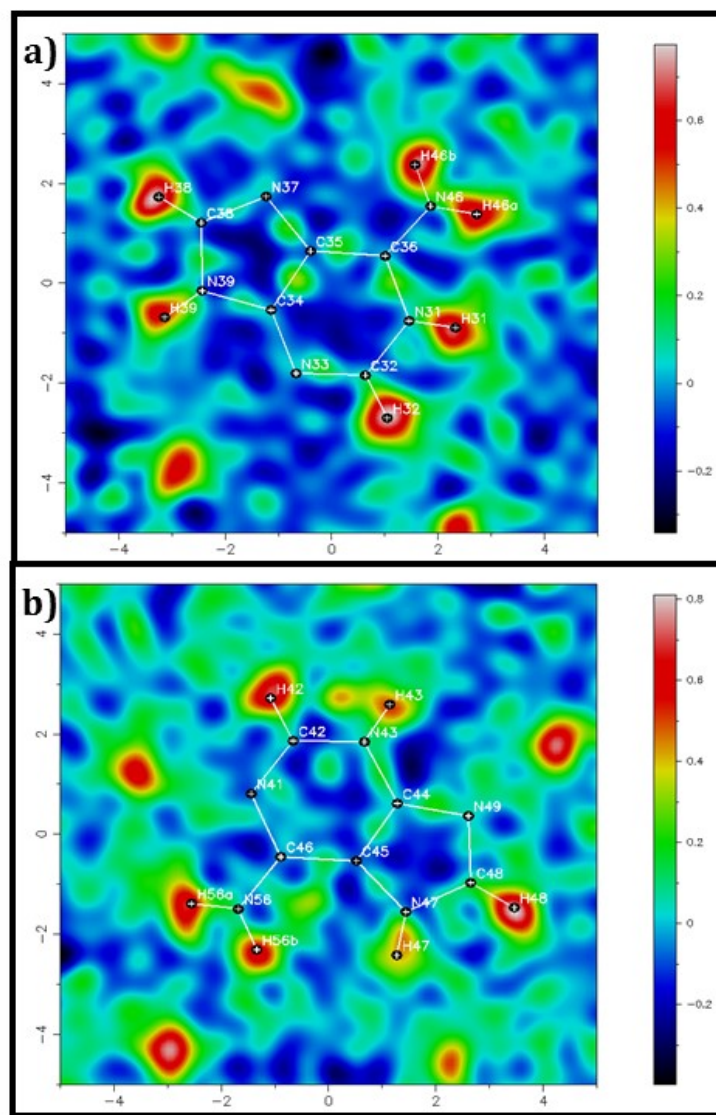


Figure 4.9: Difference Fourier maps showing the location of hydrogen atoms in the cations: a) protonation of [1H,9H AdH⁺]; b) protonation of [3H,7H AdH⁺]

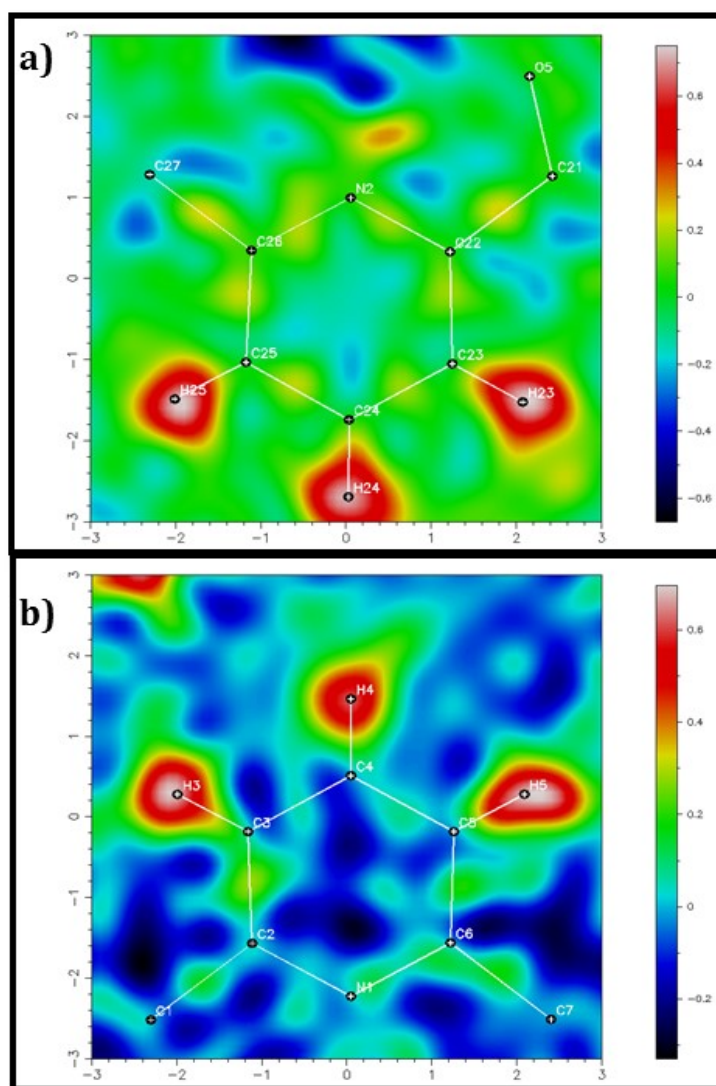


Figure 4.10: Difference Fourier maps showing the location of hydrogen atoms in the ligand: a) protonation of the first dipicolinato ligand; b) protonation of the second dipicolinato ligand

Location of hydrogen atoms in the structure was aided by Fourier maps. The difference map was especially useful for correctly locating the hydrogen atoms in the protonated adenine moieties. It is evident from Figure 4.9 a) and b) that one of the adeninium cations is protonated at the N1 site, whereas the other is protonated at the N3 site. Examination of literature reveals that there are 8 protonated forms of adenine tautomers. However, only two have been reported to be the most stable ones. These are the [1H, 9H]-adeninium and [3H, 7H]-adeninium with the former being the more stable by 32 kJ mol⁻¹.⁶¹

Further evidence for the correct assignment of protons was obtained by examining bond angles at the site of protonation. Singh⁹⁴ highlighted that heterocyclic nitrogen angles which lie in the range $125 \pm 3^\circ$ indicate the attachment of a hydrogen to the nitrogen, whereas angles that lie in the range $116 \pm 3^\circ$ indicates a non-protonated nitrogen. The present structure is consistent with these findings. Table 4.1 shows the bond angles for this structure at the possible sites of protonation. In addition, Figure 4.9 c) and d) show the hydrogen atoms attached to in both dipicolinato moieties clearly.

Table 4.1: Bond angles of neutral and protonated nitrogen atoms

Cation	Bond locations	Bond Angle (°)
[1H, 9H]-adeninium	C32-N31-C36	123.8(2)
	C32-N33-C34	111.7(2)
[3H, 7H]-adeninium	C42-N41-C46	119.8(2)
	C42-N43-C44	117.19(19)

It is evident from the Fourier map that in [1H, 9H]-adeninium position N31 is protonated and this agrees with the bond angle increase to $123.8(2)^\circ$, whereas the neutral N33 position has a smaller bond angle as predicted by Singh. On the other hand, there appears to be a discrepancy with Singh's results in [3H, 7H]-adeninium where the protonated N41 and the neutral N43 have very close bond angles, but that of the protonated site is significantly larger.

Selected hydrogen bonds are listed in Table 4.2.

Table 4.2: Hydrogen-bond parameters of (B)

D-H	A	d (D-H) (Å)	d (H...A) (Å)	d (D...A) (Å)	<D-H...A (°)
N31-H31	N41 ⁱ	0.88	2.118	2.943(3)	155.94
N39-H39	O2 ⁱⁱ	0.88	1.865	2.738(3)	170.82
N43-H43	N37 ⁱⁱⁱ	0.88	1.973	2.845(3)	170.23
N46-H46A	O8	0.88	1.993	2.752(3)	143.7
N46-H46B	N49 ^{iv}	0.88	2.124	2.990(3)	167.75
N47-H47	O6 ^v	0.88	2.115	2.872(2)	143.76
N47-H47	O1W ^v	0.88	2.342	2.937(3)	124.99
N56-H56A	O1 ^{vi}	0.88	1.979	2.773(3)	149.49
N56-H56B	O6 ^v	0.88	1.868	2.736(3)	168.51
O1W-H1A	O5	0.84(2)	1.94(2)	2.779(2)	176(3)
O3W-H3A	O7	0.79(2)	1.93(2)	2.722(3)	177(3)
O1W-H1B	O2W	0.81(2)	1.94(2)	2.750(3)	170(3)
O2W-H2A	O3 ^{vii}	0.80(2)	2.00(2)	2.795(3)	169(3)
O3W-H3B	O2 ^{viii}	0.80(2)	2.14(2)	2.935(3)	178(3)
O2W-H2B	O3W ^{ix}	0.81(2)	1.93(2)	2.745(3)	176(4)

ⁱ [x-1, y, z]; ⁱⁱ [-x+1, -y+1, -z+1]; ⁱⁱⁱ [x+1/2, -y+1/2, z+1/2]; ^{iv} [x-1/2, -y+1/2, z-1/2];
^v [-x+3, -y+1, -z+2]; ^{vi} [x+1, y, z]; ^{vii} [-x+5/2, y+1/2, -z+3/2]; ^{viii} [-x+3/2, y-1/2, -z+3/2];
^{ix} [-x+3/2, y+1/2, -z+3/2]

Bond length variations were noted in the coordination of the nickel (II) and cobalt (II) with the ligand. Table 4.3 shows that cobalt-ligand bonds are generally longer than the nickel-ligand bonds reflecting the slightly larger size of the cobalt (II) ion.

Table 4.3: Differences in metal-ligand bond lengths for the nickel (II) complex (A) and cobalt (II) complex (B)

Bond	Length Co (Å)	Length Ni (Å)
M(1)-N(1)	2.0189(18)	1.964(3)
M(1)-N(2)	2.0206(18)	1.963(2)
M(1)-O(1)	2.1737(15)	2.143(2)
M(1)-O(4)	2.1046(15)	2.090(2)
M(1)-O(5)	2.1538(15)	2.113(2)
M(1)-O(8)	2.1484(14)	2.126(2)

4.4.3.2 Structure of $[1\text{H CytH}^+]_2[\text{Co}(\text{dip})_2(\text{H}_2\text{O})_3]$

The metal-dipicolinato complexes of cytosine with nickel(II), complex **(C)**, and cobalt(II), complex **(D)**, crystallise in the triclinic space group $P\bar{1}$. Since these structures are isostructural, only the structure of the cobalt(II) analogue is discussed. Figure 4.11 shows the asymmetric unit of **(D)**, which contains one cobalt(II) coordinated by two tridentate dipicolinate anions to generate an approximately octahedral geometry. Two symmetry independent cytosinium cations and five water molecules complete the asymmetric unit.

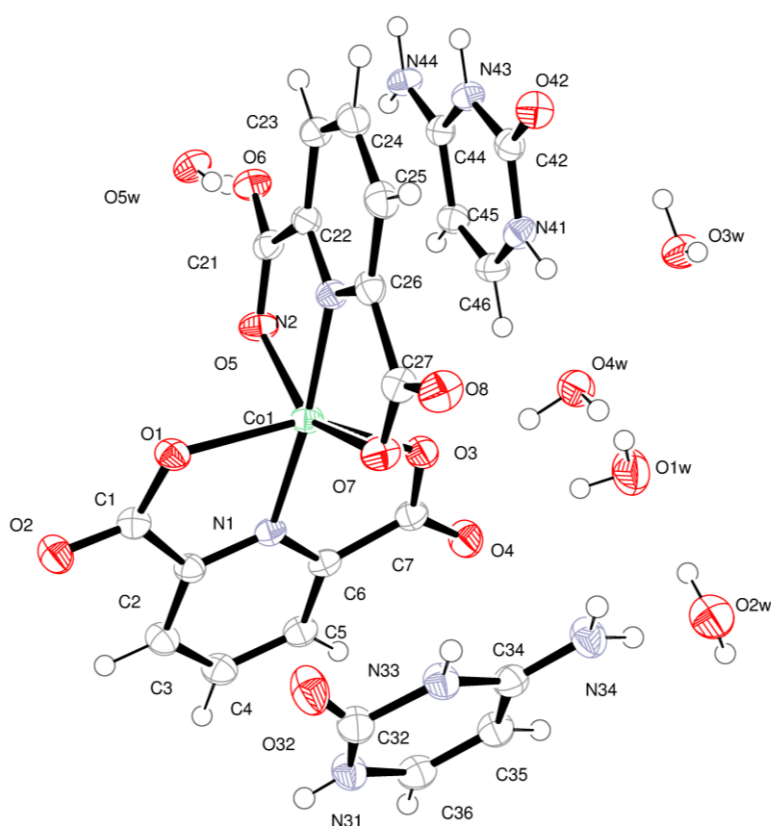


Figure 4.11: Asymmetric unit of compound **(D)** with atoms drawn as 50% probability ellipsoids

Crystal packing in the structure is governed by hydrogen bonding between the alternating organic cations and inorganic anions. The five water molecules in the structure provide further cohesion to the crystal structure. Contrary to the adeninium case discussed earlier, cytosinium cations do not interact directly with each other to form infinite ribbons. Instead, there is a pronounced hydrophobic interaction in the form of π - π stacking of each cation with the dipicolinato ligands. The mean separation plane for the first cytosinium cation is 3.73(3) Å (centroid to centroid 4.049(4) Å), whereas the second cation is stacked with the dipicolinato ligand with a mean plane separation of 3.294(16) Å (centroid to centroid 3.91(5) Å). It therefore transpires that the first cytosinium cation has weaker π - π stacking compared to the second cytosinium cation, but this is compensated with hydrogen bonding of this cation to two water molecules.

The two symmetry independent cytosinium cations display distinct hydrogen bonding motifs. The first cytosinium cation (depicted in Figure 4.12a) interacts with O2W and O3W. It also forms a hydrogen bond with the anion *via* its N31 site, but this has been omitted from the figure for clarity. The second cytosinium cation, depicted in Figure 4.12b), displays a different hydrogen bonding motif. Apart from interacting with two anions *via* the two hydrogens in the amine group N44, this cation is assisted by a water molecule (O4W) to interact with its symmetry generated counterpart. This interaction generates a $R_4^4(12)$ heterosynthon. This is an example of water inclusion to assist the interaction between bases. Both cytosinium molecules display an imbalance in the ratio of hydrogen bond donors and acceptors. There are four strong hydrogen bond donors and only one hydrogen bond acceptor in each of the cations. It was argued that inclusion of water molecules in such cases may take place in an attempt to reduce the imbalance between hydrogen bond donors and acceptors.¹⁸² In addition, Etter *et al.*²¹ argue that all good hydrogen bond donors and acceptors are involved in hydrogen bonding. Based on this argument, hydration helps one of the cations to interact with its symmetry generated counterpart because water is indeed a good hydrogen bond donor and acceptor.

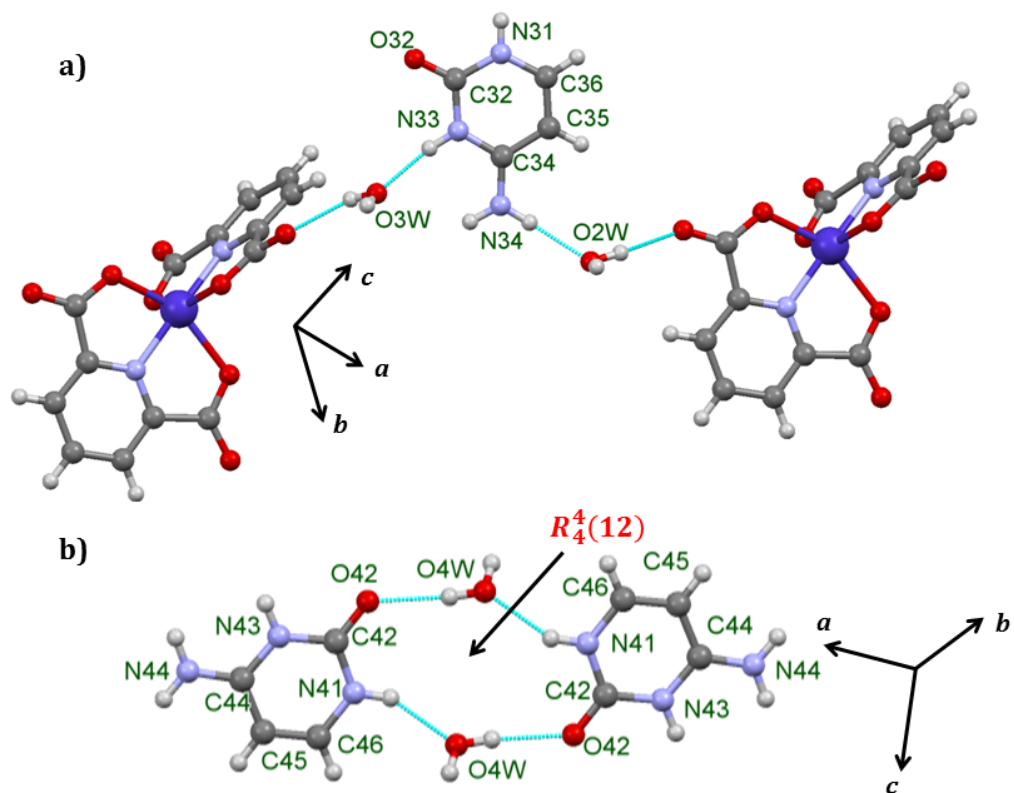


Figure 4.12: Hydrogen bonding motifs in two symmetry independent cytosinium cations. (Direct interactions with the anion have been omitted for clarity.)

Table 4.4: Hydrogen bond parameters for (D)

D-H	A	d (D-H) (Å)	d (H···A) (Å)	d (D···A) (Å)	<D-H···A (°)
N31-H31	O2 ⁱ	0.872	1.961	2.833(2)	176.52
N33-H33	O3W	0.88	1.83	2.700(2)	168.88
N34-H34A	O42 ⁱⁱ	0.898	2.128	2.873(2)	139.72
N34-H34A	O3W	0.898	2.557	3.249(2)	134.39
N34-H34B	O2W ⁱⁱⁱ	0.898	1.895	2.782(2)	168.88
N41-H41	O4W ^{iv}	0.884	1.939	2.756(2)	152.87
N43-H43	O5W	0.88	1.892	2.770(2)	175.24
N44-H44A	O6	0.886	1.927	2.7774(18)	160.36
N44-H44B	O1 ^v	0.886	1.945	2.802(2)	162.01
O3W-H3B	O8 ⁱⁱⁱ	0.885(18)	1.896(18)	2.7769(19)	174(3)
O3W-H3B	O7 ⁱⁱⁱ	0.885(18)	2.53(2)	3.1414(19)	127(2)
O2W-H2A	O4 ^{vi}	0.867(18)	1.865(19)	2.731(2)	177(3)
O5W-H5B	O6	0.82(3)	1.96(3)	2.7471(19)	163(3)
O4W-H4A	O42 ^{vii}	0.85(2)	1.949(19)	2.7908(19)	173(3)
O4W-H4B	O3	0.842(18)	1.965(18)	2.7602(18)	157(3)
O5W-H5A	O2 ⁱⁱⁱ	0.870(19)	1.92(2)	2.777(2)	169(3)
O2W-H2B	O1W	0.854(18)	1.933(18)	2.783(3)	174(3)
O3W-H3A	O8 ^{vii}	0.846(18)	1.99(2)	2.7741(19)	155(2)
O1W-H1A	O4W	0.864(18)	2.11(2)	2.944(2)	163(3)
O1W-H1B	O4	0.842(18)	1.948(19)	2.779(2)	169(3)

ⁱ [-x+1, -y, -z+2]; ⁱⁱ [x, y+1, z]; ⁱⁱⁱ [x+1, y, z]; ^{iv} [-x+2, -y, -z+1]; ^v [-x+1, -y, -z+1]; ^{vi} [-x+1, -

y+1, -z+2]; ^{vii} [x-1, y+1, z]; ^{viii} [x-1, y+1, z]

Fourier maps were utilised for the correct assignment of hydrogen atoms in the crystal structure. As it can be seen from Figure 4.13 a) and b), both cytosinium cations are protonated and these images provide further evidence on the imbalance between hydrogen bond donors and acceptors in the crystal. Figure 4.14 a) and b) confirm the location of hydrogen atoms in the two dipicolinato moieties.

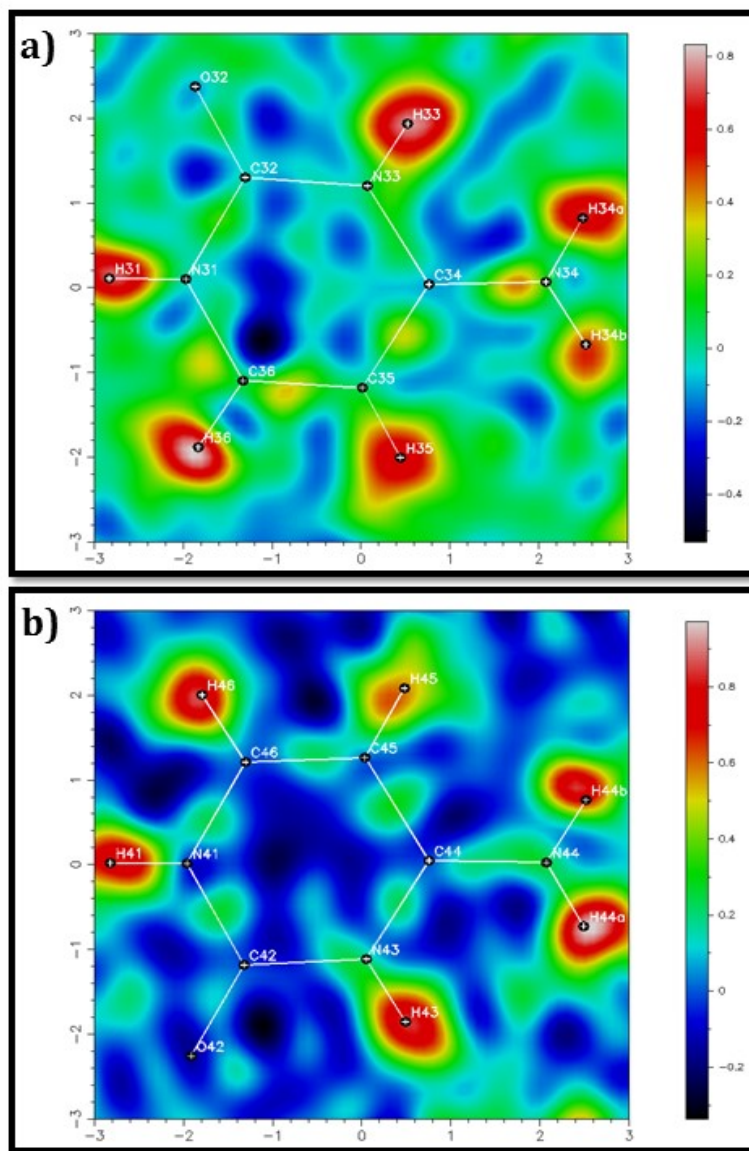


**Figure 4.13: Difference Fourier maps showing the location of hydrogen atoms:
a) protonation of first cytosinium cation b) protonation of second cytosinium cation**

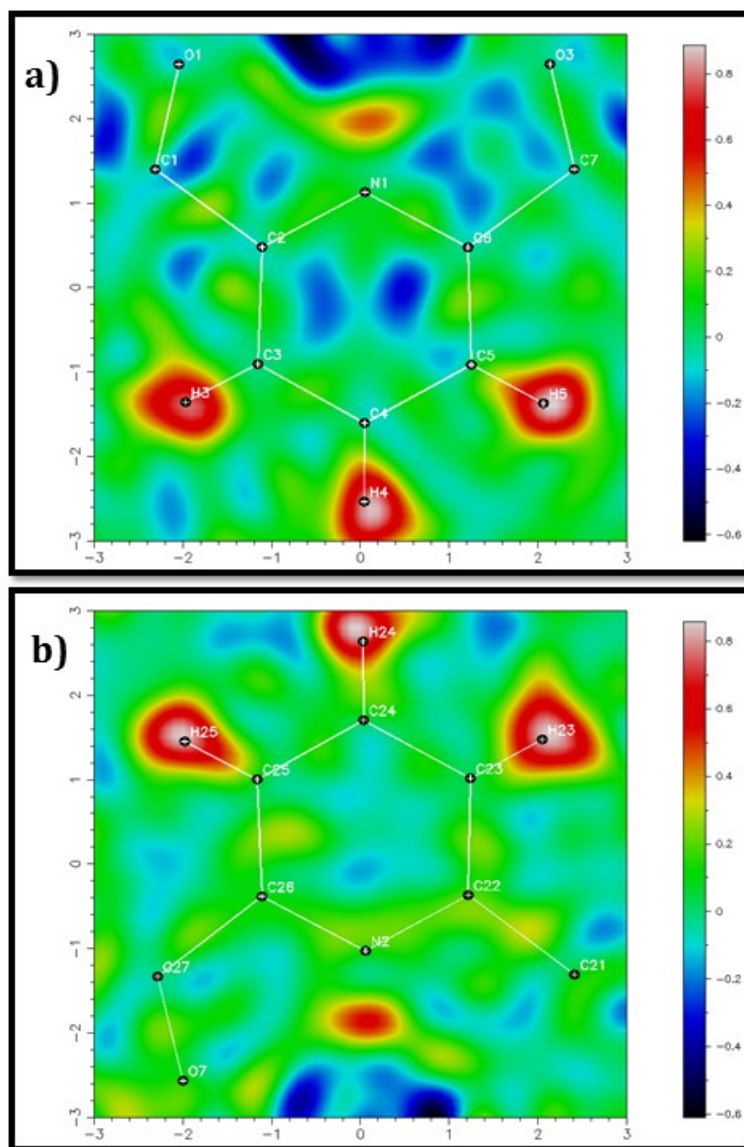


Figure 4.14: Difference Fourier maps showing the location of hydrogen atoms in the ligands: a) proton locations in the first dipicolinato ligand; b) proton locations in the second dipicolinato ligand

4.4.3.3 Structure of [1H CytH⁺]₂[Co(dip)₂] – anhydrous form

A novel material was obtained following treatment of the cobalt-dipicolinato mixture with cytosine in methanol. The crystals produced were red and block-shaped. This compound, **(E)**, crystallises in the triclinic space group $P\bar{1}$. The asymmetric unit of **(E)** contains one *bis*-dipicolinato cobalt(II) complex. Similar to the examples described above, the ligand is coordinated in a tridentate fashion to generate a distorted octahedral geometry. Two symmetry independent cytosinium molecules complete the asymmetric unit. This crystal contains no water molecules and the overall packing and hydrogen bonding motifs will be compared to the pentahydrate form.

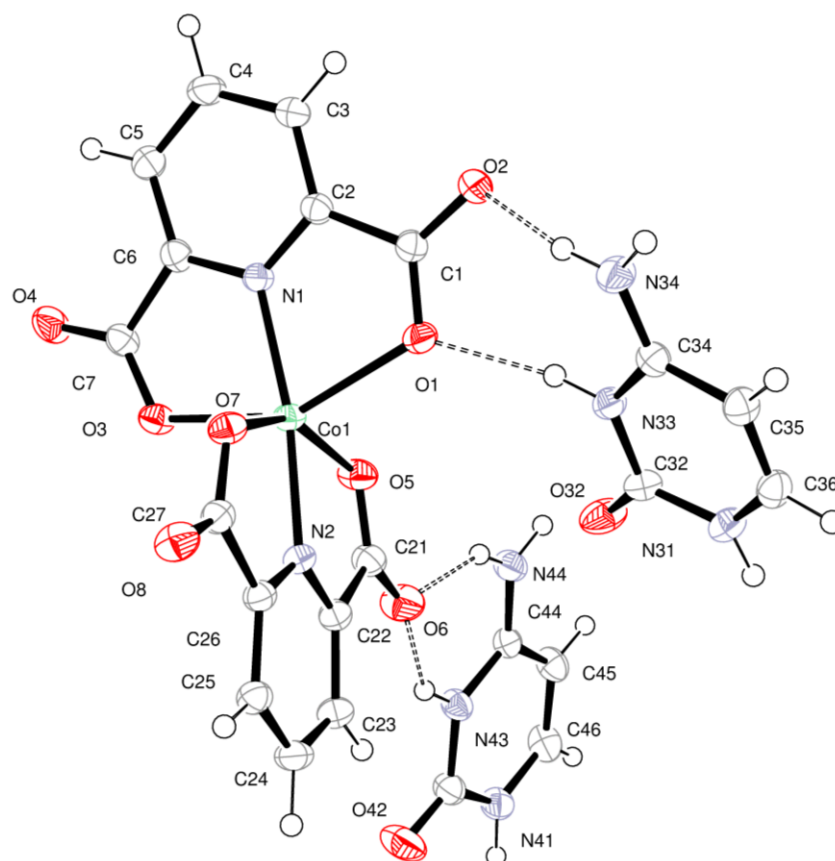


Figure 4.15: Asymmetric unit of **(D)** with atoms drawn as shown 50% probability ellipsoids. Dashed lines represent hydrogen bonds

Hydrogen bonding interactions between the anion and the cation generate layers of alternating organic and inorganic species as shown in Figure 4.16. Each symmetry independent cytosinium cation acts as a donor and forms hydrogen bonds with the metal-ligand complex.

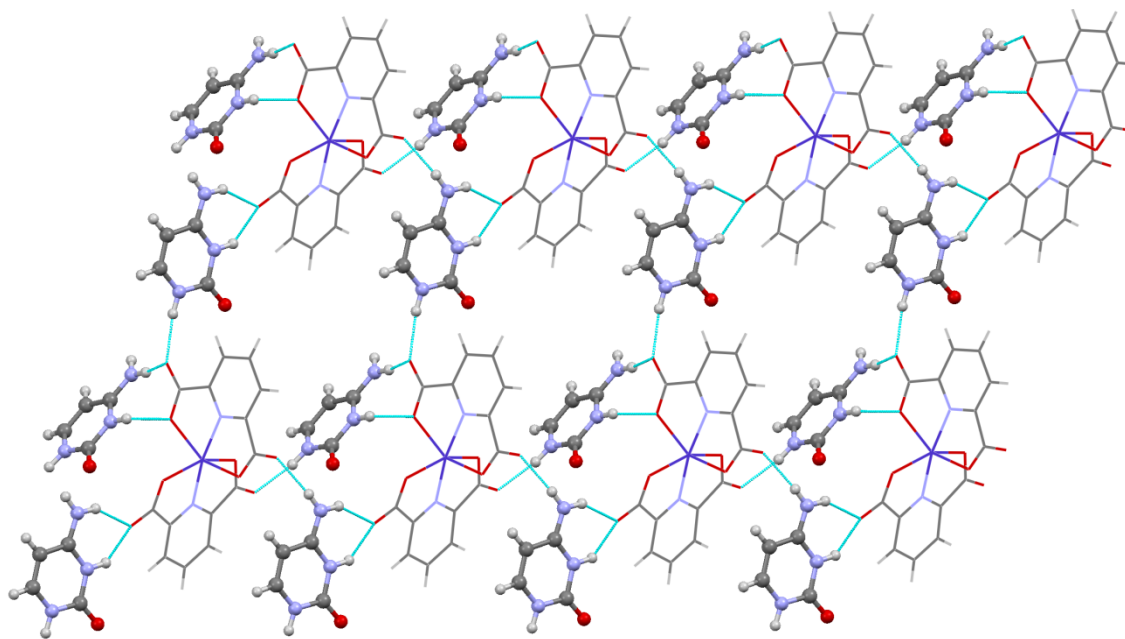


Figure 4.16: Crystal packing in (D) viewed along *b*-axis

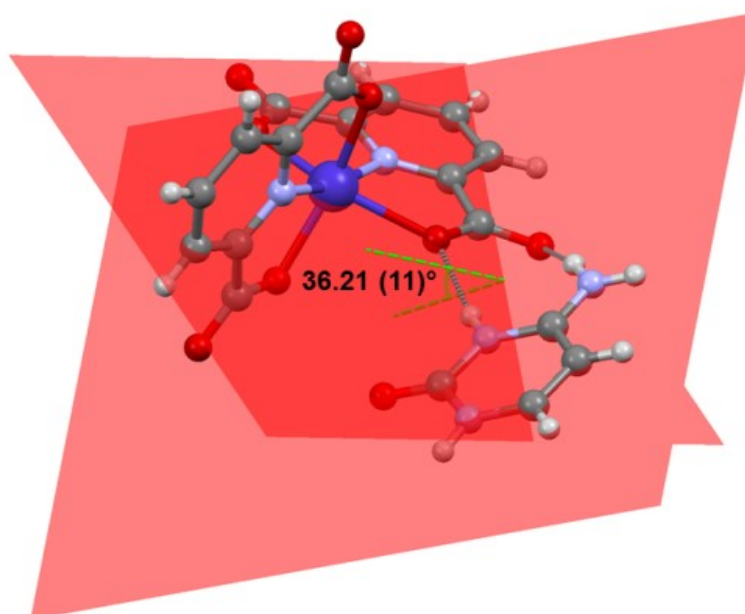


Figure 4.17: Deviation of $R_2^2(8)$ heterosynthon from planarity by $36.21(11)^\circ$

A $R_2^2(8)$ heterosynthon is formed between the first cytosinium cation and the dipicolinato fragment. The heterosynthon is generated *via* N34—H34A···O2 of length 2.792(2) Å and N33—H33···O1 of length 2.805(2) Å and both of these distances are normal despite the twist, where the deviation from planarity was calculated as 36.2(11)° as shown in Figure 4.17. The second cytosinium interacts with the other dipicolinato fragment to generate a $R_2^1(7)$ heterosynthon. Similar to the hydrated form of cytosinium discussed earlier, cytosinium cations do not form a ribbon either. However, in the anhydrous form the first cytosinium cation interacts with its symmetry generated counterpart *via* π - π stacking. The mean plane separation between these two is 3.23(3) Å (centroid to centroid 3.7195 (4) Å) and is generated by the following symmetry operator: 1-x, 1-y, -z. Such plane separation is suggestive of rather strong π - π stacking interactions. The two stacked cations are further stabilised by the carboxylate group of the anion *via* N31—H31···O8 and N34—H34B···O7 hydrogen bonds as shown in Figure 4.18. The second cytosinium interacts with the anion *via* N41—H41···O2 and is placed perpendicular to each of the stacked cytosinium cations. Hydrogen bond parameters are shown in Table 4.5.

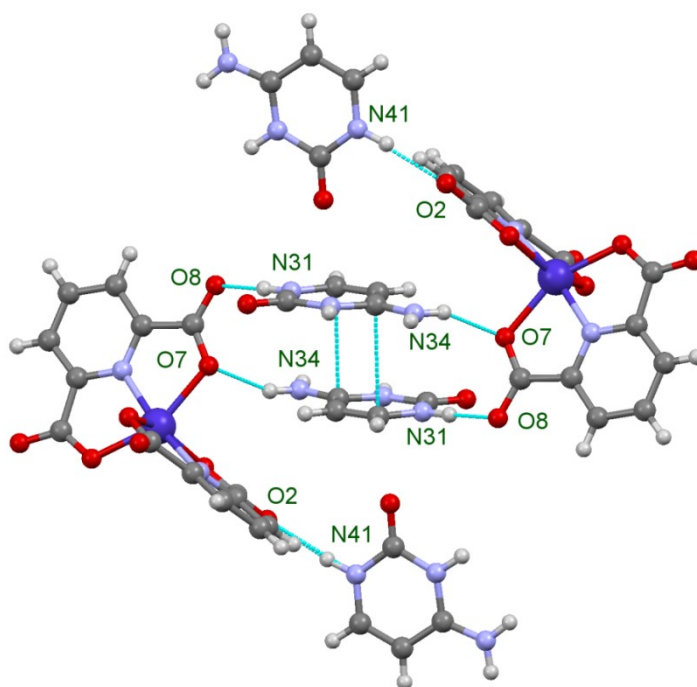


Figure 4.18: Cation-cation stacking for the first cytosinium with a mean plane separation of 3.23(3) Å and centroid to centroid distance of 3.7195 (4) Å

Table 4.5: Hydrogen bond parameters for (D)

D-H	A	d (D-H) / (Å)	d (H...A) (Å)	d (D...A) (Å)	<D-H...A (°)
C3-H3	O5 ⁱ	0.95	2.38	2.929(2)	116.0
C23-H23	O32 ⁱⁱ	0.95	2.43	3.107(2)	127.8
C36-H36	O4 ⁱⁱⁱ	0.95	2.2	3.058(2)	149.9
C46-H46	O3 ^{iv}	0.95	2.29	3.153(2)	150.8
N31-H31	O8 ^v	0.89	1.89	2.763(2)	168.1
N33-H33	O1	0.91	1.94	2.805(2)	159.2
N34-H34A	O2	0.89	1.93	2.792(2)	164.7
N34-H34B	O7 ^{vi}	0.89	1.96	2.798(2)	157.2
N41-H41	O2 ^{vii}	0.91	1.97	2.878(2)	171.4
N43-H43	O6	0.91	1.95	2.754(2)	147
N44-H44A	O6	0.88	1.96	2.743(2)	146.6
N44-H44B	O4 ^v	0.88	1.96	2.744(2)	147.5

ⁱ [-x, -y, -z]; ⁱⁱ [-x+1, -y+1, -z+1]; ⁱⁱⁱ [x+1, y+1, z]; ^{iv} [-x+1, -y, -z+1]; ^v [x+1, y, z];

^{vi} [-x, -y+1, -z]; ^{vii} [x+1, y, z+1]

4.4.3.3.1 Anhydrous vs pentahydrate form

Contrary to the structure with adeninium where ribbon formation between cations was observed, the cytosinium analogues (both anhydrous and pentahydrate) displayed no such hydrogen bonding motif. Hydrophobic interactions appear to be the dominating interaction between two symmetry equivalent cytosinium cations, which are π - π stacked. The second cation displays neither π - π stacking nor hydrogen bonding interactions with its symmetry equivalent. It is simply stabilised *via* hydrogen bonding to the metal-ligand anion.

However, inclusion of water molecules was associated with remarkable changes in crystal packing compared to the anhydrous form. Water molecules acts as spacers and assist the interaction between two symmetry equivalent cytosinium cations by generating a $R_4^4(12)$ heterosynthon. This is another example where inclusion of water changes the crystal packing to maximise favourable hydrogen bonding in the crystal. The second cytosinium did not form any interaction with its symmetry equivalent counterpart. Presumably, in the

presence of water, this molecule is incorporated in the structure and form hydrogen bonds to generate the lowest energy form. But, in the absence of water, the structure is different and the minimum energy structure observed is stabilised by different intermolecular interactions.

4.4.3.4 Unsuccessful Reactions with Guanine, Thymine and Uracil

The design of similar architectures with guanine and thymine was also envisaged during this project. However, these attempts failed to produce crystals mainly due to solubility challenges. Guanine proved difficult to dissolve, whereas reactions with thymine were associated with the precipitation of this molecule. Challenges with the solubility of guanine were prevalent throughout this research. It proved possible to overcome this challenge by altering the pH of the system. Similar attempts have been tried while treating guanine with the metal-dipicolinato mixture; however, this approach did not yield any crystals.

A plausible explanation for the precipitation of thymine could be the fact that it has no basic sites available for protonation. It is evident from our examples that complexation of with metal (II) acetate with dipicolinic acid generates an approximately octahedral geometry with a -2 charge. Charge neutralisation in these systems is achieved by protonation of the nucleobases. While adenine and cytosine have such sites available, thymine does not. Hence, it could conceivably be argued that this is the reason why thymine precipitates and does not get incorporated in the crystal. Similar reaction with uracil were also associated with uracil precipitation. Therefore, the same explanation can be extended to uracil given that, apart from the missing methyl group, it is structurally similar to thymine.

4.5 Engineering of H-Bonded Networks with Carboxylic Acid Derivatives of Nucleobases: Thymine Acetic Acid and Orotic Acid

4.5.1 Introduction

Throughout the research described in this thesis, thymine and uracil posed synthetic challenges due to their rapid precipitation. To circumvent these problems, alternative synthetic approaches were sought. The prime aim was to explore the hydrogen bonding interactions displayed by these two bases. One of the approaches entailed the use of carboxylic acid derivatives of thymine and uracil. The idea was that these chelating agents could both can bind metal centres and can be involved in hydrogen bonding *via* peripheral sites.¹⁸³ It was envisaged that deprotonation of the carboxylic acid group in aqueous media would ameliorate the overall solubility. This, in turn, would enable us to engineer hydrogen bonded networks containing these two nucleobases.

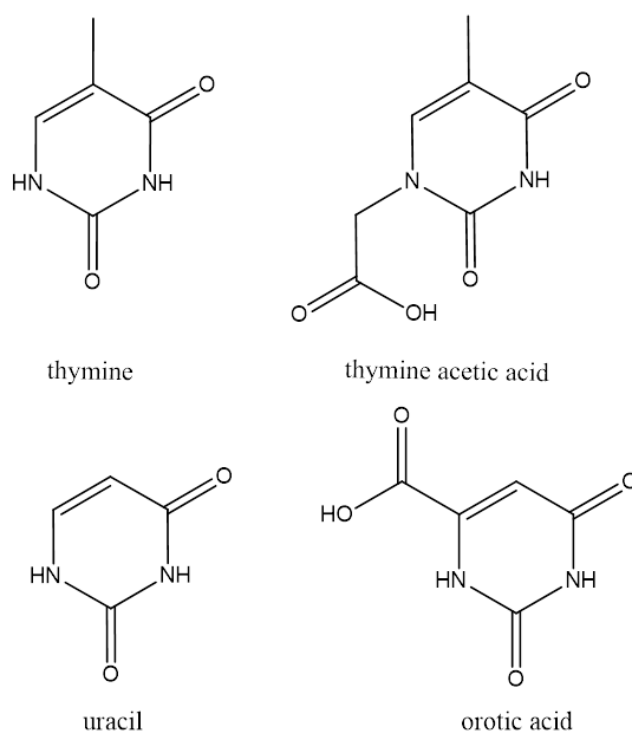


Figure 4.19: Carboxylic acid derivatives of thymine and uracil

4.5.1.1 CSD Survey

The Cambridge Structural Database¹³ (CSD version 5.35, November 2013) was searched for crystals containing thymine acetic acid and orotic acid. The search was carried out using the software ConQuest and the following filter was applied: “3D coordinates determined”. The search for thymine acetic acid revealed 7 entries, none of which contained complexation with metals. On the other hand, the search for orotic acid produced 151 entries, of which 94 displayed the complexation of orotic acid with transition metals.

4.5.1.2 Thymine Acetic Acid Binding

The discrepancy in the number of structures in metal-ligand complexes with orotic acid and thymine acetic acid is striking. It appears that complexation of thymine acetic acid has either not been explored at all, or there could be other challenges which inhibit crystal growth. This may be a reflection of the ease with which deprotonated orotic acid forms 5-membered chelate rings.

4.5.1.3 Orotic Acid Binding

Orotic acid or Vitamin B13¹⁸⁴ is a member of pyrimidine carboxylic acids. The existence of 94 crystal structures of its complexation with metals is an indication that this compound is a good metal binder. From a supramolecular perspective, orotic acid is a useful tool in the construction of supramolecular architectures. The reason for this is twofold: it has proton donors and acceptors capable of hydrogen bonding and it is also able to interact *via* π - π interactions.¹⁸⁵

The acid is a very poor binder to metals, but when deprotonated it displays a multidentate coordination behaviour. Examination of its structure reveals that there are various sites for coordination to the metal atom upon deprotonation. Complexation to a metal can occur via one of the two N atoms from the pyrimidine ring, the carboxylate group and the two carbonyl oxygen atoms. However, the latter is unlikely.

Complexation of orotic acid varies depending on the level of deprotonation. The monoanionic orotate arises due to the deprotonation of the carboxylic acid group, and it has a $pK_{a1}=2.09$.¹⁸⁶ The dianionic orotate forms upon the deprotonation of both the carboxylic group and the N(3) hydrogen, with a $pK_{a2}=9.45$.¹⁸⁶ Figure 4.20 shows the two deprotonated versions of orotic acid. The level of deprotonation affects the coordination behaviour with the metal. Kose *et al.*¹⁸⁷ divide the complexes in mononuclear or polynuclear complexes.

It is evident from Figure 4.20 that the singly deprotonated orotate anion **(b)** acts as a bidentate ligand, whereas the doubly deprotonated orotate anion **(c)** is likely to act as a bidentate chelate ligand. The coordination in **(c)** via the N atom of the pyrimidine ring and the carboxylic group leads to the formation of a five-membered chelate ring as reported by Wysokinski *et al.*¹⁸⁸ and Mutikainen *et al.*¹⁸⁹

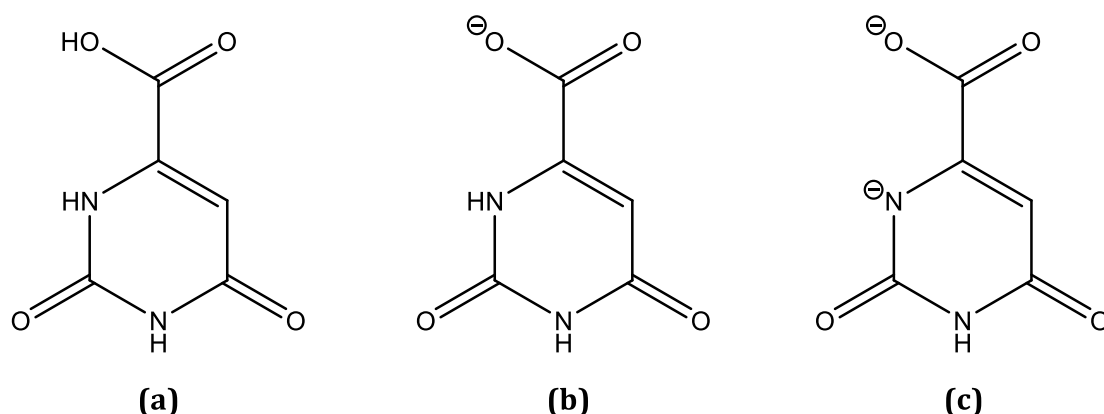


Figure 4.20: Deprotonation of orotic acid: (a) orotic acid; (b) monoanionic orotate; (c) dianionic orotate¹⁸⁶

Kose *et al.*¹⁸⁷ described the mononuclear complexes as structures where the orotate dianions act as a bidentate ligand by coordinating to the metal centre via the two deprotonated sites shown in Figure 4.20 **(c)** and in this way forming a five-membered ring.

4.5.2 Structures with orotic acid

4.5.2.1 Orotic acid as the sole organic ligand

Structures with the coordination of orotic acid or its halide substituted derivatives to metals were first reported in 1980. Sabat *et al.*¹⁹⁰ studied the structure of nickel(II) orotatotetraaqua monohydrate and highlighted the hydrogen bonding in the structure. Sabat and co-workers observed the existence of strong intermolecular and intramolecular interactions in the structure. Similar work was also conducted by Karipides *et al.*¹⁹¹ in 1986, who reported the structures of nickel(II) and zinc(II) orotate complexes. These structures were similar to those presented by Sabat *et al.* with comparable bond angles within the five-membered chelate ring.

In 2002, Wysokinski *et al.*¹⁸⁸ reinvestigated the structure of nickel(II) orotatotetraaqua monohydrate and reported the emergence of new structural features relating to the position of lattice water molecules and the hydrogen bonding in the crystal. Wysokinski *et al.* compared their work with that of Sabat *et al.* and pointed out that, contrary to Sabat's reports, there is hydrogen bonding between two orotate molecules, which lead to the formation of a $R_2^2(8)$ centrosymmetric dimer as categorised by Etter *et al.*³¹ in 1990. Substituted orotates have also been used for complexation with transition metals. For example, Schneider *et al.*¹⁹² reported the complexation of 5-fluoroorotic acid with nickel (II).

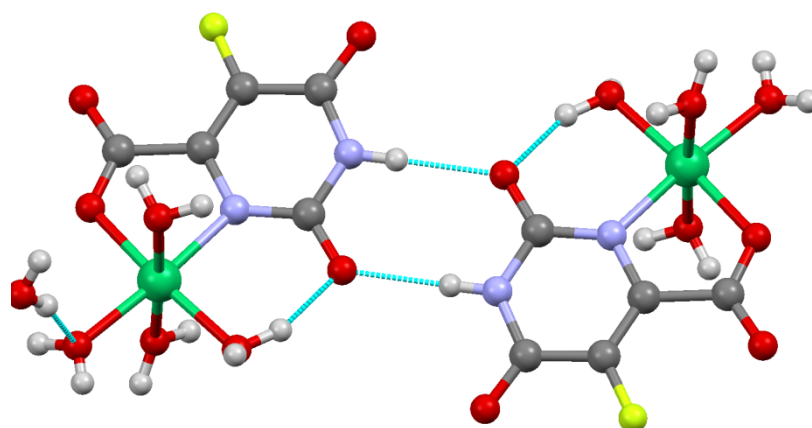


Figure 4.21: Complexation of nickel (II) with fluoro-orotic acid¹⁹²

4.5.2.2 Orotic acid with N-donors

The monodentate binding of imidazoles was exploited by Ucar *et al.*¹⁸⁴ in order to design crystals which incorporate the coordination of both the imidazole and the orotate ligand to the metal. The title compound reported by Ucar *et al.* consisted of the orotate ligand bound to the metal in a bidentate fashion, two monodentate imidazole ligands and two water molecules completing the octahedron.

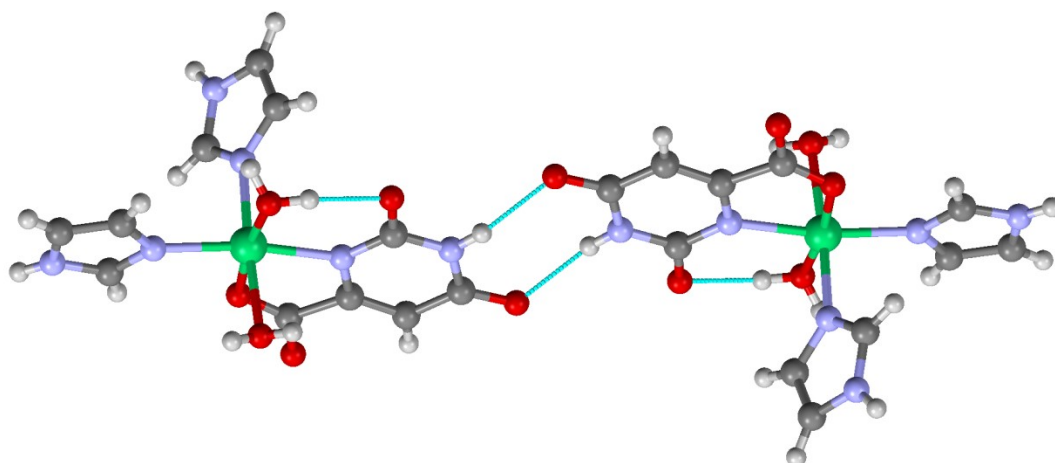


Figure 4.22: Complexation of orotic acid and imidazoles with nickel¹⁸⁴

It was reported that the crystal packing in this complex is facilitated by the presence of strong intermolecular hydrogen bonding, π - π interactions. Ucar *et al.* put emphasis on the formation of a $R_2^2(8)$ centrosymmetric dimer between the orotate ligands. The emergence of this dimer was previously reported by Wysokinski and co-workers.

Analysis of the CSD revealed further crystal structures, where organic bases are used in conjunction with orotic acid. These organic bases bind to the metal centre via their tertiary N atom. Other examples found in CSD involving organic bases include 2-methylimidazole reported by Erer *et al.*¹⁹³, methylethylenediamine reported by Yesilel *et al.*¹⁹⁴ where each metal centre is bound in an octahedral geometry.

4.5.3 Experimental

4.5.3.1 Single crystal preparation

4.5.3.1.1 [Ni(oro)(py)₂(H₂O)₂]

Nickel (II) acetate (0.125 g, 0.5 mmol) and orotic acid (0.087 g, 0.5 mmol) were dissolved in 20 mL water:ethanol (15:5) and stirred for 30 min at 60 °C. Pyridine (8 μ L, 0.5 mmol) was added to the mixture and this was stirred for further 10 min. Blue block-shaped crystal were obtained after three weeks.

4.5.3.1.2 Cobalt analogue: Form (G) and Form (H)

Cobalt (II) acetate (0.125 g, 0.5 mmol) and orotic acid (0.087 g, 0.5 mmol) were dissolved in 20 mL water:ethanol (15:5) and stirred for 30 min at 60 °C. Pyridine (8 μ L, 0.5 mmol) was added to the mixture and this was stirred for further 10 min. Orange block-shaped crystal were obtained after three weeks.

4.5.3.1.3 [Ni(oro)(3-nic)(H₂O)₆]

Nickel (II) acetate (0.125 g, 0.5 mmol) and orotic acid (0.087 g, 0.5 mmol) were dissolved in water (20 mL) and stirred for 30 min at 60 °C. 3-nicotinamide (0.061 g, 0.5 mmol)

dissolved in water (5 mL) was added to the mixture, which was stirred for further 10 min. Blue block-shaped crystal were obtained after few days.

4.5.3.1.4 [Ni₂(oro)₂(4-nic)₂(H₂O)₉]

Nickel (II) acetate (0.125 g, 0.5 mmol) and orotic acid (0.087 g, 0.5 mmol) were dissolved in water (20 mL) and stirred for 30 min at 60 °C. 4-nicotinamide (0.061 g, 0.5 mmol) dissolved in water (5 mL) was added to the mixture, which was stirred for further 10 min. Blue block-shaped crystal were obtained after few days.

4.5.3.2 Single Crystal X-ray measurements

Routine single crystal data collection procedures outlined previously were followed. Refinement of the two cobalt polymorphs was performed with isotropic displacement parameters due to the low percentage of observed data. Further explanation is provided in the structure analysis section.

4.5.4 Results and Discussion

The five novel crystal structures presented herein are divided into two parts. The first part (Section 4.5.4.1 and 4.5.4.1.2) is focused upon the complexation of nickel (II) and cobalt (II) with orotic acid in the presence of pyridine. Emergence of two polymorphs in the cobalt (II) analogue is analysed. Structural differences between the two polymorphs are compared to one another and to the nickel (II) analogue, which is monomorphous.

The second part (Section 4.5.4.1.3) presents results on the complexation of orotic acid with transition metals in the presence of 3-nicotinamide. This study investigates the effect of varying hydration levels and pseudo-symmetry on synthon formation and crystal packing.

4.5.4.1 Metal-Orotate in the presence of pyridine

4.5.4.1.1 Structure of [Ni(oro)(py)₂(H₂O)₂]

[Ni(oro)(py)₂(H₂O)₂], hereafter referred to as compound **(F)**, crystallises in the monoclinic space group *P*2₁/*c*. The asymmetric unit of **(F)**, depicted in Figure 4.23, contains one nickel (II) coordinated by one bidentate orotate forming the commonly encountered five-membered chelate ring.¹⁸⁹ Two pyridine molecules are bound to the nickel centre and they are positioned in a *cis* manner to one another. Two coordinated water molecules, coordinated in a *cis* manner to each other, complete the asymmetric unit leading to a distorted octahedral geometry.

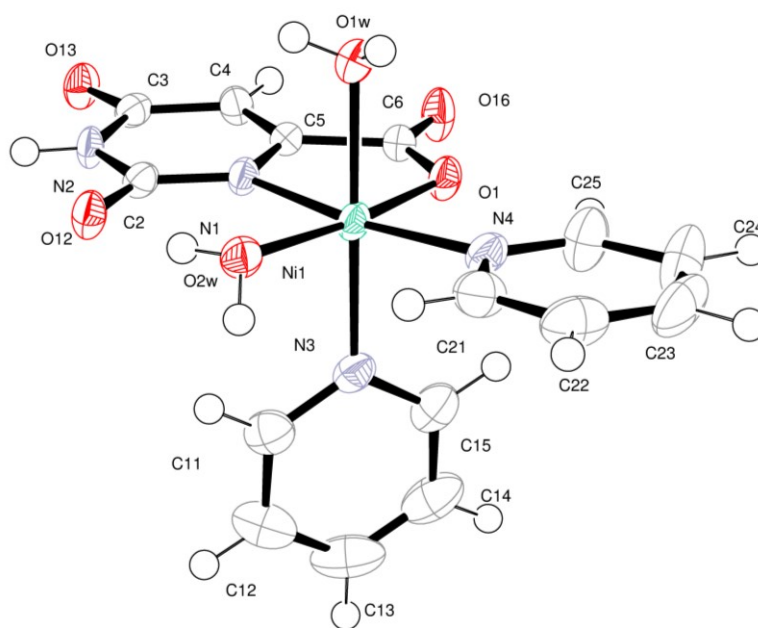


Figure 4.23: Asymmetric unit of (F) with atoms drawn as 70% probability ellipsoids.

All non-H atoms were refined with anisotropic displacement parameters. Chemically sensible restraints were applied to O—H bond lengths and H—O—H bond angles in the two water molecules. In addition, constraints were applied to the C—H bond lengths in the two pyridine moieties.

The structure, depicted in Figure 4.25, contains layers of metal-ligand complexes which are stabilised by two forms of interactions: hydrophilic and hydrophobic interactions.

Classical hydrogen bonds are involved in stabilising the structure. Examination of the hydrogen bond table reveals the presence of a strongly directing N2—H2...O13 interaction with a hydrogen bond angle 172.7°. This is the $R_2^2(8)$ homosynthon between two symmetry related orotate ligands, which ensure stability within one layer. The homosynthon is shown in Figure 4.24. In addition, the complex contains an intramolecular hydrogen bond between the O2W and the exocyclic carbonyl oxygen. The two coordinated water molecules are also responsible for connecting adjacent layers. They act as hydrogen bond donors to the exocyclic carbonyl oxygens. These interactions are O1W—H1WB...O13 (O...O distance 2.7290(14) Å and angle 162.6(17)°) and O2W—H2WB...O16 (O...O distance 2.6838(13) Å and angle 170.8(17)°).

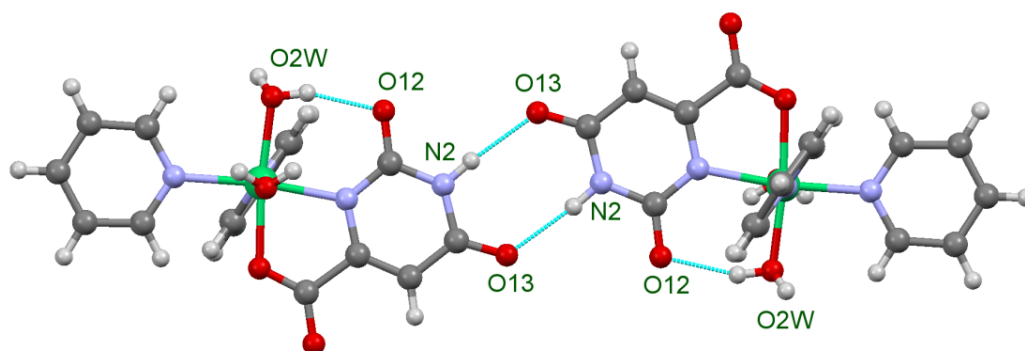


Figure 4.24: Centrosymmetric $R_2^2(8)$ orotate-orotate homosynthon between two symmetry related orotate molecules generated by: $[-x, -y, -z+2]$

Table 4.6: Hydrogen bond parameters in compound (F)

D-H	A	d (D-H) (Å)	d (H...A) (Å)	d (D...A) (Å)	<D-H...A (°)
O1W-H1WA	O12 ⁱ	0.818(14)	1.975(15)	2.7863(13)	170.9(17)
O2W-H2WA	O12	0.841(14)	1.899(15)	2.7050(14)	160.0(17)
O2W-H2WB	O16 ⁱⁱ	0.816(14)	1.875(15)	2.6838(13)	170.8(17)
O1W-H1WB	O13 ⁱⁱⁱ	0.834(14)	1.922(15)	2.7290(14)	162.6(17)
N2-H2	O13 ^{iv}	0.88	1.99	2.8684(14)	172.7

ⁱ $[-x+1, -y, -z+2]$; ⁱⁱ $[-x+1, y-1/2, -z+3/2]$; ⁱⁱⁱ $[x+1, y, z]$; ^{iv} $[-x, -y, -z+2]$

Apart from classical hydrogen bonds, each of the complexes interacts with adjacent complexes *via* π - π stacking. Dashed lines in Figure 4.25 represent these interactions. The offset orotate-pyridine stacking is labelled a), the offset pyridine-pyridine stacking is labelled b), the T-shaped/edge-to-face $C-H\cdots\pi$ ⁵⁰ interaction between two pyridines is labelled c). The mean separations for a) and b) are: 3.24(9) Å and 3.418(2) Å, respectively. The separations for a) and b) are also quoted as centroid to centroid distances: 4.0078 (3) Å and 3.8470 (2) Å, respectively.

The T-shaped/edge-to-face $C-H\cdots\pi$ interaction is quoted using both the donor-aromatic plane distance ($C\cdots\pi = 3.602$ (1) Å) (centroid to centroid 3.6432 (2) Å) and the hydrogen-aromatic plane distance ($H\cdots\pi = 2.67$ (2) Å) (centroid to centroid 2.7417 (15) Å) as suggested by Desiraju and Steiner.³⁸ Figure 4.26 provides a summary of these interactions.

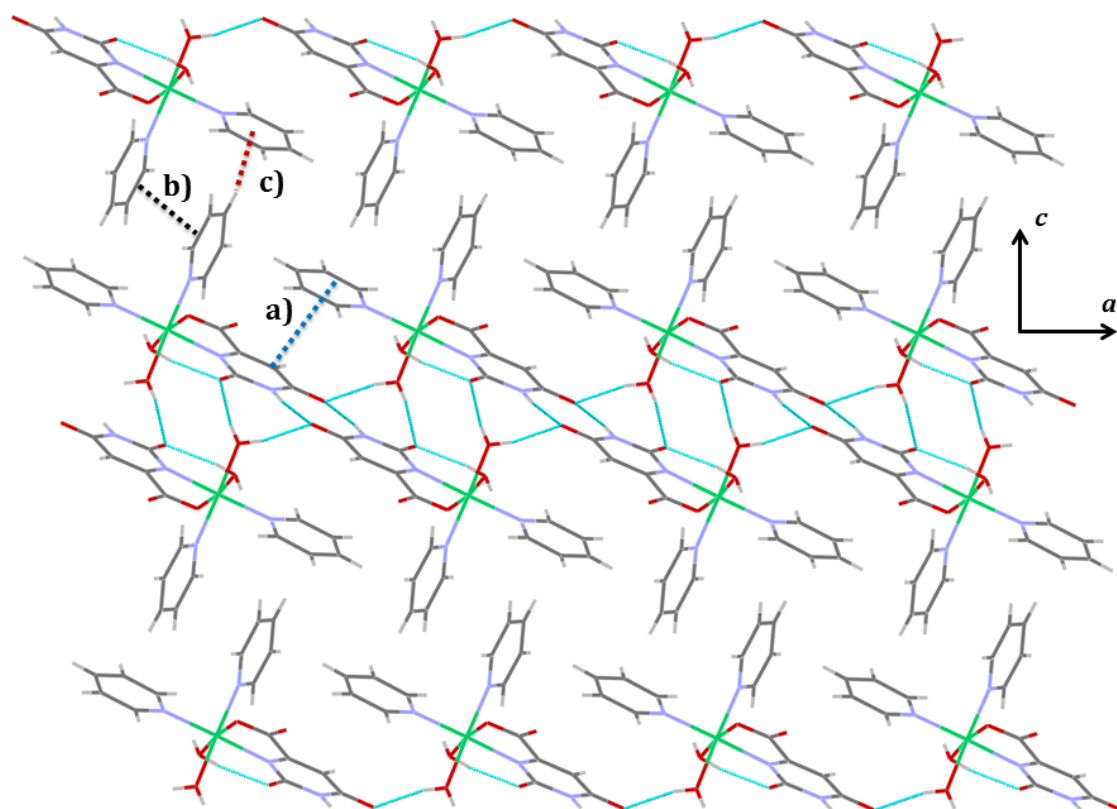


Figure 4.25: Crystal packing in (F). Hydrogen bonding and two distinct types of stacking interactions govern the crystal packing. Green lines represent hydrogen bonding.

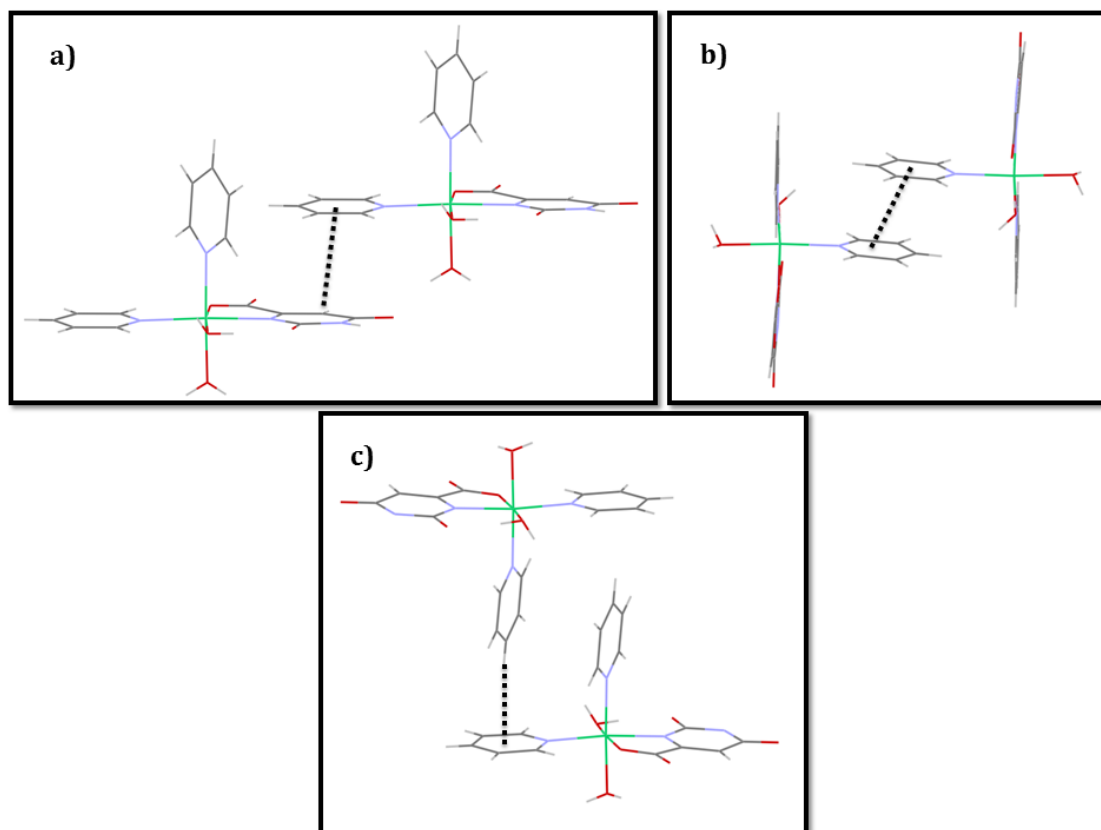


Figure 4.26: Stacking interactions in (F). Dashed black lines represent: a) orotate-pyridine offset stacking; b) offset pyridine-pyridine stacking; c) the T-shaped/edge-to-face C—H \cdots π interaction between two pyridines;

The thermal behaviour of compound (F) was studied using thermogravimetric analysis. The sample was heated up to 900 °C and it displays a multi-step decomposition. As it can be seen from Figure 4.27, the first water molecule which is bound to the metal is lost at approximately 195 °C. This loss accounts for a 4.45% of the total sample weight. When it comes to the second water molecule, there is no clear step of such loss in the thermogram. Exposing the sample to temperature higher than 215 °C resulted in further weight loss, but it was not clear which moieties of compound (F) were decomposing. It was calculated that the loss of two water molecules and one pyridine would occur *circa.* 285 °C accounting for 28% weight loss.

While there is a sharp weight loss in this temperature region, this could not be specifically assigned to the loss of two water molecules and pyridine. Similarly, the loss of two water molecules and the orotate ligand was expected at 360 °C, but there is no clear step to indicate this. However, inspection of the thermogram reveals that heating beyond 550 °C is not associated with any remarkable weight loss. The remaining sample after this point accounts for 18.35% of the total sample weight. Subsequent calculations showed that this is likely to be NiO.

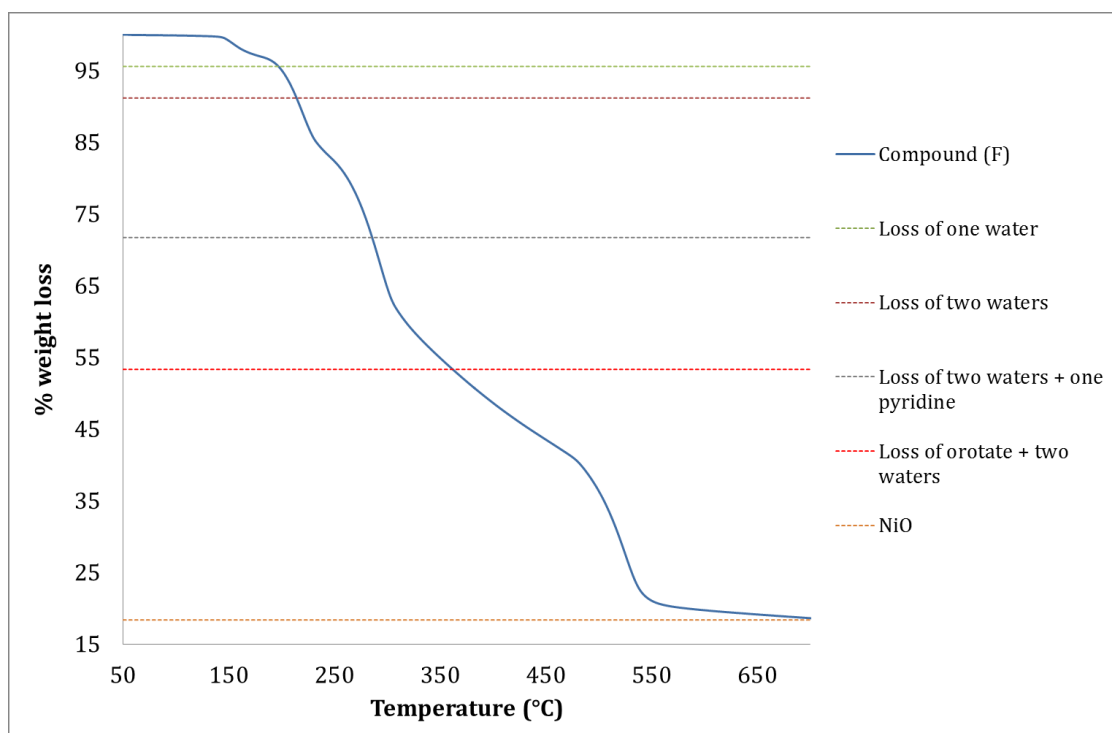


Figure 4.27: Thermal behaviour of compound (F)

4.5.4.1.2 Dimorphism and polymeric coordination in cobalt (II) orotate with pyridine

Performing the experiment with cobalt (II) acetate under the same conditions and with the same method produced block-shaped orange crystals. After routine data collection, examination of reflections revealed two different crystal forms. The data for each form were handled separately. Routine structure solution and refinement revealed the emergence of two polymorphic forms of this system. Form (G) crystallises in the triclinic space group $P\bar{1}$, whereas Form (H) crystallises in the monoclinic space group $P2/n$.

A large number of crystals were examined. None of these were very suitable for data collection. Eventually one was selected for which it was apparent there was a dominant crystalline domain. Scattering from this was used to solve compound (H). Further weaker spots were used to solve the structure of compound (G).

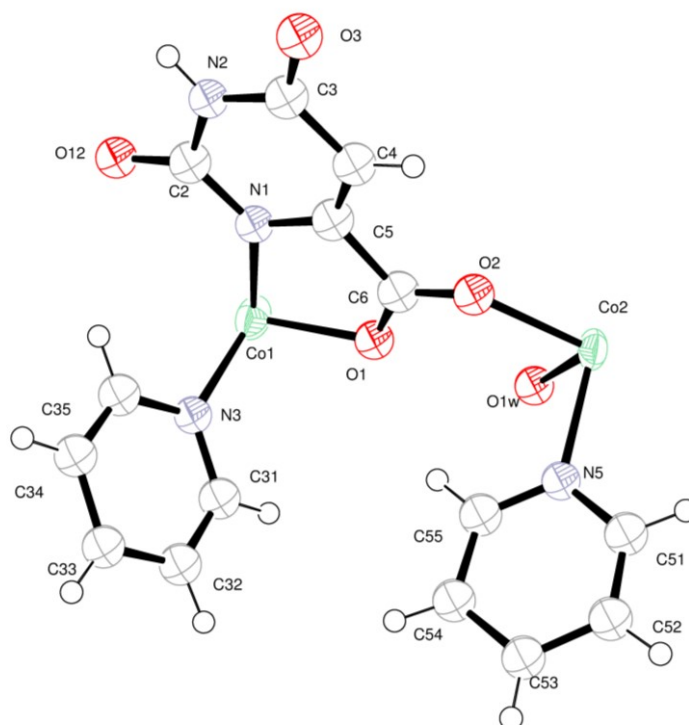


Figure 4.28: Asymmetric unit of (G) with atoms drawn as 55% probability ellipsoids

Figure 4.28 shows the asymmetric unit of Form (G). The asymmetric unit of Form (G) contains one orotate ligand which bridges two cobalt (II) metal centres *via* its carboxylate oxygen atoms. The ligand binds Co1 in a chelate manner as observed in the previous examples. A pyridine ligand also binds this metal centre and a distorted octahedral geometry is generated by symmetry (inversion centre through Co1). The second metal centre Co2 is coordinated to a pyridine molecule and a water molecule. A distorted octahedral geometry is also achieved by an inversion centre through the metal. Form (G) displays binding characteristics of the orotate ligand which differ from the nickel (II) analogue. In this example, the ligand is acting simultaneously as a chelating and a bridging ligand. In addition, the pyridine molecules are oriented differently to each other.

The crystal was weakly scattering and a long exposure time was required. It would have taken a prohibitively long time to collect a full set of unique intensity data. Approximately 47.6% of unique data were recorded. The refinement employed anisotropic displacement parameters for the cobalt ions but isotropic displacement parameters were used for all other atoms. For this refinement the data-to-parameter ratio is 16.7.

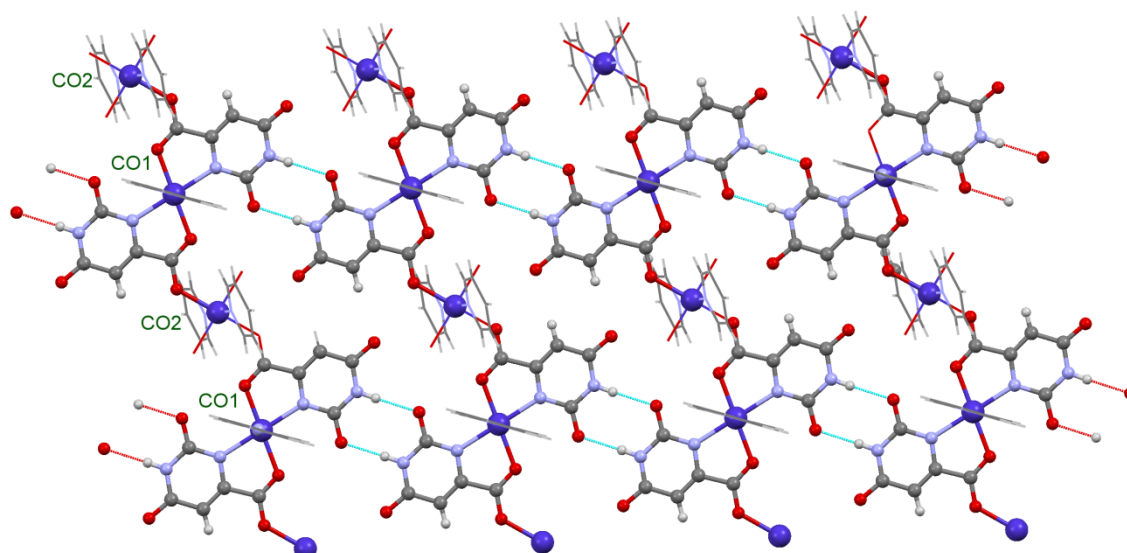


Figure 4.29: Crystal packing in Form (G). The orotate-orotate homosynthon extends parallel to *b*-axis

Contrary to the nickel (II) analogue, Form (**G**) is an infinite polymer. Orotate ligands interact *via* hydrogen bonding and generate a $R_2^2(8)$ homosynthon. This interaction creates an infinite layer of Co1 complex which extends parallel to the *b*-axis. The Co2 complexes lie adjacent to the Co1 complex and the two are bridged by the homosynthon between the orotate ligands.

It should be noted that the orotate ligand binds the metal ions in a manner which was not predicted during the experimental design stage. The binding of orotate to the metal ion was predicted to be in a chelate bidentate manner, similar to the case observed for the nickel (II) analogue. However, the orotate ligand bridges the two metal ions in this system as shown in Figure 4.30.

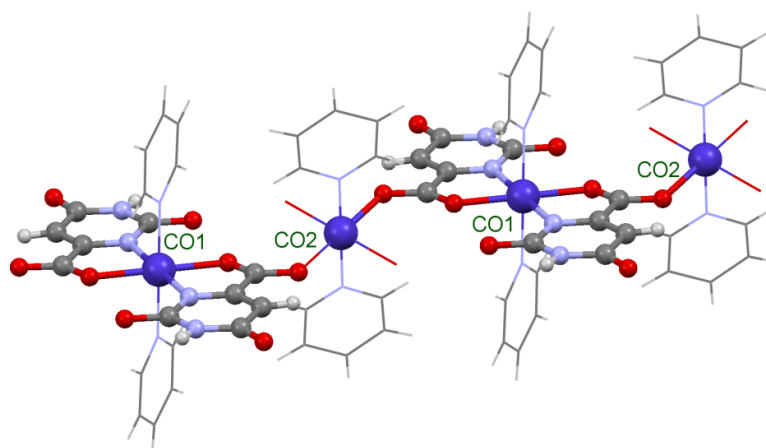


Figure 4.30: Coordination about each cobalt ion showing the bridging orotate

Apart from the cobalt atoms, the refinement of Form (**H**) has also been performed with isotropic displacement parameters and the data-to-parameter ratio was recorded as 27.7. The asymmetric unit of Form (**H**) is shown in Figure 4.31. It contains two fragments and both of these fragments contain an orotate ligand. Both of these ligands bind to the metal centres in a monodentate and bidentate fashion simultaneously. The first orotate ligand chelates Co1 *via* its endocyclic nitrogen and carboxylate oxygen. This ligand bridges Co1 and Co2 by coordinating to Co2 in a monodentate manner *via* its carbonyl oxygen in the carboxylate group. Two half pyridine molecules are bound to Co1 in a *trans* manner. The

other half of these molecules is generated by symmetry. This operation overall creates a distorted octahedral geometry. There are one two half pyridine molecules which binds Co2 in a *trans* manner and the other molecule is generated by symmetry. The same is applicable to a water molecule bound to Co2 which is also generated by symmetry.

In the second fragment, the orotate ligand displays similar coordination behaviour to the one seen in the first fragment. It chelates Co4 *via* the endocyclic nitrogen and carboxylate anion and it also bridges Co4 and Co3 by binding to Co3 *via* its carbonyl oxygen of the carboxylate group. One half pyridine molecules is bound to Co4 in a *trans* manner. The rest of the molecule is generated by symmetry. There are also two half pyridine molecules which bind Co3 in a *trans* manner and the other half is generated by symmetry. The same is applicable to one water molecule bound to this metal centre.

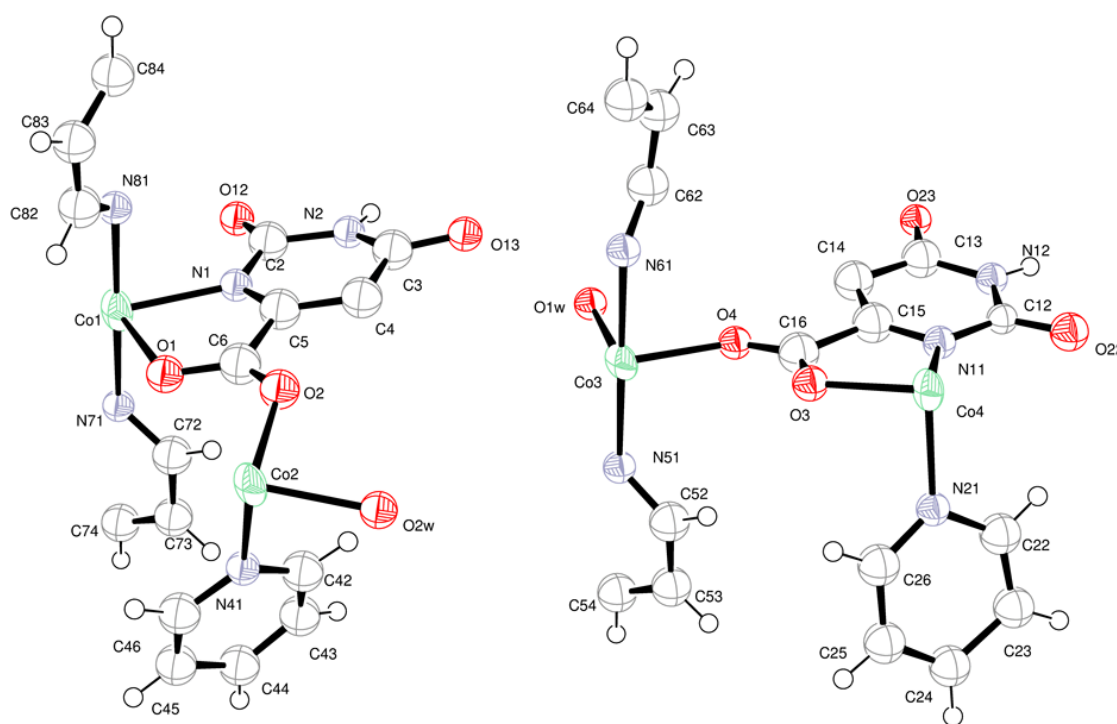


Figure 4.31: Asymmetric unit of (H) with atoms drawn as 55% probability ellipsoids

Form **(H)** is also arranged in way that it forms infinite polymers. There are chains, which alternate to form layers of Co1/Co2 metal centres and Co3/Co4 metal centres. A chain is extended *via* the interaction of orotate ligands which generate a $R_2^2(8)$ homosynthon. A hydrogen bond table was not generated due to the limitations related to data quality (*i.e.* there are no hydrogen atoms on water molecules).

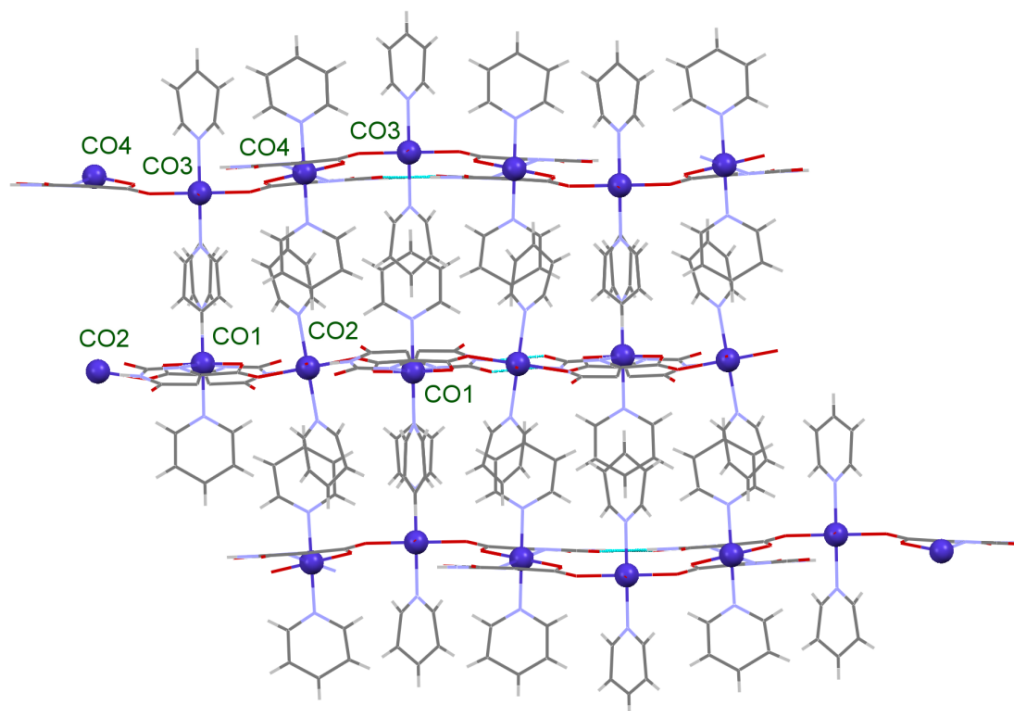
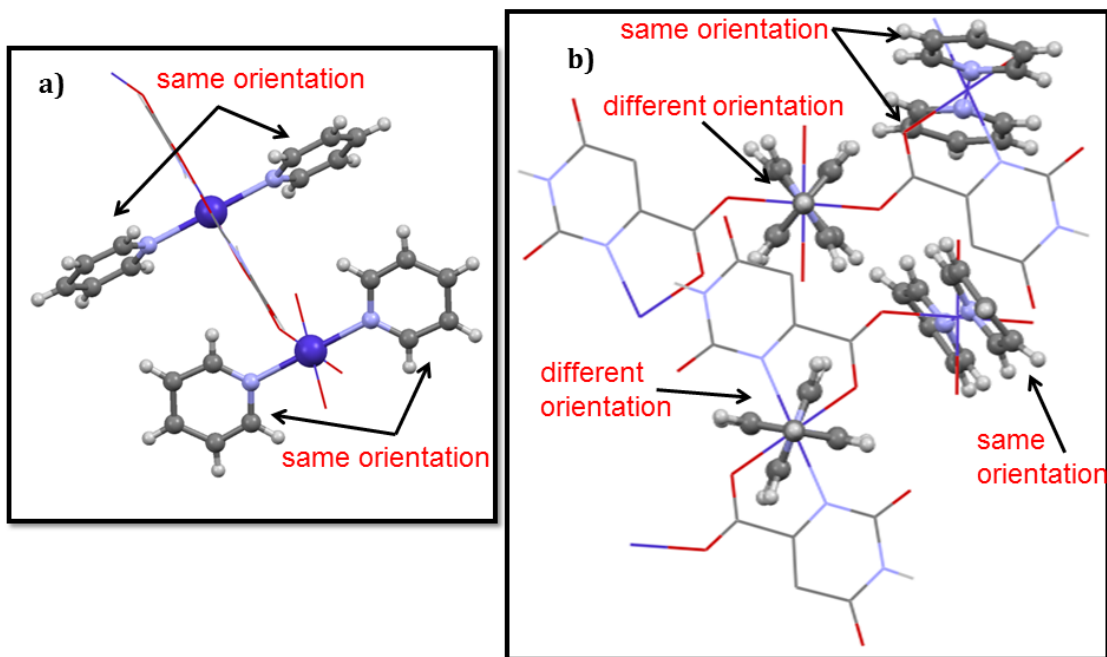


Figure 4.32: Crystal packing in Form (H)

It is evident from Figure 4.32, that there are variations in the orientation of pyridine ligands. It could be argued that this is the reason for the emergence of two polymorphs in this compound. The main differences between Form **(G)** and Form **(H)** lie in the orientation of their pyridine molecules. In Form **(G)** two pyridine ligands binding the metal centre are arranged in the same orientation to each other. This, however, is not the case in Form **(H)**, wherein two pyridine molecules binding the metal centre in a *trans* manner are perpendicular to each other. Figure 4.33 shows differences between two forms. Both of these forms must be close in energy to be obtained together.



**Figure 4.33: Differences in pyridine orientation between the two polymorphs:
a) Form (G) and b) Form (H)**

Examination of the two structures obtained from treatment with cobalt (II) acetate and comparison with the nickel (II) analogue reveals some differences. In the nickel (II) analogue there is no bridging by the orotate ligand. In addition, the two pyridine ligands are bound arranged in a *cis* manner to one another. This is contrary to the cobalt (II) analogue. In both forms, the orotate ligands act as bridging ligands between two metal centres. In contrast to the nickel compound, the pyridine molecules are coordinated to the metal centre in a *trans* manner.

Table 4.7: Crystal parameters for Compounds (G) and (H)

Identification code	Compound (G)	Compound (H)
Empirical formula	C ₁₄ H ₁₂ Co N ₅ O ₅	C ₃₀ H ₂₂ Co ₂ N ₈ O ₁₀
Formula weight	387.22	772.41
Temperature (K)	150(2)	150 (2)
Wavelength	0.71073 Å	0.71073 Å
Crystal system	Triclinic	Monoclinic
Space group	<i>P</i> $\bar{1}$	<i>P</i> 2/n
Unit cell dimensions	<i>a</i> = 9.344(9) Å; α = 117.19(8)° <i>b</i> = 10.274(8) Å; β = 104.15(8)° <i>c</i> = 10.791(13) Å; γ = 101.75(7)°	<i>a</i> = 12.321(6) Å; α = 90° <i>b</i> = 15.950(5) Å; β = 92.42(5)° <i>c</i> = 17.213(11) Å; γ = 90°
Volume (Å ³)	831.6(16)	3380(3)
Z	2	4
Density (calculated) (mg/m ³)	1.546	1.518
Absorption correction	Not applied	Not applied
F(000)	394	590
Theta range for data collection	2.269 to 25.827°.	1.277 to 25.885°.
Index ranges	-9 ≤ <i>h</i> ≤ 11, -12 ≤ <i>k</i> ≤ 12, -13 ≤ <i>l</i> ≤ 10	-13 ≤ <i>h</i> ≤ 15, -19 ≤ <i>k</i> ≤ 19, -20 ≤ <i>l</i> ≤ 11
Reflections collected	1840	8609
Independent reflections	1536 [R(int) = 0.0837]	4929 [R(int) = 0.1955]
Completeness to theta = 25.242°	47.6 %	75.2 %
Refinement method	Full-matrix least-squares on F ²	Full-matrix least-squares on F ²
Data / restraints / parameters	1536 / 0 / 92	4929 / 9 / 178
Goodness-of-fit on F ²	0.719	0.676
Final R indices [I > 2σ(I)]	R1 = 0.0699, wR2 = 0.1420	R1 = 0.0919, wR2 = 0.2023
R indices (all data)	R1 = 0.1707, wR2 = 0.1655	R1 = 0.3173, wR2 = 0.2691
Largest diff. peak and hole	0.399 and -0.319 e.Å ⁻³	0.628 and -1.035 e.Å ⁻³

4.5.4.1.3 Crystal packing in structures with different hydration levels

The aim of this study was to design hydrogen bonded networks with orotic acid using two different N-donor compounds: 3-nicotinamide and 4-nicotinamide. Complexation of nickel (II) with orotic acid and 3-nicotinamide has been previously reported by Kose and co-workers.¹⁹⁵ This structure of Ni(oro)(3-nic)(H₂O)₅ (CSD ref code: VEVZIG) was somewhat understudied since hydrogen bonding interactions in the crystal were not analysed in the original paper. As a result, it was decided to further probe its structural features by resynthesising it. Attempts to grow the same crystals using the method of Kose *et al.*¹⁹⁵ were not successful due powder precipitation. As a result, the synthesis was amended by using the synthetic method developed as part of this project, which is detailed in Section 4.5.3.1.3. This method yielded block-shaped blue crystals labelled as compound (I). Some crystals from compound (I) were isolated, dried and analysed by X-ray powder diffraction. The pattern collected from this compound was compared to the simulated pattern of VEVZIG. Inspection of the two patterns revealed that compound (I) has different features compared to simulated VEVZIG. (Figure 4.34).

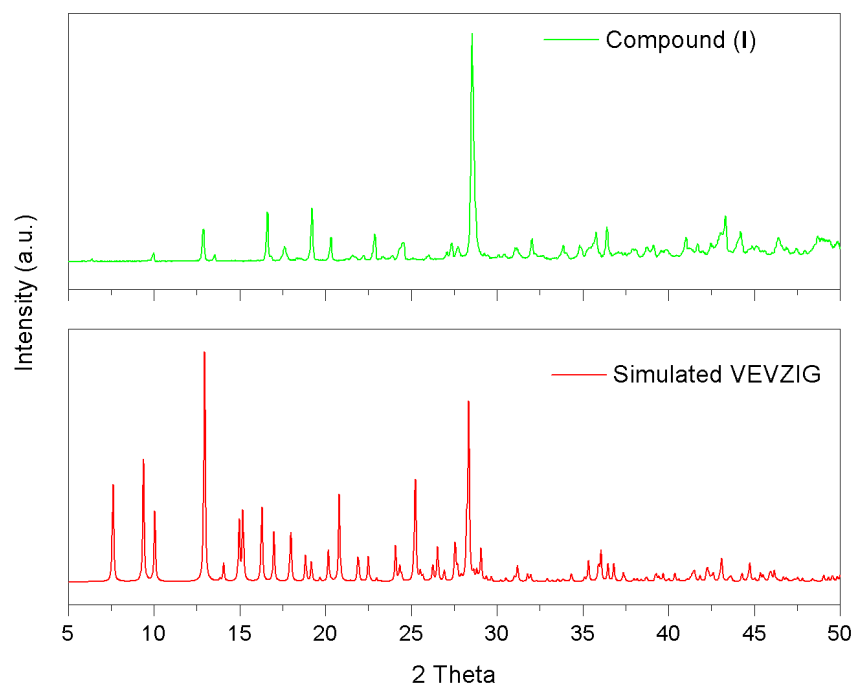


Figure 4.34: Pattern from compound (I) compared to the simulated VEVZIG pattern

Differences in patterns prompted further investigations on compound **(I)**. As a result, routine single crystal data collection was performed. Comparison of unit cell parameters revealed that compound **(I)** has a volume of 1555.5 (3) Å³, whereas the unit cell volume of VEVZIG was recorded as 820.34(12) Å³. Subsequent structure solution revealed the emergence of a novel crystal, named Ni₂(oro)₂(3-nic)₂(H₂O)₉, henceforth compound **(I)**. This compound crystallises in the triclinic space group $P\bar{1}$. The initial indexing was performed using strong reflections from the diffraction images. However, inspection of the diffraction images revealed the presence of weak reflections. As a result, the indexing was done using the larger cell, which was double the size of the original cell. Subsequent, structure solution revealed that compound **(I)** is a system where $Z' \neq 1$ and there are two moieties/fragments in the asymmetric unit ($Z' = 2$).

In compound **(I)**, each fragment has an orotate ligand bound to a nickel metal centre *via* the endocyclic nitrogen and the carboxylate oxygen. The orotate binds in a bidentate manner similar to other structures discussed previously in this thesis. Furthermore, each fragment contains one 3-nicotinamide ligand which binds the metal centre *via* its pyridine nitrogen. Two water molecules bound to each metal centre generate a distorted octahedral geometry in both metal-ligand complexes.

In addition, there are three unbound water molecules. These are O4W which occurs in each fragment and O5W which is only present in the second fragment. The fact that there is no counterpart of O5W breaks the symmetry and explains the emergence of this compound, which is different from VEVZIG. Compared to VEVZIG which has one formula unit in the asymmetric unit $Z' = 1$, compound **(I)** has two formula units ($Z' = 2$). The asymmetric unit of compound **(I)** is shown in Figure 4.35.

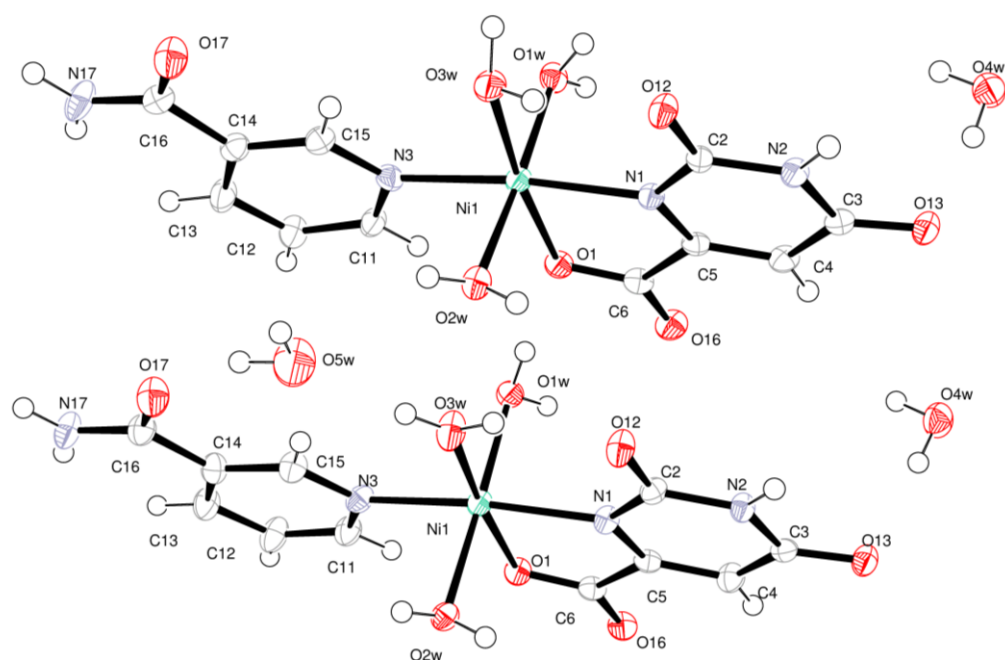


Figure 4.35: Asymmetric unit of compound (I) with atoms drawn as 70% probability ellipsoids

The missing water molecule on the upper fragment shown in Figure 4.35 has implications on breaking the symmetry and this is associated with major changes in synthons, orientation of hydrogens atoms in O3W and the overall crystal packing. The two fragments in compound (I) are related to one another by a pseudo-translation of $(0, \frac{1}{2}, 0)$ as it can be seen in Figure 4.35. The fact that this system has $Z' \neq 1$ could be attributed to O5W. This molecule is involved in different modes of hydrogen bonding with each of the two moieties in the asymmetric unit.

Within our group, a programme has been developed for calculating the deviation from complete overlap between two molecular fragments related by pseudo-symmetry.¹⁹⁶ A dimensionless parameter, F , is used to quantify deviation from complete overlap between two atoms related by pseudo translational symmetry. For compound (I) a deviation of $F = 0-0.086$ for nickel, carbon and nitrogen atoms was determined, which agrees with the

overlay of two moieties shown in Figure 4.36. This range is also applicable to hydrogens in the crystal with the exception of H3AW_1 and H3AW_2. The F-parameter for these two atoms was 0.75, which is considerably larger than the other atoms. These values are much greater than those for the other atoms and highlight that H3AW_1 and H3AW_2 are in a pseudo-symmetric relationship. (Appendix 2) It could be argued that difference in the two orientations gives different hydrogen bonding. The directional nature of hydrogen bonding exhibited by O5W in the lower fragment changes the orientation of H3AW_2 in a way that enables classical hydrogen bonding between O5W and O3W_2. Examination of the hydrogen bond parameters shown Table 4.8 reveal that the angle of O3W_2—H3AW_2...O5W is 176 (5)°. These parameters demonstrate that this is a favourable interaction and the hydrogen atom changes its orientation due to the attraction from the O5W acceptor. Given that there is no water molecule in close proximity to O3W_1, this water molecule is not involved in hydrogen bonding and this is why H3AW_1 is oriented differently.

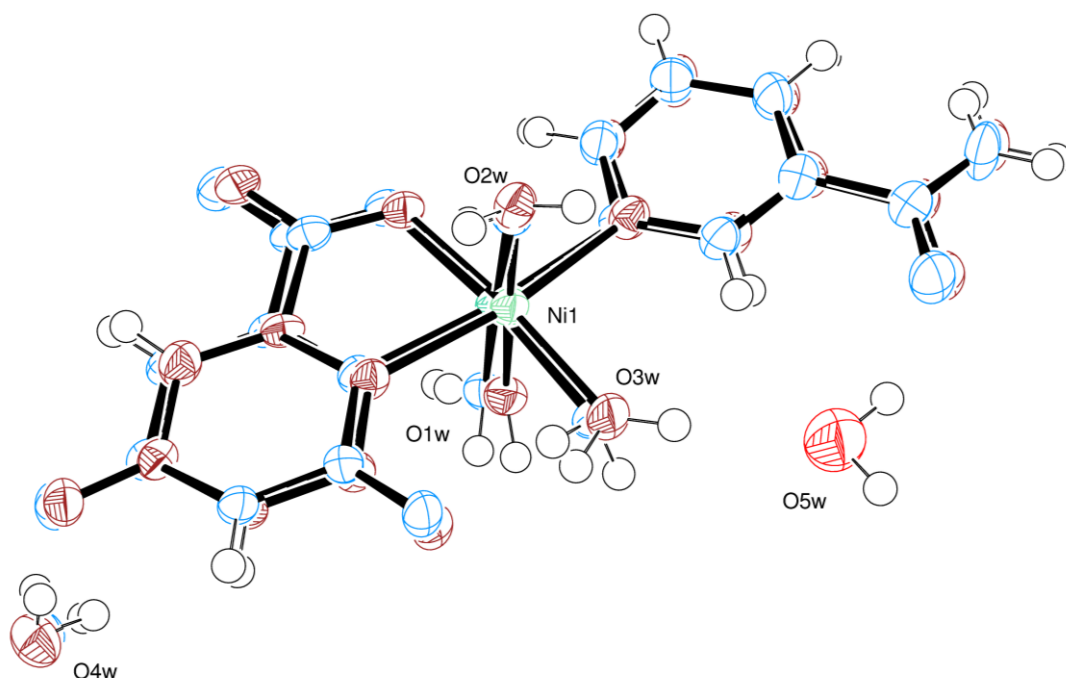


Figure 4.36: Depiction of pseudo-symmetry generated by a translation of $(0, \frac{1}{2}, 0)$

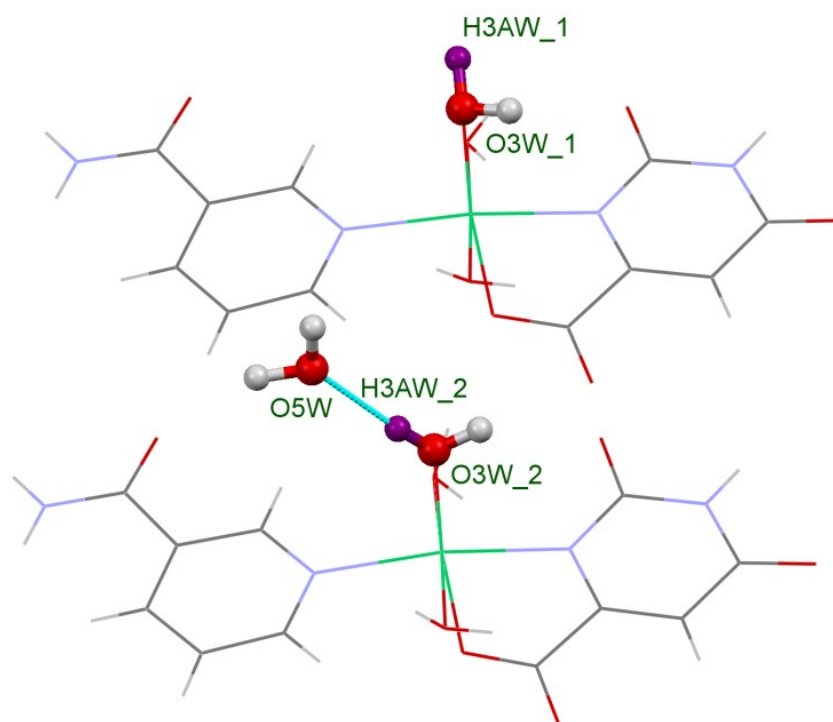


Figure 4.37: Structural implications of O5W

Inspection of VEVZIG, which has one fragment in the asymmetric unit, reveals the presence of a $R_2^2(8)$ orotate-nicotinamide heterosynthon. This heterosynthon creates infinite chains. Each chain interacts with the adjacent chains *via* two forms of interactions: hydrogen bonding between water molecules and orotate ligand as well as π - π stacking between 3-nicotinamide ligands. In this particular compound, the formation of the orotate-nicotinamide heterosynthon is more favoured than the formation of the orotate-orotate homosynthon commonly encountered in orotate systems as shown in Figure 4.38.

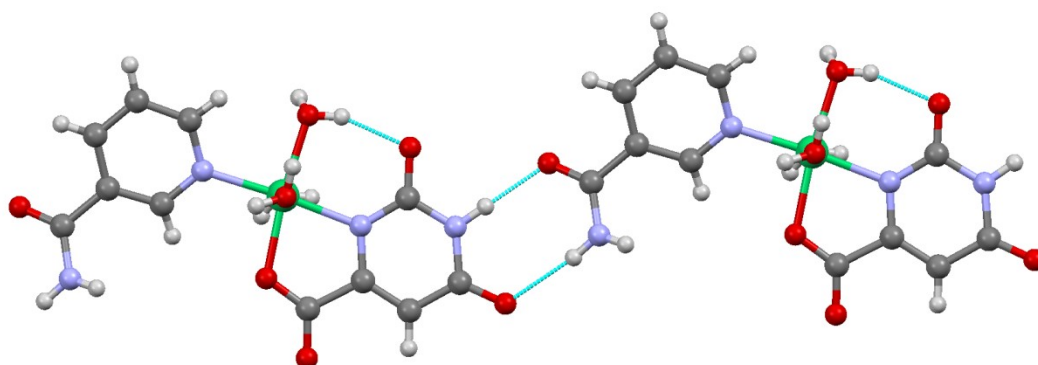


Figure 4.38: Formation of orotate-nicotinamide heterosynthon in VEVZIG

Since compound **(I)** and VEVZIG both contain orotic acid and 3-nicotinamide as ligands, it would have been logical to expect the formation of an orotate-nicotinamide heterosynthon in compound **(I)** same as in the case of VEVZIG. However, compound **(I)** behaves differently and this is an important example. This example highlights how even the smallest and most subtle change in the composition of a compound can have unpredictable implications on the crystal packing. The missing water molecule (O5W) in the upper moiety breaks the symmetry and changes the hydrogen bonding in the structure. This change in the level of hydration is sufficient to dictate an alternative form of crystal packing. The absence of this water molecule changes the crystal packing in such a way that it inhibits the formation of the orotate-nicotinamide heterosynthon observed in VEVZIG. Instead, the two fragments in compound **(I)** interact with each other *via* hydrogen bonding and form a $R_2^2(8)$ orotate-orotate homosynthon, (Figure 4.39) which extends parallel to the *c*-axis. The synthon is held together *via* N2_1—H22_1...O12_2 and N2_2—H22_2...O12_1 hydrogen bonds with distances 2.829 (4) Å and 2.869 (4) Å and H-bond angles 175.5° and 178° as shown in Figure 4.39.

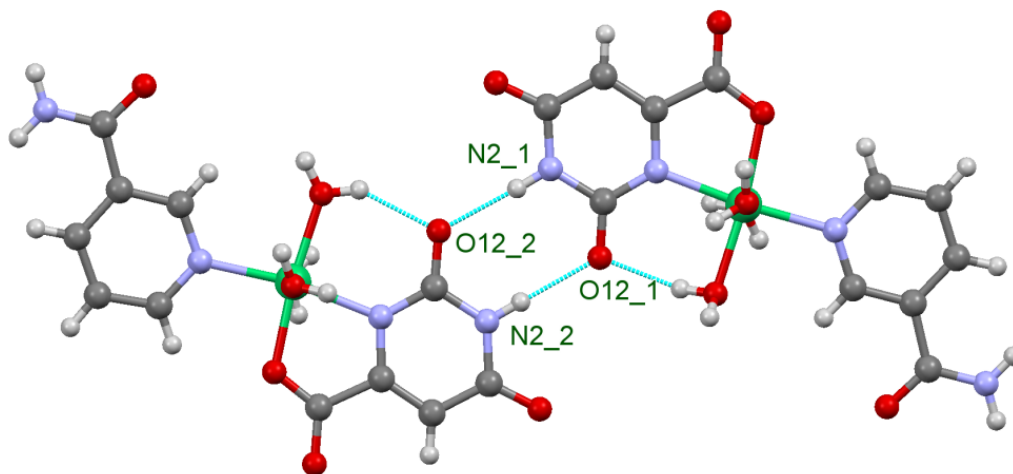


Figure 4.39: Orotate-orotate homosynthon between two fragments in compound (I)

Hydrogen bonding is not the only form of interaction between orotate ligands, since they are also involved in π - π interactions as shown in Figure 4.40. The orotate from the first fragment is π - π stacked with its symmetry related counterpart with a mean plane separation 3.247 (9) Å and centroid to centroid distance 3.6254 (4) Å. The orotate from the second fragment is also π - π stacked with its symmetry related counterpart with a mean plane separation of 3.337 (5) Å and centroid to centroid distance: 3.6582 (4) Å.

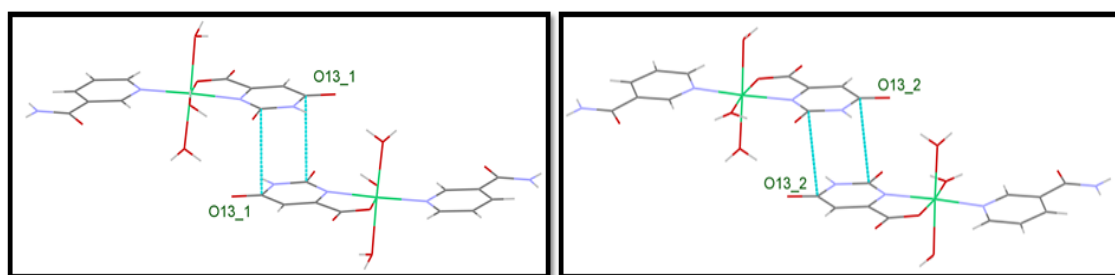


Figure 4.40: Stacking interaction in compound (J)

Two water molecules which are bound to the metal in a *trans* manner also form hydrogen bonds. Both of these water molecules (O1W and O2W in both fragments) stabilise adjacent layers *via* hydrogen bonding. They act as hydrogen bond donors and assist in generating a supramolecular architecture as shown in Figure 4.41.

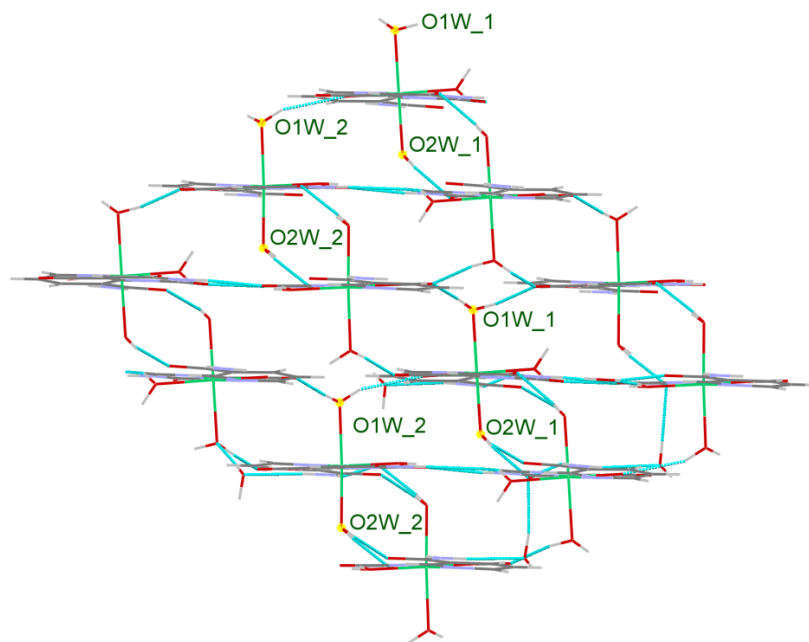


Figure 4.41: Crystal packing in (I) as viewed from *c*-axis. O1W and O2W interconnect the adjacent layers by acting as hydrogen bond donors

Table 4.8: Selected hydrogen bond parameters for compound (I)

D-H	A	d (D-H) / (Å)	d (H...A) (Å)	d (D...A) (Å)	<D-H...A (°)
O5W-H5AW	O17_2	0.91(2)	1.93(3)	2.787(4)	156(4)
O5W-H5BW	O17_1 ⁱ	0.88(2)	2.15(3)	2.943(4)	150(4)
N2_1-H22_1	O12_2 ⁱⁱ	0.86	1.97	2.829(4)	175.5
N17_1-H17A_1	O13_1 ⁱⁱⁱ	0.86	2.1	2.934(4)	162.8
N17_1-H17B_1	O4W_2 ⁱⁱⁱ	0.86	2.1	2.931(5)	161.8
O3W_1-H3AW_1	O1_2 ^{iv}	0.85(2)	2.31(3)	3.021(4)	143(4)
O3W_1-H3BW_1	O12_1	0.85(2)	1.91(3)	2.690(3)	152(5)
O2W_1-H2AW_1	O17_1 ⁱ	0.84(2)	1.96(2)	2.793(4)	169(5)
O2W_1-H2BW_1	O13_1 ⁱⁱ	0.83(2)	1.88(3)	2.685(4)	161(4)
O1W_1-H1AW_1	O1_2 ^{iv}	0.84(2)	2.46(3)	3.188(4)	146(4)
O1W_1-H1AW_1	O16_2 ^{iv}	0.84(2)	2.03(3)	2.808(4)	155(4)
O1W_1-H1BW_1	O16_2 ^v	0.85(2)	1.89(3)	2.698(4)	158(5)
O4W_1-H4AW_1	O1W_1 ^{vi}	0.85(2)	2.04(2)	2.888(4)	177(4)
O4W_1-H4BW_1	O13_1	0.85(2)	1.94(2)	2.776(4)	168(5)
N2_2-H22_2	O12_1 ⁱⁱ	0.86	2.01	2.869(4)	178
N17_2-H17A_2	O13_2 ⁱⁱⁱ	0.86	2.1	2.946(4)	165.7
N17_2-H17B_2	O4W_1 ^{vii}	0.86	2.09	2.933(5)	164.7
O4W_2-H4AW_2	O1w_2 ^v	0.85(2)	2.03(2)	2.872(4)	170(5)
O4W_2-H4BW_2	O13_2	0.84(2)	1.97(2)	2.815(4)	177(5)
O3W_2-H3AW_2	O5W	0.82(2)	2.00(2)	2.824(4)	176(5)
O3W_2-H3BW_2	O2W_1	0.83(2)	2.49(4)	2.922(4)	113(4)
O3W_2-H3BW_2	O12_2	0.83(2)	1.99(3)	2.720(3)	146(4)
O2W_2-H2AW_2	O17_2 ^{viii}	0.85(2)	1.86(2)	2.705(4)	172(4)
O2W_2-H2BW_2	O13_2 ^{ix}	0.83(2)	1.93(3)	2.732(4)	161(4)
O1W_2-H1AW_2	O1_1	0.82(2)	2.13(3)	2.917(4)	160(5)
O1W_2-H1BW_2	O16_1 ^v	0.85(2)	1.90(2)	2.747(4)	177(5)

ⁱ [-x+1, -y, -z]; ⁱⁱ [-x+1, -y, -z+1]; ⁱⁱⁱ [x, y, z-1]; ^{iv} [x, y-1, z]; ^v [-x, -y+1, -z+1]; ^{vi} [-x, -y, -z+1];

^{vii} [x, y+1, z-1]; ^{viii} [-x+1, -y+1, -z]; ^{ix} [-x+1, -y+1, -z+1];

In order to verify that the single crystal of compound (**I**) is representative of the bulk, X-ray powder diffraction was performed and the pattern was compared to the simulated pattern of compound (**I**). As it can be seen from Figure 4.42, the two patterns match and therefore a single phase of compound (**I**) has been obtained.

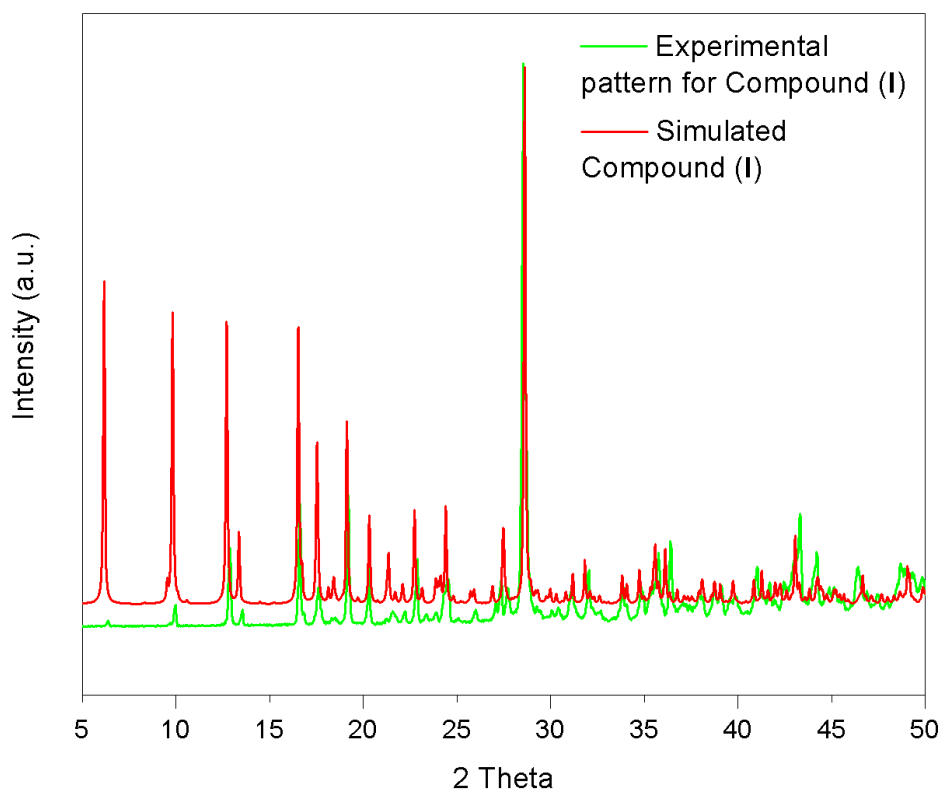


Figure 4.42: Overlay of simulated and experimental patterns showing the presence of a single phase

4.5.4.1.4 Structural Implications of replacing 3-nicotinamide with 4-nicotinamide

The previous section demonstrated that that pseudo-symmetry in nickel (II) orotate 3-nicotinamide system can alter the hydrogen bonding and crystal packing. Given the conclusions drawn from the previous section, an investigation was conducted to examine the effects of changing the position of the amide functional group by replacing 3-nicotinamide with 4-nicotinamide. All other variables in the synthesis were kept the same as the 3-nicotinamide analogue, in line the method detailed in Section 4.5.3.1.4. It was initially predicted that having the amide group in the *para* position would facilitate the formation of the orotate-nicotinamide heterosynthon as observed in VEVZIG. The rationale behind this prediction is based on the fact that the *para* position would be less sterically hindered than the *ortho* position.

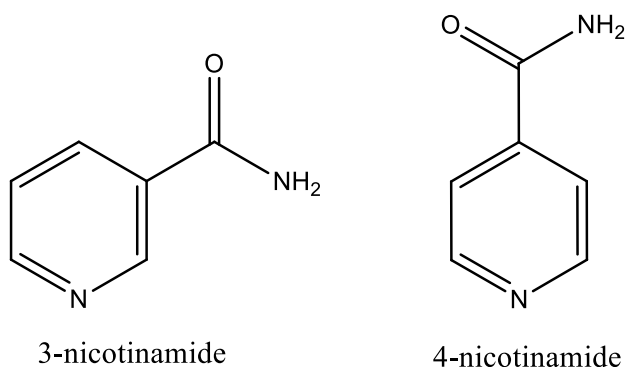


Figure 4.43: Structure of 3-nicotinamide and 4-nicotinamide

Compound (J) crystallises in the triclinic space group $P\bar{1}$. The asymmetric unit contains one orotate ligand which is bound to the nickel centre in a bidentate manner *via* its endocyclic nitrogen and carboxylate oxygen. One molecule of 4-nicotinamide binds the nickel centre through its pyridine nitrogen. The asymmetric unit is completed with six water molecules: three bound to the metal and three unbound. One of the water molecules is involved in intramolecular hydrogen bonding with the carbonyl oxygen of the orotate.

The asymmetric unit contains also three intermolecular hydrogen bonds between water molecules and the orotate ligand. (Figure 4.44).

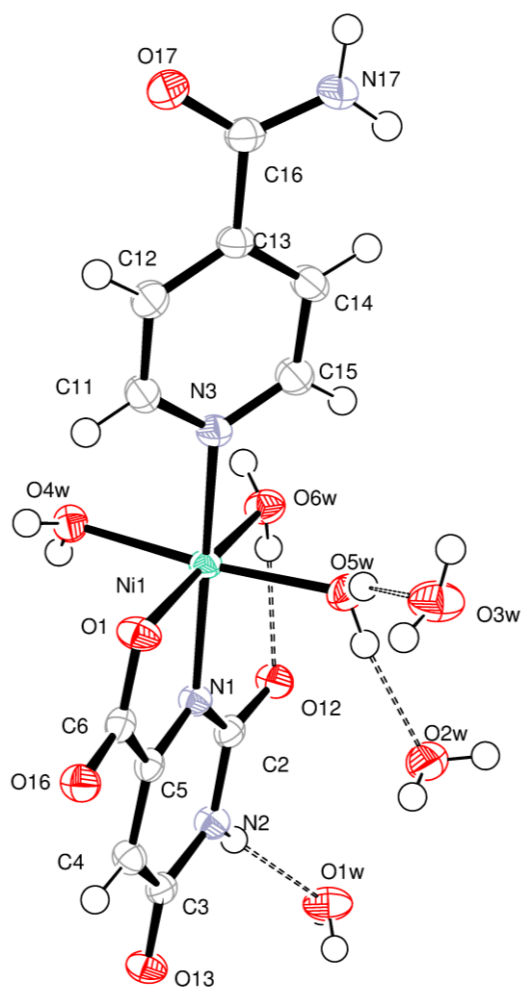


Figure 4.44: Asymmetric unit of compound (J) with atoms drawn as 70% probability ellipsoids. Dashed lines represent hydrogen bonds.

Compound (J) is remarkable in that it does not display the orotate-nicotinamide heterosynthon observed in the 3-nicotinamide analogue (VEVZIG). However, it also does not form the orotate-orotate homosynthon either which was encountered in compounds (F), (G), (H) described in this thesis and other compounds reported in literature.^{184 192}

Compound (J) represents an important example which shows how changing the position of the functional group can significantly alter synthon formation and crystal packing. While this structure displays no synthons between orotate ligands, these ligands interact with each other *via* hydrophobic interactions. The mean plane separation between two π - π stacked orotate ligands was calculated as 3.317 (3) Å and the centroid to centroid distance was recorded as 3.7156 (4) Å. Crystal packing in the structure is governed by hydrogen bonding interactions of water molecules between themselves, the orotate ligand and the amide functional group of 4-nicotinamide. The supramolecular architecture obtained from these interactions is depicted in Figure 4.45. The three unbound water molecules are arranged in channels formed between adjacent metal-ligand complexes.

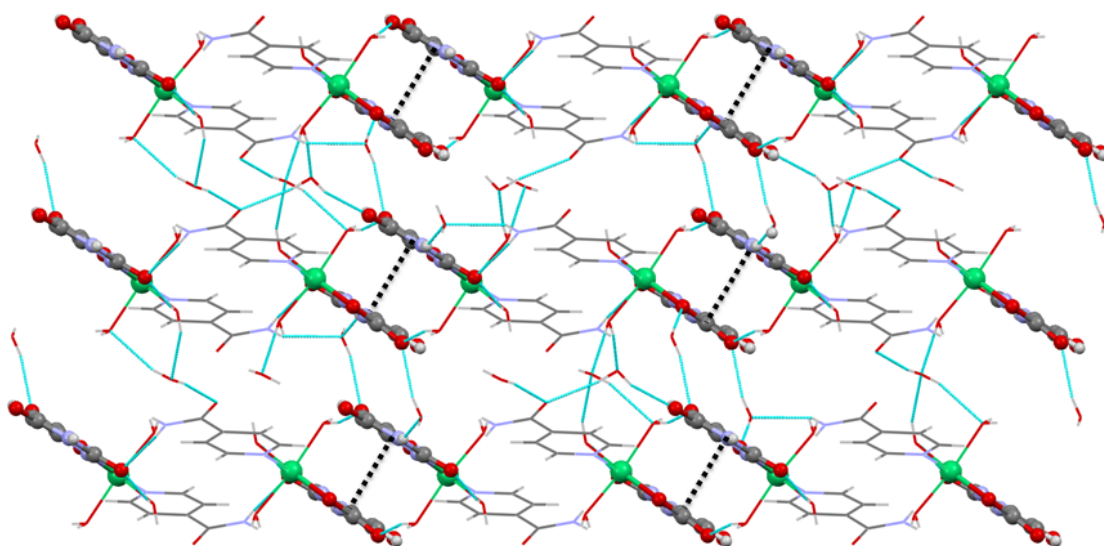


Figure 4.45: Crystal packing in (I) showing π - π stacking between two orotate ligands, which replaces the orotate-orotate homosynthon

While the change in the position of the amide functional group in compound (**J**) inhibits any synthon formation with orotate, it could be argued that the emergence of π - π stacking interactions compensates for the lack of the synthons. This system seeks to maximise its favourable interactions. It is therefore evident that the orotate-orotate homosynthon or orotate-nicotinamide heterosynthon are not strong enough in the hierarchy of intermolecular interactions in the crystal. This suggests that, in this system, the formation of the orotate-orotate homosynthon or the orotate-nicotinamide heterosynthon does not generate the lowest energy forms. It is remarkable to note that two of the water molecules in compound (**J**) (O1W and O3W) are in their second most common hydrogen bonding environment. These include four hydrogen bonds per water molecule: two as donor and two as acceptors.⁹⁵ The most common environment is three hydrogen bonds. The hydrogen bond parameters shown in Table 4.9 demonstrate that all water molecules in the structure are involved in 12 hydrogen bonds and their angles range from 145.1 – 178.6°. Thus, it could be argued that the cumulative effect of all these interactions was more energetically favourable than the formation of a homosynthon or heterosynthon in the structure.

Table 4.9: Selected hydrogen bonds for compound (J**)**

D-H	A	d (D-H) / (Å)	d (H...A) (Å)	d (D...A) (Å)	<D-H...A (°)
N17-H77B	O12 ⁱⁱ	0.86	2.19	3.0232(17)	164.4
O2W-H2AW	O13 ⁱ	0.794(16)	1.978(16)	2.7470(16)	163(2)
O2W-H2AW	O13 ⁱ	0.794(16)	1.978(16)	2.7470(16)	163(2)
N2-H10	O1W	0.86	2.08	2.8749(17)	153.7
O4W-H4BW	O13 ^{iv}	0.761(16)	2.006(16)	2.7569(15)	169(2)
O4W-H4AW	O16 ⁱⁱⁱ	0.789(16)	1.955(17)	2.7142(15)	161(2)
O6W-H6AW	O3W ^v	0.781(16)	2.217(18)	2.8928(16)	145(2)
O1W-H1BW	O1 ^{vi}	0.775(16)	2.012(16)	2.7870(15)	179(2)
O2W-H2BW	O17 ^{vii}	0.809(16)	2.067(16)	2.8694(17)	172(2)
O5W-H5BW	O3W	0.806(16)	1.920(17)	2.7004(16)	163(2)
O5W-H5AW	O2W	0.795(16)	1.893(16)	2.6814(16)	171(2)
O3W-H3AW	O4W ^{viii}	0.807(16)	2.187(17)	2.8904(16)	146(2)
O3W-H3BW	O17 ^{ix}	0.810(16)	1.982(16)	2.7844(16)	170(2)

ⁱ [-1-x, -y, -z]; ⁱⁱ [-x, -y+1, -z+1]; ⁱⁱⁱ [-x, -y+1, -z]; ^{iv} [-x, -y, -z]; ^v [x+1, y, z]; ^{vi} [x, y-1, z];

^{vii} [x-1, y-1, z]; ^{viii} [x-1, y, z]; ^{ix} [-x, -y+2, -z+1]

4.6 Metal-Orotate complexes with DNA bases

During the experimental work for this project, research was also conducted on synthesising H-bonded networks of metal-orotate complexes with DNA bases. Crystal growth for these systems was performed by varying different parameters such as: the solvent, ratios of the precursors, the order of addition, pH, reaction times and reaction temperature. One of the endeavours in these synthetic tasks was to achieve full control of the coordination modes of the orotate anion. As a result, varying stoichiometric amounts of orotic acid were used in order to facilitate the coordination of one or two orotate anions to the metal centre. The organic bases used for these reactions were the DNA bases: adenine, thymine, cytosine and guanine.

It was anticipated that there would be strong hydrogen bonding interactions between DNA bases and orotic acid, given that orotic acid could recognise DNA bases. A survey of the CSD revealed that no work had been reported on the hydrogen bonded networks of orotic acid with DNA bases. Given the previously reported binding modes of adenine to the metal centre^{105, 197}, it was predicted that using stoichiometric amounts of metal (II) acetate, orotic acid and adenine would give rise to a neutral coordination complex as shown below in Figure 4.46.

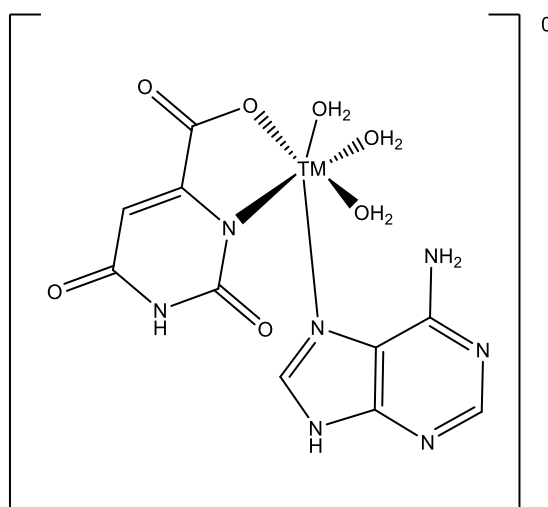


Figure 4.46: Possible coordination of orotic acid and adenine to transition metals

It is clear from Figure 4.46 that the overall charge in the complex is zero. At this phase of method development, the logical step was to alter the stoichiometric amounts wherein the concentration of the orotic acid in the system would be double that of the metal (II) and adenine. It was hypothesised that such preparation would lead to two chelate bindings of the ligand to the metal which, in turn, would lead to an overall charge 2-. Therefore, neutrality in the molecule would be achieved by two adeninium molecules hydrogen-bonded to the two orotate ligands shown in Figure 4.47. The inspiration for this work came from the findings with 2,6-dipicolinic acid and adeninium discussed in results section 4.4.3.1 of this thesis and work of Das and co-workers.¹⁰⁶

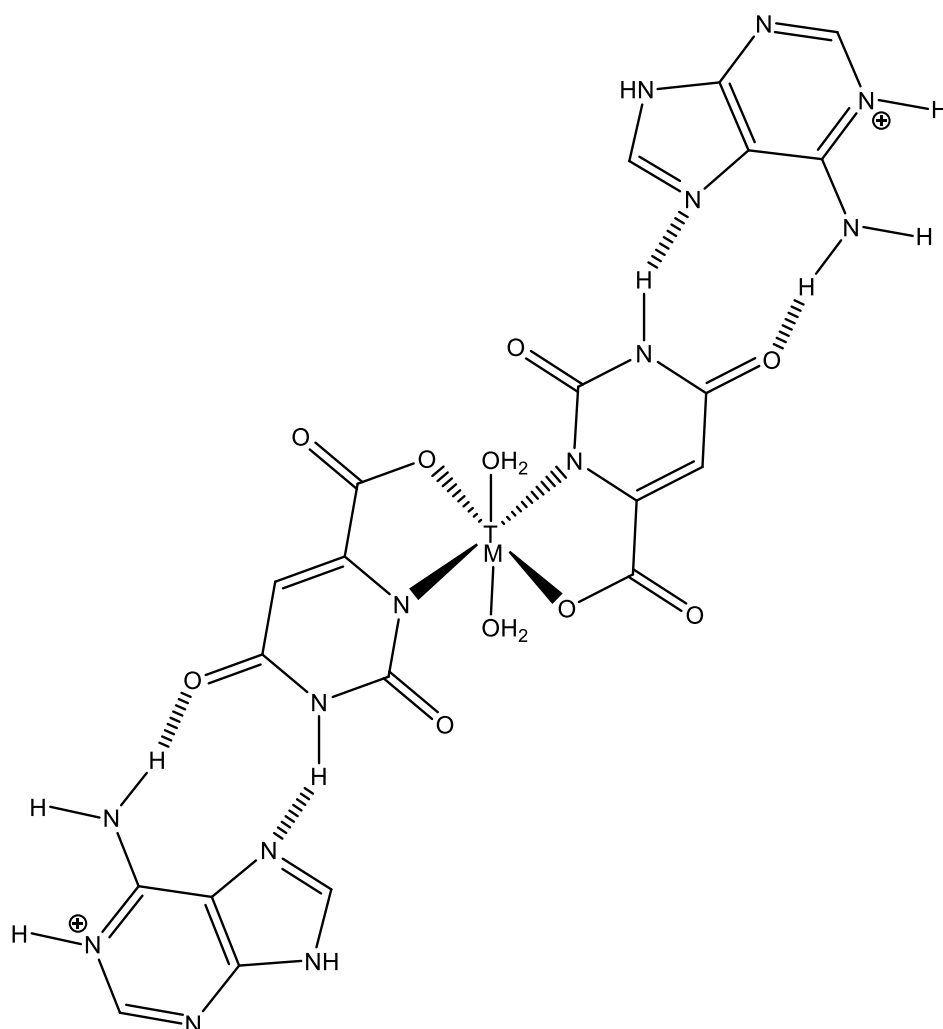


Figure 4.47: Predicted hydrogen bonding between adeninium and orotate ligand

It is evident from Figure 4.47 that the expected adeninium-ototate intermolecular interaction would lead to a $R_2^2(9)$ heterosynthon involving the Hoogsteen mode of hydrogen bonding in adenine. Since the most stable protonated form of adenine is [1H, 9H]-adeninium⁶¹, it was initially predicted that this form could be incorporated in the crystal. Based on this prediction, adeninium would interact with the ligand *via* its Hoogsteen sites. However, neither of the two approached yielded crystals.

4.7 Chapter Outlook and Conclusions

The results discussed in this chapter demonstrate the ability of nucleobases or their derivatives to be incorporated in coordination complexes. The objective of this study was to exploit both the hydrogen bonding and the metal coordination sites of nucleobases in generating hydrogen-bonded networks. The work presented in this chapter expands further the understanding on the way in which nucleobases interact in the presence of transition metals. Solubility challenges encountered during the work present in Chapter 3, persisted also for the research conducted as part of this chapter. However, it was observed that in many cases the deprotonation of the ligand generated a more acidic solution, which assisted the dissolution of the DNA bases.

Metal-dipicolinate complexes treated with DNA bases afforded hydrogen-bonded networks where protonated DNA bases interacted with the ligand *via* hydrogen bonding. In the adeninium example, two protonated forms were observed which interact with one another to generate ribbons. This, however, was not observed in the case of cytosinium, which did not form any direct interaction with itself. This chapter provides further evidence on the role of water molecules in a system by evaluating the anhydrous cytosinium-metal-dipicolinate complex *versus* the pentahydrate complex. The similarity in both systems is that neither of the protonated cytosinium molecules interacts directly *via* hydrogen bonding. However, incorporation of water increases the interaction of two cytosinium molecules by forming a $R_4^4(12)$ heterosynthon. Both these systems also

displayed π - π stacking interactions. It was found that performing the reaction in an aqueous solution leads to the incorporation of water in the structure. These water molecules formed hydrogen bonds to generate the lowest energy form. However, performing the reaction in the absence of water afforded a different structure.

The chelating nature of orotic acid was exploited extensively in growing hydrogen-bonded networks with various N-donors. The work presented herein demonstrates that a minor change in the level of hydration has major implications on synthon formation and crystal packing. The 3-nicotinamide analogue (compound **(I)**) presented in this thesis is different from the one reported in literature (VEVZIG) in that it lacks a water molecule and this breaks the symmetry. This is associated with a change in the crystal packing so that the orotate-nicotinamide heterosynthon observed in VEVZIG is not present in this structure. Instead, the formation of an orotate-orotate homosynthon was observed. The initial prediction based on synthon theory was that an orotate-nicotinamide heterosynthon would form. However, the emergence of the unexpected orotate-orotate homosynthon shows limitations of the synthon theory and demonstrates that the presence of water molecules complicates predictions based on this theory.

The chapter also demonstrates how changing the position of the amide functional group has major ramifications on crystal packing and synthon formation. The 4-nicotinamide analogue (compound **(J)**) obtained is interesting in that it does not form the orotate-orotate homosynthon or the orotate-nicotinamide heterosynthon. These two synthons were observed in compound **(I)** and VEVZIG. Instead, other forms of interactions govern the crystal packing in compound **(J)**. These are π - π stacking interactions and the hydrogen bonding of water molecules.

Some of the conclusions drawn from Chapter 3 are also applicable for the systems described in Chapter 4. While the work presented in this chapter expands the understanding of interactions between carboxylic acid derivatives of DNA bases, it also shows that the crystal engineer continues to face the challenges previously described by John Maddox in 1988.¹

It remains a challenge to predict which synthons will prevail in a crystal simply by scrutinising the structure of the individual molecules. This demonstrates the need for a deeper understanding of the cumulative effect of intermolecular interactions in a given crystal. These challenges are likely to persist until we reach a stage where computation on crystal structure prediction (CSP) is optimised and can handle more complex systems, which would help in rationalising the synthon theory.

5.0 APPENDICES

Appendix 1 – Crystal Data and Structure Refinement Tables

The content below provides information on the crystal structures discussed in the thesis “DNA Bases in Crystal Engineering”.

CHAPTER 3

- Table for Guaninium Sulphate Hydrate/Anhydrous structures (1a), (1b), (1c)
- Table for Cytosine:Phenanthroline co-crystals (cyt:phen)
- Table for Melaminium Nitrilotriacetate Trihydrate salt $(MH^+)_2nta^{2-}\cdot 3H_2O$
- Table for Thymine Acetic Acid Dihydrate (tac \cdot 2H₂O)
- Table for Cytosine:2-nitroterephthalic acid co-crystals (caff:2

Table for Guaninium Sulphate Hydrate/Anhydrous structures (1a), (1b), (1c)

Identification	1a	1b	1c
Empirical formula	C ₂₀ H ₃₀ N ₂₀ O ₁₇ S ₂	C ₂₀ H ₃₀ N ₂₀ O ₁₅ S ₂	C ₂₀ H ₂₄ N ₂₀ O ₁₂ S ₂
Formula weight	886.78	854.78	800.73
Temperature (K)	150(2)	120(2)	120(2)
Wavelength (Å)	0.71073	0.71073	0.71073
Crystal system	Triclinic	Triclinic	Triclinic
Space group	$P\bar{1}$	$P\bar{1}$	$P\bar{1}$
Unit cell dimensions	$a = 9.6300(19) \text{ \AA}$; $\alpha = 78.627(15)^\circ$ $b = 9.8613(19) \text{ \AA}$; $\beta = 71.518(15)^\circ$ $c = 10.5872(19) \text{ \AA}$; $\gamma = 63.260(14)^\circ$	$a = 9.607(2) \text{ \AA}$; $\alpha = 77.400(19)^\circ$ $b = 9.796(3) \text{ \AA}$; $\beta = 71.603(18)^\circ$ $c = 10.542(2) \text{ \AA}$; $\gamma = 63.343(18)^\circ$	$a = 9.663(6) \text{ \AA}$; $\alpha = 85.44(5)^\circ$ $b = 12.692(8) \text{ \AA}$; $\beta = 85.65(5)^\circ$ $c = 13.139(8) \text{ \AA}$; $\gamma = 87.73(5)^\circ$
Volume (Å ³)	849.8(3)	837.9(3)	1600.8(18)
Z	1	1	2
Density (calculated) (Mg/m ³)	1.733	1.694	1.661
F(000)	458	442	824
Crystal size (mm ³)	0.48 × 0.09 × 0.04	0.46 × 0.19 × 0.07	0.45 × 0.05 × 0.04
Theta range for data collection	2.03 to 26.63°	2.34 to 26.16°	1.55 to 18.06°
Index ranges	-12 ≤ h ≤ 12, -12 ≤ k ≤ 12, -12 ≤ l ≤ 13	-10 ≤ h ≤ 11, -11 ≤ k ≤ 12, 0 ≤ l ≤ 12	-8 ≤ h ≤ 7, -11 ≤ k ≤ 11, -11 ≤ l ≤ 11
Reflections collected	10880	3303	6244
Independent reflections	3558 [R(int) = 0.0735]	3303 [R(int) = 0.1290]	2116 [R(int) = 0.1296]
Completeness to θ	99.6 % ($\theta = 26.63^\circ$)	98.7 % ($\theta = 26.16^\circ$)	94.8 % ($\theta = 18.06^\circ$)
Absorption correction	Analytical	Analytical	None performed
Max. and min. Transmission	0.9895 and 0.8831	0.9833 and 0.9161	0.8915 and 0.9896
Refinement method	Full-matrix least-squares on F ²	Full-matrix least-squares on F ²	Full-matrix least-squares on F ²
Data / restraints / parameters	3558 / 13 / 283	3303 / 10 / 274	2116 / 84 / 211
Goodness-of-fit on F ²	0.832	0.979	0.801
Final R indices [I > 2 σ (I)]	R1 = 0.0460, wR2 = 0.1063	R1 = 0.0684, wR2 = 0.1992	R1 = 0.0858, wR2 = 0.1845
R indices (all data)	R1 = 0.0850, wR2 = 0.1170	R1 = 0.1155, wR2 = 0.2131	R1 = 0.2090, wR2 = 0.2295
Largest diff. peak and hole	0.534 and -0.435 eÅ ⁻³	0.568 and -0.432 eÅ ⁻³	0.470 and -0.480 eÅ ⁻³

Table for Cytosine:Phenanthroline co-crystals (cyt:phen)

Identification code	cyt:phen
Empirical formula	C ₃₂ H ₂₆ N ₁₀ O ₂
Formula weight	582.63
Temperature	100(2) K
Wavelength	0.71073 Å
Crystal system	Monoclinic
Space group	P2 ₁ /c
Unit cell dimensions	$a = 20.765(2) \text{ \AA}$; $\alpha = 90^\circ$ $b = 9.4741(5) \text{ \AA}$; $\beta = 101.612(8)^\circ$ $c = 14.1307(13) \text{ \AA}$; $\gamma = 90^\circ$
Volume	2723.0(4) Å ³
Z	4
Density (calculated)	1.421 Mg/m ³
F(000)	1216
Crystal size	0.36 × 0.21 × 0.19 mm ³
Theta range for data collection	2.371 to 25.995°.
Index ranges	-24 ≤ h ≤ 25, -11 ≤ k ≤ 10, -17 ≤ l ≤ 17
Reflections collected	14509
Independent reflections	5269 [R(int) = 0.0993]
Completeness to theta = 25.242°	98.4 %
Absorption correction	Analytical
Max. and min. transmission	0.9856 and 0.9720
Refinement method	Full-matrix least-squares on F ²
Data / restraints / parameters	5269 / 0 / 397
Goodness-of-fit on F ²	0.867
Final R indices [I > 2σ(I)]	R1 = 0.0646, wR2 = 0.1527
R indices (all data)	R1 = 0.1035, wR2 = 0.1687
Largest diff. peak and hole	0.668 and -0.394 e.Å ⁻³

Table for Melaminium Nitrilotriacetate Trihydrate salt (MH⁺)₂nta²⁻·3H₂O

Identification code	(MH⁺)₂nta²⁻·3H₂O
Empirical formula	C ₁₂ H ₂₇ N ₁₃ O ₉
Formula weight	497.43
Temperature	150(2) K
Wavelength	0.71073 Å
Crystal system	Triclinic
Space group	<i>P</i> $\bar{1}$
Unit cell dimensions	$a = 6.7117(11)$ Å; $\alpha = 82.714(15)^\circ$ $b = 12.1495(19)$ Å; $\beta = 89.252(16)^\circ$ $c = 13.102(3)$ Å; $\gamma = 83.238(13)^\circ$
Volume (Å ³)	1052.4(3) Å ³
Z	2
Density (calculated)	1.563 Mg/m ³
Absorption coefficient	0.133 mm ⁻¹
F(000)	520
Crystal size (mm ³)	0.36 × 0.16 × 0.04
Theta range for data collection	1.70 to 25.30°
Index ranges	-8 ≤ h ≤ 7, -14 ≤ k ≤ 14, -15 ≤ l ≤ 15
Reflections collected	10946
Independent reflections	10946 [R(int) = 0.0000]
Completeness to θ	98.2 % $\theta = 25.30^\circ$
Absorption correction	Analytical
Max. and min. Transmission	0.9937 and 0.9566
Refinement method	Full-matrix least-squares on F ²
Data / restraints / parameters	10946 / 6 / 322
Goodness-of-fit on F ²	0.953
Final R indices [I > 2sigma(I)]	R1 = 0.0854, wR2 = 0.2175
R indices (all data)	R1 = 0.1423, wR2 = 0.2477
Largest diff. peak and hole	0.440 and -0.484 e.Å ⁻³

Table for Thymine Acetic Acid Dihydrate (tac•2H₂O)

Identification code	tac•2H₂O
Empirical formula	C ₇ H ₁₂ N ₂ O ₆
Formula weight	220.19
Temperature	150(2) K
Wavelength	0.71073 Å
Crystal system	Triclinic
Space group	<i>P</i> $\bar{1}$
Unit cell dimensions	<i>a</i> = 5.0805(9) Å; α = 103.221(14)° <i>b</i> = 7.6528(14) Å; β = 90.142(14)° <i>c</i> = 13.108(2) Å; γ = 103.123(14)°
Volume	482.37(15) Å ³
Z	2
Density (calculated)	1.516 Mg/m ³
Absorption coefficient	0.134 mm ⁻¹
F(000)	232
Crystal size	0.340 × 0.320 × 0.120 mm ³
Theta range for data collection	2.812 to 29.216°.
Index ranges	-6 ≤ <i>h</i> ≤ 5, -10 ≤ <i>k</i> ≤ 10, -16 ≤ <i>l</i> ≤ 17
Reflections collected	5094
Independent reflections	2574 [R(int) = 0.0418]
Completeness to theta = 25.242°	99.3 %
Absorption correction	Analytical
Max. and min. Transmission	0.9846 and 0.9581
Refinement method	Full-matrix least-squares on F ²
Data / restraints / parameters	2574 / 6 / 152
Goodness-of-fit on F ²	0.972
Final R indices [I > 2σ(I)]	R1 = 0.0332, wR2 = 0.0833
R indices (all data)	R1 = 0.0481, wR2 = 0.0881
Largest diff. peak and hole	0.345 and -0.188 e.Å ⁻³

Table for Cytosine:2-nitroterephthalic acid co-crystals (caf:2nitroTA)

Identification code	caf:2nitroTA
Empirical formula	C ₁₆ H ₁₅ N ₅ O ₈
Formula weight	405.33
Temperature	150(2) K
Wavelength	0.71073 Å
Crystal system	Monoclinic
Space group	<i>P</i> 2 ₁ /n
Unit cell dimensions	<i>a</i> = 8.1774(5) Å; α = 90° <i>b</i> = 7.1683(5) Å; β = 95.534(5)° <i>c</i> = 29.436(2) Å; γ = 90°
Volume	1717.4(2) Å ³
Z	4
Density (calculated)	1.568 Mg/m ³
Absorption coefficient	0.128 mm ⁻¹
F(000)	840
Crystal size	0.33 × 0.16 × 0.10 mm ³
Theta range for data collection	1.390 to 25.417°.
Index ranges	-7 ≤ <i>h</i> ≤ 9, -7 ≤ <i>k</i> ≤ 8, -35 ≤ <i>l</i> ≤ 35
Reflections collected	9282
Independent reflections	3147 [R(int) = 0.0506]
Completeness to theta = 25.242°	99.8 %
Absorption correction	Analytical
Max. and min. Transmission	0.9905 and 0.9792
Refinement method	Full-matrix least-squares on F ²
Data / restraints / parameters	3147 / 3 / 272
Goodness-of-fit on F ²	0.800
Final R indices [I > 2σ(I)]	R1 = 0.0385, wR2 = 0.0825
R indices (all data)	R1 = 0.0694, wR2 = 0.0878
Largest diff. peak and hole	0.313 and -0.222 e.Å ⁻³

CHAPTER 4

- **Table for compound (A) and (B)**
- **Table for compound (C) and (D)**
- **Table for compound (E)**
- **Table for compound (F)**
- **Table for compound (G) and (H)**
- **Table for compound (I)**
- **Table for compound (J)**

Table for compound (A) and (B)

Identification code	Compound (A)	Compound (B)
Empirical formula	C ₂₄ H ₂₄ N ₁₂ Ni O ₁₁	C ₂₄ H ₂₄ Co N ₁₂ O ₁₁
Formula weight	715.26	715.48
Temperature	150(2) K	150(2) K
Wavelength	0.71073 Å	0.71073 Å
Crystal system	Monoclinic	Monoclinic
Space group	<i>P</i> 2 ₁ /n	<i>P</i> 2 ₁ /n
Unit cell dimensions	$a = 9.6158(12) \text{ \AA}; \alpha = 90^\circ$ $b = 18.6175(19) \text{ \AA}; \beta = 6.674(9)^\circ$ $c = 16.1241(18) \text{ \AA}; \gamma = 90^\circ$	$a = 9.6494(10) \text{ \AA}; \alpha = 90^\circ$ $b = 18.6115(15) \text{ \AA}; \beta = 99.792(7)^\circ$ $c = 16.1731(14) \text{ \AA}; \gamma = 90^\circ$
Volume	2867.0(6) Å ³	2862.2(5)
Z	4	4
Density (calculated)	1.657 Mg/m ³	1.660 Mg m ⁻³
Absorption coefficient	0.761 mm ⁻¹	0.684 mm ⁻¹
F(000)	1472	1468
Crystal size	0.15 × 0.11 × 0.10 mm ³	0.33 × 0.32 × 0.17
Theta range for data collection	1.677 to 26.016°.	2.53 to 29.00°
Index ranges	-11 ≤ h ≤ 11, -22 ≤ k ≤ 22, -19 ≤ l ≤ 19	-13 ≤ h ≤ 13, -25 ≤ k ≤ 23, -21 ≤ l ≤ 22
Reflections collected	18239	27181
Independent reflections	5612 [R(int) = 0.0653]	7456 [R(int) = 0.0809]
Completeness to theta	99.8 % $\theta = 25.242^\circ$	98.0 % $\theta = 29.00^\circ$
Absorption correction	0.9155 and 0.8574	0.9036 and 0.8789
Max. and min. transmission		
Refinement method	Full-matrix least-squares on F ²	Full-matrix least-squares on F ²
Data / restraints / parameters	5612 / 10 / 453	7456 / 9 / 453
Goodness-of-fit on F ²	0.808	0.948
Final R indices [I > 2σ(I)]	R1 = 0.0405, wR2 = 0.0811	R1 = 0.0446, wR2 = 0.1110
Largest diff. peak and hole	0.587 and -0.509 e.Å ⁻³	0.580 and -1.020 e.Å ⁻³

Table for compound (C) and (D)

Compound	Compound (C)	Compound (D)
Empirical formula	C ₂₂ H ₂₈ N ₈ NiO ₁₅	C ₂₂ H ₂₈ CoN ₈ O ₁₅
Formula weight	703.23	703.45
Temperature	150(2) K	150(2) K
Wavelength	0.71073 Å	0.71073 Å
Crystal system	Triclinic	Triclinic
Space group	$P\bar{1}$	$P\bar{1}$
Unit cell dimensions	$a = 9.3875(10)$ Å; $\alpha = 77.396(8)^\circ$ $b = 11.7119(13)$ Å; $\beta = 84.807(8)^\circ$ $c = 13.3876(13)$ Å; $\gamma = 82.662(9)^\circ$	$a = 9.3277(11)$ Å; $\alpha = 78.002(10)^\circ$ $b = 11.7705(14)$ Å; $\beta = 4.360(10)^\circ$ $c = 13.4074(17)$ Å; $\gamma = 82.993(9)^\circ$
Volume (Å ³)	1421.7(3) Å ³	1425.1(3)
Z	2	2
Density (calculated)	1.643 Mg/m ³	1.639 Mg m ⁻³
Absorption coefficient	0.772 mm ⁻¹	0.691 mm ⁻¹
F(000)	728	726
Crystal size (mm ³)	0.400 × 0.380 × 0.160	0.5 × 0.4 × 0.065
Theta range for data collection	2.608 to 29.997°	2.59 to 29.00°
Index ranges	-11 ≤ h ≤ 13, -16 ≤ k ≤ 16, -18 ≤ l ≤ 18	-12 ≤ h ≤ 12, -5 ≤ k ≤ 16, -18 ≤ l ≤ 18
Reflections collected	22495	16790
Independent reflections	8275 [R(int) = 0.0478]	7537 [R(int) = 0.0454]
Completeness to theta	99.9 % $\theta = 25.242$	99.4 % $\theta = 29.00^\circ$
Absorption correction	Analytical	Analytical
Max. and min. transmission	0.7352 and 0.8848	0.7254 and 0.9511
Refinement method	Full-matrix least-squares on F ²	Full-matrix least-squares on F ²
Data / restraints / parameters	8275 / 47 / 463	7537 / 47 / 463
Goodness-of-fit on F ²	0.951	0.829
Final R indices [I > 2σ(I)]	R1 = 0.0392, wR2 = 0.0963	R1 = 0.0332, wR2 = 0.0685
R indices (all data)	R1 = 0.0558, wR2 = 0.1017	R1 = 0.0582, wR2 = 0.0730
Largest diff. peak and hole	0.518 and -0.981 e.Å ⁻³	0.457 and -0.619 e.Å ⁻³

Table for compound (E)

Compound	Compound (E)
Empirical formula	C ₂₂ H ₁₈ CoN ₈ O ₁₀
Formula weight	613.37
Temperature	150(2) K
Wavelength	0.71073 Å
Crystal system	Triclinic
Space group	$P\bar{1}$
Unit cell dimensions	$a = 9.7016(10)$ Å; $\alpha = 108.236(8)^\circ$ $b = 9.8965(10)$ Å; $\beta = 108.146(8)^\circ$ $c = 14.1311(14)$ Å; $\gamma = 91.213(8)^\circ$
Volume (Å ³)	1213.9(2)
Z	2
Density (calculated)	1.678 Mg m ⁻³
Absorption coefficient	0.784 mm ⁻¹
F(000)	626
Crystal size (mm ³)	0.31 × 0.17 × 0.07
Theta range for data collection	2.91 to 32.50°
Index ranges	-14 ≤ h ≤ 14, -14 ≤ k ≤ 14, -21 ≤ l ≤ 21
Reflections collected	35433
Independent reflections	8770 [R(int) = 0.0849]
Completeness to θ	99.9 % $\theta = 32.50^\circ$
Absorption correction	Analytical
Max. and min. transmission	0.9484 and 0.7922
Refinement method	Full-matrix least-squares on F ²
Data / restraints / parameters	8770 / 27 / 382
Goodness-of-fit on F ²	0.998
Final R indices [I > 2sigma(I)]	R1 = 0.0436, wR2 = 0.1083
R indices (all data)	R1 = 0.0647, wR2 = 0.1160
Largest diff. peak and hole	0.599 and -1.163 e.Å ⁻³

Table for compound (F)

Identification code	Compound (F)
Empirical formula	C ₁₅ H ₁₆ N ₄ Ni O ₆
Formula weight	407.01
Temperature	150(2) K
Wavelength	0.71073 Å
Crystal system	Monoclinic
Space group	<i>P</i> 2 ₁ / <i>c</i>
Unit cell dimensions	<i>a</i> = 8.8680(5) Å; α = 90°; <i>b</i> = 13.5207(10) Å; β = 97.161(5)°; <i>c</i> = 14.4961(10) Å; λ = 90°;
Volume	1724.5(2) Å ³
Z	4
Density (calculated)	1.568 Mg/m ³
Absorption coefficient	1.166 mm ⁻¹
F(000)	840
Crystal size	0.34 × 0.22 × 0.22 mm ³
Theta range for data collection	2.07 to 29.15°
Index ranges	-11 ≤ <i>h</i> ≤ 12, -18 ≤ <i>k</i> ≤ 18, -19 ≤ <i>l</i> ≤ 16
Reflections collected	24358
Independent reflections	4633 [R(int) = 0.0472]
Completeness to $\theta = 29.15^\circ$	99.8 %
Absorption correction	Analytical
Max. and min. Transmission	0.8380 and 0.7251
Refinement method	Full-matrix least-squares on F ²
Data / restraints / parameters	4633 / 16 / 260
Goodness-of-fit on F ²	0.765
Final R indices [I > 2σ(I)]	R1 = 0.0211, wR2 = 0.0410
R indices (all data)	R1 = 0.0383, wR2 = 0.0420
Largest diff. peak and hole	0.272 and -0.270 e.Å ⁻³

Table for compound (G) and (H)

Identification code	Compound (G)	Compound (H)
Empirical formula	C ₁₄ H ₁₂ Co N ₅ O ₅	C ₃₀ H ₂₂ Co ₂ N ₈ O ₁₀
Formula weight	387.22	772.41
Temperature (K)	150(2)	150 (2)
Wavelength	0.71073 Å	0.71073 Å
Crystal system	Triclinic	Monoclinic
Space group	$P\bar{1}$	P 2/n
Unit cell dimensions	$a = 9.344(9) \text{ \AA}$; $\alpha = 117.19(8)^\circ$ $b = 10.274(8) \text{ \AA}$; $\beta = 104.15(8)^\circ$ $c = 10.791(13) \text{ \AA}$; $\gamma = 101.75(7)^\circ$	$a = 12.321(6) \text{ \AA}$; $\alpha = 90^\circ$ $b = 15.950(5) \text{ \AA}$; $\beta = 92.42(5)^\circ$ $c = 17.213(11) \text{ \AA}$; $\gamma = 90^\circ$
Volume (Å ³)	831.6(16)	3380(3)
Z	2	4
Density (calculated) (mg/m ³)	1.546	1.518
Absorption correction	Not applied	Not applied
F(000)	394	590
Theta range for data collection	2.269 to 25.827°.	1.277 to 25.885°.
Index ranges	-9 ≤ h ≤ 11, -12 ≤ k ≤ 12, -13 ≤ l ≤ 10	-13 ≤ h ≤ 15, -19 ≤ k ≤ 19, -20 ≤ l ≤ 11
Reflections collected	1840	8609
Independent reflections	1536 [R(int) = 0.0837]	4929 [R(int) = 0.1955]
Completeness to theta = 25.242°	47.6 %	75.2 %
Refinement method	Full-matrix least-squares on F ²	Full-matrix least-squares on F ²
Data / restraints / parameters	1536 / 0 / 92	4929 / 9 / 178
Goodness-of-fit on F ²	0.719	0.676
Final R indices [I > 2σ(I)]	R1 = 0.0699, wR2 = 0.1420	R1 = 0.0919, wR2 = 0.2023
R indices (all data)	R1 = 0.1707, wR2 = 0.1655	R1 = 0.3173, wR2 = 0.2691
Largest diff. peak and hole	0.399 and -0.319 e.Å ⁻³	0.628 and -1.035 e.Å ⁻³

Table for compound (I)

Identification code	Compound (I)
Empirical formula	C ₂₂ H ₃₄ N ₈ Ni ₂ O ₁₉
Formula weight	831.94
Temperature	150(2) K
Wavelength	0.71073 Å
Crystal system	Triclinic
Space group	<i>P</i> $\bar{1}$
Unit cell dimensions	<i>a</i> = 10.2282(11) Å; α = 81.421(9)° <i>b</i> = 11.2512(12) Å; β = 72.160(9)° <i>c</i> = 15.0832(18) Å; γ = 70.516(8)°.
Volume	1555.5(3) Å ³
Z	2
Density (calculated)	1.776 Mg/m ³
Absorption coefficient	1.310 mm ⁻¹
F(000)	860
Crystal size	0.28 x 0.16 x 0.09 mm ³
Theta range for data collection	1.923 to 27.514°.
Index ranges	-13 ≤ <i>h</i> ≤ 13, -14 ≤ <i>k</i> ≤ 12, -19 ≤ <i>l</i> ≤ 19
Reflections collected	16228
Independent reflections	7111 [R(int) = 0.0785]
Completeness to theta = 25.300°	99.2 %
Absorption correction	Analytical
Max. and min. Transmission	0.8912 and 0.7791
Refinement method	Full-matrix least-squares on F ²
Data / restraints / parameters	7111 / 27 / 517
Goodness-of-fit on F ²	0.859
Final R indices [<i>I</i> > 2σ(<i>I</i>)]	R1 = 0.0432, wR2 = 0.0942
R indices (all data)	R1 = 0.0841, wR2 = 0.1039
Largest diff. peak and hole	1.002 and -0.846 e.Å ⁻³

Table for compound (I)

Identification code	Compound (I)
Empirical formula	C ₁₁ H ₂₀ N ₄ Ni O ₁₁
Formula weight	442.99
Temperature	150(2) K
Wavelength	0.71073 Å
Crystal system	Triclinic
Space group	<i>P</i> $\bar{1}$
Unit cell dimensions	<i>a</i> = 7.2762(8) Å ; α = 106.335(8)° <i>b</i> = 9.9677(11) Å ; β = 93.241(9)° <i>c</i> = 12.5961(14) Å ; γ = 101.848(9)°
Volume	851.63(17) Å ³
Z	2
Density (calculated)	1.728 Mg/m ³
Absorption coefficient	1.208 mm ⁻¹
F(000)	460
Crystal size	0.48 × 0.35 × 0.16 mm ³
Theta range for data collection	1.697 to 29.175°
Index ranges	-9 ≤ <i>h</i> ≤ 9, -13 ≤ <i>k</i> ≤ 13, -17 ≤ <i>l</i> ≤ 17
Reflections collected	8458
Independent reflections	4456 [R(int) = 0.0358]
Completeness to theta = 25.242°	98.5 %
Absorption correction	Analytical
Max. and min. Transmission	0.9224 and 0.8762
Refinement method	Full-matrix least-squares on F ²
Data / restraints / parameters	4456 / 18 / 282
Goodness-of-fit on F ²	0.942
Final R indices [<i>I</i> > 2σ(<i>I</i>)]	R1 = 0.0256, wR2 = 0.0632
R indices (all data)	R1 = 0.0329, wR2 = 0.0647
Largest diff. peak and hole	0.448 and -0.348 e.Å ⁻³

6.0 REFERENCES

1. J. Maddox, *Nature*, 1988, **335**, 201.
2. G. M. Schmidt, *J. Pure Appl. Chem.*, 1971, **27**, 647.
3. R. Pepinsky, *Phys. Rev.*, 1955, **100**, 971.
4. M. Simard, D. Su and J. D. Wuest, *J. Am. Chem. Soc.*, 1991, **113**, 4696-4698.
5. G. R. Desiraju, *Crystal engineering : the design of organic solids*, Elsevier, Amsterdam ; Oxford, 1989.
6. A. Anthony, G. R. Desiraju, R. K. R. Jetti, S. S. Kuduva, N. N. L. Madhavi, A. Nangia, R. Thaimattam and V. R. Thalladi, *Crystal Engineering*, 1998, **1**, 1-18.
7. G. R. Desiraju, J. J. Vittal and A. Ramanan, *Crystal Engineering A Textbook*, World Scientific Publishing Co. Pte. Ltd., Singapore, 2011.
8. G. R. Desiraju, *Angew. Chem., Int. Ed.*, 2011, **50**, 52-59.
9. J. D. Dunitz, *X-Ray Analysis and the Structure of Organic Molecules*, 1979.
10. W. H. Bragg, *Proc. Phys. Soc. London*, 1921, **34**, 33.
11. G. R. Desiraju, *J. Am. Chem. Soc.*, 2013, **135**, 9952-9967.
12. J. D. Dunitz, *Chem. Commun.*, 2003, 545.
13. F. Allen, *Acta Crystallogr. Sect. B*, 2002, **58**, 380-388.
14. A. V. Trask, W. D. S. Motherwell and W. Jones, *Chem. Commun.*, 2004, 890-891.
15. G. R. Desiraju, *Angew. Chem., Int. Ed. Engl.*, 1995, **34**, 2311-2327.
16. G. R. Desiraju, J. J. Vittal and A. Ramanan, World Scientific Publishing Co. Pte. Ltd., Singapore, 2011, p. 216.
17. G. R. Desiraju, *The crystal as a supramolecular entity*, Wiley, Chichester, 1995.
18. A. I. Kitaigorodskii, *Molecular Crystals and Molecules*, 1973.
19. J. D. Dunitz and A. Gavezzotti, *Angew. Chem., Int. Ed.*, 2005, **44**, 1766-1787.
20. G. R. Desiraju, *Angew. Chem., Int. Ed.*, 2007, **46**, 8342-8356.
21. M. C. Etter, *J. Phys. Chem.*, 1991, **95**, 4601-4610.
22. M. C. Etter, *Acc. Chem. Res.*, 1990, **23**, 120-126.
23. A. Gavezzotti, *Synlett*, 2002, 201-214.
24. T. Beyer, T. Lewis and S. L. Price, *CrystEngComm*, 2001, **3**, 178-212.
25. G. R. Desiraju, *CrystEngComm*, 2002, **4**, 499-499.
26. J. D. Dunitz and W. B. Schweizer, *CrystEngComm*, 2007, **9**, 266-269.
27. T. Steiner, *Angew. Chem., Int. Ed.*, 2002, **41**, 48-76.
28. E. Arunan, G. R. Desiraju, R. A. Klein, J. Sadlej, S. Scheiner, I. Alkorta, D. C. Clary, R. H. Crabtree, J. J. Dannenberg, P. Hobza, H. G. Kjaergaard, A. C. Legon, B. Mennucci and D. J. Nesbitt, *Pure Appl. Chem.*, 2011, **83**, 1619-1636.
29. L. Pauling, *Nature of the Chemical Bond*, 3rd Edition., Cornell University Press, [S.l.], 1960.
30. E. Arunan, G. R. Desiraju, R. A. Klein, J. Sadlej, S. Scheiner, I. Alkorta, D. C. Clary, R. H. Crabtree, J. J. Dannenberg, P. Hobza, H. G. Kjaergaard, A. C. Legon, B. Mennucci and D. J. Nesbitt, *Pure Appl. Chem.*, 2011, **83**, 1637.
31. M. C. Etter, J. C. MacDonald and J. Bernstein, *Acta Crystallogr. Sect. B*, 1990, **46**, 256-262.
32. J. Bernstein, R. E. Davis, L. Shimoni and N. L. Chang, *Angew. Chem., Int. Ed.*, 1995, **34**, 1555-1573.
33. G. A. Jeffrey, *An Introduction to Hydrogen Bonding*, Oxford University Press, New York, 1997.
34. G. Gilli, F. Bellucci, V. Ferretti and V. Bertolasi, *J. Am. Chem. Soc.*, 1989, **111**, 1023-1028.
35. J. D. Watson and F. H. C. Crick, *Nature*, 1953, **171**, 737.

36. K. Hoogsteen, *Acta Crystallographica*, 1959, **12**, 822-823.
37. R. Taylor and O. Kennard, *J. Am. Chem. Soc.*, 1982, **104**, 5063-5070.
38. G. R. Desiraju and T. Steiner, *The weak hydrogen bond in structural chemistry and biology*, Oxford University Press, Oxford, 1999.
39. G. R. Desiraju, *Acc. Chem. Res.*, 1991, **24**, 290-296.
40. J.-M. Lehn, *Angew. Chem., Int. Ed. Engl.*, 1988, **27**, 89-112.
41. G. R. Desiraju, *J. Mol. Struct.*, 2003, **656**, 5-15.
42. F. H. Allen, W. D. S. Motherwell, P. R. Raithby, G. P. Shields and R. Taylor, *New J. Chem.*, 1999, **23**, 25.
43. W. Jones, C. R. Theocharis, J. M. Thomas and G. R. Desiraju, *J. Chem. Soc., Chem. Commun.*, 1983, **0**, 1443-1444.
44. G. R. Desiraju, *Acc. Chem. Res.*, 2002, **35**, 565-573.
45. S. S. Kuduva, D. C. Craig, A. Nangia and G. R. Desiraju, *J. Am. Chem. Soc.*, 1999, **121**, 1936-1944.
46. D. Musumeci, C. A. Hunter, R. Prohens, S. Scuderi and J. F. McCabe, *Chem. Sci.*, 2011, **2**, 883-890.
47. J. L. Cook, C. A. Hunter, C. M. R. Low, A. Perez-Velasco and J. G. Vinter, *Angew. Chem., Int. Ed. Engl.*, 2007, **46**, 3706-3709.
48. E. A. Losev and E. V. Boldyreva, *CrystEngComm*, 2014, **16**, 3857-3866.
49. C. B. Aakeroy, T. K. Wijethunga and J. Desper, *New J. Chem.*, 2014.
50. C. Janiak, *J. Chem. Soc. Dalton Trans.*, 2000, 3885-3896.
51. C. A. Hunter and J. K. M. Sanders, *J. Am. Chem. Soc.*, 1990, **112**, 5525-5534.
52. C. A. Hunter, J. F. McCabe and A. Spitaleri, *CrystEngComm*, 2012, **14**, 7115.
53. C. R. Martinez and B. L. Iverson, *Chem. Sci.*, 2012, **3**, 2191-2201.
54. A. D. Richards and A. Rodger, *Chem. Soc. Rev.*, 2007, **36**, 471-483.
55. L. Pauling and R. B. Corey, *Nature*, 1953, **171**, 346-346.
56. L. Pauling and R. B. Corey, *Proc. Natl. Acad. Sci. USA*, 1953, **39**, 84-97.
57. E. Chargaff, *Cell. Mol. Life Sci.*, 1950, **6**, 201-209.
58. J. D. Watson and F. H. C. Crick, *Nature*, 1953, **171**, 964-967.
59. L. J. Thompson, N. Elias, L. Male and M. Tremayne, *Cryst. Growth Des.*, 2013.
60. S. Mahapatra, S. K. Nayak, S. J. Prathapa and T. N. Guru Row, *Cryst. Growth Des.*, 2008, **8**, 1223-1225.
61. C. Marian, D. Nolting and R. Weinkauff, *Phys. Chem. Chem. Phys.*, 2005, **7**, 3306-3316.
62. I. J. Bruno, J. C. Cole, P. R. Edgington, M. Kessler, C. F. Macrae, P. McCabe, J. Pearson and R. Taylor, *Acta Crystallogr. Sect. B*, 2002, **58**, 389-397.
63. E. Vischer and E. Chargaff, *J. Biol. Chem.*, 1947, **168**, 781-782.
64. W. Clegg, A. J. Blake, R. O. Gould and P. Main, *Crystal Structure Analysis: Principles and practice*, Oxford University Press, 2001.
65. J. Pickworth Glusker and K. N. Toublewood, *Crystal Structure Analysis - A primer*, Oxford University Press, New York, 1985.
66. A. J. Blake, W. Clegg, J. M. Cole, J. S. O. Evans, P. Main, S. Parsons, and D. J. Watkin, *Crystal Structure Analysis*, International Union of Crystallography Texts on Crystallography, 2001.
67. C. Giacovazzo, H. L. Monaco, D. Viterbo, F. Scordari, G. Gilli, G. Zanotti and M. Catti, *Fundamentals of Crystallography*, International Union of Crystallography, New York, 1992.
68. W. C. Röntgen, Nobelprize.org, 1901.
69. L.-L. Ooi, *Principles of X-ray Crystallography*, Oxford University Press, Oxford, 2010.
70. M. Laing, *An Introduction to the Scope, Potential and Application of X-ray Analysis*, International Union of Crystallography, 1997.
71. Y. Waseda, E. Matsubara and K. Shinoda, *X-Ray Diffraction Crystallography: Introduction, Examples and Solved Problems*, Springer, 2011.
72. C. P. Brock and J. D. Dunitz, *Acta Crystallogr., Sect. B*, 1982, **38**, 2218-2228.

73. P. Main, in *Crystal Structure Analysis: Principles and Practice*, Oxford University Press., 2009.
74. W. Clegg, A. Blake, J. Cole, J. Evans, P. Main, S. Parson and D. Watkin, in *Crystal Structure Analysis: Principles and Practice*, Oxford University Press, 2009.
75. P. Muller, R. Herbst-Imer, A. Spek, T. Schneider and M. Sawaya, *Crystal Structure Refinement: A Crystallographer's Guide to SHELXL (International Union of Crystallography Texts on Crystallography)*, IUCr, 2006.
76. J. Evans, in *Crystal Structure Analysis: Principles and Practice*, Oxford University Press, 2009.
77. D. H. Williams and I. Fleming, *Spectroscopic Methods in Organic Chemistry*, McGraw Hill, 1995.
78. B. Stuart, *Infrared Spectroscopy: Fundamentals and Applications*, Wiley, 2004.
79. A. W. Coats and J. P. Redfern, *Analyst*, 1963, **88**, 906-924.
80. R. Thakuria, A. Delori, W. Jones, M. P. Lipert, L. Roy and N. Rodríguez-Hornedo, *Int. J. Pharm.*, 2013, **453**, 101-125.
81. T. Frišćić and W. Jones, *J. Pharm. Pharmacol.*, 2010, **62**, 1547-1559.
82. C. B. Aakeroy and D. J. Salmon, *CrystEngComm*, 2005, **7**, 439-448.
83. A. R. Ling and J. L. Baker, *J. Chem. Soc.*, 1893, **63**, 1314.
84. N. Shan and M. J. Zaworotko, *Drug Discov. Today*, 2008, **13**, 440-446.
85. S. L. Childs, G. P. Stahly and A. Park, *Mol. Pharm.*, 2007, **4**, 323-338.
86. Ö. Almarsson and M. J. Zaworotko, *Chem. Commun.*, 2004, 1889.
87. K.-S. Huang, D. Britton, t. late Margaret C. Etter and S. R. Byrn, *J. Mater. Chem.*, 1997, **7**, 713-720.
88. B. R. Bhogala, S. Basavoju and A. Nangia, *CrystEngComm*, 2005, **7**, 551-562.
89. Z. J. Li, Y. Abramov, J. Bordner, J. Leonard, A. Medek and A. V. Trask, *J. Am. Chem. Soc.*, 2006, **128**, 8199-8210.
90. C. B. Aakeröy, I. Hussain and J. Desper, *Cryst. Growth Des.*, 2005, **6**, 474-480.
91. A. Cherouana, R. Bousboua, L. Bendjeddou, S. Dahaoui and C. Lecomte, *Acta Crystallogr., Sect. E*, 2009, **65**, o2285-o2286.
92. B. E. Hingerty, J. R. Einstein and C. H. Wei, *Acta Crystallogr., Sect. B*, 1981, **37**, 140-147.
93. V. Langer, K. Huml and J. Zachova, *Acta Crystallogr., Sect. B*, 1979, **35**, 1148-1152.
94. C. Singh, *Acta Crystallogr.*, 1965, **19**, 861-864.
95. A. L. Gillon, N. Feeder, R. J. Davey and R. Storey, *Cryst. Growth Des.*, 2003, **3**, 663-673.
96. M. U. A. Ahlqvist and L. S. Taylor, *Int. J. Pharm.*, 2002, **241**, 253-261.
97. C. L. Anderton, in *Pharmaceutical Analysis*, eds. D. C. Lee and M. Webb, Blackwell, Oxford, 2003, p. 221.
98. H. P. Stahl, in *Towards Better Safety of Drugs and Pharmaceutical Products: proceedings of the 39th International Congress of Pharmaceutical Sciences of F.I.P.*, ed. D. D. Braimar, Elsevier/North-Holland Biomedical Press, Amsterdam, 1980.
99. S. Byard, A. Abraham, P. J. T. Boulton, R. K. Harris and P. Hodgkinson, *J. Pharm. Sci.*, 2012, **101**, 176-186.
100. K. Fucke and J. W. Steed, *Water*, 2010, **2**, 333-350.
101. A. R. Kennedy, M. O. Okoth, D. B. Sheen, J. N. Sherwood, S. J. Teat and R. M. Vrcelj, *Acta Crystallogr., Sect. C*, 2003, **59**, o650-o652.
102. E.-E. Bendeif, S. Dahaoui, N. Benali-Cherif and C. Lecomte, *Acta Crystallogr. Sect. B*, 2007, **63**, 448-458.
103. A. Cherouana, N. Benali-Cherif and L. Bendjeddou, *Acta Crystallogr. Sect. E*, 2003, **59**, o180-o182.
104. M. Byres, P. J. Cox, G. Kay and E. Nixon, *CrystEngComm*, 2009, **11**, 135-142.
105. S. Verma, A. K. Mishra and J. Kumar, *Acc. Chem. Res.*, 2009, **43**, 79-91.
106. B. Das and J. B. Baruah, *Cryst. Growth Des.*, 2010, **10**, 3242-3249.
107. C. B. Aakeroy and K. R. Seddon, *Chem. Soc. Rev.*, 1993, **22**, 397-407.

108. Y. Aoyama, H. Onishi and Y. Tanaka, *Tetrahedron Lett.*, 1990, **31**, 1177-1180.
109. A. Kozma, S. Ibanez, R. Silaghi-Dumitrescu, P. J. Sanz Miguel, D. Gupta and B. Lippert, *Dalton Trans.*, 2012, **41**, 6094-6103.
110. in *X-AREA v 1.64*, STOE & Cie GmbH, Darmstadt, 2012.
111. G. Sheldrick, *Acta Crystallogr. Sect. A*, 2008, **64**, 112-122.
112. L. Palatinus and G. Chapuis, *J. Appl. Crystallogr.*, 2007, **40**, 786-790.
113. V. Petricek, M. Dusek, L. Palatinus and (2006), *Jana2006. The crystallographic computing system.*, 2006, Institute of Physics, Praha, Czech Republic.
114. K. Hoxha and T. J. Prior, *Solid State Sci.*, 2013, **23**, 102-108.
115. L. Farrugia, *J. Appl. Crystallogr.*, 1997, **30**, 565.
116. J. D. Watson, *The Double Helix: A personal account of the discovery of structure of DNA*, 1968.
117. J. N. Low, P. Tollin, D. W. Young and S. N. Scrimgeour, *Acta Crystallogr. Sect. C*, 1986, **42**, 1045-1047.
118. D. Matkovic-Calogovic and K. Sankovic, *Acta Crystallogr. Sect. C*, 1999, **55**, 467-469.
119. L. Bendheif, K. Bouchouit and N. Benali-Cherif, *Acta Crystallogr. Sect. E*, 2003, **59**, o1407-o1409.
120. T. C. Lewis and D. A. Tocher, *Acta Crystallogr. Sect. E*, 2005, **61**, o1023-o1025.
121. N. Schultheiss and A. Newman, *Cryst. Growth Des.*, 2009, **9**, 2950-2967.
122. P. Vishweshwar, J. A. McMahon, J. A. Bis and M. J. Zaworotko, *J. Pharm. Sci.*, 2006, **95**, 499-516.
123. N. Qiao, M. Li, W. Schlindwein, N. Malek, A. Davies and G. Trappitt, *Int. J. Pharm.*, 2011, **419**, 1-11.
124. M. Zegarac, E. Leksic, P. Sket, J. Plavec, M. Devcic Bogdanovic, D.-K. Bucar, M. Domic and E. Mestrovic, *CrystEngComm*, 2014, **16**, 32-35.
125. B. Puschner, R. H. Poppenga, L. J. Lowenstine, F. M. S. and P. A. Pesavento, *J. Vet. Diagn. Invest.*, 2007, **19**, 616-624.
126. T. Lee and P. Y. Wang, *Cryst. Growth Des.*, 2010, **10**, 1419-1434.
127. A. V. Trask, W. D. S. Motherwell and W. Jones, *Cryst. Growth Des.*, 2005, **5**, 1013.
128. T. Frišćić and W. Jones, *Cryst. Growth Des.*, 2009, **9**, 1621-1637.
129. H. Rietveld, *Journal of Appl. Crystallogr.*, 1969, **2**, 65-71.
130. A. C. Larson and R. B. Von Dreele, *General Structure Analysis System (GSAS), Los Alamos National Laboratory Report LAUR 86-748 (2000)*.
131. A. J. Cruz-Cabeza, S. Karki, L. Fabian, T. Friscic, G. M. Day and W. Jones, *Chem. Commun.*, 2010, **46**, 2224-2226.
132. A. J. Cruz-Cabeza, G. M. Day and W. Jones, *Chem.-Eur. J.*, 2008, **14**, 8830-8836.
133. N. Issa, P. G. Karamertzanis, G. W. A. Welch and S. L. Price, *Cryst. Growth Des.*, 2009, **9**, 442.
134. B. Sridhar, J. B. Nanubolu and K. Ravikumar, *CrystEngComm*, 2012, **14**, 7065-7074.
135. T. Balasubramanian, P. T. Muthiah and W. T. Robinson, *Bull. Chem. Soc. Jpn.*, 1996, **69**, 2919-2922.
136. S. R. Perumalla, E. Suresh and V. R. Pedireddi, *Angew. Chem., Int. Ed.*, 2005, **44**, 7752-7757.
137. C. C. P. da Silva, R. de Oliveira, J. C. Tenorio, S. B. Honorato, A. P. Ayala and J. Ellena, *Cryst. Growth Des.*, 2013, **13**, 4315-4322.
138. K. Radhakrishnan, N. Sharma and L. M. Kundu, *RSC Advances*, 2014, **4**, 15087-15090.
139. M. Tutughamiarso and E. Egert, *Acta Crystallogr., Sect. B*, 2012, **68**, 444-452.
140. A. Morales and M. I. Toral, *Analyst*, 1985, **110**, 1445-1449.
141. S. Ramakrishnan, E. Suresh, A. Riyasdeen, M. A. Akbarsha and M. Palaniandavar, *Dalton Trans.*, 2011, **40**, 3524-3536.
142. L. L. Koh, Y. Xu, A. K. Hsieh, B. Song, F. Wu and L. Ji, *Acta Crystallogr., Sect. C*, 1994, **50**, 884-886.
143. S. R. Perumalla, V. R. Pedireddi and C. C. Sun, *Cryst. Growth Des.*, 2013, **13**, 429-432.

144. S. Cherukuvada, G. Bolla, K. Sikligar and A. Nangia, *Cryst. Growth Des.*, 2013, **13**, 1551-1557.
145. J. Zhang, Y. Kang, Y.-H. Wen, Z.-J. Li, Y.-Y. Qin and Y.-G. Yao, *Acta Crystallogr., Sect. E*, 2004, **60**, o462-o463.
146. G. J. Perpetuo and J. Janczak, *Acta Crystallogr., Sect. C*, 2002, **58**, o112-o114.
147. B. Froschauer and M. Weil, *Acta Crystallogr., Sect. E*, 2012, **68**, o2553-o2554.
148. S. Eppel and J. Bernstein, *Cryst. Growth Des.*, 2009, **9**, 1683-1691.
149. H.-R. Xu, Q.-C. Zhang, Y.-P. Ren, H.-X. Zhao, L.-S. Long, R.-B. Huang and L.-S. Zheng, *CrystEngComm*, 2011, **13**, 6361-6364.
150. G. J. Perpétuo and J. Janczak, *Acta Crystallogr., Sect. C*, 2007, **63**, o301-o302.
151. K. Hoxha and T. J. Prior, *Acta Crystallogr., Sect. E*, 2013, **69**, o1674-o1675.
152. A. Mukherjee, P. Grobelny, T. S. Thakur and G. R. Desiraju, *Cryst. Growth Des.*, 2011, **11**, 2637.
153. B. Colthup, L. H. Daly and S. E. Wiberley, *Introduction to infrared and Raman spectroscopy*, Academic Press, 1975.
154. A. Huczyński, J. Janczak and B. Brzezinski, *J. Mol. Struct.*, 2009, **922**, 77-82.
155. S. Fujita, A. Takenaka and Y. Sasada, *Bull. Chem. Soc. Jpn.*, 1984, **57**, 1707-1712.
156. R. E. Marsh, R. Bierstedt and E. L. Eichhorn, *Acta Crystallogr.*, 1962, **15**, 310-316.
157. M.-C. Liu, W. Feng and J.-C. Ding, *Acta Crystallogr. Sect. E*, 2004, **60**, o1611-o1612.
158. T. J. Prior and A. J. Sharp, *J. Chem. Crystallogr.*, 2010, **40**, 630-633.
159. H. D. Clarke, K. K. Arora, H. Bass, P. Kavuru, T. T. Ong, T. Pujari, L. Wojtas and M. J. Zaworotko, *Cryst. Growth Des.*, 2010, **10**, 2152-2167.
160. G. Portalone, *Acta Crystallogr. Sect. E*, 2008, **64**, o656.
161. D. K. Bučar, R. F. Henry, X. Lou, T. B. Borchardt and G. G. Z. Zhang, *Chem. Commun.*, 2007, 525.
162. A. Mercer and J. Trotter, *Acta Crystallogr. Sect. B*, 1978, **34**, 450-453.
163. J. Wouters and L. Quéré, *Pharmaceutical Salts and Cocrystals*, 2012.
164. A. K. Mahapatra, P. Sahoo, S. Goswami and H.-K. Fun, *J. Mol. Struct.*, 2010, **963**, 63-70.
165. D. Braga, *J. Chem. Soc. Dalton Trans.*, 2000, 3705-3713.
166. G. R. Desiraju, *J. Chem. Soc. Dalton Trans.*, 2000, 3745-3751.
167. L. Brammer, *Chem. Soc. Rev.*, 2004, **33**, 476-489.
168. A. D. Burrows, C.-W. Chan, M. M. Chowdhry, J. E. McGrady and D. M. P. Mingos, *Chem. Soc. Rev.*, 1995, **24**, 329-339.
169. B. Lippert, *Coord. Chem. Rev.*, 2000, **200-202**, 487-516.
170. S. Sivakova and S. J. Rowan, *Chem. Soc. Rev.*, 2005, **34**, 9-21.
171. E. Freisinger, S. Meier and B. Lippert, *J. Chem. Soc. Dalton Trans.*, 2000, 3274-3280.
172. R. O. Sigel, E. Freisinger and B. Lippert, *J. Biol. Inorg. Chem.*, 2000, **5**, 287-299.
173. J. Thomas-Gipson, G. Beobide, O. Castillo, J. Cepeda, A. Luque, S. Perez-Yanez, A. T. Aguayo and P. Roman, *CrystEngComm*, 2011, **13**, 3301-3305.
174. S. Pérez-Yáñez, G. Beobide, O. Castillo, J. Cepeda, A. Luque and P. Román, *Cryst. Growth Des.*, 2012, **12**, 3324-3334.
175. G. Beobide, O. Castillo, J. Cepeda, A. Luque, S. Pérez-Yáñez, P. Román and J. Thomas-Gipson, *Coord. Chem. Rev.*, 2013, **257**, 2716-2736.
176. Y. Song, X. Yin, B. Tu, Q. Pang, H. Li, X. Ren, B. Wang and Q. Li, *CrystEngComm*, 2014, **16**, 3082-3085.
177. D. K. Patel, A. Domínguez-Martín, M. d. P. Brandi-Blanco, D. Choquesillo-Lazarte, V. M. Nurchi and J. Niclós-Gutiérrez, *Coord. Chem. Rev.*, 2012, **256**, 193-211.
178. P. Amo-Ochoa and F. Zamora, *Coord. Chem. Rev.*, 2014, **276**, 34-58.
179. D. Dobrzyńska and L. B. Jerzykiewicz, *J. Am. Chem. Soc.*, 2004, **126**, 11118-11119.
180. J. P. García-Terán, O. Castillo, A. Luque, U. García-Couceiro, G. Beobide and P. Román, *Inorg. Chem.*, 2007, **46**, 3593-3602.
181. J. P. García-Terán, O. Castillo, A. Luque, U. García-Couceiro, G. Beobide and P. Román, *Cryst. Growth Des.*, 2007, **7**, 2594-2600.

182. G. R. Desiraju, *J. Chem. Soc., Chem. Commun.*, 1991, 426-428.
183. E. Tynan, P. Jensen, A. C. Lees, B. Moubaraki, K. S. Murray and P. E. Kruger, *CrystEngComm*, 2005, **7**, 90-95.
184. I. Ucar, A. Bulut, O. Z. Yesilel, H. Olmez and O. Buyukgungor, *Acta Crystallogr., Sect C*, 2004, **60**, m563-m566.
185. O. Z. Yeşilel and O. Büyükgüngör, *Solid State Sci.*, 2007, **9**, 485-490.
186. Shugar D. and Fox J. J., *Biochim. Biophys. Acta*, 1952, **9**, 199.
187. D. A. Köse, B. Zümreoglu-Karan, O. Şahin and O. Büyükgüngör, *J. Mol. Struct.*, 2006, **789**, 147-151.
188. R. Wysokiński, B. Morzyk-Ociepa, T. Głowiak and D. Michalska, *J. Mol. Struct.*, 2002, **606**, 241-251.
189. I. Mutikainen, *Inorg. Chim. Acta*, 1987, **136**, 155-158.
190. M. Sabat, D. Zglinska and B. Jézowska-Trzebiatowska, *Acta Crystallogr., Sect. B*, 1980, **36**, 1187-1188.
191. A. Karipides and B. Thomas, *Acta Crystallogr., Sect. C*, 1986, **42**, 1705-1707.
192. A. G. Schneider, H. W. Schmalle, F. Arod and E. Dubler, *J. Inorg. Biochem.*, 2002, **89**, 227-236.
193. H. Erer, O. Z. Yeşilel, C. Darcan and O. Büyükgüngör, *Polyhedron*, 2009, **28**, 3087-3093.
194. O. Z. Yeşilel, H. Erer, G. Kaştaş and İ. Kani, *Polyhedron*, 2010, **29**, 2600-2608.
195. D. A. Kose, B. Zumreoglu-Karan, C. Unaleroglu, O. Sahin and O. Buyukgungor, *J. Coord. Chem.*, 2006, **59**, 2125-2133.
196. S. Fellows and T. J. Prior, Unpublished work, 2013.
197. M. A. Salam and K. Aoki, *Inorg. Chim. Acta*, 2000, **311**, 15-24.

